MINISTÉRIO DA CIÊNCIA, TECNOLOGIA E INOVAÇÃO
INSTITUTO NACIONAL DE PESQUISAS ESPACIAIS

**sid.inpe.br/mtc-m21d/2023/05.12.20.36-TDI**

# OBSERVATIONAL AND SIMULATION STUDY OF RAPID AND SMALL AMPLITUDE CO-SEISMIC IONOSPHERIC DISTURBANCES DURING WEAK TO STRONG EARTHQUAKES

Saúl Alejandro Sánchez Juarez

Doctorate Thesis of the Graduate Course in Space Geophysics, guided by Drs. Eurico Rodrigues de Paula, Esfhan Alam Kherani, and Elvira Astafyeva, approved in May 22, 2023.

URL of the original document:
<http://urlib.net/8JMKD3MGP3W34T/494KCJL>

INPE
São José dos Campos
2023

**PUBLISHED BY:**

Instituto Nacional de Pesquisas Espaciais - INPE
Coordenação de Ensino, Pesquisa e Extensão (COEPE)
Divisão de Biblioteca (DIBIB)
CEP 12.227-010
São José dos Campos - SP - Brasil
Tel.:(012) 3208-6923/7348
E-mail: pubtc@inpe.br

MINISTÉRIO DA CIÊNCIA, TECNOLOGIA E INOVAÇÃO
INSTITUTO NACIONAL DE PESQUISAS ESPACIAIS

**sid.inpe.br/mtc-m21d/2023/05.12.20.36-TDI**

# OBSERVATIONAL AND SIMULATION STUDY OF RAPID AND SMALL AMPLITUDE CO-SEISMIC IONOSPHERIC DISTURBANCES DURING WEAK TO STRONG EARTHQUAKES

Saúl Alejandro Sánchez Juarez

Doctorate Thesis of the Graduate Course in Space Geophysics, guided by Drs. Eurico Rodrigues de Paula, Esfhan Alam Kherani, and Elvira Astafyeva, approved in May 22, 2023.

URL of the original document:
<http://urlib.net/8JMKD3MGP3W34T/494KCJL>

INPE
São José dos Campos
2023

Cataloging in Publication Data

Sánchez Juarez, Saúl Alejandro.

Sa55o Observational and simulation study of rapid and small amplitude co-seismic ionospheric disturbances during weak to strong earthquakes / Saúl Alejandro Sánchez Juarez. – São José dos Campos : INPE, 2023.

xxiv + 167 p. ; (sid.inpe.br/mtc-m21d/2023/05.12.20.36-TDI)

Thesis (Doctorate in Space Geophysics) – Instituto Nacional de Pesquisas Espaciais, São José dos Campos, 2023.

Guiding : Drs. Eurico Rodrigues de Paula, Esfhan Alam Kherani, and Elvira Astafyeva.

1. Earthquakes. 2. Seismo-Atmosphere-Ionosphere (SAI). 3. Simulation of the SAI numerical and analytical code. 4. TEC-GNSS. 5. Coseismic ionospheric disturbances or Ionoquakes. I.Title.

CDU 550.34

MINISTÉRIO DA CIÊNCIA, TECNOLOGIA E INOVAÇÃO

**INSTITUTO NACIONAL DE PESQUISAS ESPACIAIS**

Serviço de Pós-Graduação - SEPGR

**DEFESA FINAL DE TESE DE SAÚL ALEJANDRO SÁNCHEZ JUAREZ**
**REG. 142573/2019, BANCA Nº 111/2023**

No dia 22 de maio de 2023, de forma online, o(a) aluno(a) mencionado(a) acima defendeu seu trabalho final (apresentação oral seguida de arguição) perante uma Banca Examinadora, cujos membros estão listados abaixo. O(A) aluno(a) foi APROVADO(A) pela Banca Examinadora, por unanimidade, em cumprimento ao requisito exigido para obtenção do Título de Doutor em Geofísica Espacial/Ciências do Ambiente Solar-Terrestre, com a exigência de que o trabalho final a ser publicado deverá incorporar as correções sugeridas pela Banca Examinadora, com revisão pelo(s) orientador(es).

**Título: "**Observational and simulation study of rapid and small amplitude co-seismic ionospheric disturbances during weak to strong earthquakes**"**

**Observações da banca:** o aluno tem 60 dias para incorporar as correções dos membros da banca no texto.

**Membros da banca:**

Dr. Marlos Rockenbach da Silva – Presidente – INPE
Dr. Eurico Rodrigues de Paula – Orientador – INPE
Dr. Esfhan Alam Kherani – Orientador – INPE
Dra. Elvira Astafyeva – Orientadora– IPGP
Dr. Alexandre Alvares Pimenta – Membro Interno – INPE
Dr. Jonas Rodrigues de Souza – Membro Interno – INPE
Dra. Virginia klausner de Oliveira – Membro externo – UNIVAP
Dr. Marcio Tadeu de Assis Honorato Muella - Membro externo - UNIVAP

Declaração de aprovação da Orientadora Elvira Astafyeva anexa ao processo.

---

sei! assinatura eletrônica

Documento assinado eletronicamente por **Marlos Rockenbach da Silva**, **Pesquisador**, em 28/06/2023, às 15:50 (horário oficial de Brasília), com fundamento no § 3º do art. 4º do Decreto nº 10.543, de 13 de novembro de 2020.

---

sei! assinatura eletrônica

Documento assinado eletronicamente por **MARCIO TADEU DE ASSIS HONORATO MUELLA (E)**, **Usuário Externo**, em 28/06/2023, às 16:20 (horário oficial de Brasília), com fundamento no § 3º do art. 4º do Decreto nº 10.543, de 13 de novembro de 2020.

---

sei! assinatura eletrônica

Documento assinado eletronicamente por **Jonas Rodrigues de Souza**, **Pesquisador**, em 28/06/2023, às 16:42 (horário oficial de Brasília), com fundamento no § 3º do art. 4º do Decreto nº 10.543, de 13 de novembro de 2020.

---

Documento assinado eletronicamente por **Eurico Rodrigues de Paula**, **Pesquisador**, em 28/06/2023, às 17:03 (horário oficial de Brasília), com fundamento no § 3º do art. 4º do Decreto nº 10.543, de 13 de novembro de 2020.

Documento assinado eletronicamente por **Alexandre Alvares Pimenta**, **Pesquisadora**, em 29/06/2023, às 11:16 (horário oficial de Brasília), com fundamento no § 3º do art. 4º do Decreto nº 10.543, de 13 de novembro de 2020.

Documento assinado eletronicamente por **Virginia Klausner de Oliveira (E)**, **Usuário Externo**, em 29/06/2023, às 18:35 (horário oficial de Brasília), com fundamento no § 3º do art. 4º do Decreto nº 10.543, de 13 de novembro de 2020.

Documento assinado eletronicamente por **Esfhan Alam Kherani**, **Pesquisador**, em 03/07/2023, às 07:28 (horário oficial de Brasília), com fundamento no § 3º do art. 4º do Decreto nº 10.543, de 13 de novembro de 2020.

A autenticidade deste documento pode ser conferida no site https://sei.mcti.gov.br/verifica.html, informando o código verificador **11139490** e o código CRC **4652571E**.

**Referência:** Processo nº 01340.003878/2023-11 SEI nº 11139490

*A meus pais **Alejandro** e **Justina**, à meus irmãos*
***Hildebrando** e **Fraklin***

## ACKNOWLEDGEMENTS

I would like to thank my advisors from INPE Drs. Eurico Rodrigues de Paula and Esfhan Alam Kherani, and Dra. Elvira Astafyeva from IPGP/France for their constant guidance and support throughout my academic career and in the completion of this doctoral thesis. It was a privilege and an honor to work with the three people I admire. Their experience and knowledge in the field have been invaluable to me and I cannot thank them enough for all they have done for me.

I would like to thank the Brazilian government through CAPES for the Doctoral fellowship at INPE.

I thank my colleagues, friends, and family for their support and encouragement throughout this process. Your words of encouragement and understanding have been a constant source of motivation for me.

To the institutes that maintain the networks of GNSS receivers and seismographs in operation: UNAVCO, CDDIS, terras.gsi.go.jp, GEONET, IGP, CSN, SONEL, RBMC, EMBRACE, LISN, RAMSAC, UNAVCO, IRIS, USGS and NIED-F-net for providing the data.

Last but not least, I want to express my gratitude to all the people who work at the Brazilian INPE, especially the postgraduate program in Space Geophysics, and to all the professors I have had throughout my academic career. Their knowledge and teachings have been essential for my academic and personal training.

**ABSTRACT**

The ionosphere hosts co-seismic ionospheric disturbances or Ionoquakes during earthquakes due to Seismo-Atmosphere-Ionosphere (SAI) coupling, in which seismic vibration at the surface of the Earth triggers coupled energetics into the atmosphere and ionosphere in the form of various atmospheric/plasma waves. Ionoquake detection from Doppler radars, Total-Electron-Content (TEC) measurements from GNSS receivers, and magnetometers have revealed them to be the potential candidate for monitoring earthquake energetics in space. Continuous coverage around the globe from GNSS networks made it possible to monitor disturbances in TEC around seismic faults with high spatial/temporal resolutions and to detect ionoquakes unambiguously. This monitoring mode offers the possibility to connect ionoquakes energetics with earthquake energetics such as the magnitude, vertical ground velocity (or "uplift"), seismic energy, and epicenter location of an earthquake. Moreover, continuous monitoring may facilitate the rapid detection of the ionoquakes in Near-Real-Time (NRT) when the earthquake mainshock is still on. Currently, no reliable tools provide information on earthquake energetics from monitoring the attributes of ionoquakes. Also, no report is available on the rapid ionoquake detection in less than 400 seconds from the mainshock, a progressive scenario towards NRT monitoring of ionoquakes. This thesis aims to deal with these unresolved research topics and focuses on the following specific issues: (1) Detection of the ionoquakes associated with moderate and weak earthquakes, (2) Detection of the rapid ionoquakes and their validation with the simulation, (3) Quantification of the relation between ionoquake and earthquake energetics. The thesis executes the following tasks to address these issues: (1) Develop a strategy to detect ionoquakes associated with moderate and weak earthquakes (Chapter 3), (2) Development of the fast mathematical solver for the ionoquake simulation (Chapter 4), (3) Development of methods to detect and monitor the energetics of rapid ionoquakes during few selected strong earthquakes (Chapter 5), (4) Validation of rapid ionoquake detections using fast simulation (Chapter 6), (5) Selection of recent 50 strong earthquakes for which TEC and seismometer data are available (Chapter 7). The main results of the thesis are the following: (1) In the combined framework of observation and simulation, ionoquake detection from moderate and weak earthquakes is possible; (2) New methodology detects rapid ionoquakes in 250-400 seconds from the time of peak seismic uplift; (3) The simulation validates the rapid ionoquake detection by producing the ionoquakes of similar energetics as those from observation; (4) The simulation produces rapid ionoquakes in a simulation time faster than their detection time; (5) Positive correlation larger than 0.8 between earthquake and ionoquake energetics.

Keywords: Earthquakes. Seismo-Atmosphere-Ionosphere (SAI). Simulation of the SAI numerical and analytical code. TEC-GNSS. Co-seismic ionospheric disturbances or Ionoquakes. Rapid ionoquakes.

## ESTUDO OBSERVACIONAL E DE SIMULAÇÃO DE DISTÚRBIOS IONOSFÉRICOS CO-SÍSMICOS RÁPIDOS E DE PEQUENA AMPLITUDE DURANTE TERREMOTOS FRACOS A FORTES


### RESUMO

A ionosfera hospeda distúrbios ionosféricos co-sísmicos ou Ionoquakes durante terremotos devido ao acoplamento sismo-atmosfera-ionosfera (SAI), no qual a vibração sísmica na superfície da Terra desencadeia energias acopladas na atmosfera e ionosfera na forma de vários efeitos ondas atmosféricas/ondas de plasma. A detecção de ionoquake de radares Doppler, medições de conteúdo total de elétrons (TEC) de receptores GNSS e magnetômetros revelaram que eles são o candidato potencial para monitorar a energia do terremoto no espaço. A cobertura contínua em todo o mundo a partir de redes GNSS tornou possível monitorar distúrbios no TEC em torno de falhas sísmicas com altas resoluções espaço/temporais e detectar ionoquakes inequivocamente. Este modo de monitoramento oferece a possibilidade de conectar energias de ionoquakes com energias de terremotos, como magnitude, velocidade vertical do solo (ou "elevação"), energia sísmica e localização do epicentro de um terremoto. Além disso, o monitoramento contínuo pode facilitar a detecção rápida dos ionoquakes em tempo quase real (NRT) quando o tremor principal do terremoto ainda está ativo. Atualmente, nenhuma ferramenta confiável fornece informações sobre a energia dos terremotos a partir do monitoramento dos atributos dos ionoquakes. Além disso, nenhum relatório está disponível sobre a detecção rápida de ionoquake em menos de 400 segundos a partir do tremor principal, um cenário progressivo em direção ao monitoramento NRT de ionoquakes. Esta tese visa lidar com esses tópicos de pesquisa não resolvidos e se concentra nas seguintes questões específicas: (1) Detecção dos ionoquakes associados a sismos moderados e fracos, (2) Detecção dos ionoquakes rápidos e sua validação com a simulação, (3) Quantificação da relação entre ionoquakes e energia sísmica. A tese executa as seguintes tarefas para abordar essas questões: (5) Desenvolver uma estratégia para detectar ionoquakes associados a terremotos moderados e fracos (Capítulo 3), (2) Desenvolvimento do solucionador matemático rápido para a simulação de ionoquake (Capítulo 4), (3) Desenvolvimento de métodos para detectar e monitorar a energia de ionoquakes rápidos durante alguns terremotos fortes selecionados (Capítulo 5), (4) Validação de detecções rápidas de ionoquake usando simulação rápida (Capítulo 6), (1) Seleção de 50 terremotos fortes recentes para os quais dados TEC e sismômetros estão disponíveis (Capítulo 7). Os principais resultados da tese são os seguintes: (1) No quadro combinado de observação e simulação, é possível a detecção de ionoterremotos de terremotos moderados e fracos. (2) Nova metodologia detecta ionoquakes rápidos em 250-400 segundos a partir do momento do pico da elevação sísmica; (3) A simulação valida a detecção rápida de ionoquake produzindo os ionoquakes de energéticas similares aos da observação; (4) A simulação produz ionoquakes rápidos em um tempo de simulação mais rápido que o tempo de detecção; (5) Correlação positiva maior que 0,8 entre as energéticas de terremotos e ionoterremotos.



Keywords: Terremotos. Sismo-Atmosfera-Ionosfera (SAI). Simulação de SAI do código numérico e analítico. TEC-GNSS. Distúrbios ionosféricos co-sísmicos ou ionoquakes. Ionoquakes rápidos.

## LIST OF FIGURES

## LIST OF TABLES

**Page**

## LIST OF SYMBOLS

| | |
|---|---|
| $\rho$ | – Atmospheric density |
| $\gamma$ | – Adiabatic constant |
| $p$ | – Atmospheric pressure |
| $R$ | – Gas constant |
| $T$ | – Atmospheric temperature |
| $\vec{g}$ | – Gravitational acceleration |
| $\eta_1$ | – First dynamic viscosity |
| $\eta_2$ | – Second dynamic viscosity |
| $\vec{u}_0$ | – Atmospheric background wind |
| $\eta_1'$ | – First kinematic viscosity |
| $\eta_2'$ | – Second kinematic viscosity |
| $c$ | – Speed of sound |
| $\Pi_\nu$ | – Contributions of viscosity |
| $\Pi_{nl}$ | – Contributions of nonlinear saturation |
| $\omega$ | – Angular frequency of the wave |
| $(k_h, k_z)$ | – Wave numbers in the horizontal and vertical directions |
| $\omega_a$ | – Acoustic cut-off frequency |
| $\omega_g$ | – Brunt-Väisälä frequency |
| $\vec{V}$ | – Final movement or disturbed ionosphere |
| $\vec{\mathrm{v}}_{s=i/e}$ | – Plasma motion of ions/electrons |
| $n_s$ | – Number density |
| $\vec{\mathrm{v}}_s$ | – Velocity of the ionospheric plasma fluid |
| $\vec{\mathrm{B}}$ | – Earth's magnetic field |
| $\vec{\mathrm{E}}$ | – Electric field |
| $\underline{\sigma}$ | – Ionospheric conductivity tensor |
| $s_l$ | – Speed of light in vacuum |
| $\vec{J}_w$ | – Ionospheric current density |
| $\vec{\mathrm{v}}_i^w$ | – Ion velocitie |
| $\vec{\mathrm{v}}_e^w$ | – Electron velocitie |
| $\nu_s$ | – Collision frequency |
| $H$ | – Scale height |
| sTEC | – Slant TEC |
| vTEC | – Vertical TEC |
| $r_e$ | – Earth's radius |
| $H_{ION}$ | – Altitude of the ionospheric thin layer |
| $\theta_{el}$ | – Elevation angle of the satellite |
| $\mathrm{C_{cf}}$ | – Cross-correlation coefficient |
| $\mathrm{V_{SISM}}$ | – Vertical ground velocity or uplift |
| $\Omega_b$ | – Non-isothermal non-hydrostatic Brunt-Vaisala frequency |
| $u_z$ | – Vertical propagation of AGWs |
| $u_y$ | – Horizontal propagation of AGWs |
| $\frac{\omega}{k_z}$ | – Vertical phase velocity |

CONTENTS

Page

## 1 INTRODUCTION

Earthquakes (EQs) can generate disturbances in the ionosphere, referred to as Co-seismic Ionospheric disturbances (CID, or "ionoquakes"). The seismic vibrations at the ground trigger coupled energetics in the overlying geosphere that transfer a significant part of the seismic energy and momentum to the atmosphere and ionosphere (CALAIS; MINSTER, 1995; CALAIS; MINSTER, 1998; ARTRU et al., 2004; LOGNONNÉ, 2009; ASTAFYEVA et al., 2014; AFRAIMOVICH et al., 2013; ASTAFYEVA, 2019b; SANCHEZ et al., 2022; SUNIL et al., 2022). This Seismo-Atmosphere-Ionosphere (SAI) coupling involves upward propagating atmospheric waves, namely, the Acoustic-Gravity waves (AGWs) that amplify the seismic vibration by 3-4 orders of magnitudes at the ionospheric heights and causes disturbances in ionospheric density and currents (KHERANI et al., 2009). Ionoquakes are more often detected in the form of Total Electron Content (TEC) disturbances, deducted from the networks of Global Navigation Satellite System (GNSS) where the TEC is the integrated electron density along the line-of-sight (LOS) that connects the receiver and satellite (CALAIS; MINSTER, 1998; HEKI; PING, 2005; ASTAFYEVA et al., 2009; ROLLAND et al., 2011b; CAHYADI; HEKI, 2015). Ionoquake detections from other instruments such as magnetometers (IYEMORI et al., 2005; UTADA et al., 2011; IYEMORI et al., 2013), barometers (IYEMORI et al., 2013) and, ionospheric Doppler radars (DAVIES; BAKER, 1965; ARTRU et al., 2004) have confirmed the fundamental role of SAI coupling mechanism energized by AGWs in the generation of ionoquakes.

One of the most important seismological features of an EQ is the moment magnitude (Mw) and position of the co-seismic crustal vertical displacement, which serves as a source for generating ionoquakes (CAHYADI; HEKI, 2015; ASTAFYEVA; SHULTS, 2019). The main characteristic of the ionoquakes is the amplitude, which has a very strong dependence on the Mw of an EQ, that is, the more powerful the EQ, the greater its impact on the ionosphere (ASTAFYEVA et al., 2013; ASTAFYEVA et al., 2014; CAHYADI; HEKI, 2015; SUNIL et al., 2021; BRAVO et al., 2022). However, the amplitude of the ionoquakes depends on other EQ parameters, such as focal mechanism, focal depth, seismic energy, vertical ground displacement, and vertical ground velocity (DUCIC et al., 2003; ASTAFYEVA et al., 2009; KHERANI et al., 2012; HEKI, 2021; SUNIL et al., 2021; BRAVO et al., 2022; SANCHEZ et al., 2022). Also, the amplitude of the ionoquakes is affected by background atmospheric/ionospheric conditions. This is because the background parameters vary significantly due to different solar and magnetic activity conditions, as well as seasonal, latitudinal, daytime, and nighttime variability (ROLLAND et al., 2013; ASTAFYEVA et al., 2014; CAHYADI; HEKI, 2015). Another aspect that must be taken into account to calculate the amplitude of the ionoquakes by the GNSS-TEC method is the geometry of the LOS of the satellite receiver. When the wave vectors of the ionoquakes and the LOS are perpendicular to each other, the disturbance measurements are of greater amplitude and when the wave vector is parallel to the LOS they have a minimum amplitude (AFRAIMOVICH et al., 2001; BAGIYA et al., 2019; ASTAFYEVA, 2019b; MANTA et al., 2020). Finally, also, the data analysis method to estimate the CID amplitude (ASTAFYEVA et al., 2014). In the past, several studies found that the amplitude of ionoquakes increases with the magnitude of an EQ and with the vertical ground displacement (ASTAFYEVA et al., 2013; CAHYADI; HEKI, 2015; SUNIL et al., 2021; BRAVO et al., 2022) though not all parameters were considered in these surveys. Astafyeva et al. (2013) investigated 11 impulse-only type EQs to correlate the Mw to the ionoquakes amplitudes and found a positive correlation. However, not all parameters that influence the TEC amplitude were taken into account and a bandpass filter was used in the analysis. Later, Cahyadi and Heki (2015) also compiled TEC data from 21 EQs, considering the three types of seismic faults: reverse, normal, and slip. Considering the maximum amplitude of the ionoquakes as a reference, they confirmed the positive correlation of this amplitude with the magnitude and moment of the EQs, but not with the vertical ground displacement. In addition, the data analysis used polynomial fitting to derive the TEC disturbances. Also Astafyeva et al. (2014) reported that slip fault EQs generate ionospheric disturbances of similar amplitude as normal fault EQs, while Cahyadi and Heki (2015) found that slip fault EQs generate minor disturbances. Bravo et al. (2022) as well shows the dependence of the ionoquakes on Mw for some earthquakes in South America, however, not all parameters were also considered. In addition, they only presented effects for very few EQs. On the other hand, one can also relate the amplitude of the ionoquakes with the seismic energy (e.g.; Heki (2021)) and vertical displacement (SUNIL et al., 2021). The present thesis focuses on the issue of quantifying the relation between earthquake and ionoquake energetics with minimal subjectivity conditions from the data analysis.

TEC disturbances have revealed the presence of various wavefronts of ionoquakes that propagate with acoustic speeds (i.e., 600 m/s - 1 km/s) and are detected within 480 - 600 seconds after the mainshock onset over the near-field seismic zone (HEKI; PING, 2005; KHERANI et al., 2012; CAHYADI; HEKI, 2015; THOMAS et al., 2018; ASTAFYEVA, 2019b). Such fast propagation facilitates the possibility of using ionoquakes to enhance the capability of early earthquake warnings (OCCHIPINTI,

2015; ASTAFYEVA; SHULTS, 2019).

In recent years, a few studies have reported early and rapid detection of ionoquakes, i.e., less than the "nominal" 480-600 seconds after the mainshock. For instance, the first ionoquakes for the 2011 Tohoku-oki EQ (Japan) were detected as early as 420-464 seconds from the EQ onset time (ASTAFYEVA et al., 2011; BAGIYA et al., 2020; CHUM et al., 2016). Early ionoquake detections (440 - 480 sec) have also been reported for the Mw 7.4 March 9, 2011, Sanriku-oki EQ in Japan (THOMAS et al., 2018; ASTAFYEVA, 2019b). As well, Kherani et al. (2012) has shown by simulation the development of TEC disturbances within 360 sec after the onset of the mainshock for the Tokyo-Oki EQ. Co-seismic geomagnetic disturbances seem to be even faster than the ionoquakes (e.g., Yen et al. (2015), Liu et al. (2016)), however, this thesis was focused on the TEC (observational and simulation) disturbances to detect the ionoquakes in less than 400 seconds from the mainshock onset.

Not all EQs can generate disturbances large enough to be detected in the ionosphere. Previously, it was reported that only EQs with magnitudes greater than 6.6 can generate detectable ionoquakes (CAHYADI; HEKI, 2015). Also, deep earthquakes are less efficient in the generation of ionoquakes (SUNIL et al., 2021). However, in some cases, even minor events can also be detected. This thesis demonstrates that the EQ of Mw 6.4 (Ridgecrest California, USA) of 4 July 2019 is the smallest event, ever recorded till date to produce the ionoquakes (SANCHEZ et al., 2022).

## 1.1 Thesis outline

The remaining chapters of this thesis are organized as follows:

- Chapter 2 presents a theoretical review of lithospheric waves generated by EQs. In turn, it explains how lithospheric waves can generate Acoustic-Gravity waves (AGWs). Later, it will be explained that the AGWs can generate the ionoquakes. Also, this chapter explains how ionoquakes are detected with GNSS-TEC. Additionally, it presents all the properties of the ionoquakes that are known up to now.

- Chapter 3 demonstrates for the first time the detection of Ionoquakes with TEC data for moderate/weak Ridgecrest EQs. The magnitudes of the EQs are Mw 6.4 (main shock) and Mw 4.6 (aftershock). This chapter demonstrates the potential of TEC measurement to detect ionospheric counterparts of moderate and weak EQs.

- Chapter 4 presents a theoretical framework to simulate the rapid ionoquakes, based on Seismo-Atmosphere-Ionosphere (SAI) coupling energized by AGWs. This chapter presents a fast analytical simulation code, SAI-ANA code, of the SAI coupling mechanism for a typical EQ of magnitude 8. It also shows for the first time the rapid arrival of AGWs at ionospheric heights and the development of ionoquakes in less than 6 minutes from the mainshock onset. These rapid ionoquakes are among the most promising products of Near-Real-Time (NRT) ionospheric seismology.

- Chapter 5 presents a new methodology to compute the detection time and detection altitudes of ionoquakes. The methodology uses data from near-epicenter seismic stations to calculate the seismic peak time as an alternative to the EQ onset. This chapter presents the first report on the detection of ionoquake as soon as 400 seconds after the mainshock onset and 250-430 seconds after the seismic peak time.

- Chapter 6 presents the validation of rapid ionoquake detection using fast SAI-ANA code and associates them with the vertically fast propagating AGWs in the atmosphere.

- Chapter 7 presents an analysis of 50 EQs with Mw $\geq$ 6.6 and depth $<$ 60 km, which is associated with the EQs that occurred worldwide from 1994 to 2021. This chapter explains the amplitude relationship of ionoquakes with the characteristics of EQs such as Mw and vertical velocity, using data measurements from seismometers and TEC-GNSS, respectively.

# 2 LITERATURE REVIEW

## 2.1 Seismic and Atmospheric waves

### 2.1.1 First observations

The ionospheric effects produced by seismic activity have been known since the 1960s (BOLT, 1964; DAVIES; BAKER, 1965; BUCHACHENKO et al., 1996; SHALIMOV; GOKHBERG, 1998). There is currently an extensive literature documenting examples of coupling between terrestrial events and the ionosphere (LOGNONNÉ, 2009; ASTAFYEVA et al., 2009; ROLLAND et al., 2011b; UTADA et al., 2011; ASTAFYEVA et al., 2013; ASTAFYEVA et al., 2014; CAHYADI; HEKI, 2015; ASTAFYEVA, 2019b; SANCHEZ et al., 2022). This was caused by the need for timely prediction of large EQs that cause innumerable destructions and many hundreds of human deaths a year. In this regard, the study of the state of the ionosphere in response to large EQs is one of the most important tasks in geophysics.

### 2.1.2 Seismic waves

During an EQ, ground acceleration is measured in three directions: vertically (V or UD, up to down) and two perpendicular horizontal directions (H1 and H2), usually north-south (NS) and east-west (EW). This ground acceleration causes seismic waves that can be classified as primary (P), secondary (S), Rayleigh, and Love waves (KEAREY et al., 2002; LOWRIE, 2007). The graphical representation of the waves can be observed in Figure 2.1. P waves are longitudinal waves where the soil is alternately compressed and expanded in the propagation direction, S waves are transverse or shear waves that move the soil perpendicular to the propagation direction, alternately to one side and the other. Normally, the S wave has a greater amplitude than the P wave and therefore causes stronger horizontal disturbances (KEAREY et al., 2002). When a solid has a free surface, such as the Earth's surface, waves can be generated and travel across this surface. These waves have their maximum amplitude at the free surface, which decreases exponentially with depth, and are known as Rayleigh and Love waves (KEAREY et al., 2002). Rayleigh waves are the only type of seismic waves whose signatures have been evidently detected in the ionosphere. The horizontal speed of Rayleigh surface waves depends on their frequency and wavelength but typically varies between 3.3 and 4 km/s (ASTAFYEVA, 2019b).

Figure 2.1 - Representation of the movement caused by the three types of seismic waves.

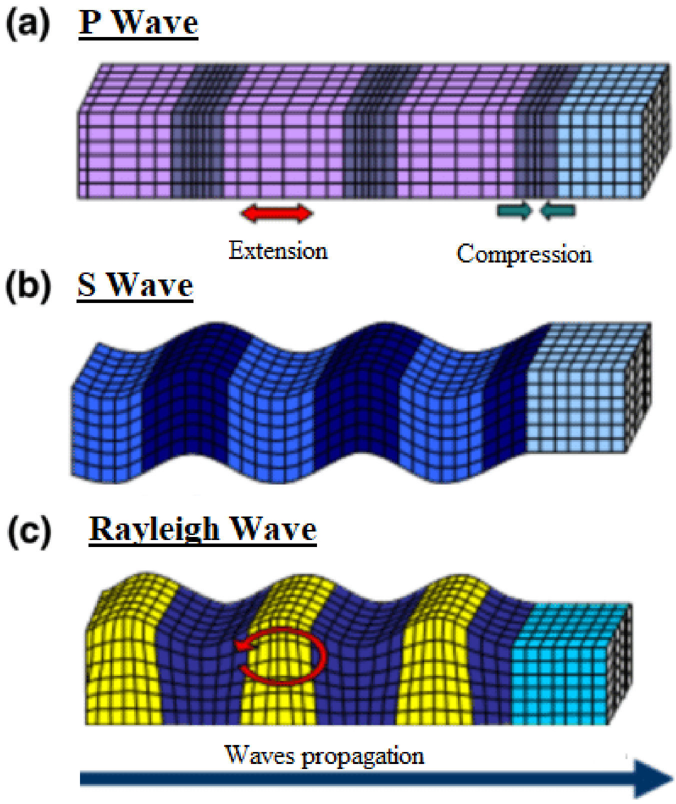


Elastic deformations and particle movements in the ground associated with the passage of ground waves: P wave, S wave, and Rayleigh wave. The blue arrow represents the direction of energy transmission. The little red and green arrows show the directions in which the ground would vibrate at a given point as each type of wave passes.

SOURCE: Modified from Sastry and Chandra (2016).

### 2.1.3 Dynamics of the Acoustic-Gravity Waves (AGWs) in the atmosphere

The basic physics of the aforementioned waves was developed in the 1960 by Hines (1960). Fundamentally, the interaction of the compressional ($\nabla.\vec{u}$), gravity ($-\nabla p/\rho$) and inertial ($d\vec{u}/dt$) forces generates Acoustic-Gravity waves (AGWs) in the atmosphere (KELLEY, 2009). Such dynamics can be described by the following Navier-Stokes equations, such as Equation 2.1 of continuity, Equation 2.2 of momentum, and Equation 2.3, energy:

$$\frac{\partial\rho}{\partial t} + \nabla.(\rho\vec{u}) = 0; \quad \vec{u} = \vec{\mathrm{u}} + \vec{u}_0 \tag{2.1}$$

$$\frac{\partial\vec{u}}{\partial t} + (\vec{u}.\nabla)\vec{u} = -\frac{1}{\rho}\nabla p + \vec{g} + \frac{1}{\rho}(\eta_1\nabla^2\vec{u} + (\eta_2 + \frac{\mu}{3})\nabla(\nabla.\vec{u})), \tag{2.2}$$

$$\frac{\partial p}{\partial t} + (\vec{u}.\nabla)p + \gamma p\nabla.\vec{u} = 0, \tag{2.3}$$

where $\rho$, $\gamma$, $p = R\rho T$, $T$ are the mass density, adiabatic constant, atmospheric pressure and temperature, respectively. The parameter $\vec{g}$ is the gravitational acceleration, $\eta_1$ and $\eta_2$ are the first and second dynamic viscosity, respectively, whereas $\vec{\mathrm{u}}$ is the disturbance neutral motion or wind (or the amplitude of the AGWs), $\vec{u}_0$ is the background wind horizontal wind model. In Equation 2.2, the Coriolis force and ionic drag forces are neglected for wave periods shorter than 2 h (KHERANI et al., 2011). The time derivative of Equation 2.2 leads to the following equation:

$$\frac{\partial^2\vec{u}}{\partial t^2} = \frac{\gamma p}{\rho}\nabla^2\vec{u} + \nabla.\vec{u}\frac{1}{\rho}\nabla(\gamma p) - \frac{\nabla p}{\rho^2}\nabla.(\rho\vec{u}) + \frac{1}{\rho}\nabla(\vec{u}.\nabla)p$$
$$+\frac{\partial}{\partial t}(\eta_1'\nabla^2\vec{u} + (\eta_2' + \frac{\nu}{3})\nabla(\nabla.\vec{u})) + \frac{\partial}{\partial t}(\vec{u}.\nabla\vec{u}) \tag{2.4}$$

where ($\eta_1' = \eta_1/\rho, \eta_1' = \eta_2/\rho$) are the first and second kinematic viscosity. Another way to represent the Equation 2.4 is following Equation 2.5, derived by (KHERANI et al., 2016):

$$\frac{\partial^2\vec{u}}{\partial t^2} = \frac{\gamma p}{\rho}\nabla(\nabla.\vec{u}) + (\gamma - 1)\frac{\nabla p}{\rho}\nabla.\vec{u} - \frac{\nabla p}{\rho}(\vec{u}.\nabla)log\rho + \frac{1}{\rho}\nabla(\vec{u}.\nabla)p + \Pi_\nu + \Pi_{nl} \tag{2.5}$$

$$\Pi_\nu = \frac{\partial}{\partial t}(\eta_1'\nabla^2\vec{u} + (\eta_2' + \frac{\nu}{3})\nabla(\nabla.\vec{u})); \quad \Pi_{nl} = \frac{\partial}{\partial t}(\vec{u}.\nabla\vec{u})$$

$$\mu = 1.3\frac{p}{\nu}; \quad c^2 = \frac{\gamma p}{\rho}; \quad \nu = \pi r_a^2\rho_n c$$

On the right side of Equation 2.5, the first term, ($\frac{\gamma p}{\rho}\nabla(\nabla.\vec{u})$) represents the contribution of the compressible flow ($\nabla.\vec{u} \neq 0$) that is, of the acoustic wave; the second term, ($(\gamma - 1)\frac{\nabla p}{\rho}\nabla.\vec{u}$) represents the coupling between the compression and buoyancy; the next two terms, ($\frac{\nabla p}{\rho}(\vec{u}.\nabla)log\rho$ and $\frac{1}{\rho}\nabla(\vec{u}.\nabla)p$) represent the advection contributions of density and pressure force and correspond to the gravity wave. These first four terms correspond to the non-dissipative AGWs and lead to the dispersion relationship for the AGWs under normal mode analysis (KHERANI et al., 2012). The terms ($\Pi_\nu$ e $\Pi_{nl}$) represent the contributions of viscosity and nonlinear saturation respectively (KHERANI et al., 2011).

In the equilibrium state, $\rho$ and $p$ are proportional to $exp(-z/2H)$, where $H = c^2/\gamma\mathbf{g}$ is the scale height, $c = \sqrt{\gamma p/\rho}$ is the speed of sound and $z$ is the altitude. Assuming:

a) $\vec{u}_0 = 0$,

b) no energy loss (i.e. $\Pi_\nu = 0, \quad \Pi_{\rm nl} = 0$), and

c) a two-dimensional planar wave solution of the form $\delta\mathrm{a}\exp[\mathrm{i}(\omega\mathrm{t} - \mathrm{k_h h} - \mathrm{k_z z})]$ where $\delta\mathrm{a} = \delta\rho, \delta\mathrm{p}, \delta\tilde{\mathrm{u}} << 1$, $\omega$ is the angular frequency of the wave, and $(k_h, k_z)$ are the wave numbers ($k = 2\pi/\lambda$) in the horizontal and vertical directions.

The dispersion relation of the AGWs is given by the following equation (PROLSS, 2004):

$$\omega^4 - \omega^2[c^2(k_h^2 + k_z^2) + (\gamma g/2c)^2] + (\gamma - 1)g^2 k_h^2 = 0, \tag{2.6}$$

$$\omega \geq \omega_a, \quad \omega_a = \gamma g/2c, \tag{2.7}$$

or

$$\omega \leq \omega_g, \quad \omega_g = (\gamma - 1)^{1/2} g/c, \tag{2.8}$$

The propagation solutions, with $k_h$ and $k_z$ being real values, exist for two frequency bands: where $\omega_a$, $\omega_g$ are the acoustic cut-off frequency and Brunt-Väisälä frequency respectively and normally $\omega_a/2\pi = 3.3$ mHz and $\omega_g/2\pi = 2.9$ mHz in the lower atmosphere (ARTRU et al., 2004) The acoustic modes in Equation 2.7 are mainly governed by compression, while the gravity modes in Equation 2.8 are governed mainly by buoyancy.

### 2.1.4 Atmosphere-ionosphere coupling

As the ionosphere is a part of the ionized fluid in the atmosphere, collisions between neutral and ionized fluids lead to the exchange of moments and energy and coupling energetics. Since the density of the atmosphere is 3-5 orders of magnitude greater than the plasma density, neutral constituents transfer energy more rapidly to ionized fluids. The time scale of this exchange is determined by collision frequency ($\nu$). In this coupling, the atmospheric motion ($\vec{u}$) generates motion $\vec{V}$ of the ionosphere plasma. The differential plasma motion ($\vec{\mathrm{v}}_{s=i/e}$) of ions/electrons generates current ($\vec{\mathrm{J}}_w$) which then gives rise to an accumulation of charges, as $\nabla.\vec{\mathrm{J}}_w \neq 0$. Since ionospheric plasma does not allow charge accumulation, an electromotive force ($\vec{\mathrm{E}}$) is generated that drives a reverse current ($\vec{\mathrm{J}}_e = \sigma.\vec{\mathrm{E}}$), such that $\nabla.(\vec{\mathrm{J}}_w + \vec{\mathrm{J}}_e) = 0$. This process is called the dynamo process, in which the atmospheric motion i.e., the wind generates an electric field. Finally, the final movement ($\vec{\mathrm{V}}$) is determined by this electromotive field and the wind, in addition to other forces such as gravity and pressure forces.

The dynamics described above are represented with the following hydromagnetic equations (a more detailed description of the equations can be found in Kelley (2009), Kherani et al. (2012)):

$$\frac{\partial \vec{\mathrm{v}}_s}{\partial t} = \frac{q_s}{m_s}(\vec{\mathrm{v}}_s \times \vec{\mathrm{B}}) - \nu_s(\vec{\mathrm{v}}_s - \vec{u}), \tag{2.9}$$

$$\vec{\mathrm{J}}_w = e(n_i \vec{\mathrm{v}}_i^w - n_e \vec{\mathrm{v}}_e^w); \quad \nabla.(\vec{\mathrm{J}}) = \nabla.(\underline{\sigma}.\vec{\mathrm{E}}) + \nabla.\vec{\mathrm{J}}_w = 0, \tag{2.10}$$

$$\frac{\partial \vec{\mathrm{V}}}{\partial t} + \vec{\mathrm{V}}.\nabla\vec{\mathrm{V}} = -\frac{1}{nm}\nabla p + \vec{g} + \frac{q}{m}(\vec{\mathrm{E}} + \vec{\mathrm{V}} \times \vec{\mathrm{B}}) - \nu(\vec{\mathrm{V}} - \vec{u}), \text{ and} \tag{2.11}$$

$$\frac{\partial n_s}{\partial t} + \nabla.(n_s \vec{\mu}_s) = P - L, \tag{2.12}$$

$$\nabla^2\vec{\mathrm{E}} - \nabla(\nabla.\vec{\mathrm{E}}) - \frac{1}{s_l^2}\frac{\partial^2 \vec{\mathrm{E}}}{\partial t^2} - \mu\frac{\partial \vec{\mathrm{J}}}{\partial t} = 0. \tag{2.13}$$

Here $n_s$, $\vec{\mathrm{v}}_s$ is the number density and velocity of the ionospheric plasma fluid, where $s$ denotes both ions($i$) and electrons($e$) - ($q_i = +Z_i e$, $q_e = -e$, $Z_i = 1$). $\vec{\mathrm{E}}$ and $\vec{\mathrm{J}}$ are the electric field and the total ionospheric current, respectively; $\vec{v}_i^w$ and $\vec{v}_e^w$ are the ion and electron velocities without the electric field derived from Equation 2.9; $\vec{J}_w$ is the corresponding ionospheric current density; $\nu_s$ is the collision frequency between charged and neutral species $s$; $\vec{B}$ is the Earth's magnetic field; $\underline{\sigma}$ is the ionospheric conductivity tensor, and ($s_l = \frac{1}{\sqrt{\mu_0 \varepsilon_0}}$) is the speed of light in vacuum. P and L are the terms for the production and loss of ions and electrons by photoionization and chemical reactions.

### 2.1.5 Atmospheric-Ionospheric Disturbances (AIDs)

The Equations 2.1-2.13 form a closed set of equations to study the temporal and spatial variations of AIDs, where the atmospheric wind ($\vec{u}$) drives the atmospheric density/pressure ($\rho/p$) disturbances and disturbances in the ionospheric density ($n$), electric field ($\vec{E}$) and magnetic field ($\vec{B}$) (KHERANI et al., 2016). In this specific case, Atmospheric-ionospheric disturbances (AIDs) are disturbances in the atmosphere and ionosphere generated by AGWs. Observations associate these AIDs with the activities of tropospheric convections, energetic particle precipitation, and seismic events (KHERANI et al., 2011; KHERANI et al., 2012; KHERANI et al., 2016).

Ionoquakes are a subgroup of Traveling Ionospheric Disturbances (TIDs) generated during an earthquake. TIDs are also a subgroup of AIDs, which occur in the ionosphere, primarily in the $F$ region. They are characterized as disturbances in density and electric field that propagate with horizontal wavelengths of 10 km -1000 km and periods of 2 minutes to 2 hours (HINES, 1974). TIDs are an important ionospheric phenomenon, generally divided into three scale categories: Small Scale Traveling Ionospheric Disturbance (SSTID), Medium Scale Traveling Ionospheric Disturbance (MSTID) e Large Scale Traveling Ionospheric Disturbance (LSTID) (PIMENTA et al., 2008). The first studies of TIDs date back to the 1940s (MUNRO, 1948). However, they gained greater prominence in the 1960s with the work of Hines (1960). Since then, TIDs have been studied using different equipment, such as incoherent scattering radar (BEHNKE, 1979), satellites (EVANS et al., 1983), GNSS (JONAH et al., 2016; FIGUEIREDO et al., 2017; SANCHEZ et al., 2022), ionosondes (CANDIDO et al., 2011) and using All-Sky imagers (PIMENTA et al., 2008). Ionoquakes are more often detected in the form of TEC disturbances (AFRAIMOVICH et al., 2001; LOGNONNÉ et al., 2006; ASTAFYEVA et al., 2009; ROLLAND et al., 2011b; ROLLAND et al., 2013) and disturbances in the geomagnetic field (KOSHEVAYA et al., 2001; IYEMORI et al., 2005; UTADA et al., 2011; IYEMORI et al., 2013; KLAUSNER et al., 2017).

### 2.1.6 Seismo-Atmosphere-Ionosphere (SAI) coupling mechanism

During an EQ, the energy and momentum released by the ground uplift from the seismic and Rayleigh waves perturb the overlying atmosphere (ARTRU et al., 2005; HEKI; PING, 2005; ASTAFYEVA et al., 2009; KHERANI et al., 2021). The resulting atmospheric disturbances propagate upward in the form of energized AGWs and give rise to the ionoquakes. Since the density ($\rho$) of the atmosphere decreases exponentially with height, conservation of energy ($\rho\vec{u}^2/2$) implies that the amplitude ($\vec{u}$) of AGWs increases approximately as $exp(z/2H)$ during its vertical propagation, amplifying up to 3 to 4 orders of magnitude at the ionospheric heights, as compared to their origin at the ground. Therefore, even a tiny ground uplift (usually $\sim$ millimeter/seconds) due to the ground uplift can lead to vertical atmospheric and ionospheric motions of about 10 m/s at the ionospheric heights (ARTRU et al., 2005; ROLLAND et al., 2011b) and gives rise to about 10% disturbances in ionospheric density and currents. The time it takes for this propagation to reach ionospheric altitudes is about 4-10 min (GALPERIN, 1985; KOSHEVAYA et al., 2001; LOGNONNÉ et al., 2006; ASTAFYEVA et al., 2013; KHERANI et al., 2012). Therefore, the ionoquake detection time can be 4-10 minutes from the peak ground uplift.

## 2.2 GNSS-TEC measurements and ionoquakes

### 2.2.1 Global Navigation Satellite Systems (GNSS)

GNSS is a generic term denoting a satellite navigation system (e.g. GPS, Glonass, Galileo, Compass or Beidou-2 and IRNSS or NAVIC) that has the ability to transmit radio signal bands used for continuous positioning and location at any given time and any point on the earth's surface, consisting of constellations of satellites. Currently, these systems are used for navigation, transport, geodesic, hydrographic, agricultural, and other similar purposes. In the majority of cases, for ionoquake detection, GNSS-TEC measurements are used.

### 2.2.2 GPS and GLONASS

The GPS system consists of a constellation of 32 satellites in total such that there are at least four satellites within sight of virtually any point on the planet, orbiting approximately at 20,200 km altitude in six planes, and with an inclination of 55° with a period of 12 hours (HOFMANN-WELLENHOF et al., 2001; MONICO, 2008). The orbits are almost circular, with an eccentricity less than 0.02, and a semi-major axis of 26,560 km (SUBIRANA et al., 2013).

The system Global'naya Navigatsionnaya Sputnikovaya (GLONASS) consists of 24 satellites that orbit at an altitude of 19,100 km and are divided into three separate orbital planes of 120° with an inclination of 64.8°, where each plane contains eight equally spaced satellites. They have a nominal period of 11 hours, 15 minutes, and 44 seconds, repeating the geometry every eight days (SUBIRANA et al., 2013).

Each GPS satellite transmits the $L_1$, $L_2$, and $L_5$ carrier waves at the following frequencies and wavelengths: $f_1 = 1575{,}42$ MHz and $\lambda_1 \cong 19$ cm $f_2 = 1227{,}60$ MHz and $\lambda_2 \cong 24$ cm; and $f_5 = 1176{,}45$ MHz and $\lambda_5 \cong 25{,}5$ cm, respectively (HOFMANN-WELLENHOF et al., 2001; MONICO, 2008). For GLONASS satellites, the transmitted signals are ($f_1 = 1602 + k \times 0{,}5625$ MHz and $f_2 = 1246 + k \times 0{,}4375$ MHz, with $-7 \leq k \leq 6$ value varying with satellites (GLONASS interface control document (ROLLAND et al., 2013)). These frequencies are generated simultaneously, allowing users to correct most of the effects caused by the ionosphere.

### 2.2.3 TEC calculation

The ionosphere is a medium formed by ions and free electrons, therefore, it affects the propagation of the GNSS signal that crosses it. The propagation speed of a radio wave in the ionosphere depends on the amount of free electrons in the signal path. This quantity is called Slant TEC (sTEC) and is defined as the number of electrons in a cylinder of 1 $m^2$ section that extends between the satellite and the receiver (MISRA; ENGE, 2006). Its mathematical expression is given by:

$$\mathrm{sTEC} = \int_S^R n_e(l)dl, \tag{2.14}$$

where $n_e(l)$ is the variable electron density along the signal path and the integral extends along the path between the satellite and the receiver. Since this effect of electron density depends directly on the frequency, the sTEC are estimated by using the phase and code measurements from ground-based GNSS-receivers (HOFMANN-WELLENHOF et al., 2008), based on Equation 2.15,

$$\mathrm{sTEC} = \frac{1}{40.3}\left(\frac{\mathrm{f_i^2 f_j^2}}{\mathrm{f_i^2 + f_j^2}}\right)(\mathrm{L_i}\lambda_\mathrm{i} - \mathrm{L_j}\lambda_\mathrm{j}), \tag{2.15}$$

where $\mathrm{f_i}$ and $\mathrm{f_j}$ are carrier wave frequencies that correspond to GPS or GLONASS, $\lambda_i = \mathrm{s_l/f_i}$ and $\lambda_j = \mathrm{s_l/f_j}$ are the corresponding wavelengths of the additional signal paths caused by phase delay in the ionosphere, where $s_l$ is the speed of light, and $\mathrm{L_i}$ and $\mathrm{L_j}$ are the carrier phases. The vTEC is derived from sTEC using the following conversion Equation 2.16, (KLOBUCHAR, 1987)

$$\mathrm{vTEC} = \mathrm{sTEC} \times cos\left[arcsin\left(\frac{r_e}{r_e + H_{ION}} cos\theta_{el}\right)\right], \tag{2.16}$$

where $r_e$ is the Earth's radius, $H_{ION}$ is the altitude of the ionospheric thin layer, and $\theta_{el}$ is the elevation angle of the satellite. TEC is measured in TEC-units (TECU) (1TECU= $10^{16}$ $e/m^2$). For this work, we use the relative TEC estimated from the phase measurements as explained above. The precision of TEC estimation from phase measurements is about 0.01–0.02 TECU (COSTER et al., 2013).

## 2.3 Ionoquakes energetics

The ionoquake energetics are primarily determined by the SAI coupling energetics such as the earthquake magnitude/ground uplift, focal mechanism, background atmospheric/ionospheric conditions, geomagnetic field orientation and satellite-receiver geometry (CALAIS; MINSTER, 1995; AFRAIMOVICH et al., 2001; KHERANI et al., 2009; ROLLAND et al., 2013; ASTAFYEVA et al., 2014; CAHYADI; HEKI, 2015; HEKI, 2021).

### 2.3.1 Amplitudes of the ionoquakes

Ionoquake amplitudes, detected by the GNSS-TEC, must be carefully analyzed and compared since they depend heavily on the conditions of registration (HEKI; PING, 2005; ASTAFYEVA et al., 2014). The main factors that control the amplitude of an ionoquakes are described in the following.

#### 2.3.1.1 The magnitude of an EQ

EQs with larger magnitudes generate TEC perturbations of larger amplitudes, so the biggest factor influencing ionoquakes amplitudes is the EQ magnitude (ASTAFYEVA et al., 2013; ASTAFYEVA et al., 2014; CAHYADI; HEKI, 2015; SUNIL et al., 2021; BRAVO et al., 2022). Astafyeva et al. (2013) compiled data from 11 EQs with clear ionoquakes observations at TEC and investigated the correlation between Mw and ionoquakes amplitudes. Later, Cahyadi and Heki (2015) also compiled TEC data from 21 EQs, taking the measure of the maximum amplitude of the disturbance in each event as a reference. In all cases of this work and that of Astafyeva et al. (2013), the results are similar: stronger EQs produce stronger responses in the ionosphere. In fact, the seismic momentum of an event with Mw7 and an event with Mw9 is different by three orders of magnitude (CAHYADI; HEKI, 2015).

#### 2.3.1.2 Focal mechanism

There are several different types of faults, but most can be divided into three categories, as shown in Figure 2.2, which are reverse or impulse (upward movement when the two plates collide and bend over backwards), normal (the top plate moves down) and sliding (the plates move horizontally one after the other). The first two cause larger vertical crustal movements than the third. Therefore, it is important to know the dependence that the amplitude of the ionoquakes has on the magnitude and focal mechanism of the EQ (CAHYADI; HEKI, 2015; ASTAFYEVA, 2019b).

Figure 2.2 - Representation of the three main types of focal mechanisms.

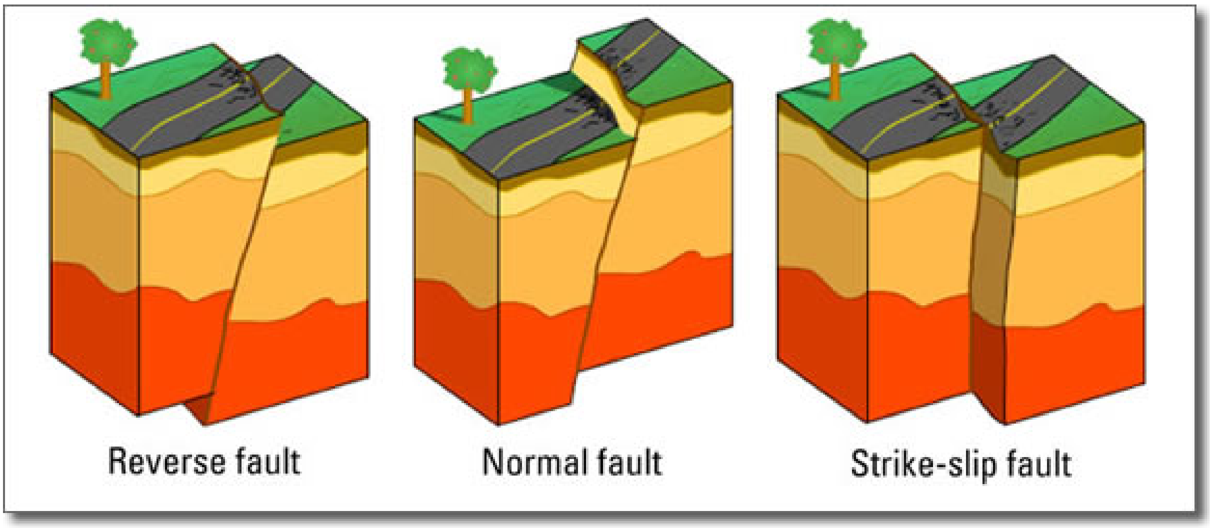


Failure types. Reverse (mostly lifting), Normal (mostly subsidence) and Slip (mostly horizontal movement).

SOURCE: SMS Tsunami Warning (2023).

#### 2.3.1.3 The distance between the epicenter and the SIP

The epicentral distance of the ionoquakes record needs to be taken into account, because of the dependence of the ionoquakes amplitude on the distance (ASTAFYEVA et al., 2014). The ionoquakes generated directly by the crustal displacements are detected up to $\sim$ 600-700 km from the source, while the ionoquakes observed at $\sim$ 600-3000 km from the source correspond to the propagation of Rayleigh waves (ASTAFYEVA et al., 2013). The ionoquakes generated by the crustal displacements after $\sim$ 700 km will be almost imperceptible in the raw data time series, leaving only the Rayleigh wave signatures that are of smaller amplitude.

#### 2.3.1.4 Background atmospheric/ionospheric conditions

The ambient ionospheric density, in the EQ recording area, plays an important role in the amplitude value of the ionoquakes (ASTAFYEVA et al., 2014; BAGIYA et al., 2019). This is because the background atmospheric/ionospheric parameters vary significantly due to different conditions of solar and magnetic activity, as well as seasonal, latitudinal, diurnal, and nighttime variability (ASTAFYEVA et al., 2014). Consequently, the energy and momentum transfer of neutral waves in the ionospheric plasma is different for each EQ. Therefore, to compare ionoquakes amplitudes generated by different EQs, normalization with the ionospheric background parameters is necessary (CAHYADI; HEKI, 2015; HEKI, 2021).

#### 2.3.1.5 $H_{ION}$ detection height

The detection altitude of $H_{\mathrm{ION}}$ is a sensitive point, because it cannot be found accurately. As can be seen in Figure 2.3, any point that is in LOS and that is in the ionospheric layer can be $H_{\mathrm{ION}}$, but it can be suggested from physical principles (ASTAFYEVA, 2019b). It is generally assumed that the disturbances detected by GNSS-TEC are concentrated around the maximum ionospheric ionization altitude. however, Thomas et al. (2018) for the Mw7.4 earthquake of March 9, 2011 at Sanrikuoki in Japan, reports that the first detection of ionoquake is around $H_{\mathrm{ION}}$=130 km. Also, Astafyeva and Shults (2019) for the same earthquake considering the arrival for the first maximum amplitude of the ionoquakes, reports that the detection altitude was between 180 - 200 km, i.e. in both studies the detection is below the ionization maximum of 275 km indicated by the IRI model. It should be noted that changing the $H_{\mathrm{ION}}$ will change the ionoquakes amplitude, and the IPP coordinates. As a result of this change, the SIP, latitude, longitude, and detection time will also be changed. The geometric representation of what has been explained is shown in

Figure 2.3. Therefore, the choice of $H_{\mathrm{ION}}$ is extremely important for the ionospheric images of the seismic source (ASTAFYEVA et al., 2013). One way to estimate the true $H_{\mathrm{ION}}$ is explained in Subsection 5.3.2.

Figure 2.3 - Representation of a GNSS sounding of the ionosphere.

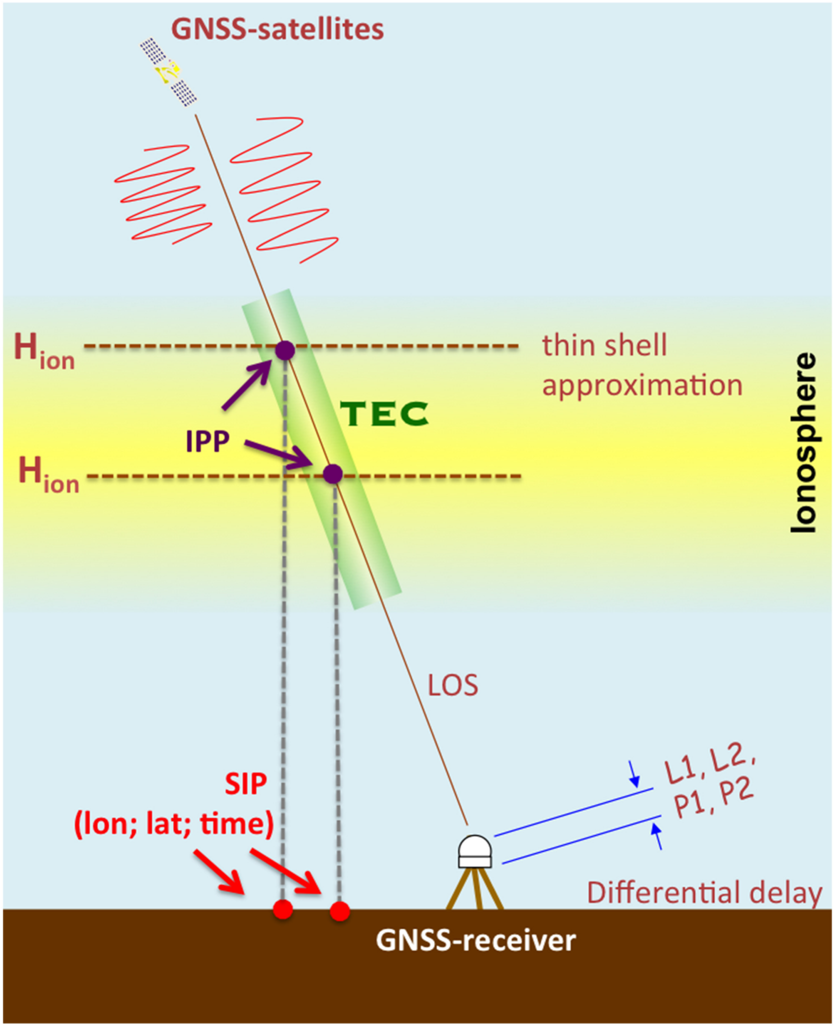


Intersection point between the LOS and $H_{\mathrm{ION}}$ within a thin layer approximation and the IPP projection onto the surface of the SIP Earth. Knowing the coordinates of a satellite and a receiver, one can calculate the SIP coordinates.

SOURCE: Astafyeva (2019b).

#### 2.3.1.6 Geomagnetic field dependency and ionoquake directivity

Similar to TIDs from non-seismic sources, ionoquakes reveal dependency on the geomagnetic dip angle. It is due to the fact that the TIDs are primarily due to the ionospheric dynamics perpendicular to the geomagnetic field. Since geomagnetic lines sustain such dynamics against gravitation force more effectively at low dip angles, EQ at low dip angle produces stronger ionoquakes, in comparison to the identical EQ at large dip angle. Moreover, owing to extremely large conductivity along geomagnetic field lines, ionoquakes propagate long distances along the field lines, while limited within $\sim$ 100-150 km epicentral distance (ASTAFYEVA et al., 2009; ROLLAND et al., 2013). Astafyeva et al. (2014) analyzed the parameters of the geomagnetic field at the epicenters of six events. In five events, the geomagnetic field favors the almost strict propagation of the ionoquakes towards the equator, except for one event, where the geomagnetic field declination is 26°. They concluded that the GPS probe geometry and the geomagnetic field parameters confirm that we always observe larger amplitudes at smaller angles between the ionoquakes wave vector and the geomagnetic field lines.

Cahyadi and Heki (2015) analyzed in 21 EQs, they found that the detection position of the largest amplitude of ionoquakes will be to the south region for EQs that occur in the Northern hemisphere, while this amplitude will be the largest to the north region for EQs that occur in the Southern hemisphere. Later, Sunil et al. (2021) found ionoquakes for 19 EQs during moderate to large magnitude events. They categorized events occurring within ±40° and events beyond ±40° according to the geomagnetic inclination angle at the epicenters. In analyzing the correlation between the amplitude of the ionoquakes and Mw corresponding to the events, they obtained correlation coefficients equal R = 0.79 and R = 0.76 for both cases, respectively.

However, other study shows no conclusive evidence of the geomagnetic field dependence (CHEN et al., 2011; NAYAK et al., 2021). This is due to the fact that besides the angle between AGWs propagation direction and geomagnetic field, the amplitude of AGWs determines the coupling energetics between the atmosphere and ionosphere. Therefore, the complex nature of this coupling reflects on the inconclusive evidence of the geomagnetic field dependence of the ionoquakes.

#### 2.3.1.7 The satellite-receiver Line-Of-Sight geometry

It is known that the recording of the ionoquake amplitude by the GNSS-TEC method varies according to the LOS geometry of the satellite-receiver. This is because of the integrated nature of TEC along the satellite-receiver LOS. When the wave vectors of the ionoquakes and the LOS are perpendicular to each other, the disturbance measurements are of greater amplitude and when the wave vector is parallel to the LOS they have a minimum amplitude (AFRAIMOVICH et al., 2001; BAGIYA et al., 2019; ASTAFYEVA, 2019b; MANTA et al., 2020).

Cahyadi and Heki (2015) compiled TEC data from 21 EQs, taking into account the location of the GNSS stations, the position of the epicenter and the location of detection of the ionoquakes along the IPP trajectories, also taking the measure of the maximum amplitude of the disturbance in each event as a reference. In all cases of this work, the maximum amplitudes of the ionoquake were found between the epicenter and the receptor. This scenario is described by Cahyadi and Heki (2015) as being the most favorable for ionoquakes to attain significant amplitude, but there are some exceptions. Manta et al. (2020) report, for example, that for 6 April 2010 Mw 7.8 Banyaks EQ had very weak ionoquakes, despite favorable geometries.

#### 2.3.1.8 Spectral analysis

The filtering method applied in the TEC time series processing significantly modifies the ionoquakes amplitudes, in addition to generating time shifts. For example, Sunil et al. (2015) analyzed the 2012 Sumatra EQ (mainshock) and obtained the ionoquakes amplitude of ∼0.24 TECU as a result, with observations of PRN 32 at the **umlh** seismic station. Also Cahyadi and Heki (2015) analyzed the same EQ, and obtained as a result an amplitude of ionoquakes ∼ 2.6 TECU.

### 2.3.2 Ionoquakes propagation speed

As mentioned earlier, ionoquakes are caused by different atmospheric waves generated by EQ. Ionoquakes are found to propagate away from the epicenter with speeds of about 3.8 - 4 km/s (HEKI; PING, 2005; ASTAFYEVA et al., 2009), consistent with the speed of Rayleigh waves, and propagate farther than direct acoustic waves due to less geometric decay (ROLLAND et al., 2011b). Ionoquakes are also found to propagate with a speed of about 600 m/s - 1.5 km/s which is the speed of AGWs at the thermospheric height (ASTAFYEVA et al., 2009; GALVAN et al., 2012). High-frequency AGWs i.e., acoustic waves triggered by ground uplift around the epicenter, or by Rayleigh propagating surface waves reach altitudes of maximum ionospheric electron density (∼ 280 km – 300 km) in less than 10 minutes (KHERANI et al., 2012; THOMAS et al., 2018). On the other hand, low-frequency AGWs i.e., gravity waves typically require more than 30 minutes (to an hour) to propagate to the ionosphere heights (KHERANI et al., 2012; KHERANI et al., 2016; TSUGAWA et al., 2011).

### 2.3.3 Ionoquakes resonant oscillations

AGWs generated by EQs cause acoustic resonant oscillation at 3.7 and 4.4 mHz. These frequencies were identified in the TEC oscillation (CHOOSAKUL et al., 2009; ROLLAND et al., 2011a) and the peak frequencies observed were ±4 mHz (CAHYADI; HEKI, 2015). Iyemori et al. (2005) observed with magnetometer data, during the Sumatra EQ in 2004, resonant magnetic oscillations in the D and Z components with values of 4.6 and 5.5 mHz, and values of 1.8, 4, 6, and 5.5 mHz for the H component. Also, Iyemori et al. (2013) observed oscillations of this nature in the Chilean EQ occurred in 2010. In this case, the long-period magnetic oscillations observed in the north-south direction (H) had two main resonance modes at 3.65 and 4.35 mHz.

The visibility of the resonant oscillations with TEC would depend on several factors, such as the actual extent of the oscillation occurrence, the Line-Of-Sight (LOS) incidence angle between a GNSS satellite and a GNSS receiver with the wavefront (CAHYADI; HEKI, 2015). The motion of the neutral atmosphere must also have components parallel to the ambient geomagnetic field so that the electrons can oscillate together (ROLLAND et al., 2011b). In short, it can resonate at various frequencies between 1-10 mHz, that is, in the frequency range of normal earth modes (ARTRU et al., 2004; SANCHEZ et al., 2022).

# 3 ANALYSIS OF IONOSPHERIC RESPONSE TO MODERATE/WEAK EQS OF MAGNITUDE (Mw) LESS THAN 6.6

This section presents a review of the paper *"Ionospheric Disturbances Observed Following the Ridgecrest Earthquake of 4 July 2019 in California, USA"* (SANCHEZ et al., 2022).

In this chapter, we analyze the ionospheric response to two moderate EQs that occurred on 4 July 2019 in California, USA. The magnitudes of the EQs are Mw 6.4 (main shock) and Mw 4.6 (aftershock). The ionoquakes occurred as TIDs in TEC data. These seismic-origin TIDs acquire unique wave characteristics that distinguish them from TIDs of non-seismic origin arising from a moderate geomagnetic activity on the same day. Their spectral characteristics relate them to the Earth's normal modes and atmospheric resonance modes. The vertical ground velocity associated with the mainshock, rather than the vertical ground displacement, is found to satisfy the threshold criteria required for generation of detectable ionoquakes in TEC measurements. The cross-correlation analysis is used to quantify the wave parameters and their role in the identification of $\Delta$TEC of seismic origin. Numerical simulation confirms that the Seismo-Atmosphere-Ionosphere coupled dynamics energized by the atmospheric waves is responsible for the generation of the observed ionoquakes. Our work demonstrates the potential of TEC measurement to detect ionospheric counterparts of moderate and weak EQs. We found a new vertical ground velocity threshold at 2-6 mHz of approximately 0.1-0.6 cm/s, which can generate an ionospheric drift corresponding to approximately 60-360 m/s. Therefore, these drifts are sufficient to generate ionoquakes detectable in TEC data series.

## 3.1 The 4 July 2019 Ridgecrest EQs

On 4 July 2019 (referred as the event day), a moderate EQ with magnitude Mw 6.4 (the mainshock) occurred in eastern California (USA), north and northeast of the town of Ridgecrest. The mainshock struck at 17:33 UT, and a series of aftershocks followed during the next two hours (Table 3.1). According to the U.S. Geological Survey (USGS), the mainshock resulted from shallow strike-slip faulting (<https://earthquake.usgs.gov/earthquakes/eventpage/ci38443183/technical>, which means that the co-seismic crustal displacements were mostly horizontal.

In this study, we used 600 GNSS receivers near the epicenter of the EQ of the permanent ground-based network UNAVCO (<http://www.unavco.org>). Satellite PRN19 was selected for the present analysis because the corresponding ionospheric

Table 3.1 - Selected EQs of the Ridgecrest sequence, USGS database, magnitude $\geq$ 3.55, 4 July 2019, California, USA.

| No. | Time (UT) | Lat, lon (degrees) | Depth (km) | Magnitude | Location |
|---|---|---|---|---|---|
| 1 | 17:33:49 | 35.71, -117.50 | 10.50 | 6.40 | Ridgecrest EQ Sequence |
| 2 | 18:08:45 | 35.71, -117.47 | 1.2 | 3.55 | 9km SW of Searles Vallay |
| 3 | 18:27:59 | 35.75, -117.55 | 6.64 | 4.23 | 14km W of Searles Valley |
| 4 | 18:39:44 | 35.60, -117.60 | 2.81 | 4.59 | 7km ESE of Ridgecrest |
| 5 | 18:47:06 | 35.67, -117.49 | 8.53 | 4.34 | 13km SW of Searles Valley |
| 6 | 18:54:13 | 35.60, -117.60 | 5.33 | 4.07 | 7km ESE of Ridgecrest |
| 7 | 18:56:06 | 35.72, -117.56 | 1.92 | 4.58 | 15km NE of Ridgecrest |
| 8 | 18:56:22 | 35.71, -117.55 | 1.16 | 4.21 | 15km NE of Ridgecrest |
| 9 | 19:21:32 | 35.67, -117.49 | 5.16 | 4.50 | 13km SSW of Searles Valley |

SOURCE: Sanchez et al. (2022).

piercing point (IPP) trajectories, i.e., the trajectories of the satellite projected at the ionospheric height of 300 km, cover the EQ shake zone around the epicenter during the EQs (17:33:49 UT and 18:39:44 UT), as evident from Figure A.2 (Appendix A).

## 3.2 Development of wave decomposition method for moderate EQs

This wave decomposition method is designed to obtain perturbations that we cannot easily distinguish. It is able to provide a time-frequency-energy description of practically any type of time series, allowing the analysis of the signal without the need for previous processing, and providing results that are easy to interpret. This feature is particularly useful in detecting EQ signatures in GPS data. The method is based on the calculation of the convolution using the hat wavelet transform to obtain a smoothed linear structure at various frequencies. The code developed for this thesis with the wave decomposition method is available in Appendix C.1, under the name signal-alam. An example of analysis is shown in Figure A.1(B). Where the TEC of Figure A.1(A) is decomposed into several frequencies in 1–10 mHz, that is, in the frequency range of Earth's normal modes (ARTRU et al., 2004).

## 3.3 Estimation of ground vertical velocity and displacement from recorded ground motion

We employed the ObsPy library of Python to process the recorded ground motions (in counts format) from the seismometers around the epicenter (KRISCHER et al., 2015). The module downloads the data in counts format and estimates the velocity and displacement of ground motion with the instrumental response corrections that include the removal of frequency response of the seismometers, the effects of any amplifiers, of analog and digital filters, and of the digitalization. We also used data from the 10 ground seismometer stations with sampling of 0.025 s, located within 1° of the epicentral distance (IRIS network: <http://ds.iris.edu/wilber3/find_event>).

### 3.4 Ionoquakes during a Mainshock of Mw 6.4 and 4.6

For an analysis of the Ridgecrest EQ, Sanchez et al. (2022) first selects the availability of data from seismometers less than 1° from the epicenter, then TEC values as registered from 110 stations with elevations higher than 20°, located within a ±1.25° epicentral distance at the mainshock onset time. These selected data are shown in Figure 3.1. Interestingly, despite the strike-slip focal mechanism and being a moderate EQ, the mainshock attained a peak velocity of 6 cm/s. This is one of the factors that influence the generation of ionoquakes.

Figure 3.1 - Vertical ground velocities and TEC time series.

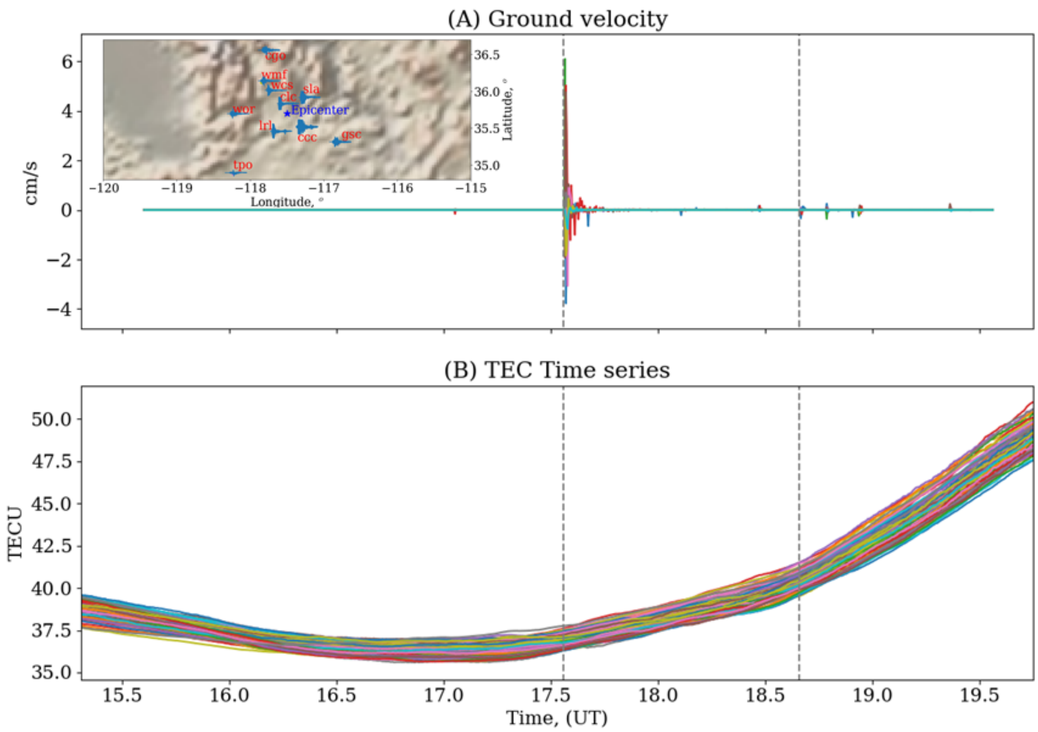


(A) Ground velocity for 10 seismic stations located within 1° epicentral distance; the inset map shows an amplification around the mainshock. (B) TEC variations as recorded from 110 stations located within 1° epicentral distance. Vertical dashed lines indicate the onset time of the mainshock of Mw 6.4 and the largest aftershock of Mw 4.6.

SOURCE: Sanchez et al. (2022).

Sanchez et al. (2022) shows in Figure 3.2 the temporal variations in ΔTEC in the space around the epicenter. Panel B reveals the surge in intensified wave oscillations after the mainshock onset on EQ day, but such an increase cannot be observed in panels A and C on the day before or the day after, respectively. Therefore, from this spatio-temporal analysis, they concluded that the enhanced TEC disturbances in panel B were probably seismic in origin.

Figure 3.2 - TEC disturbance (ΔTEC) along the IPP trajectories on the previous day on 3 July (**A**), on the event day on 4 July (**B**), and on the day after on 5 July 2019 (**C**).

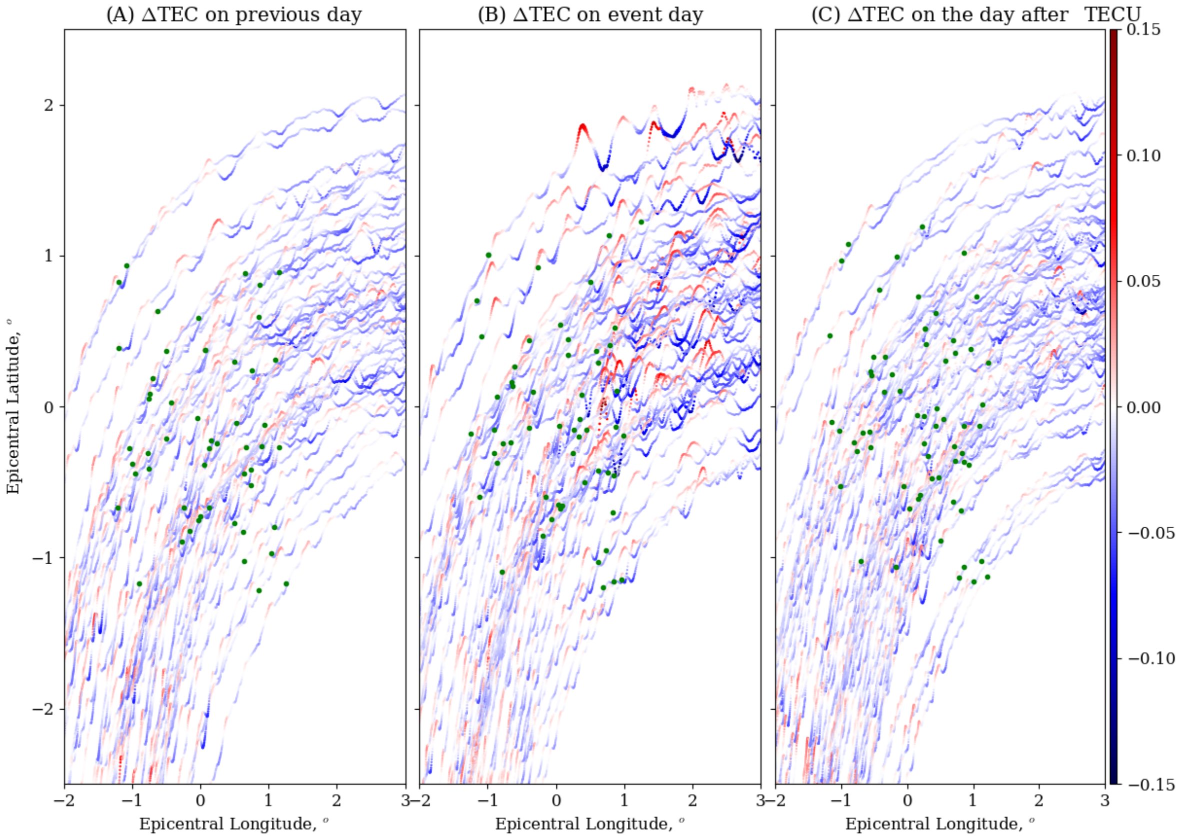


The disturbances were extracted from the raw TEC data by applying a bandpass moving average filter spanning 1–10 mHz. Small circles represent the locations of the IPP at the mainshock time. The epicentral latitude and longitude are defined as $lat - lat_{ep}$ and $lon - lon_{ep}$, respectively.

SOURCE: Sanchez et al. (2022).

In addition, Sanchez et al. (2022) analyzes the spectral characteristics of ΔTEC (Figure 3.3A). They observed that the oscillations intensified ~30 min after the mainshock onset. This timing suggests the seismic-origin nature of the intensified ΔTEC disturbances, as also shown in Figure 3.3B. In particular, the intensification concentrated in AGWs frequency range of 1 –6 mHz, which efficient seismic–ionospheric coupling has been also previously reported (ARTRU et al., 2004; ROLLAND et al., 2011a).

Figure 3.3 - Spectrograms of the ΔTEC (**A**) and the vertical ground velocity (**B**) on EQ day (4 July 2019).

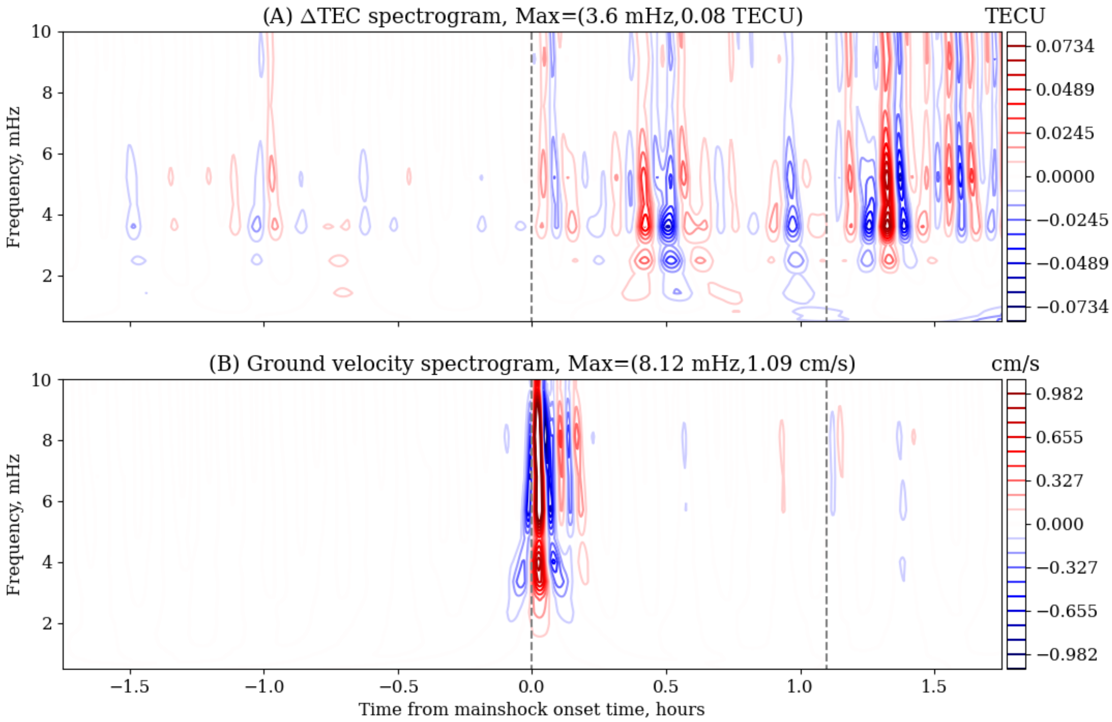


TEC and velocities results shown are the averages over all the stations. Red and blue contours represent the positive and negative values, respectively, with the corresponding maximum values denoted as Max at the top of the panel. These maximum values belong to the 1–10 mHz frequency range. Vertical dashed lines indicate the onset time of the mainshock of Mw 6.4 and the aftershock of Mw 4.6. The time window of the data is ±2.25 h, therefore, in 1–10 mHz, the data in ±1.75 h remain unperturbed from the boundary effects arising from the filtering. For this reason, the time axis in this figure and in the rest of the figures is restricted to ±1.75.

SOURCE: Sanchez et al. (2022).

### 3.5 Development of a cross-correlation method for moderate EQs

Continuing the analysis of the Ridgecrest EQ, to examine the wave nature of $\Delta$TEC oscillations, we carry out the cross-correlation analysis. The cross-correlation of two spatially-separated time series (i, j), $\Delta TEC_i(t)$ and $\Delta TEC_j(t)$, is defined as follows:

$$C_{ij}(t) = \text{convolve}(\Delta TEC_i(t), \Delta TEC_j(t)), \quad 1 \leq i \leq N, \quad 1 \leq j \neq i \leq N \tag{3.1}$$

where N=110 is number of $\Delta$TEC time series shown in Figure 3.2(B), i.e. number of GNSS receivers used in the analysis and $(i, j)$ are the index for two IPP trajectories of GNSS with epicentral distance $(d_i, d_j)$. This generates N(N-1) number of time series of $C_{ij}$ with relative distance $d_{ij} = d_j - d_i$. From these time series, N(N-1) number of maximum values of $C_{ij}$ and corresponding N(N-1) values of time denoted by 'tmx', are estimated. The cross-correlation coefficient $(C_{cf})$, is obtained as follows:

$$C_{cf} = \frac{C_{ij}(tmx)}{\max(C_{ij}(tmx))} \tag{3.2}$$

The time scales and length scales associated with $\Delta$TEC for the three IPP trajectories $(i, j, k)$ are defined as follows:

$$\tau = tmx_{ij} - tmx_{ik}, \quad \lambda = d_{ij} - d_{ik} \tag{3.3}$$

From these scales, frequency and wavelength of wave characteristics of $\Delta$TEC are estimated from the following expressions:

$$\omega = \frac{2\pi}{\tau}, \quad k = \frac{2\pi}{\lambda} \tag{3.4}$$

#### 3.5.1 Cross-correlation method validation

In order to demonstrate the validity of the cross-correlation analysis, we perform the test analysis of $\Delta$TEC of known periodicity/wavelength of the following forms:

$$\text{TEST1} : \Delta TEC = \cos(\omega t - ky), \quad \omega = \frac{2\pi}{8}s^{-1}, \quad \lambda = \frac{2\pi}{8}km^{-1} \tag{3.5}$$

$$\text{TEST2}: \Delta\text{TEC} = e^{-(t-t_0)^2/\sigma_t^2} e^{-(y-y_0)^2/\sigma_d^2} \cos(\omega t - ky), \quad \omega = \frac{2\pi}{8}s^{-1}, \quad \lambda = \frac{2\pi}{8}km^{-1} \tag{3.6}$$

$$\text{TEST3}: \Delta\text{TEC} = e^{-(t-t_0)^2/\sigma_t^2} e^{-(y-y_0)^2/\sigma_y^2} \sum_{i=2}^{4}\sum_{j=2}^{4} \cos(\frac{\omega}{i}t - \frac{k}{j}y), \quad \omega = \frac{2\pi}{4}s^{-1}, \quad \lambda = \frac{2\pi}{4}km^{-1} \tag{3.7}$$

We note that in TEST1 and TEST2, ΔTEC is monochromatic that oscillates with 8 seconds periodicities and has wavelength of 8 km. In TEST3, ΔTEC is interference of oscillations with periods of 8, 12, 16 seconds and wavelengths with 8, 12 and 16 km.

In Appendix A Figure (A.5), we present the results from the cross-correlation analysis for TEST1. We note that $C_{cf}$ is significant at (ymx; tmx) where ΔTEC attains peak. That affirms the correct estimation of $C_{cf}$.

Interestingly, the spectrograms in Figures A.5 (B-C) in Appendix A reveal large $C_{cf}$ evolves around at periodicity (around 8 seconds) and wavelength (around 8 km), whereas power spectral density (gray curves in Appendix A Figure A.5(B-C) attains peak in the FFT spectrum. In other words, the cross-correlation analysis estimates correct periodicity and wavelength.

In Figure A.6, we present the results from the cross-correlation analysis for TEST2. We note that $C_{cf}$ is significant at (ymx; tmx) where ΔTEC attains peak values. That affirms the correct estimation of $C_{cf}$. Moreover, the spectrogram also reveals spectral evolution around the periodicity of 8 seconds and wavelength of 8 km.

In Figure A.7, we present the results from the cross-correlation analysis for TEST3. We note that $C_{cf}$ is significant at (ymx; tmx) where ΔTEC attains peak values. That affirms the correct estimation of $C_{cf}$. Moreover, the spectrogram also reveals spectral evolution around the periodicities between 8-16 seconds and wavelength between 8-16 km. It is consistent with the spectral peaks derived from the FFT.

## 3.6 Analysis of the Ridgecrest EQ of 4 July 2019 with Cross-correlation method

In ΔTEC hodogram in Figure 3.4, distribution of $C_{cf}$ is shown. We note the surge of dense clusters of $C_{cf}$ during 0.5-1 hours from the mainshock onset which is indicative of coherent wave generation after the mainshock onset. The surge coincides with the time of intensified oscillations in Figure 3.3(A), that had revealed spectral evolution similar to those of previously reported ionoquakes (ROLLAND et al., 2011a). Few of the dense clusters distribute along those wavefronts that emerge near the epicenter during the surge. These wavefronts are more explicit in Figure A.3. Therefore, the mainshock triggers new and intensified waves in the vicinity of the epicenter, characterized by dense clusters of $C_{cf}$, in contrast to thin clusters before the mainshock onset.

Figure 3.4 - The Hodogram of the ΔTEC disturbances as a red-blue color code.

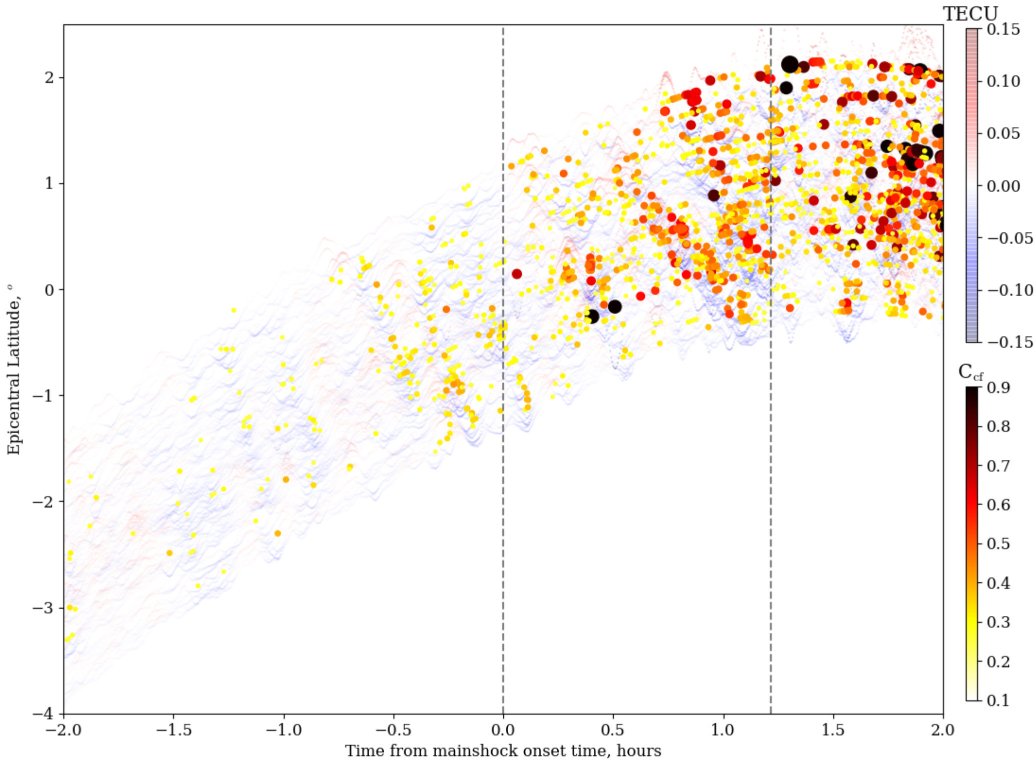


ΔTEC is derived from the TEC data by applying a bandpass filter of 1-10 mHz. Circles represent $C_{cf}$, given by expression 3.2.

SOURCE: Author's production.

The cross-spectrograms in Figure 3.5 show the surge of a sequence of dense clusters of waves after the mainshock. The first prominent cluster appears during 0.5-1 hour that affirms the generation of new coherent waves after the mainshock, as noted in Figure 3.4. The majority of these waves have frequencies in the range of 2-6 mHz and the wavelengths lower than 400 km where large values of $C_{cf}$ tend to concentrate. The dispersion diagram in Figure 3.6 finds the majority of these waves to propagate with the phase velocities lower than 1500 m/s though some of the waves attain 3000 m/s or more. These wave characteristics classify the dense cluster of waves as Medium-Scale Travelling Ionospheric Disturbances (MSTIDs). Ionoquakes in the form of MSTIDs are often reported for the strong EQs of magnitude larger than 6.6 (ARTRU et al., 2004; ASTAFYEVA et al., 2009; ROLLAND et al., 2011a). The present study reports the new finding of the MSTIDs from relatively weaker EQ of magnitude 6.4.

Figure 3.5 - The results of the Cross-correlation analysis.

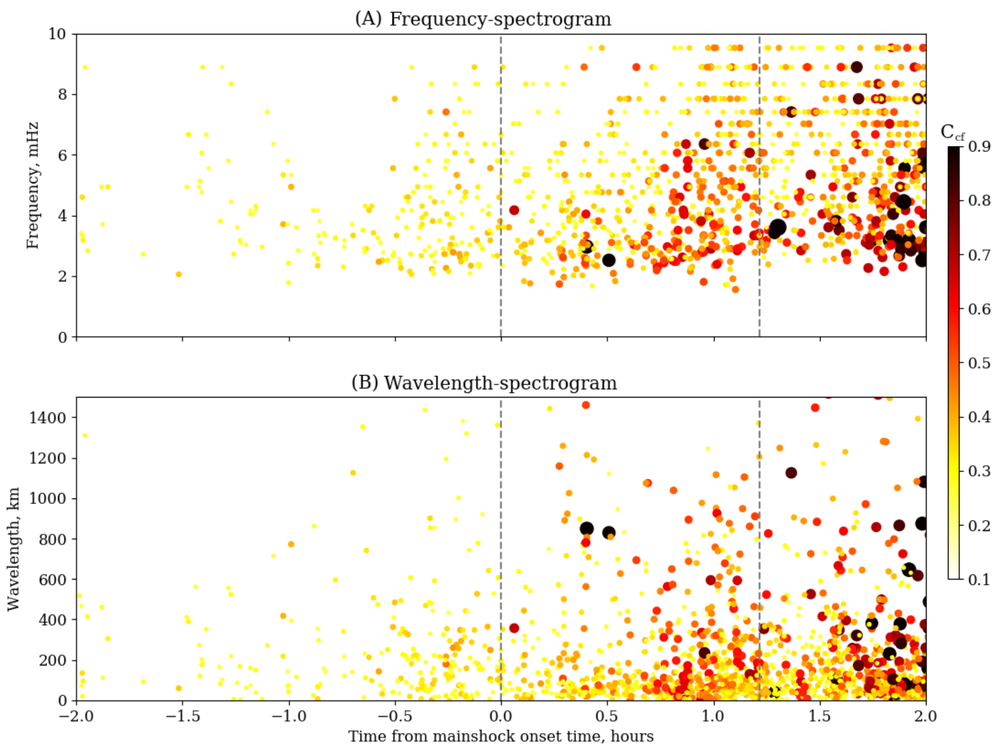


Panels (A-B) illustrate the cross-spectral frequency and wavelength spectrograms. Circle size is proportional to the $C_{cf}$ that varies between 0 to 1.

SOURCE: Author's production.

Figure 3.6 - Dispersion Diagram derived from cross-correlation analysis.

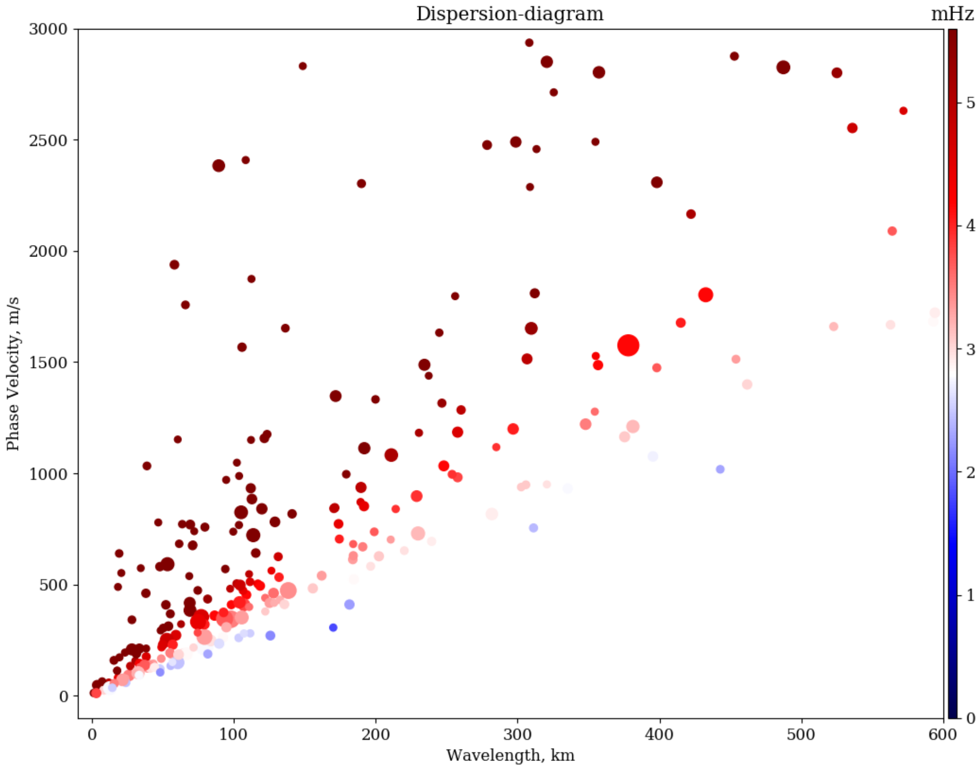


Circle size is proportional to the $C_{cf}$ that varies between 0 and 1. The color code represents the cross-spectral frequency in mHz.

SOURCE: Author's production.

## 3.7 Ionoquakes and Co-Seismic crustal displacements

Artru et al. (2004) reported observations of ionoquakes associated with the seismic ground wave recorded by the Francourville sounding station, France, that is, ~9976 km from the epicenter. They showed that the vertical ground velocity of the order of 0.001 cm/s can drive an ionospheric drift of 0.6 m/s, consistent with the ionospheric Doppler sounding measurements. Sanchez et al. (2022) have shown in Figure 3.3B the mainshock vertical ground velocity threshold at 2-6 mHz of approximately 0.1-0.6 cm/s, which can generate an ionospheric drift corresponding to approximately 60-360 m/s. Therefore, these drifts are sufficient to generate ionoquakes detectable in TEC data series.

## 3.8 Ionoquake simulation for Ridgecrest EQ of 4 July 2019

To confirm whether the SAI coupled dynamics energized by atmospheric waves is responsible for the generation of the observed ionoquakes, Sanchez et al. (2022) employed the SAI coupling simulation model (KHERANI et al., 2016) that, in the past, was used to simulate the ionoquakes from tsunamis. In the present study, instead of a tsunami wave, the forcing from the ground vibration in the form of vertical velocity was considered. Figure 3.7A illustrates the real seismic forcing in time and latitude, composed of a mainshock onset at t = 0 min and a series of aftershocks similar to the seismometer-deduced ground velocity in Figure 3.1A. To reconstruct the ground forcing from the simulation, they use the ground velocity shown in Figure 3.1. Based on the shakemap of the mainshock in Figure A.4 (Appendix A), the horizontal Gaussian width of the forcing is considered to be 1°. The simulation resulted in two southward-propagating wavefronts during 0.5–1 h in 0–2° epicentral latitudes, similar to those marked by ellipses in Figure A.3.

Figure 3.7 - Hodogram of the simulation results from the SAI coupling model.

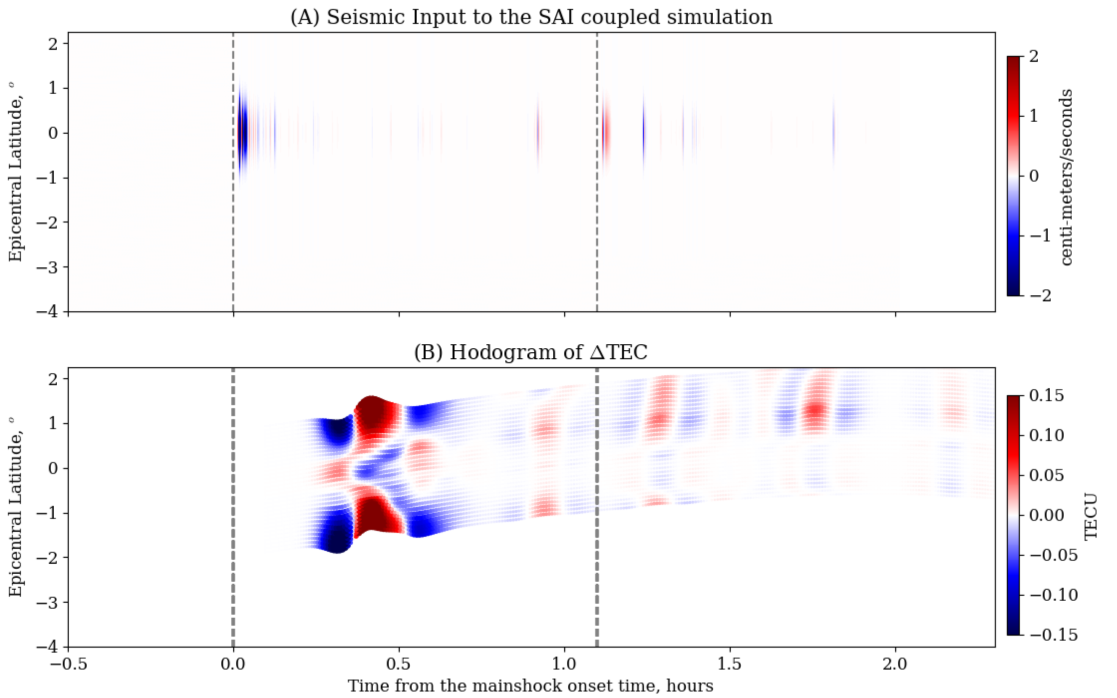


(**A**) the ground vibration at the epicenter, composed of a mainshock at t = 0.0 and a series of aftershocks. (**B**) A hodogram of the simulated ΔTEC. The hodogram was constructed by estimating the simulated ΔTEC along the IPP trajectories of the hodogram in Figure A.3.

SOURCE: Sanchez et al. (2022).

Also, Figure 3.8 reveals the generation of ionoquakes with an amplitude of about 0.05 TECU during the series of aftershocks, a clear demonstration of positive feedback from the aftershocks of magnitudes Mw of 4.6. In other words, the mainshock provides favorable conditions for the aftershock to provide its contribution in the ionoquakes. In the excitation of AGWs, the ground velocity, rather than the ground displacement, plays the determining role since the product of these waves are the atmospheric wind disturbances which in turn drive the ionospheric current and TEC disturbances. Therefore, in a SAI coupling mechanism that has satisfactorily simulated the ionoquake, the ground velocity determines the formation of TEC disturbances. In addition, significant horizontal displacements occurring beneath areas with high topography can reinforce the vertical component (SANCHEZ et al., 2022).

Figure 3.8 - Simulation results from the SAI coupling model.

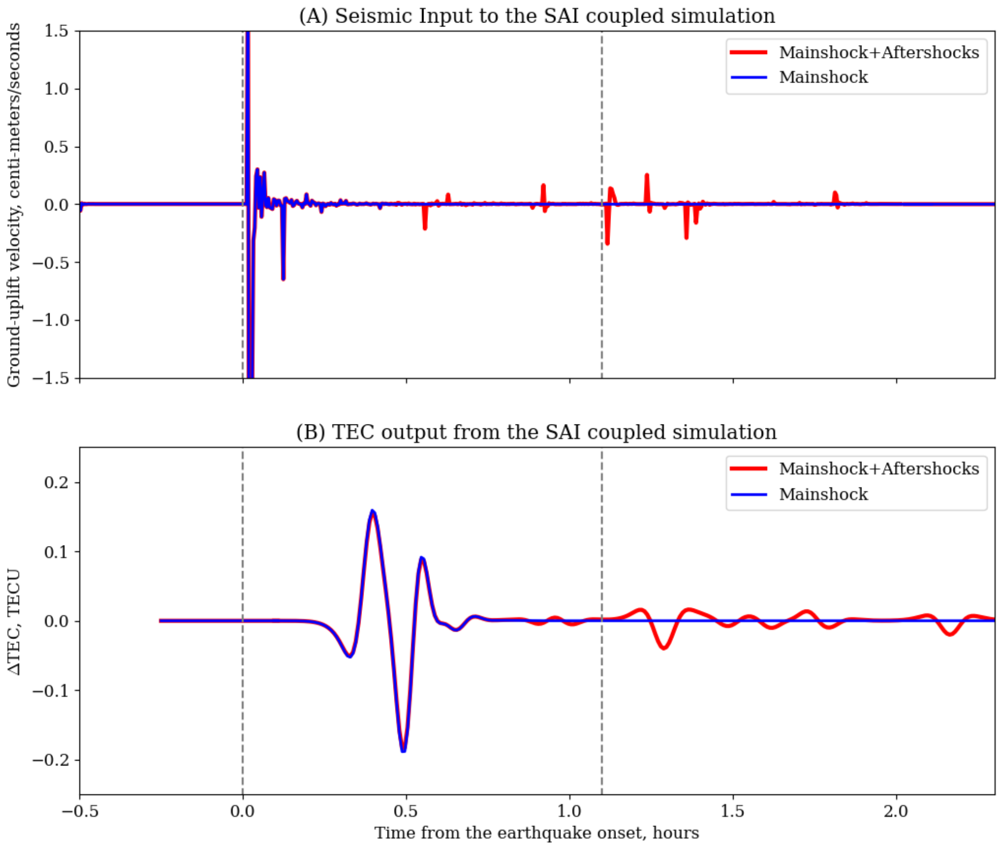


(**A**) The ground vibration at the epicenter with and without the aftershocks. (**B**) Simulated ΔTEC with and without aftershocks.

SOURCE: Sanchez et al. (2022).

### 3.9 Summary for moderate EQs

We report the ionospheric disturbances associated with the 4 July 2019 Ridgecrest EQ of Mw 6.4. The GNSS-TEC measurements register these ionoquakes as intensified wave activities in the range of 1–10 mHz after the mainshock onset and in the vicinity of the epicenter, in contrast to the weak wave activities on the pre-EQ days and post-EQ days. Based on the Seismo-Atmosphere-Ionosphere (SAI) coupling mechanism energized by the acoustic-gravity waves, we find that the ground vibration of 0.05–0.6 cm/s in the normal mode frequencies is adequate to give rise to the detectable ionoquakes of amplitude about 0.05–0.15 TECU. A major finding of the present study is that the ground velocity rather than the ground displacement, satisfies the threshold criteria for the formation of detectable ionoquakes. Therefore, though the mainshock is moderate in nature, associated ground velocity in low-frequency acoustic-gravity modes is comparable to those from mainshock of strong EQs.

The numerical simulation of the coupling mechanism not only reproduces the ionoquakes of the detectable magnitudes associated with the mainshock but also quantifies the relative contribution of mainshock and aftershocks. Interestingly, the simulated ionoquakes from aftershock have magnitude of 0.01 TECU which is well below the detectable limit of GPS-TEC measurements. Nevertheless, the simulation of the ionospheric counterpart of aftershocks manifests the robust nature of SAI coupling to facilitate the generation of ionoquakes from the small EQs. This work is among few to report the detection and simulation of ionoquakes from the Mw $\sim$6.4 EQ. Also, the work is first to report the simulation of ionoquakes of about 0.05 TECU amplitudes from the series of aftershocks of magnitude Mw 4.6.

# 4 GENERATION OF IONOQUAKES UNDER THE SAI COUPLING AND DYNAMICS OF AGWS: FAST SAI-ANA SIMULATION CODE

The generation of ionoquakes under the Seismo-Atmosphere-Ionosphere coupling energized by AGWs is investigated. One of the most acceptable mechanisms is the coupling established through AGWs. Only this coupling channel can explain ionoquakes of detectable amplitude as AGWs offer the possibility of magnifying the vertical ground velocity ($V_{SISM}$, or "uplift") in the epicenter region by about 4-5 orders of magnitude in the thermosphere which then generate ionoquakes in the ionosphere. For example, for uplift of $10^{-3}$ m/s from the epicenter of the EQ with magnitude 7, AGWs can generate a thermospheric uplift of 10 m/s which can give rise to an electric field of the order of 1 mV/m. This magnitude is enough to give rise to the uplift of the ionosphere and increase in its height scale, which is the condition for generating ionospheric disturbances of detectable magnitude.

This chapter presents the study of the generation of AGWs by the uplift of the epicenter and the formation of ionoquakes. Therefore, we developed a mathematical tool to simulate the SAI coupling. The tool includes the analytical solution of AGWs from the set of equations to model AGWs and their coupling with the ionosphere, as deduced by Kherani et al. (2016). The code developed from the analytical solution of AGWs can be found in Appendix C.2, under the name of SIA-ANA code. This code is implemented in the Python programming language. The products of the first part discussed here are the magnitudes of the AGWs, the height of their maximum amplitude, and the time of their arrival in the ionosphere. The products of the second part are the amplitude of the ionoquakes in the form of TEC and the height of the maximum amplitude of the TEC.

## 4.1 SAI-ANA code of generation and propagation of AGWs

The SAI-ANA code is an extension of the analytical model recently developed by Kherani et al. (2021) to examine the formation of co-seismic tropospheric disturbances from seismo-atmosphere coupling energized by AWs and convective instability. In Equations (B.1-B.6), starting from the wave equation of AGWs from Kherani et al. (2016), the time governing equations of AGWs in vertical (z)-horizontal (h) plane and corresponding analytical solution is presented. The derivation considers strong-gradient condition in the vertical-z direction, in comparison to the weak-gradient condition in the horizontal-h direction. In addition, it considers 2D plane-wave solution with wave vector components ($k_h$; $k_z$) of the following form:

$$u_h(h,z,t) = u_{\mathrm{hs}}(z)u_{\mathrm{ht}}(t)exp(ik_hh+ik_zz), \quad u_z(h,z,t) = u_{\mathrm{zs}}(z)u_{\mathrm{zt}}(t)exp(ik_hh+ik_zz) \tag{4.1}$$

This form of solution leads to a set of governing equations for the amplitudes of AGWs of the following form:

$$\frac{d^2u_{\mathrm{zt}}}{\mathrm{dt}^2} = -\Omega_0^2u_{\mathrm{zt}} - k_hk_zc^2\frac{u_{\mathrm{hs}}}{u_{\mathrm{zs}}}u_{\mathrm{ht}}, \quad \frac{\mathrm{du_{zs}}}{\mathrm{dz}} = -k_0u_{\mathrm{zs}} \tag{4.2}$$

$$\frac{d^2u_{\mathrm{ht}}}{\mathrm{dt}^2} = -\Omega_h^2u_{\mathrm{ht}} - k_hk_zc^2\frac{u_{\mathrm{zs}}}{u_{\mathrm{hs}}}u_{\mathrm{zt}}, \quad \frac{\mathrm{du_{hs}}}{\mathrm{dz}} = -(\gamma-1)k_0 - (\gamma-2)k_0\frac{k_zu_{zt}}{k_hu_{ht}}u_{zs} \tag{4.3}$$

$$k_0 = \frac{\zeta}{c^2}, \quad \zeta = \frac{1}{\rho}\frac{dp}{dz}, \quad c^2 = \frac{\gamma p}{\rho}, \quad \mu = \int k_0dz \tag{4.4}$$

$$\Omega_0^2 = k_z^2c^2 + \Omega_b^2, \quad \Omega_b^2 = \left[(\gamma-1)k_0^2 - \frac{k_o}{c^2}\frac{dc^2}{\mathrm{dz}}\right]c^2 \tag{4.5}$$

Here, $\Omega_b$ is the non-isothermal non-hydrostatic Brunt-Vaisala frequency (Equation 6.7a of Kelley (2009)), $\gamma$ is the ratio of the specific heats and c is the sound speed.

We note that, the governing equations of ($u_{zt}$; $u_{ht}$) represent coupled oscillators with known analytical solutions in the linear case, i.e., with ($\rho$; $T$ ) constant in time. Also, the governing equations of ($u_{zs}$; $u_{hs}$) represent a set of first order homogeneous differential equations with known analytical solutions. These solutions are derived in Appendix B in the following form:

$$u_z = u_{\mathrm{zs}}(z_0)u_{\mathrm{zt}}e^{-\mu}e^{\pm i(\omega t+k_hh+k_zz)} \tag{4.6}$$

Here,

$$u_h = -\frac{(\Omega^2-\omega^2-\Omega_h^2)}{k_hk_zc^2}u_z$$

$$\omega^2 = \frac{\Omega^2 \pm [\Omega^4 - 4\Omega_h^2\Omega_b^2]^{1/2}}{2}, \quad \Omega = \Omega_0^2 + \Omega_h^2 \tag{4.7}$$

The factor $e^{-\mu}$ in Equation 4.6 increases with altitude due to the negative values of $(\zeta;\, \mu)$. Therefore, amplitudes $(u_z;\, u_h)$ of AGWs increase exponentially with altitude, a known characteristic of AGWs. In dispersion Equation 4.7, the positive sign leads to the acoustic wave (AWs) modes since with $\Omega_b = 0$, it reduces to the following form:

$$\omega^2 = k_h^2 c^2 + k_z^2 c^2 \equiv k^2 c^2 \tag{4.8}$$

Since, in this case, $\omega^2 = \Omega^2$, therefore,

$$u_h = -\frac{(\Omega^2 - \omega^2 - \Omega_h^2)}{k_h k_z c^2} u_z \overset{\omega=\Omega}{\Rightarrow} u_h = \frac{k_h}{k_z} u_z \Rightarrow \nabla \times u = 0 \tag{4.9}$$

Since the gravity waves are associated with the shear or rotational dynamics, the irrotational velocity field implies absence of gravity wave and only excitation of AWs, a self-consistent scenario with the condition $\Omega_b = 0$. It also affirms the self-consistent nature of the analytical solution obtained in the present study.

This study focuses on the acoustic wave modes and therefore, the simulation is performed with positive sign in the dispersion relation. In the present analysis, the wavenumber components $(k_z;\, k_h)$ are made independent variables. The restriction derives from the finite grid resolutions of the discretization so that the wavenumbers $(\lambda_z = 2\pi/k_z,\, \lambda_h = 2\pi/k_h)$ remain larger than the grid resolutions. Although the analytical form of the solution is obtained, the integral in $\mu$ is to be evaluated numerically with discretization in space. The grid resolution is $\Delta_z = \Delta_h = 5$ km and the simulation domain covers 0 - 400 km in altitude; $h_{ep} \pm 40\Delta_h$ km in horizontal distance. Here, $h_{ep}$ is the epicenter of the EQ. The simulation begins a few minutes before the EQ onset time $(t_{ep})$ and spans 3 minutes with a $\Delta t = 5$ seconds, which means that this analysis can solve a velocity less than 1 km/s.

The study considers the mechanical oscillator mechanism in which the ground vibration from seismic waves couples mechanically to the atmosphere without the loss of momentum. The continuity of vertical ground velocity across the Earth's surface establishes the coupling. At the lower boundary, i.e., at $z = 0$ km, the continuity of the vertical velocity of the ground associated with the EQ acts as the forcing for the generation of the AGWs, i.e.:

$$u_z(h, z = 0, t) = V_{\mathrm{SISM}}(h, t) \tag{4.10}$$

Figure 4.1 demonstrates the temporal variation of $V_{\mathrm{SISM}}$ for a typical EQ of magnitude 8 which is obtained from the following analytical expression:

$$V_{\mathrm{SISM}}(h, t) = A_{eq} e_{skewed}^{-(t-t_0)^2/\sigma_t^2} cos(\omega_s t) e^{-(h-h_{ep})^2/\sigma_{ep}^2} \quad m/s \tag{4.11}$$

where ($A_{eq}$) determines the amplitude of the ground vibration in m/s, ($x_{ep}$; $\sigma_{ep}$) are the epicenter and fault size of the EQ and ($\sigma_t, \omega_s$) determines the duration and frequency of the EQ.

Figure 4.1 - Uplift or $V_{SISM}$ from the epicenter $u_z(z_0, h, t)$.

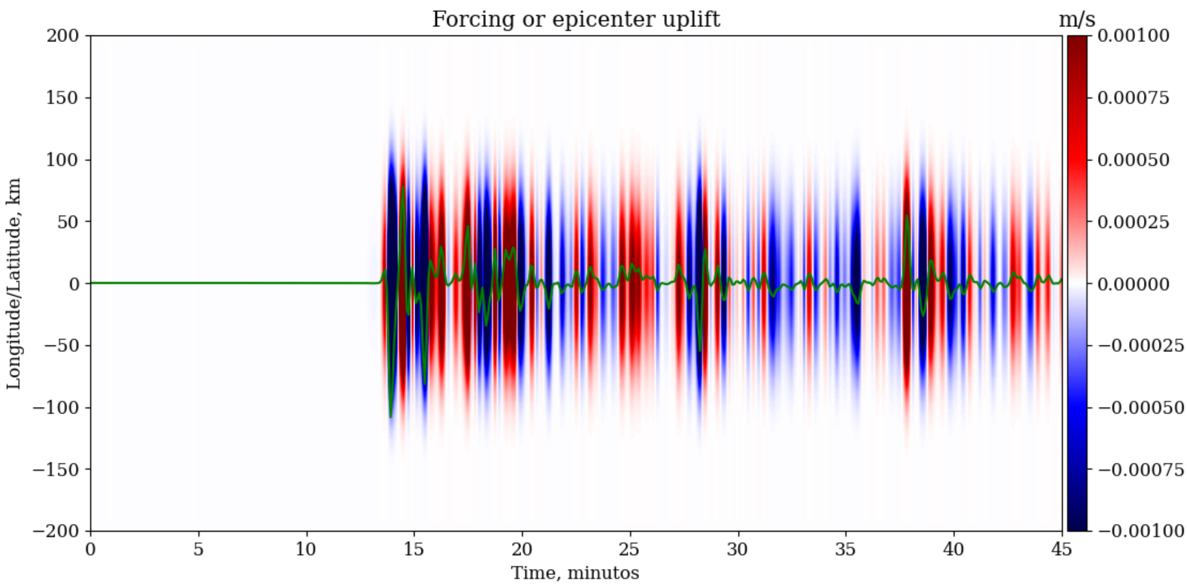


The green time series represents the uplift obtained with a seismometer. The colorbar represents the spatially decomposed uplift of the seismometer data.

SOURCE: Author's production.

The atmosphere is characterized with density ($\rho$), pressure ($p$) and speed of sound

($c$). Figure 4.2 shows profile of ($\rho, c$) from 0 to 400 km. From this atmospheric profiles, the parameters ($\zeta, k_0, \mu, \Omega_b$, and $\Omega$) are estimated.

Figure 4.2 - Profiles of the atmosphere at the time of the occurrence of the Illapel EQ.

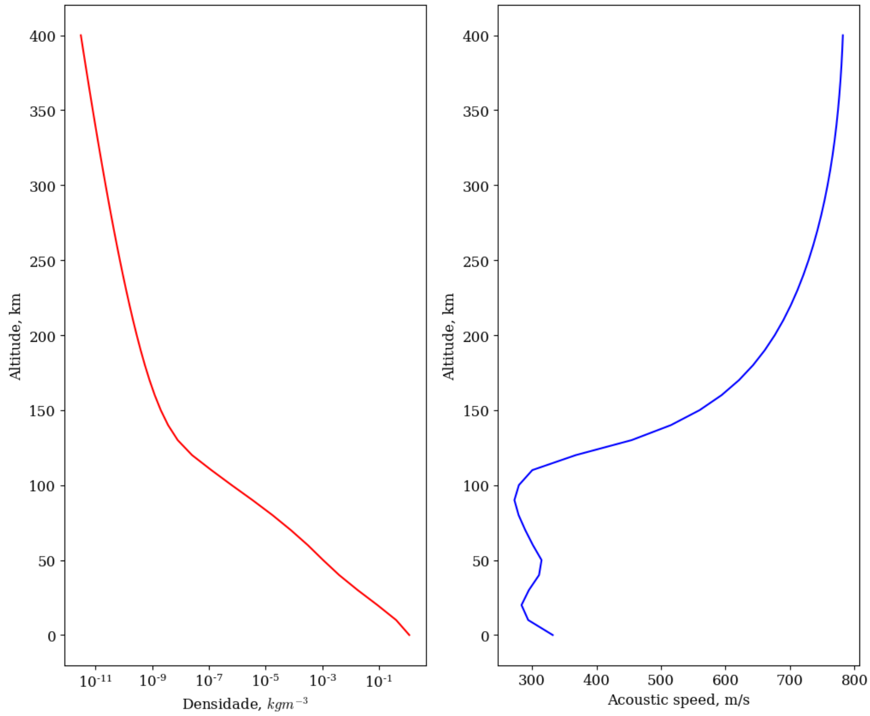


Atmospheric profiles obtained from MSISE model (PICONE et al., 2002).

SOURCE: Author's production.

In Figure 4.3(A) the propagation of AGWs in the form of the evolution of $u_z, u_h$ in time and altitude is shown. Figure 4.3(B) shows the arrival diagram of the AGWs, obtained from Figure 4.3(A). Note that arrival time=0 means the launch time of the AGWs that would happen around the start time of the uplift of the epicenter.

Figure 4.3 shows the evolution of AGWs in space. Note the following features:

a) Amplification of $V_{SISM}$ from $10^{-3}$ m/s (Figure 4.1) to 10 m/s in the mesosphere and thermosphere,

b) Amplification is greatest in the mesosphere in the duct region,

c) First arrival of the AGWs in the F region of the ionosphere at an altitude greater than 180 km, and 200 seconds after the start of the uplift,

d) First arrival of AGWs in the altitude range of 200-300 km, and within 200-350 seconds.

Figure 4.3 - Propagation of AGWs and time-of-arrival diagram.

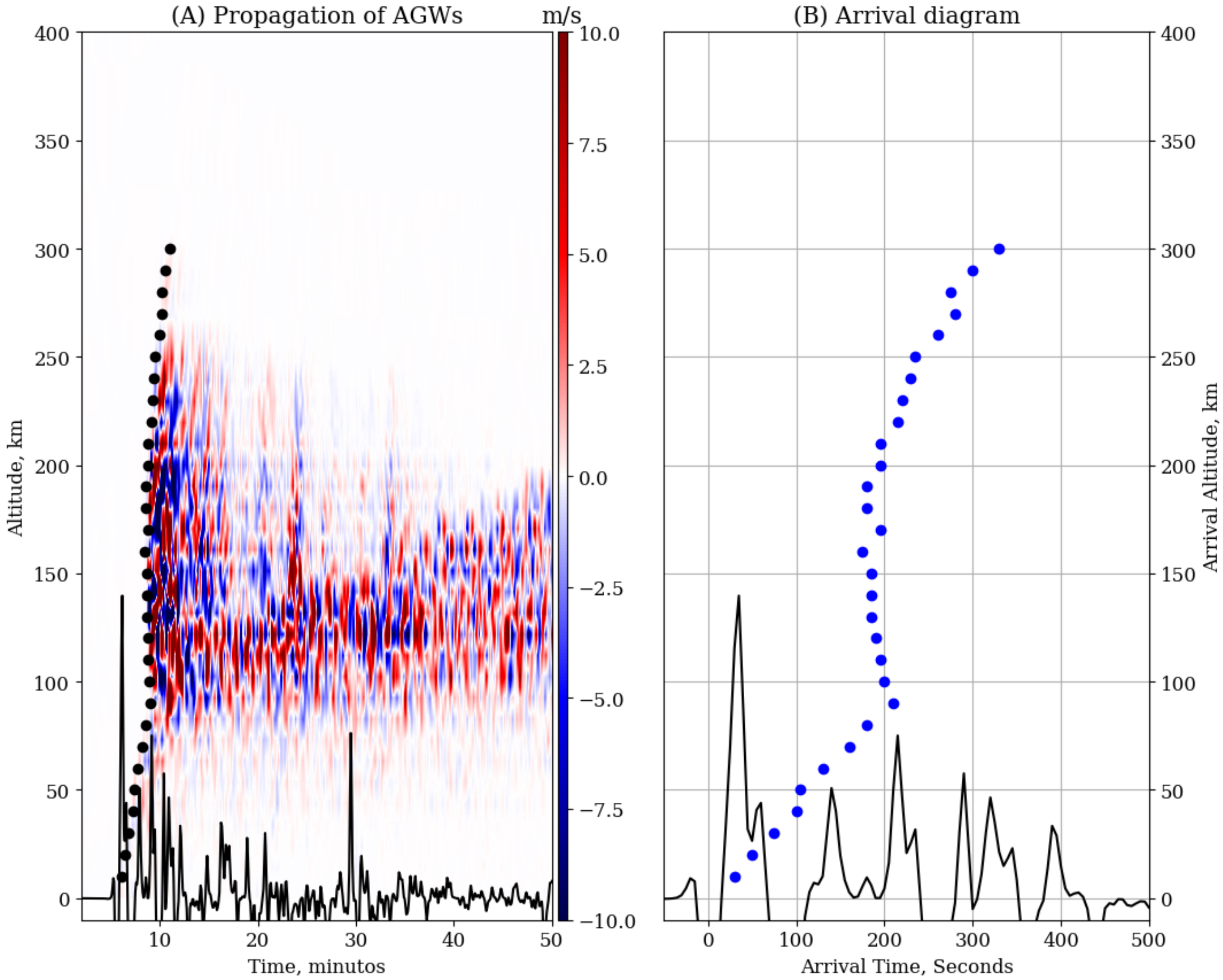


(A) Vertical propagation of AGWs, (B) time-of-arrival diagram. Note that time=0 in (A) represents the start of the simulation and time=0 in (B) represents the first launch of the AGWs because of the uplift. The black curve at altitude = 0 km represents uplift from the epicenter.

SOURCE: Author's production.

Figure 4.4 demonstrates the wave frequency of the AWs at $h = h_{ep}$, excited by the EQ. We note that the AWs with frequencies equals to and larger than the Acoustic cut-off frequency are launched in the atmosphere.

Figure 4.4 - Wave frequency for propagation angle of 45°.

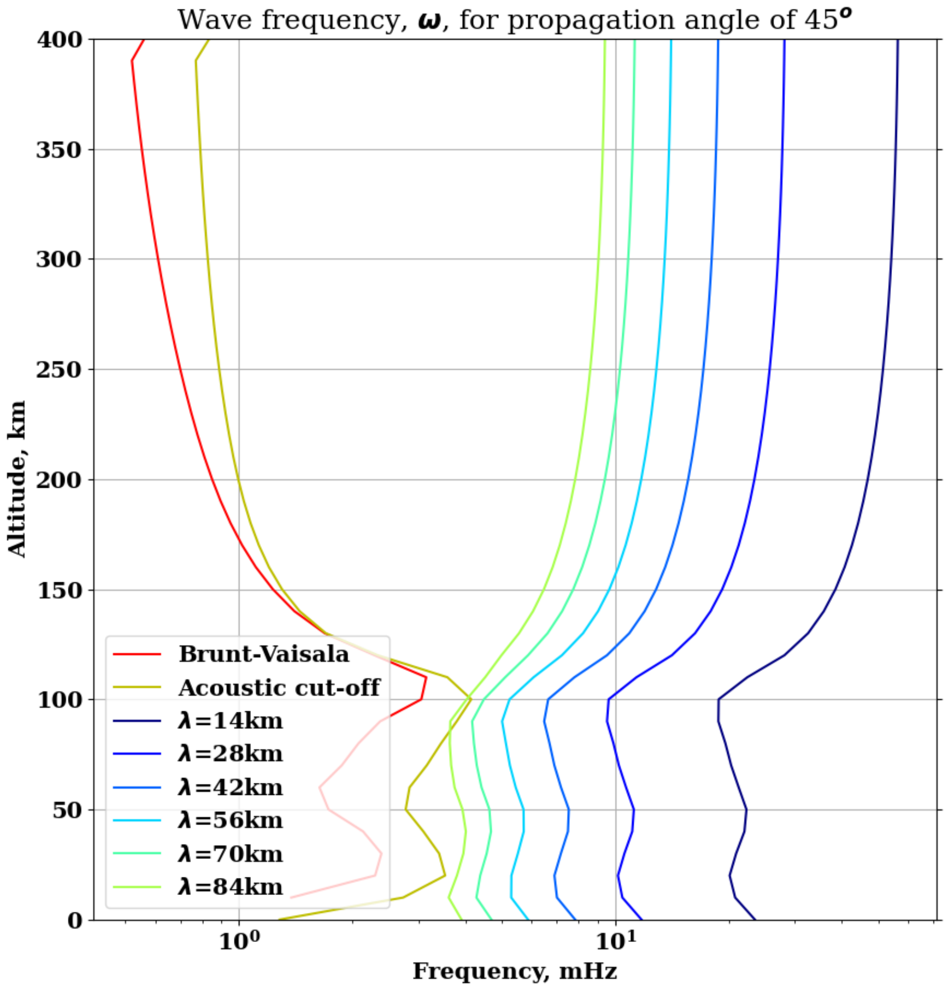


The red and yellow curves represent the frequency of Brunt-Vaisala and Acoustic cut-off, respectively. The other curves represent the frequencies of the AWs with different wavelengths for an angle of 45°.

SOURCE: Author's production.

Figure 4.5(A) shows that the oblique phase velocity for an angle of 45° has the same velocity as the velocity of sound throughout the atmosphere, with some variations for altitudes below 100 km. Figure 4.5(B) shows that the arrival time of the oblique phase velocity is very close to the arrival velocity of the speed of sound.

Figure 4.5 - Oblique phase velocity and oblique arrival time, for an angle of 45°.

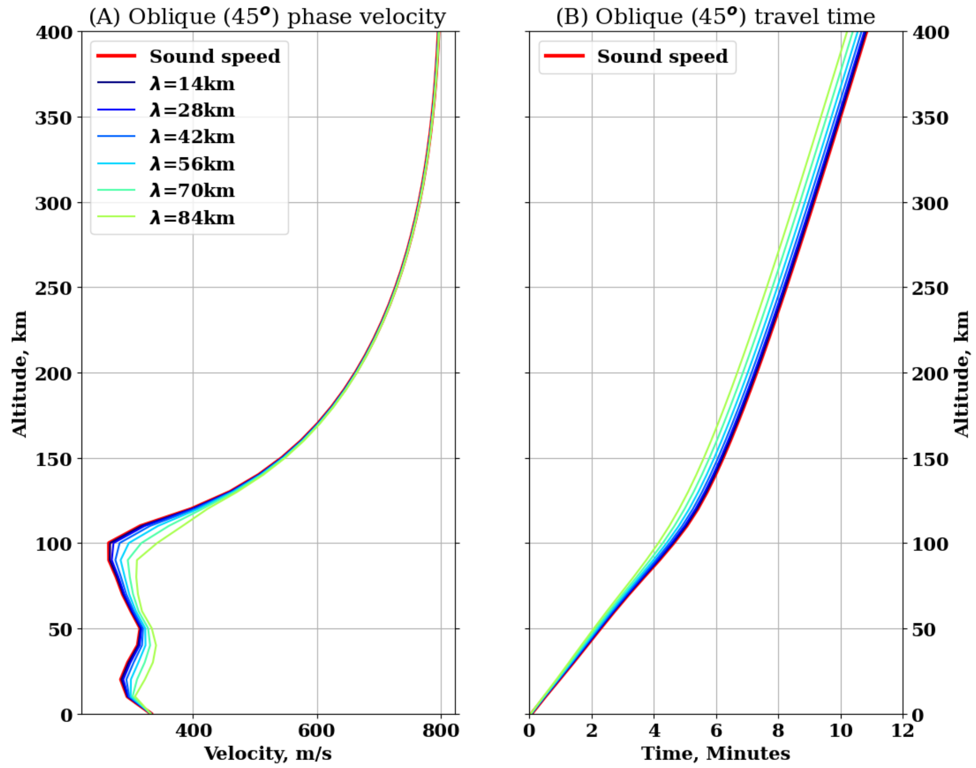


(A) Red curve represents the speed of sound, and the other curves represent the oblique phase velocity of the AW, for different wavelengths. (B) Red curve represents the arrival time of the speed of sound, and the other curves represent the oblique travel time.

SOURCE: Author's production.

Figure 4.6 demonstrates the altitude profile of vertical phase velocity and travel time above the epicenter. The Figure 4.6 reveals following characteristics:

a) The phase velocity increases with increasing vertical wavelength at all altitudes,

b) The phase velocity remains larger than the sound speed at all altitudes,

c) The travel time or arrival time of AWs at any altitude is shorter than the travel time of sound speed,

d) The fastest AWs arrival time in 150-400 km altitude is in the range of 4-8 minutes,

e) The fastest AWs have frequencies in the 4-10 mHz range.

Figure 4.6 - Vertical phase velocity and vertical travel time.

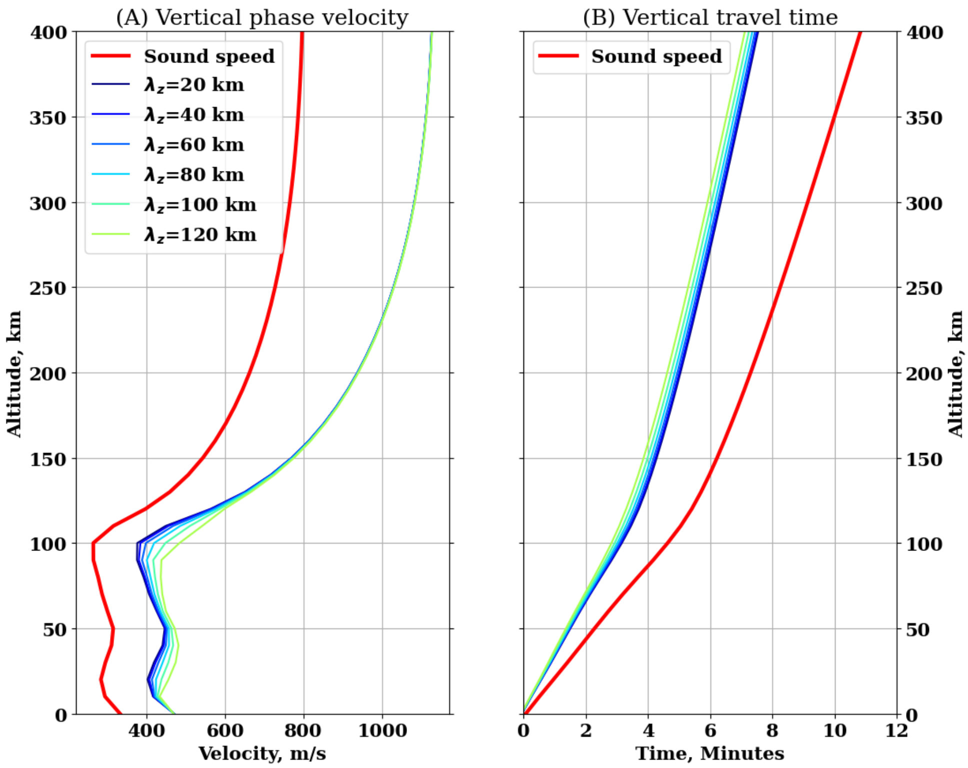


(A) Red curve represents the speed of sound, while the other curves represent the vertical phase velocity for different wavelengths ranging from 20-120 km. (B) The red curve represents the arrival time of the velocity of sound, while the other curves represent the arrival time of vertical phase velocity.

SOURCE: Author's production.

The vertical phase speed of AGWs larger than the sound speed can be understood from the approximate form of dispersion Equation 4.7:

$$\omega^2 \approx \Omega_0^2 + \Omega_h^2 = (k_z^2 + k_h^2)c^2 + \Omega_b^2 \tag{4.12}$$

Therefore, the vertical phase velocity is written as follows:

$$\frac{\omega}{k_z} = \sqrt{\left(1 + \frac{k_h^2}{k_z^2}\right)c^2 + \frac{\Omega_b^2}{k_z^2}} \xrightarrow{k_h \neq 0, \quad \Omega_b \neq 0} \frac{\omega}{k_z} > c \tag{4.13}$$

which is larger than the sound speed ($c$). Moreover, the vertical phase velocity depends on the $(k_z, k_h)$ i.e. different wavelengths acquire different vertical phase velocities, as noted in Figure 4.5. The oblique phase velocity slightly larger than the sound speed in Figure 4.6 is due to the presence of $\Omega_b$ term in the above dispersion relation.

## 4.2 AGWs+ionosphere coupling

To calculate the TEC, we use the AGW and the ionosphere coupling model, developed by Kherani et al. (2016). The products of this model are the drift ($v$) and the density ($n$) of the ionosphere. The TEC is estimated using the following integration over height ($z$), at the time ($t$) and latitude/longitude ($h$):

$$\mathrm{TEC}(t,h) = \int_{z1}^{z2} n(z,t,h)\mathrm{dz} \tag{4.14}$$

where for $z1$ we generally consider an altitude of the maximum amplitude of the AGWs and $z2$ to be the maximum density of the ionosphere. In addition, the amplitude of ionoquakes is estimated with the following formula:

$$\Delta\mathrm{TEC}(t,h) = \mathrm{TEC}(t,h) - \mathrm{TEC}_0(h) \tag{4.15}$$

where $\mathrm{TEC}_0$ is the value of TEC in the initial moment. According to Kherani et al. (2016),

$$\Delta\mathrm{TEC} \propto (u_z, u_h) \equiv \alpha_{\mathrm{iono}} u_z + \beta_{\mathrm{iono}} u_h \tag{4.16}$$

where $(\alpha, \beta)$ depends on the characteristics of the ionosphere and the geomagnetic field.

Figure 4.7 demonstrates the propagations of AWs and associated ionospheric density disturbance above the epicenter. Figure 4.8 demonstrates the temporal variation of TEC disturbance, associated with the ionospheric density disturbance and corresponding spectrum. These figures reveal the following characteristics:

a) AWs arrive to the thermosphere during 4-10 minutes from the mainshock onset,

b) AWs acquire amplitude of about 10 m/s in the thermosphere from the ground vibration of $10^{-2}$ m/s,

c) AWs energetics excite the ionospheric density disturbances that attains the magnitude of about 5% of the ambient ionospheric density,

d) The TEC disturbances, $\Delta$TEC, begins at about 3.5 minutes from the mainshock onset and attains the maximum of 0.8 TECU during 6 minutes.

Figure 4.7 - Acoustic-gravity wave amplitude and Ionospheric density disturbance.

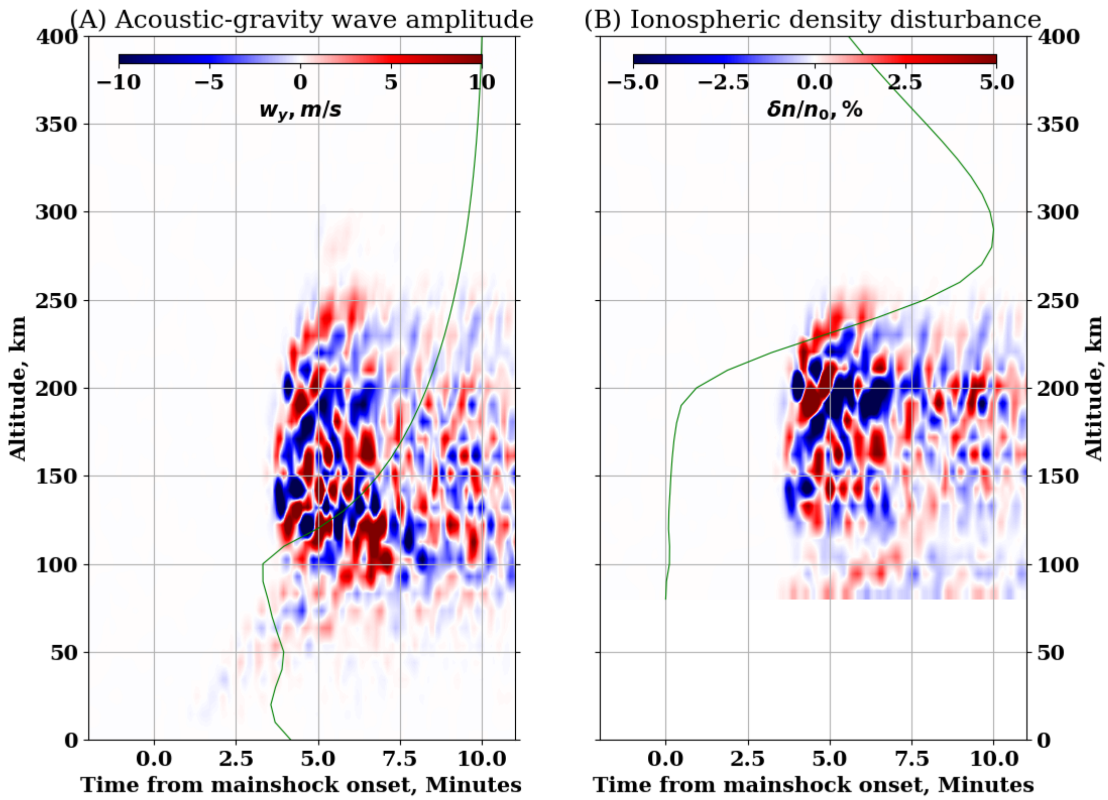


(A) Vertical propagation of AWs, and (B) ionospheric density disturbance above the epicenter.

SOURCE: Author's production.

These characteristics reveal the robust energetics of fast-propagating AWs and their role in the development of rapid ionoquakes. The robust energetics include the amplification of tiny ground vibration by a factor of $10^3$ due to the amplification factor $e^{-\mu}$ in Equation 4.6 and the rapid propagation of AWs with arrival time during 4-6 minutes, as noted in Figure 4.5. Moreover, the spectral characteristics of ionoquakes are determined by AWs in the frequency range of 4-10 mHz and wavelengths of 80-160 km that arrive earliest in the thermosphere and gives rise to the rapid ionoquakes.

## 4.3 Estimating the peak altitude of the ionoquakes

In Figure 4.8, the variation of $\Delta$TEC integrated for altitudes between 150 and 300 km is shown. These altitudes delimit the region of greatest ionization. Note in Figures 4.8 and 4.3(B) that depending on the altitude, the time of arrival of the AGWs and the time of generation of the $\Delta$TEC of the Equation 4.16 (above the epicenter) can occur in 200-300 seconds and the peak of ionoquakes can occur in 240-350 seconds. Thus, depending on the time of onset of the ionoquakes, the latitude of the peak of the ionoquakes can be estimated from the time-of-arrival diagram of Figure 4.3(B). The time-of-arrival diagram depends mainly on characteristics of the atmosphere such as the speed of sound. Thus, to estimate the peak altitude of the ionoquakes, it is necessary to know the atmospheric conditions that can be obtained from an empirical model such as MSISE (PICONE et al., 2002).

Figure 4.8 - $\Delta$TEC calculated with SAI-ANA code.

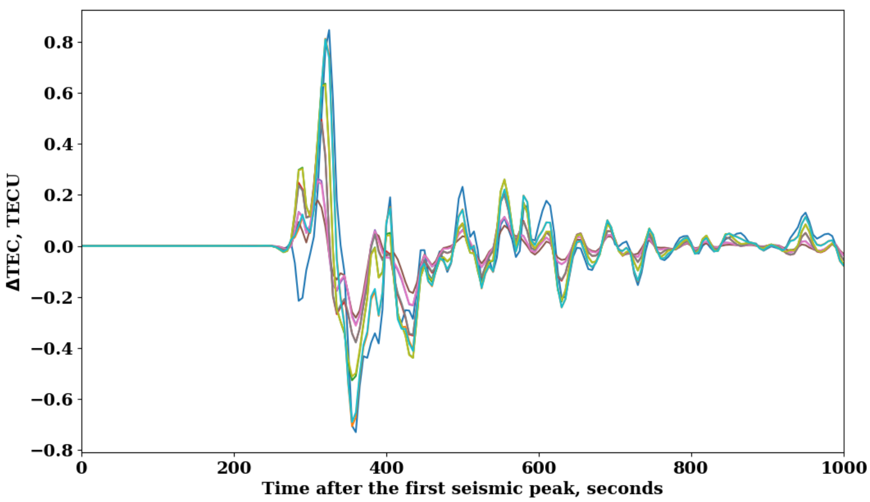


The colored time series represent the first simulated $\Delta$TEC arrivals near the epicenter, for a TEC integration between 150 to 300 km.

SOURCE: Author's production.

## 4.4 Estimating the uplift $(u_z(z_0, h, t))$ from the amplitude of two ionoquakes

In Figure 4.6B, the oblique phase propagation of two AGWs is shown. It arrives in the ionosphere much later (almost 7 minutes) compared to the vertical phase component in Figure 4.5B. This is due to the fact that the transverse component is dominated by gravity waves that propagate slowly, as opposed to the longitudinal component dominated by fast acoustic waves. Therefore, for the first pulse of ionoquakes, Equation 4.16 is approximated with:

$$\Delta\text{TEC} = \alpha_{\text{iono}} u_z \tag{4.17}$$

Using Equation 4.16,

$$\Delta\text{TEC} = \alpha_{\text{iono}} \alpha_{\text{atmos}} u_z(z_0, h, t) \tag{4.18}$$

Thus, with knowledge of the $(\alpha_{\text{iono}}, \alpha_{\text{atmos}})$ that can be obtained with empirical models of the atmosphere, ionosphere and IGRF and with the measurement of the first pulse of the ΔTEC after the EQ, the *uplift* of the EQ can be estimated.

## 4.5 Discussions on the SAI-ANA code of AGWs

The ionoquake characteristics in Figure 4.6-4.7 are similar to their observations from the previous reports. For example, Afraimovich et al. (2001) and Astafyeva et al. (2013) had reported the detections of near-field rapid ionoquakes with magnitude of $2-4\%$ during 6 - 8 minutes from the EQ onset, with oscillation periods in 30- 300 seconds, i.e., 3 - 30 mHz and velocity larger than the thermospheric sound speed. According to Heki and Ping (2005), sound ray arrives from 10 minutes onward at 200 km altitude, which is also evident from the travel time of sound ray in Figure 4.5. Therefore, the rapid ionoquake detection could not be explained from the ray tracing analysis. In Figure 4.5, the fast propagation of AWs in the lower atmosphere explains the rapid ionoquake detection, originating in altitudes as high as 350 km altitude, though their amplitude may vary significantly depending on the amplitude of AWs and availability of significant electron density.

An interesting aspect of these AWs and rapid ionoquakes is that their maximum phase velocity in the thermosphere is significantly larger than the sound speed, so they arrive earlier than the sound ray. The rapid arrival is due to their phase velocities larger than the sound speed in the lower thermosphere, as explained earlier in the context of Figure 4.5. Therefore, these rapid ionoquakes propagate horizontally with phase velocity close to the thermospheric sound speed, as evident in Figure 4.8.

### 4.6 Summary of SAI-ANA code of AGWs

Based on the SAI coupling mechanism and AGWs energetics, the present study demonstrates the rapid arrival of AGWs at the ionospheric heights and the development of ionoquakes as early as 4 minutes from the mainshock onset. Since the atmospheric acoustic speed is not uniform, the wave speed may range between minimum and maximum values, depending on local and non-local effects. The study finds the acoustic wave with a long wavelength of about 100 km, that propagates with the thermospheric acoustic speed and is responsible for the rapid ionoquakes. As the wavelength decreases, the contribution from the local acoustic speed increases, and as a result, acoustic waves with shorter wavelength propagate with an average acoustic speed that is much smaller than the thermospheric acoustic speed.

This is the first study to simulate the rapid ionoquakes with simulation time within 2 - 3 minutes, much faster than their time of development and observation which is about 8 minutes. The rapid ionoquakes are promising candidates for near-real-time ionospheric seismology. Their near-field detection from previous observations and their comparatively rapid simulation in the present study offer an integrated framework for the early warning of EQs at far-field locations. Even at near field locations, their formation from simulation can be forecasted before their detections since the simulation is analytic in nature.

# 5 RAPID DETECTION OF IONOQUAKES

In this section reviews the paper "*Rapid detection of co-seismic ionospheric disturbances associated with the 2015 Illapel, the 2014 Iquique and the 2011 Sanriku-Oki EQs*" by (SANCHEZ et al., 2023) currently submitted for publication. It presents the first report on detection of Ionoquakes 250-430 seconds from the peak seismic uplift and within 50-200 km epicentral distance. Also, the study validates CID detection methodology by finding the location of the origin of rapid-CID, near the epicenter.

Usually, ionoquakes are detected in the near-epicentral region within 8-10 minutes after an EQ onset time. In this work, we present a new methodology that allows to estimate the CID arrival time based on determining the CID peak time in TEC measurements with respect to the peak time of seismic waves registered by the nearest seismic station. Our methodology also allows to understand the altitude of GNSS detection that otherwise remains ambiguous. We apply the newly developed techniques to detect CID signatures associated with three large EQs: the 2015 Illapel, the 2014 Iquique, and the 2011 Sanriku-Oki. We show that for these events, the CID arrive 250-430 seconds after the time of the seismic wave peak, or 350-700 s after the EQ onset time. Our analysis show that the first CID are detected at the altitudes of 150-180 km (the Sanriku EQ) and of 200-300 km (the Illapel and the Iquique EQs). The disturbances represent high-frequency acoustic oscillations that propagate with a horizontal speed faster than 0.75 km/s.

In this work, we present a new methodology allowing to 1) rapidly detect CID in total electron content (TEC) data times series and to estimate the CID arrival time ; 2) estimate the altitude of ionospheric detection. We further apply this technique to analyze co-seismic ionospheric signatures due to the Mw8.3 Illapel EQ of September 16, 2015, the Mw8.2 Iquique EQ of April 01, 2014, and the Mw7.3 Sanriku-oki EQ of March 09, 2011.

## 5.1 EQ events and seismic and TEC data

The Illapel and Iquique EQs of Mw8.3 and 8.2 respectively were triggered near the Chile subduction zone, in South America. Seismicity in the Chilean region is defined by the subduction of the oceanic Nazca plate under the South American plate. This subduction zone is well known for harboring large EQs (Carrasco et al., 2019). The Illapel EQ occurred on September 16, 2015, at 22:54:32 UT. According to the U.S. Geological Survey (USGS), this EQ was generated by thrust faulting, with the epicenter located at latitude = 31.57°S and longitude = 71.67°W, at a depth of 22.4 km (<https://earthquake.usgs.gov/earthquakes/eventpage/us20003k7a/technical>). The Iquique EQ occurred on April 01, 2014, at 23:46:47 UT as a result of thrust faulting, with the epicenter located at latitude = 19.61°S and longitude = 70.77°W, at a depth of 25.5 km, (<https://earthquake.usgs.gov/earthquakes/eventpage/us20003k7a/technical>). The Sanriku-Oki EQ of Mw7.4, occurred on March 9, 2011 at 02:45:20 UT at a depth of 32 km, with an epicenter at 38.435°N, 142.842°E (<https://earthquake.usgs.gov/earthquakes/eventpage/usp000hvhj/executive>).

Figure 5.1 illustrates the epicentral location and the shake map of peak ground velocity for the Illapel, Iquique, and Sanriku-Oki EQs (source: <https://earthquake.usgs.gov/earthquakes>). The present study employs the seismic data derived from seismometers and TEC data derived from GNSS receivers. Figure 5.1 also illustrates the locations of seismic stations and GNSS receivers for the three EQ events.

Figure 5.1 - Locations of the 2015 Illapel (A), the 2014 Iquique (B) and the 2011 Sanriku-oki (C) EQs.

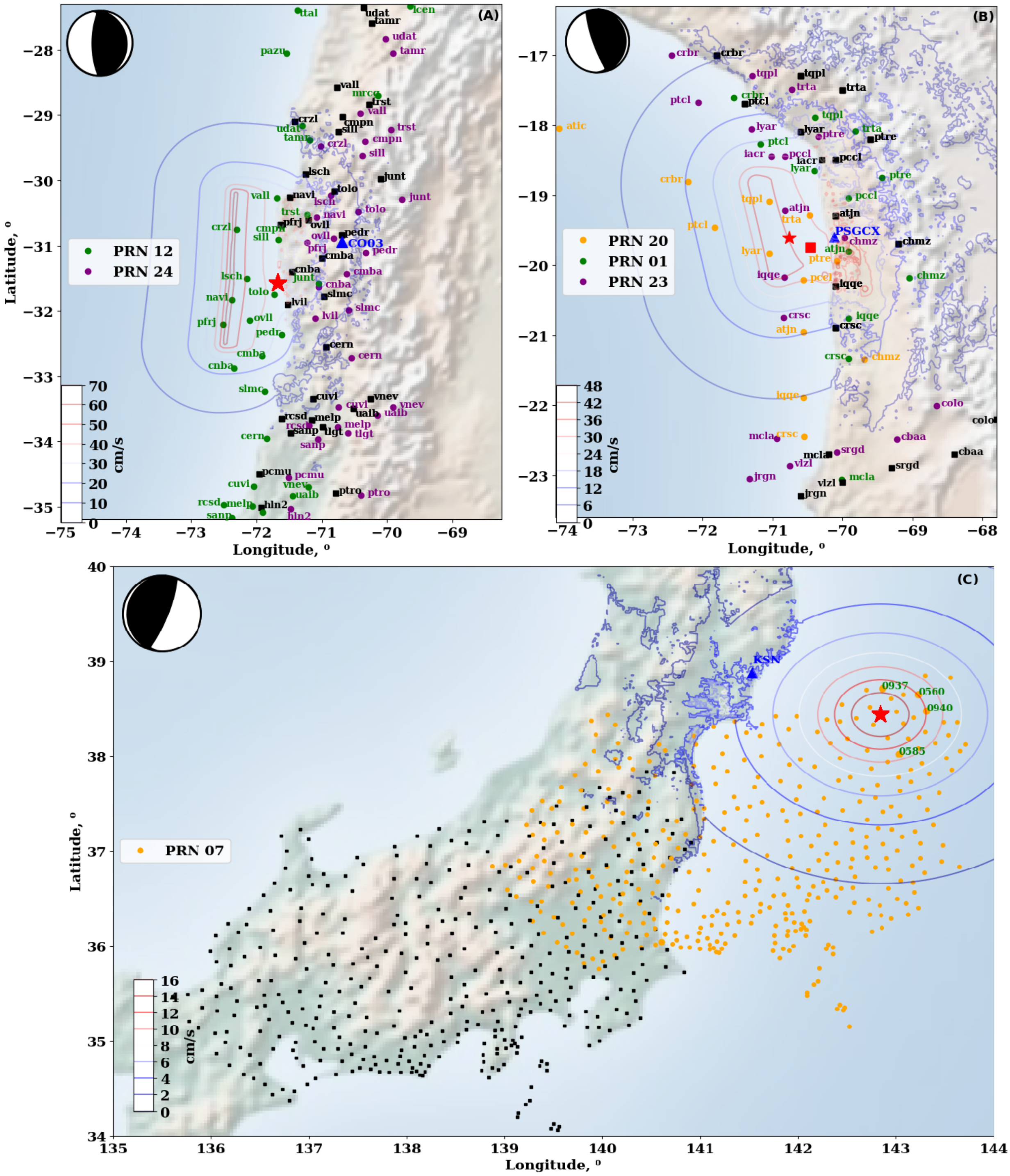


The epicenter of the EQs is represented by a red star and the blue triangles show the location of the seismic stations used in this study. The dots of different colors represent the SIPs at the time when the ionoquake occurred, each color corresponds to a particular PRN. The black squares depict the location of the GNSS stations. The colored contours represent the PGVs for each of the EQs. Beach ball shows the Global Centroid Moment Tensor.

SOURCE: Sanchez et al. (2023).

### 5.1.1 TEC data and ionoquake detection

For Illapel and Iquique EQs, we examine the TEC data with 15 seconds sampling rate, retrieved from GNSS receivers of the permanent ground-based network UNAVCO (<http://www.unavco.org>) and CSN <https://ccmc.gsfc.nasa.gov/modelweb/models/iri2016_vitmo.php>. For the analysis of the Sanriku-Oki EQ, the original TEC data is with a 1-second sampling rate, retrieved from GNSS Earth Observation Network System (GEONET). For identical spectral conditions, however, the study lowers the sampling rate from 1 second to 15 seconds.

During the EQs, multiple GNSS satellites were visible by ground-based GNSS receivers. However, here we focus on PRNs = 12 and 24 for the Illapel EQ, PRNs = 01, 20, and 23 for the Iquique EQ, and PRN = 07 for the Sanriku-Oki EQ. We have selected these PRNs since their projected locations at the ionospheric heights i.e., the Sub-Ionospheric Points (SIP) are within ∼450 km of the epicenter, and the elevation angle is more than 42°, except for the Sanriku-Oki EQ, where the elevation angle was ∼ 30°.

To monitor the ionoquake energetics in the presence of ambient ionospheric and non-seismic energetics, we employ the wave-decomposition analysis to the time series of vTEC. The analysis relies on filtering the time series at various frequencies between 0.13 mHz-33 mHz and search for new oscillations immediately after the EQ onset time and in the vicinity of the epicenter.

### 5.1.2 $V_{\mathrm{SISM}}$ estimation from seismometers

To obtain the vertical velocity ($V_{\mathrm{SISM}}$) associated with the ground vibration from the seismometers, we employ the python library: obspyDMT. ObspyDMT is an open-source toolbox for querying, retrieving, processing, and managing seismological data sets (HOSSEINI; SIGLOCH, 2017). The library downloads the data in count format, estimates the ground vibration, and minimizes the instrumental response contributions associated with the frequency response, amplifier, analog and digital filters, and digitization. We used a bandpass filter on the seismograms before deconvolution, with a tuple defining the four corner frequencies (0.02, 0.12, 10, 20) (HOSSEINI; SIGLOCH, 2017).

In the present study, $V_{\mathrm{SISM}}$ corresponds to the seismic station CO03 for the Illapel EQ, PSGCX for the Iquique EQ, and KSN for the Sanriku-Oki EQ (Figure 5.1). To match the TEC sampling rate and to achieve identical spectral conditions between the two datasets, we reduce the seismic data sampling rate from 0.05 seconds to 15 seconds. The IRIS network (<http://ds.iris.edu/wilber3/find_event>) and National Research Institute for Earth Science and Disaster Resilience (NIED)-F-net (<https://www.fnet.bosai.go.jp/>) administer the seismic data.

## 5.2 Methodology rapid ionoquakes

In contrast to previous studies that rely on the onset time of an EQ, here we suggest to use the seismic peak time of the $V_{SISM}$ for the estimation of the ionoquake detection time ($t_{detection}$). The seismic peak time represents the time of the maximum seismic oscillations rather than the beginning time of the oscillations. We note, however, that the identification of the oscillation peak in the time series is comparatively unambiguous. The analysis subjects the $V_{SISM}$ and TEC data to the spectral analysis procedure with identical spectral conditions, namely, the equal data length of 2 hours and a sampling rate of 15 seconds. Then, we examine the spectrogram in a frequency range of 0.13 mHz-33 mHz, and, for each frequency, we search for new oscillations in TEC starting from the corresponding peak onset time of $V_{SISM}$ and in the vicinity of the epicenter.

We test two independent criteria to identify the peak time. In TEST-1, the peak time corresponds to the time of the first peak in the $V_{SISM}$ and TEC oscillation. In TEST-2, the peak time corresponds to the time of the maximum in the $V_{SISM}$ and TEC oscillations, i.e., corresponds to the time of the maximum amplitude. The peaks and the maxima are estimated by using the python module "find-peaks". If the peak time of $V_{SISM}$ and ionoquake are $t_{SISM}$ and $t_{TEC}$ respectively, then the ionoquake detection time can be defined as follows:

$$t_{detection} = t_{TEC} - t_{SISM} \tag{5.1}$$

Since both $t_{SISM}$ and $t_{TEC}$ suffer identical time shift from spectral analysis, the ionoquake detection time $t_{detection}$ remains unaffected by the time shift.

## 5.3 Results and discussion of the rapid ionoquakes

We first apply our methodology to the 2015 Illapel EQ case. The time series of the seismic $V_{SISM}$ and the ionospheric TEC data are shown in Figure 5.2. The seismic data are from the seismic station CO03, which is the closest to the epicenter, and TEC data corresponds to the SIP of Line-Of-Sight between the GPS station LSCH and G12 satellite (Figure 5.1). The SIP of the trajectory of PRN 12 passes over the seismic fault region and remains close to the epicenter (Figure 5.1).

Figure 5.2 - Vertical ground velocity and TEC time series.

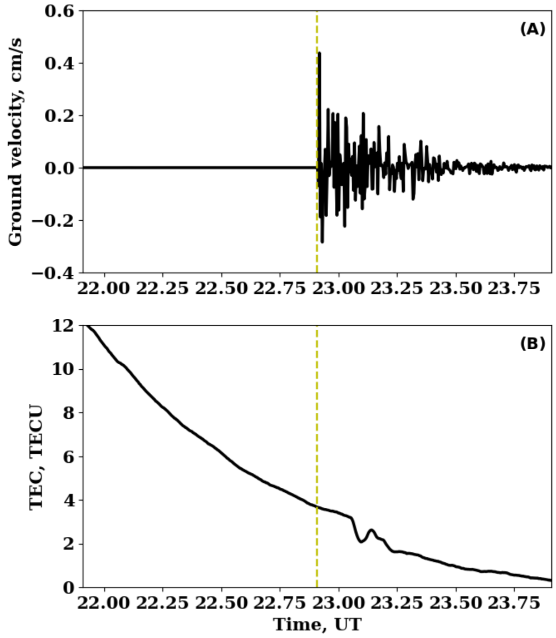


Vertical ground velocity recorded by seismic station C003 (A), TEC time series recorded by the GNSS satellite PRN G12 and the LSCH ground receiver (B), for the 2015 Illapel EQ. Both the $V_{SISM}$ and TEC time series have a resolution of 15 seconds.

SOURCE: Sanchez et al. (2023).

Figure 5.3 demonstrates the results of TEST-1 and TEST-2 in left and right panels, respectively. We note the following characteristics:

- (A1, B1) reveal that the peak onset time of the $V_{SISM}$ depends on the frequency and occurs between 22:54-23:03 UT,
- (A2, B2) reveal that the peak onset time of ionoquakes also depends on the frequency
- (A3, B3) reveal that the peak onset time of ionoquakes occurs about 250-550 seconds after the peak time of the $V_{SISM}$, depending on the frequency

and testing criteria, i.e., the detection time of ionoquakes ranges between 250-550 seconds,

- In both TEST-1 and TEST-2, the detection time of ionoquakes ranges between 250-400 seconds, for the frequency range of 2-10 mHz,

Since both TEST-1 and TEST-2 confirm the ionoquake detection time range of 250-400 seconds, it can be considered as the valid ionoquake detection time in this frequency range, invariant of the criteria.

Figure 5.3 - Spectrogram of TEC data and seismometers to calculate arrival time of the Ionoquakes.

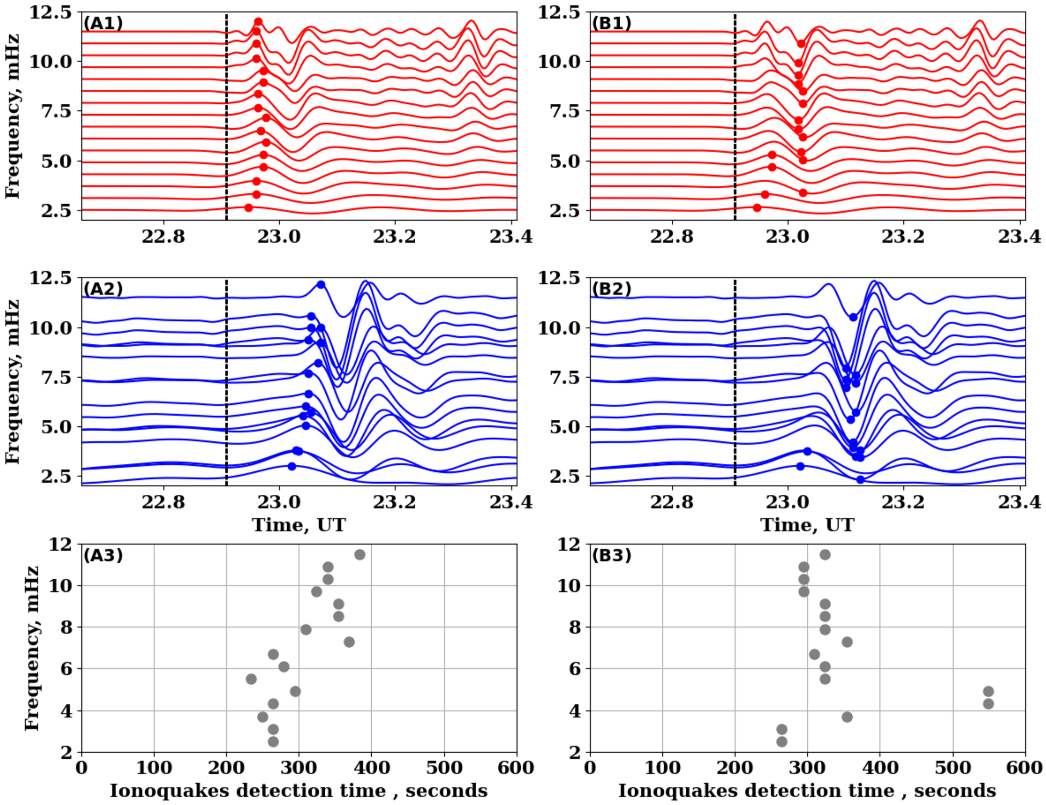


Results of TEST-1 (left) and TEST-2 (right). Panels A1-B1 show the $V_{SISM}$ time series recorded by the CO03 seismic station for different frequencies. Panels A2 and B2 show the ΔTEC time series obtained at different frequencies for the lsch PRN G12 station. The red dots in (A1) and the blue dots in (A2) show the time of the peak in the first seismic oscillation and the first ΔTEC oscillation. On the other hand, the red and blue points in (B1, B2) show the peak in the entire series of seismic and ΔTEC oscillations, respectively. The gray points in panels (A3, B3) represent the detection time of ionoquakes.

SOURCE: Sanchez et al. (2023).

To validate the methodology of the detection time estimation, we apply it to the other SIP from various GPS stations within ±400 km CO03-SIP distance that detected ionoquakes, and we further examine the relationship between the detection time and the CO03-SIP distance. Figure 5.4(A, B) demonstrates the relationship for the frequency of 3.7 mHz and a frequency range of 3.2-10 mHz, respectively. We note the expected increase of the detection time with the distance. According to Figure 5.4(B), the minimum detection time is about 200 seconds at the distance of about -125 km, corresponding to the CO03-SIP distance of LSCH-G12. Since detection time prolongs symmetrically across the minimum ionoquake detection time location, the analysis identifies this detection as the "earliest ionoquake". Noticeably, it is located very close to the epicenter and fault region (denoted as red star and purple square in Figure 5.4). Therefore, our methodology not only estimates the detection time vs. distance characteristics but also, locates the earliest ionoquake close to the epicenter, based on the minimum detection time of the ionoquake. These two findings, therefore, validate the estimation of the ionoquake detection time in the present study.

Figure 5.4 - CID/ionoquake detection time as a function of the horizontal distance from CO03 seismic station.

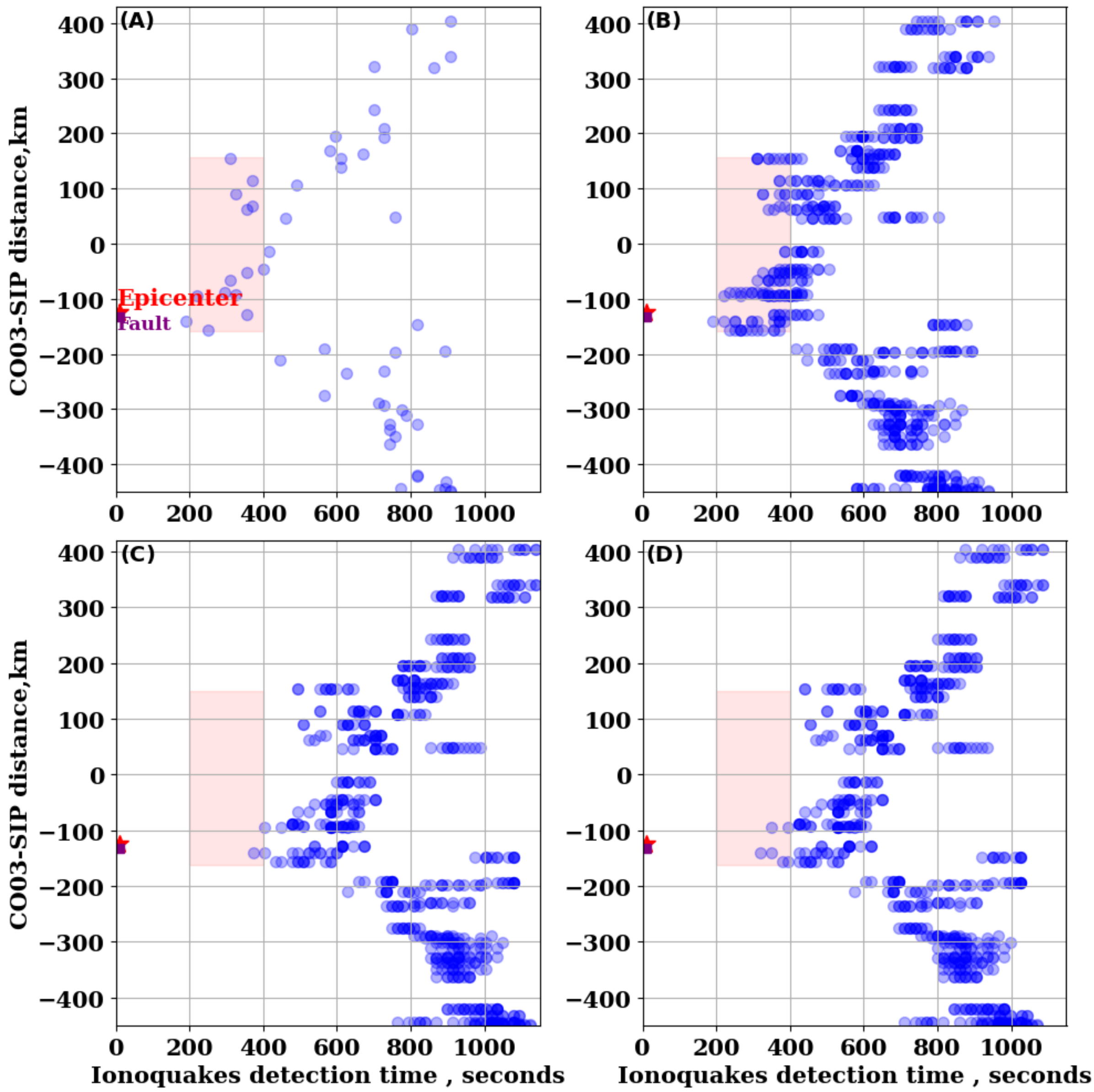


Panel (A) was calculated with the frequency of 3.7 mHz, panel (B) with frequencies from 3.2 to 10 mHz. (C) ionoquake detection time calculated with the onset time documented by the USGS 22:54:32 UT; (D) is calculated with the time of the maximum slip as estimated by the USGS. The frequency range is between 3.2 and 10 mHz. The distance of 0 km indicates the location of the CO03 seismic station.

SOURCE: Sanchez et al. (2023).

In supplementary Figure A.8, we present time snapshots of the TEC map during -300-1400 seconds where 0 seconds correspond to the peak onset time of $V_{SISM}$

at the frequency of 3.7 mHz. We note that the TEC response becomes noticeable approximately 240-300 seconds after the EQ onset, in confirmation of findings in Figures 5.3-5.4.

### 5.3.1 Possible subjectivities of the new methodology and their impacts on the ionoquake detection time

#### 5.3.1.1 Seismic station vs. Epicenter

Figure 5.4 shows the ionoquake detection time estimated with reference to a particular seismic station: CO03, instead of the epicenter location. In order to examine any possible subjectivity arising from the location of a seismic station, we carry out the ionoquake detection time estimation for various seismic stations (Figure A.9). We note that the ionoquake detection time remains within 250-400 seconds near the epicenter, independently on a choice of a seismic station. Therefore, the results of the present methodology are not subjective to a choice of seismic station.

### 5.3.2 Detection altitude for rapid ionoquakes

Figure 5.4(A, B) reveals the potential of the present methodology to identify the epicentral distance of the earliest ionoquake close to the epicenter. However, the location of CID/ionoquakes depends on the altitude ($H_{ION}$) of the thin ionospheric layer that is assumed to be $H_{ION}$= 300 km in Figure 5.4(A, B). Consequently, the horizontal distribution of ionoquakes will also depend on $H_{ION}$. To have an unambiguous ionoquake detection time, we examine the horizontal distribution of ionoquake detection time with varying $H_{ION}$=200, 250, 300, and 350 km (Figure 5.5). Interestingly, in Figure 5.5(C), for $H_{ION}$=300 km, the epicenter and the locations of minimum detection time are the closest. Therefore, the altitude region around 300 km is the most favorable altitude for the detection of the ionoquakes.

Figure 5.5 - Ionoquake detection time - distance diagram for numerous SIPs.

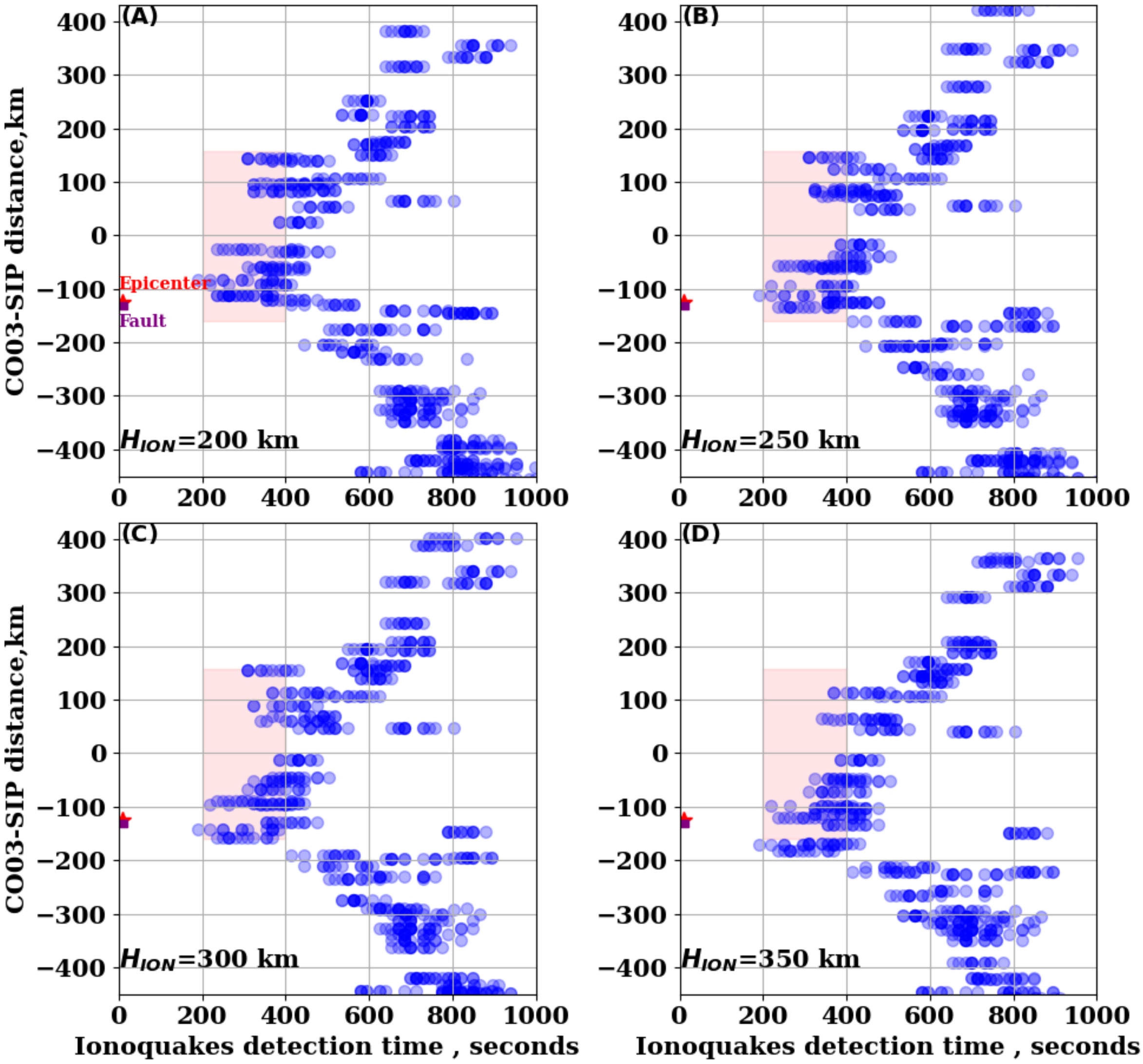


Ionoquake detection time - distance diagram for numerous SIPs for a frequency range of 3.2-10 mHz and different altitudes of detection.

SOURCE: Sanchez et al. (2023).

### 5.3.3 Onset time of EQs vs. Peak onset time of V$_{SISM}$

In previous studies, the onset time of an EQ was used as a reference for the seismic source time (ASTAFYEVA et al., 2011; ASTAFYEVA et al., 2013; ASTAFYEVA, 2019b; THOMAS et al., 2018). However, strictly speaking, the EQ onset time does not represent the source time. The theory considers the co-seismic crustal uplift to be the source of CID. Consequently, it is the time of the co-seismic uplift that should be taken as the source time. However, seismic ruptures take time to propagate and cause crustal uplifts. For large EQs that are characterized by large-dimension faults, the delay between the EQ onset and the maximum uplift can reach up to 3 minutes. For smaller events, the delay of 10 to 20 seconds is usually observed. While this time is the most correct to use, it cannot be calculated rapidly and without numerical modeling of seismic faults. Besides, different seismological and seismo-geodetic techniques provide different solutions.

Our approach suggests using the peak onset time of $V_{SISM}$ that is calculated from seismic stations. The main advantage of our method is the independence on the seismological models, and also in the fact that it allows to calculate the CID arrivals very rapidly, i.e. potentially it can be used in near-real-time.

According to the USGS solutions, the Illapel EQ onset time is 22:54:32 UT, and the maximum uplift occurred at 22:55:22 UT on the north-east from the epicenter. The peak onset time of $V_{SISM}$ varies between 22:54 and 23:03 UT (Figure 5.3(A1, B1)), i.e., it is delayed between 32 seconds and 9 minutes from the USGS onset time, and 87 seconds to nearly 10 min from the seismic uplift time.

To examine the effects of the delay and other subjectivities arising from the usage of the seismic peak onset time rather than the EQ onset time and the uplift time, we carry out the ionoquake detection time estimation with the following conventional definitions:

$$t1_{detection} = t_{TEC} - 22:54:32, \quad t2_{detection} = t_{TEC} - 22:55:25 \tag{5.2}$$

Here, $t_{TEC}$ is the peak onset time of ionoquake is the same as defined for TEST-1 in Equation (5.1). The $t2_{detection}$ in Equation (5.2) the maximum uplift time. Figure 5.4(C, D) shows the results for the $t1_{detection}$ and $t2_{detection}$. One can see that within 50 to 200 km epicentral distance, both the $t1_{detection}$ and $t2_{detection}$ are less than 400 seconds.

Moreover, we note that in Equation (5.2), the $t_{TEC}$ corresponds to the first peak of ionoquake, and it is subtracted from the EQ onset time of 22:54:32. However, in this scenario, the onset time of an ionoquake is more correct than the time of the first peak of ionoquake. This will however decrease the $t1_{detection}$. For instance, at a frequency of 4.3 mHz, the onset time of the ionoquake will occur about 116 seconds earlier than the time of the peak of the ionoquake. Therefore, in Figure 5.4(C, D), the appropriate ionoquake detection time will shift by -116 seconds at the frequency of 4.3 mHz. Consequently, in the vicinity of the epicenter the ionoquake detection time can be around 300 seconds, which might seem too short knowing that the "nominal" propagation of CID is about 7-10 minutes. Such a short timing could be related to low elevation angles during the detection of ionoquakes, that will lead to lower and much lower altitudes of detection, or higher vertical and horizontal propagation speeds because of transformation of acoustic waves into shock-acoustic waves due to non-linear effects. Below we discuss all these possible explanations.

### 5.3.4 Propagation speed and acoustic wave energetics

Relative to the location of the minimum detection time, the averaged propagation speed of the ionoquakes can be estimated as follows:

$$v = \frac{d - d_{\text{generation}}}{t - t_{\text{generation}}} \quad \Longrightarrow v1 = \frac{d - d_0}{t - t_0} \quad or \quad v2 = \frac{d - d_{eq}}{t - t_{eq}} \tag{5.3}$$

where $(d, t)$ are the coordinates of the ionoquake in Figure 5.4(A), $(\mathrm{d}_{\text{generation}}, \mathrm{t}_{\text{generation}})$ are the coordinates of the ionoquake at the time of generation, $(d_0, t_0)$ are the coordinates of the ionoquake corresponding to the minimum detection time in Figure 5.4(B), and $(d_{eq}, t_{eq})$ are the location of the epicenter and the onset time of the EQ. The speed $v1$ sets the upper limit for the actual speed since the ionoquakes are possibly generated either at the minimum detection time or slightly earlier. The speed $v2$ sets the lower limit for the actual speed since ionoquakes are certainly generated after the onset time of EQ $t_{eq}$. Therefore, the actual speed resides in between the lower $v2$ and upper $v1$ limits. Figure A.10 shows the distribution of $v1$ and $v2$ as a function of ionoquake detection time and CO03-SIP distance. We note that they are in the range of 0.25-1.5 km/s such that the early detected ionoquakes have predominantly large speeds. For instance, rapid ionoquakes with a detection time of 250-400 seconds predominantly propagate faster than 0.75 km/s which is the acoustic speed range in the upper atmosphere. Previous studies have found that acoustic-gravity waves resulting from ground vibration can efficiently couple with the ionosphere and give rise to the ionoquakes (ROLLAND et al., 2013; SANCHEZ et al., 2022). If a wave responsible for coupling propagates faster than 0.75 km/s, it arrives at 180 km or higher altitude in 250-400 seconds. Therefore, the detection time and propagation speed of rapid ionoquakes suggest the altitude of detection of rapid ionoquakes to be above 180 km altitude, i.e., in the upper atmosphere where acoustic speed is faster than 0.75 km/s. Therefore, the methodology of ionoquake detection time estimation and their propagation speed estimation validate each other. Moreover, it is correct to say that the majority of rapid ionoquakes originate in the altitude range between 180 km and $H_{\text{ION}}$=300 km. Interestingly, simulation study by Chum et al. (2016) for the Illapel EQ finds significant air particle disturbance in the altitude range of 170-250 km, raising the possibility of the majority of ionoquakes to be in this altitude range, as found in the present study. Also, the simulation study by Kherani et al. (2012) demonstrated the acoustic-gravity wave with a vertical phase speed of more than 600 m/s to give rise to the coseismic TEC disturbances within (300) 360 seconds at the height of 180 (250) km.

The lower limit $v2$ distribution in Figure A.10 also attains the lowest of about 0.25 km/s for the early detected ionoquakes in the vicinity of the epicenter. This is due to the instantaneous generation ($\mathrm{t_{generation}} = \mathrm{t_{eq}}$) assumption in (5.3) which is not quite realistic. For the large EQ of the 2011 Japan tsunami, the simulation of the SAI coupling revealed that the ionoquake can be developed within 360 seconds from the EQ onset due to the fast-propagating AGWs energetics (KHERANI et al., 2012). Therefore, the definition $v1$ in (5.3) and the corresponding distribution in Figure A.10(A) represent a realistic scenario. Moreover, in the present study, the ionoquake detection time of 250-400 seconds can be associated with the SAI coupling mechanism energized by the acoustic-gravity wave.

### 5.3.5 Ionoquake detection time during Iquique EQ of Mw8.2 on 01 April, 2014

Figures 5.6-5.7 show our results for the Iquique EQ of 01 April 2014. The temporal-spectral characteristics of $\mathrm{V_{SISM}}$ and TEC data in Figure 5.6(A1-A2) and the estimation of $\mathrm{t_{detection}}$ in Figure 5.6(A3) reveal the detection of ionoquakes starting from 430 seconds after the peak onset time of $\mathrm{V_{SISM}}$ for the frequency range of 2 mHz-10 mHz. The conventional detection time $\mathrm{t1_{detection}}$, represented by yellow circles in Figure 5.6(A3) is in between 600-700 seconds which suffers from the time shift effects, as discussed in Section 5.3.1.1 The relationship between $\mathrm{t_{detection}}$ and seismic-SIP distance in Figure 5.7 shows the two-direction propagating ionoquakes with the earliest ionoquake location near the epicenter for $H_{\text{ION}}$=200 km. We note the detection of several rapid ionoquakes in 400-430 seconds within 200 km seismic-SIP distance, i.e., within about 250 km epicentral distance. The detection of rapid ionoquakes in the case of the Iquique EQ is slightly delayed, in comparison to the much earlier detection (lower than 400 seconds) in the case of the Illapel EQ. This suggests that not all strong EQs produce rapid-ionoquakes detectable within 400 seconds from the peak onset time of the ground vibration.

Figure 5.6 - Results of TEST-1 (left) and TEST-2 (right) for the 2014 Iquique EQ.

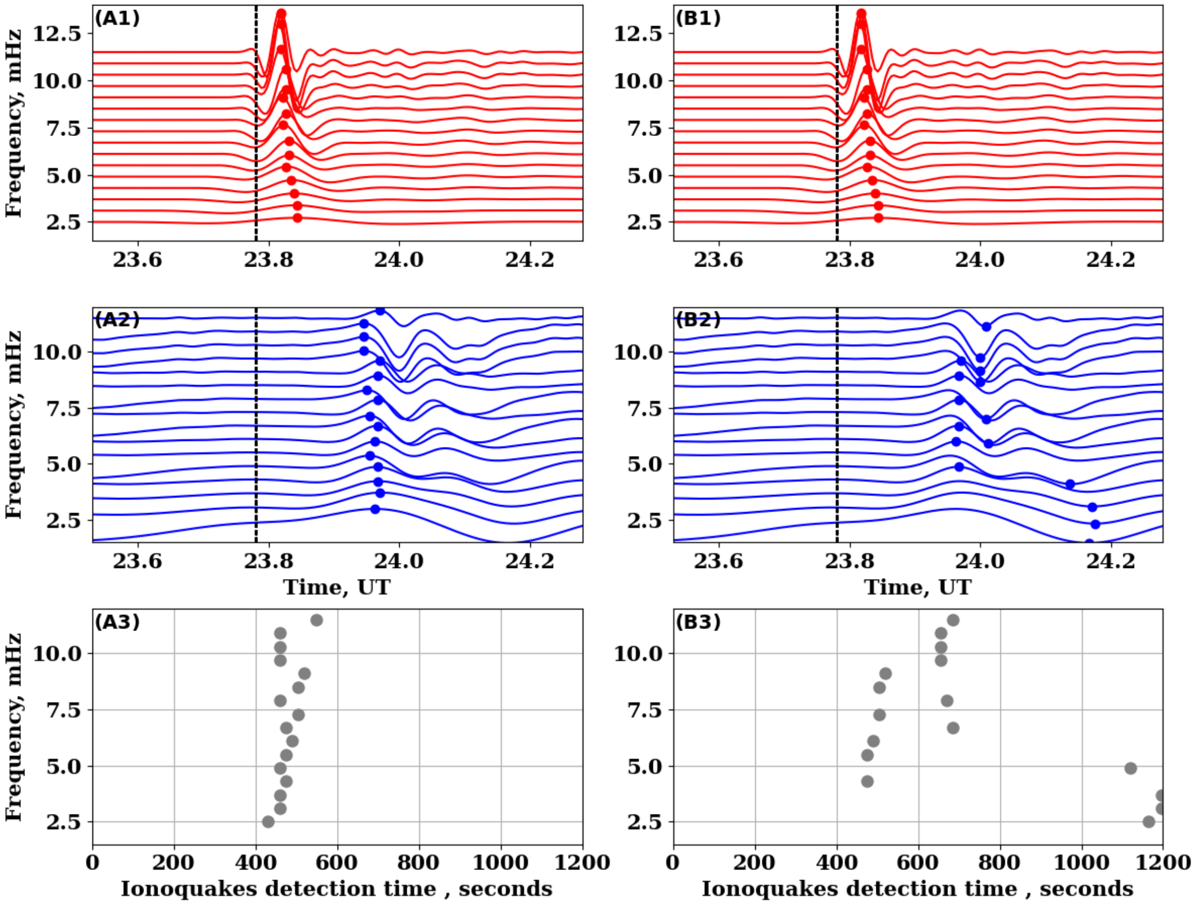


Panels A1-B1 show the $V_{SISM}$ time series recorded by the PSGCX seismic station for different frequencies. Panels A2 and B2 show the $\Delta$TEC time series obtained at different frequencies for the TRTA PRN G20 station. The red dots in (A1) and the blue dots in (A2) show the time of the peak in the first seismic oscillation and the first $\Delta$TEC oscillation. On the other hand, the red and blue points in (B1, B2) show the peak in the entire series of seismic and $\Delta$TEC oscillations, respectively. The gray points in panels (A3, B3) represent the detection time of ionoquakes.

SOURCE: Sanchez et al. (2023).

Figure 5.7 - Ionoquake detection time calculated for the Iquique EQ.

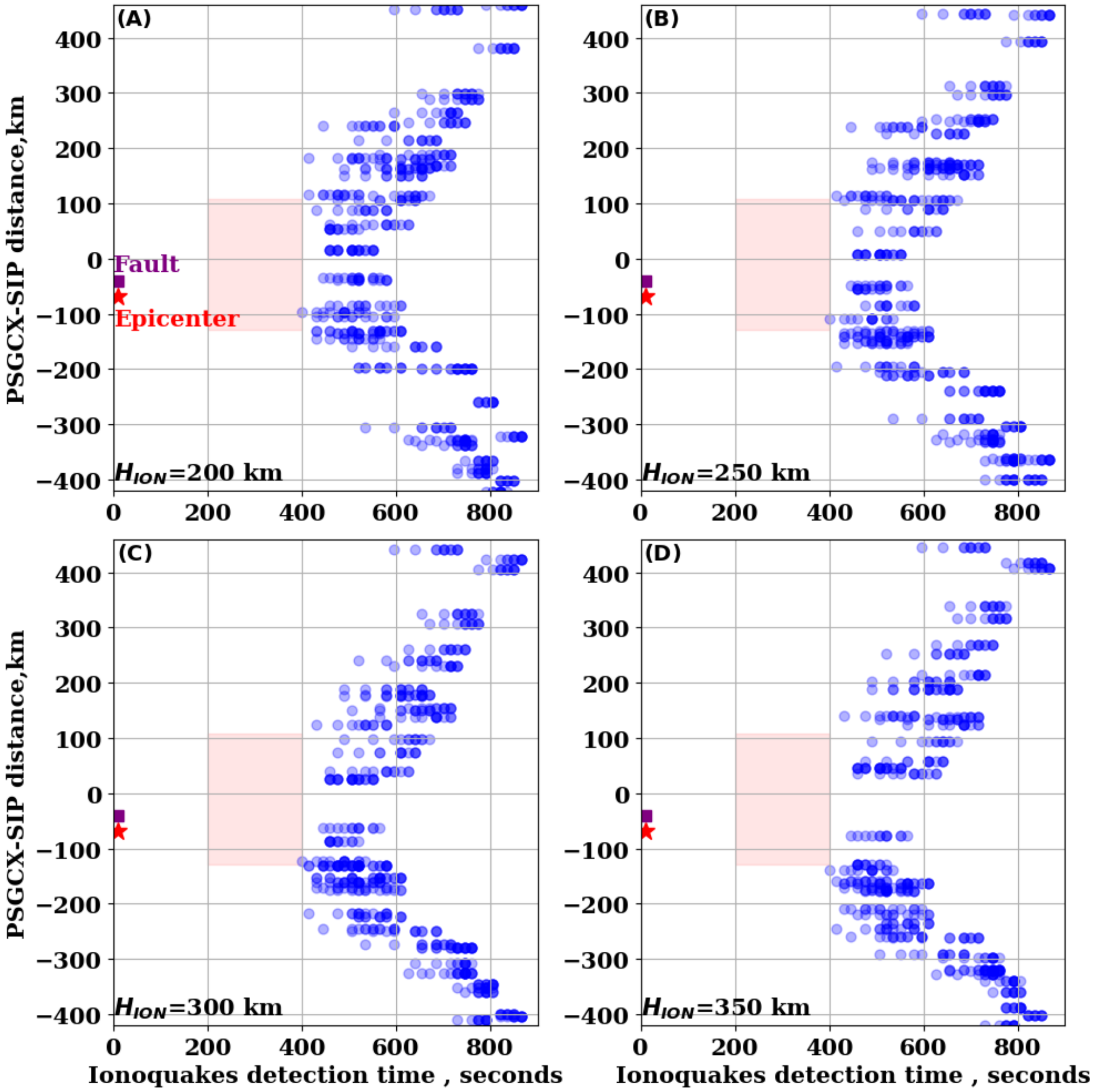


Ionoquake detection time calculated for the Iquique EQ calculated for frequencies from 3.2 to 10 mHz. The distance of 0 km indicates the location of the PSGCX seismic station.

SOURCE: Sanchez et al. (2023).

### 5.3.6 Ionoquake detection time during Sanriku-Oki EQ of Mw7.4 on March 9, 2011

We applied our newly developed method to seismic and TEC data around the epicentral area of the Sanriku-oki EQ (Figures 5.8-5.9). The temporal-spectral characteristics of $V_{SISM}$ and TEC data in Figure 5.8(A1-A2) and the estimation of

$t_{detection}$ in Figure 5.8(A3) reveal the detection of ionoquakes between 240-400 seconds for the frequency range of 2.5 mHz-10 mHz. The conventional detection time $t1_{detection} = t_{TEC} - 02:45:20$, represented by yellow circles in Figure 5.8(A3) also below 400 seconds for frequencies below 5 mHz. Figure 5.9 reveals the detection of rapid ionoquakes, as close as 100 km of the epicentral distance. The relationship between the $t_{detection}$ and the seismic-SIP distance shows two-direction propagating ionoquakes from the epicentral region for $H_{ION}$=150 km-180 km.

Figure 5.8 - Application of TEST-1 for the 9 March 2011 Sanriku-oki EQ with Mw7.3.

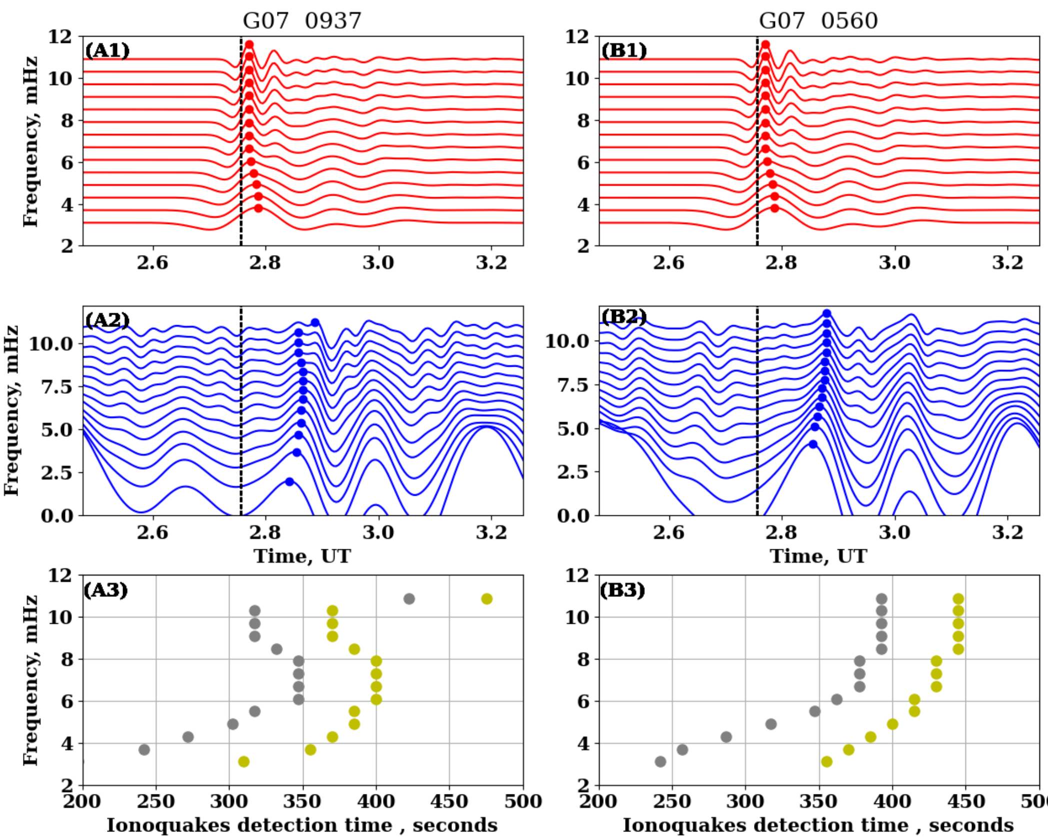


(A) is generated for the GPS station 0937 and PRN 07. (B) is generated for the GPS station 0560 and PRN 07. The seismic station is KSN. The yellow spheres in A3 and B3 indicate the points calculated with the USGS time onset.

SOURCE: Sanchez et al. (2023).

Previously, Thomas et al. (2018) and Astafyeva (2019b) reported the detection of the first ionoquakes at 430 seconds and 470-480 seconds respectively at the altitudes 150 km and 180-190 km, respectively. Our methodology applied for the same

LOS as in Thomas et al. (2018) and Astafyeva (2019b) shows quite similar results: The conventional detection time $t1_{\text{detection}}$, represented by yellow-circles in Figure A.11(A3-B3) is 430-520 seconds. However, based on the $t_{\text{detection}}$, the earliest ionoquakes are detected at about 320 to 460 seconds, as shown by the gray circles in Figure A.11(A3-B3). Moreover, $H_{\text{ION}}$=150 km-180 km of the present methodology confirms the altitude of the earliest ionoquakes reported in the previous studies of Thomas et al. (2018) and Astafyeva (2019b). Therefore, our methodology estimates the true earliest arrivals of the ionoquakes/CID, in addition to the altitude of detection.

Figure 5.9 - Ionoquakes detection time calculated for the 2011 Sanriku-oki EQ.

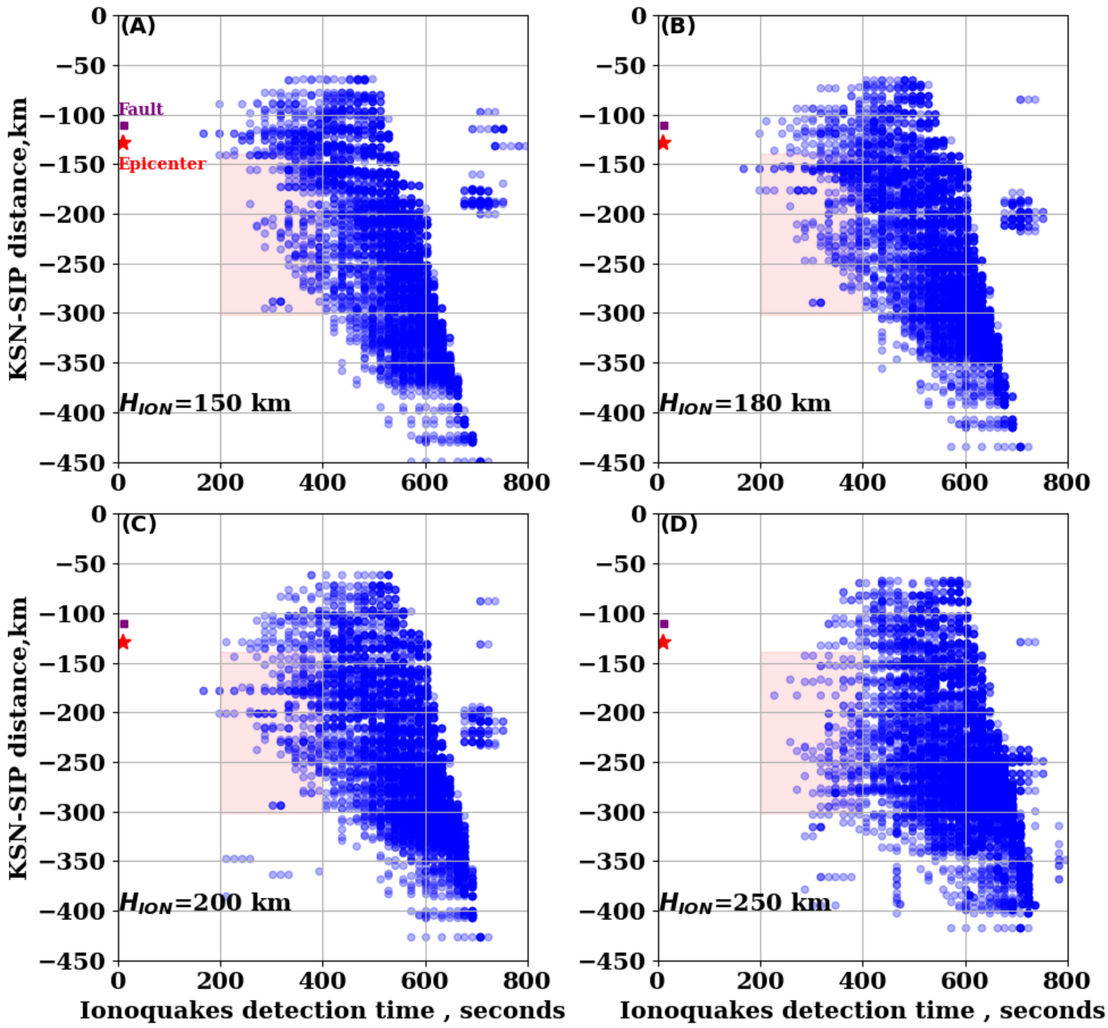


Ionoquakes detection time calculated for the 2011 Sanriku-oki EQ with frequencies from 3.2 to 10 mHz. The distance of 0 km indicates the location of the KSN seismic station.

SOURCE: Sanchez et al. (2023).

Supplementary Figure A.12(A) shows the results for conventional detection time $t1_{detection}$ in the same format as Figure 5.9(B). For comparison, Figure 5.9(B) is re-drawn as Figure A.12(B). The conventional method detects the earliest ionoquakes 350-400 seconds after the EQ onset time though they are few compared to the number of earliest ionoquakes detected from the newly developed method in Figure A.12(B). Therefore, both conventional and the newly developed methods detect the earliest ionoquakes in less than 400 seconds from the EQ onset time and from the time of the peak seismic uplift.

### 5.3.7 Rapid ionoquakes from Seismo-Atmosphere-Ionosphere coupling

Past simulation studies (e.g.,Kherani et al. (2012), Kherani et al. (2016)) have found that the SAI coupling energized by the AGWs generates rapid ionoquakes. The coupling mechanism initially excites long-wavelength AGWs from the sudden seismic impulse associated with the main shock, followed by the excitation of the short-wavelength AGWs (KHERANI et al., 2012). For the Tohoku-Oki tsunami, the simulation study had shown that the long wavelength AGWs arrive at the ionospheric heights within 360-420 seconds from the mainshock onset and generate ionoquakes in the 150-350 km altitude range and in the vicinity of the epicenter. The rapid ionoquakes of the present study are likely to be associated with this coupling mechanism. It is possible that depending on the seismic, atmospheric, and ionospheric conditions, the altitude of rapid ionoquakes varies between 150-350 km, as found in the present study.

It is important to note that the early arrival (within 360-420 seconds) of long-wavelength AGWs in the upper thermosphere and subsequent early generation of ionoquakes from the simulation study of Kherani et al. (2016) was for the case of a tsunami. For an EQ, no simulation study is available to support the early arrival within 400 seconds from the mainshock onset of the present study. The simulation study of Chum et al. (2016) for the Illapel EQ demonstrates the onset time of air particle disturbances as early as 530 seconds at 800 km epicentral distance. It is likely that the onset time of air particle disturbances in the vicinity of the epicenter is shorter than 530 seconds. This possibility is examined in the simulation study of the SAI coupling mechanism in Chapter 6.

We note that for the Illapel EQ, the present study finds the detection altitude of ionoquakes around 250 km-300 km while the simulation study by Chum et al. (2016) for this EQ finds the maximum air particle disturbance at an altitude of 170 km. However, their study also shows the presence of significant air particle disturbances up to 250 km altitude, raising the possibility of ionoquake altitude to be higher than the altitude of the maximum air particle disturbance. In fact, the ionoquake origin altitude is determined by both the air particle disturbance and ionospheric density profile (ASTAFYEVA, 2019b) so the altitude of intense ionoquake is likely to be in between the altitude of the maximum air particle disturbance and the altitude of maximum ionospheric density. Moreover, their simulation results correspond to the epicentral distance of about 800 km while the rapid ionoquakes in the present study reside within 200 km epicentral distances. How the ionoquake altitude depends on the epicentral distance is an aspect yet to be investigated in a simulation study.

## 5.4 Summary of rapid detection of ionoquakes with GNSS-TEC data

We report early detections of ionoquakes associated with the 2015 Illapel, the 2014 Iquique, and the 2011 Sanriku-Oki EQs. Using TEC and seismic measurements, the study compares ionoquakes from our new and previous methods. The new method relies on applying the same data processing procedures to the seismic and TEC data, and on estimating the time of the peak of the seismic and TEC vibrations to obtain the ionoquake detection time. The advantage of our method is its independence from the seismological models. The method produces the expected prolongation in ionoquake detection time with increasing distance from the epicenter. Moreover, the method allows locating the earliest detected ionoquakes which turns out to be near the epicenter. The localization is more accurate for the thin ionospheric layer centered around an altitude of 300 km for the Illapel, 200 km for the Iquique, and 150-180 km altitude for the Sanriku-Oki EQs. The new method also finds spectral and propagation characteristics of the earliest ionoquakes predominantly in the acoustic range. A comparative study with the conventional ionoquake detection time method highlights a new result that the detection time of earliest ionoquakes is within 400 seconds from the EQ onset time and from the time of peak seismic uplift, for the Illapel and Sanriku-Oki EQs. For the Iquique EQ, the new method detects the ionoquakes as early as 430 seconds from the time of the peak seismic uplift.

# 6 RAPID IONOQUAKE SIMULATION WITH SAI-ANA CODE

One of the unresolved issues in ionospheric seismology is the early detection of near-field ionoquakes, in less than 8 minutes from the EQ onset. In Chapter 5 we explained with GNSS-TEC data that large EQs can generate ionoquakes detection as early as 400 seconds after EQ onset and 250-430 seconds after the seismic peak. According to Astafyeva and Shults (2019), these rapid ionoquakes are the most promising products of near-real-time ionospheric seismology. The present theoretical study simulates the rapid ionoquakes, based on SAI coupling energized by AGWs. We employ a recently developed SAI-ANA code (explained in Chapter 4) of AGWs to simulate the SAI coupling, for three large EQs with Mw>7.1. This is the first study to show the rapid arrival of AWs at ionospheric heights and the development of ionoquakes in less than 7 minutes from the EQ onset. The study is also the first one to simulate the rapid ionoquakes within a simulation time of 2-3 minutes, much faster than their development and detection.

## 6.1 Application of the SAI-ANA code to large EQs

The parameters of the three EQs, i.e., the 2015 Illapel, the 2014 Iquique and the 2011 Sanriku-oki EQs that we will analyze in this chapter were already detailed in Section 5.1. Also, the processed $V_{SISM}$ data were used as input for our analytical method code.

### 6.1.1 2015 Illapel EQ

Figure 6.1 shows the propagation of the AGWs and the associated ionospheric density perturbation over the epicenter with the new SAI-ANA code implemented in Chapter 4. The SAI-ANA code is carried out with the coupled seismic uplift+AGWs+ Ionospheric disturbances numerically. In Figure 6.1(A), we note that from the surface, numerous waves with wavefronts of different slopes, i.e., of different phase speeds are launched. This is owing to the numerous scale heights and duct sizes present in the atmosphere, that allow numerous wavelengths at a given frequency to be sustained. We note that the waves with significant amplitudes arrive at 160 km altitude within 300 seconds from the mainshock onset. These waves have wavelengths comparable to the size of the longest atmospheric duct of about 150 km and at the acoustic frequencies, they propagate with a phase speed of about 600 m/s or more. In other words, owing to their longer wavelength comparable to the size of the troposphere-thermospheric duct, these waves tend to propagate with a speed equal to the local thermospheric sound speed. On the contrary, the waves with shorter wavelengths comparable to the small sizes ducts of the lower atmosphere propagate with phase speeds equal to numerous local sound speeds of the lower atmosphere. The simulation overcomes the average sound speed limitation of ray tracing, by capturing the wavefronts that propagate with numerous sound speeds that are present in the atmosphere at different heights. We note in Figure 6.1(A) that although the phase speed is about 600 m/s or more, the amplitude of the wave, i.e., the fluid oscillation is about 50 m/s, much less than the average atmospheric sound speed. Therefore, such a fast propagating wave is not a shock acoustic wave because the wave is characterized by a phase speed lesser than the average atmospheric sound speed and an amplitude comparable to the thermospheric sound speed. Figure 6.1(B) shows the result of the ionospheric density disturbances excited by the energy of AGWs. We observe that the ionospheric density disturbance reaches the magnitude of approximately 5% of the ambient ionospheric density.

Figure 6.1 - Acoustic-gravity wave amplitude and ionospheric density disturbance, during the Mw8.1 Illapel EQ of 16 September 2015.

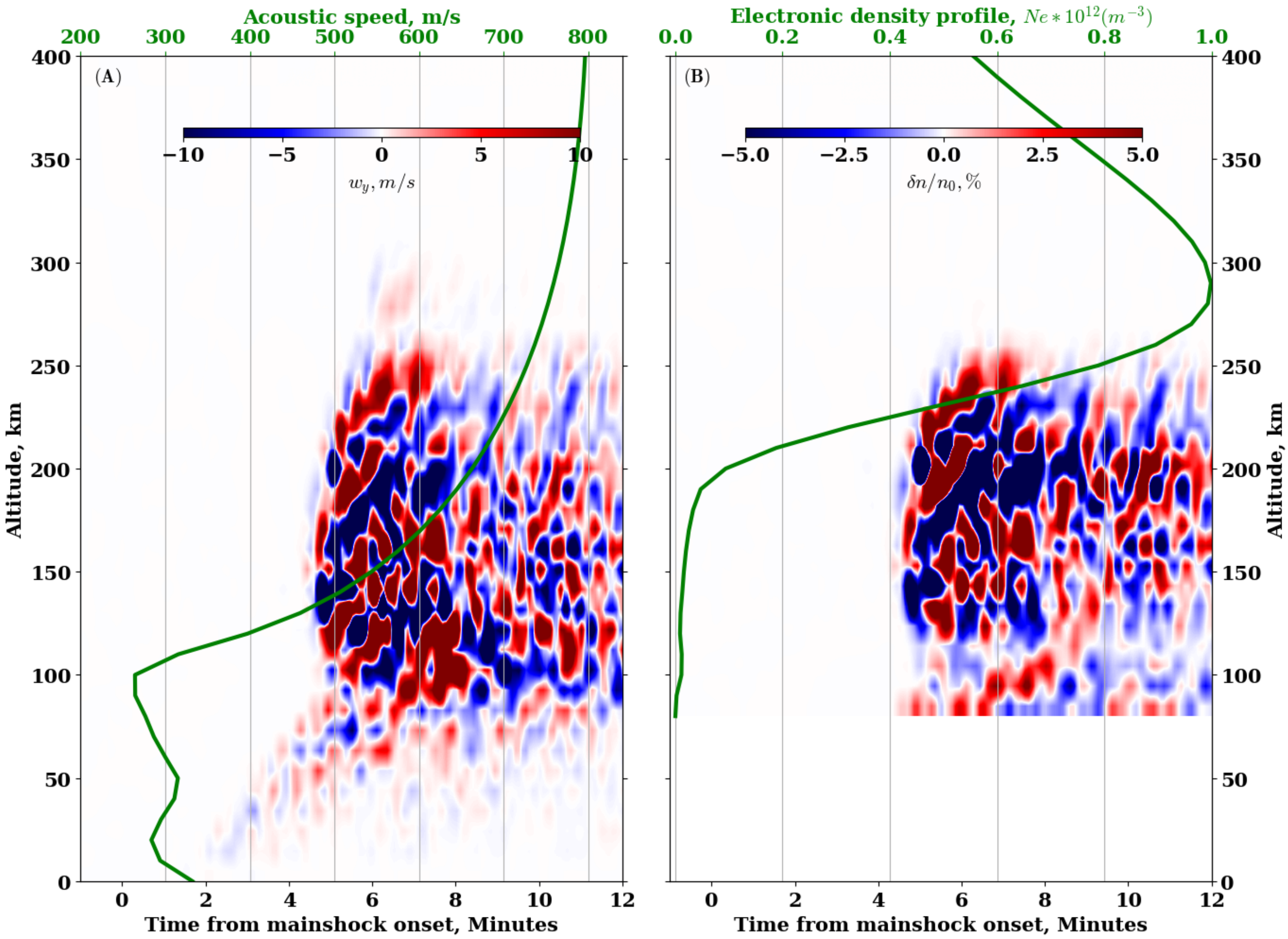


(A) Vertical propagation of AGWs and sound speed profile calculated using the atmospheric empirical model MSISE (B) Ionospheric density disturbance above the epicenter and ionospheric electron density profile as deduced from the online IRI-2016 model.

SOURCE: Author's production.

Figure 6.2(A1) reveals that the peak time of uplift depends on the frequency. Figure 6.2(A2) also reveals that the peak time of ionoquakes also depends on the frequency. Figure 6.2(A3) reveals that the ionoquake detection time ranges between 250-300 seconds from the peak time of uplift, depending on the frequency, those values are consistent with the observational data in Figure 5.3.

Figure 6.2 - Spectrogram and detection time of ionoquakes with the SAI-ANA code, for the 2015 Illapel EQ.

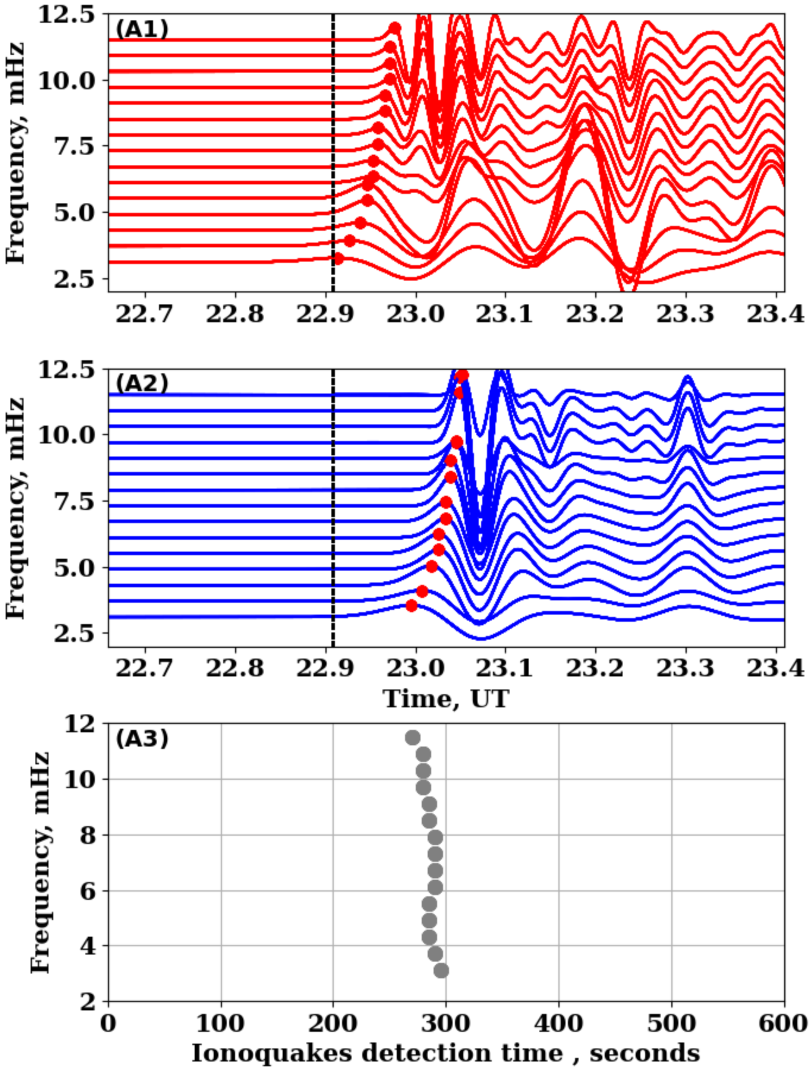


(A1) The results show the uplift time series for different frequencies. Panel A2 shows the time series of ΔTEC obtained at different frequencies for a PRN above the epicenter. The filled circles in (A1, A2) represent the time of the peak in the first seismic oscillation and the first ΔTEC oscillation, respectively. The filled circles in panel A3 represent the detection time of ionoquakes, $t_{detection}$, derived from Equation 5.1.

SOURCE: Author's production.

Using the methodology explained in Chapter 5, we estimate the detection time, for several simulated SIPs within a distance of ± 200 km from the epicenter. Figure 6.3 demonstrates that for a frequency range of 3.2-12 mHz, the detection time spreads symmetrically along the minimum location of the ionoquake detection time, in addition, the minimum time detection time is about 250 seconds. These findings, therefore, validate our ionoquake detection time results presented with observational data in Figure 5.4(B).

Figure 6.3 - Application of SAI-ANA code showing ionoquake detection time versus epicentral distance for the 2015 Illapel EQ.

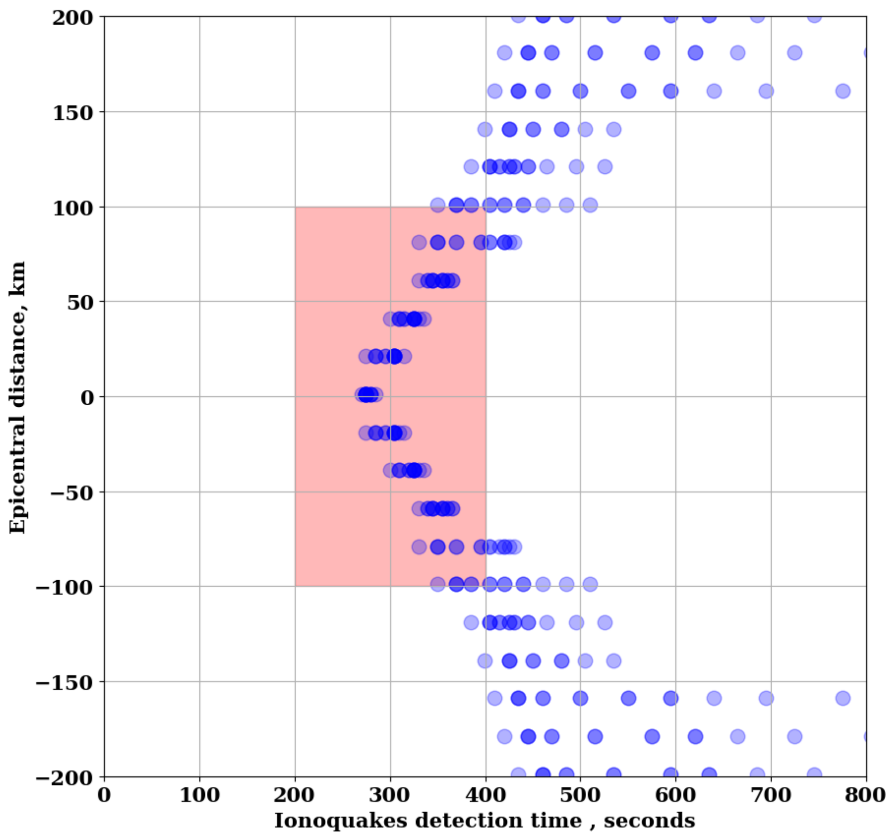


Diagram of ionoquake detection time versus epicentral distance to Sub-Ionospheric-Point (SIP) of Line-of-sight (LOS), for a frequency range 3.2-10 mHz. The distance of 0 km indicates the location of the epicenter.

SOURCE: Author's production.

In Figure 6.4, we note that the observed and SAI-ANA code waveforms of ionoquakes are fairly good in agreement. Moreover, observed and SAI-ANA code ionoquake detection times are in the same time range of 260-400 seconds, according to Figures

5.3 and 6.2. Therefore, the physical mechanism is Seismo-Atmosphere-Ionosphere coupling dynamics energized by the AGWs.

Figure 6.4 - Spectral ΔTEC comparison between observation (blue) and simulation (yellow), for the Illapel EQ.

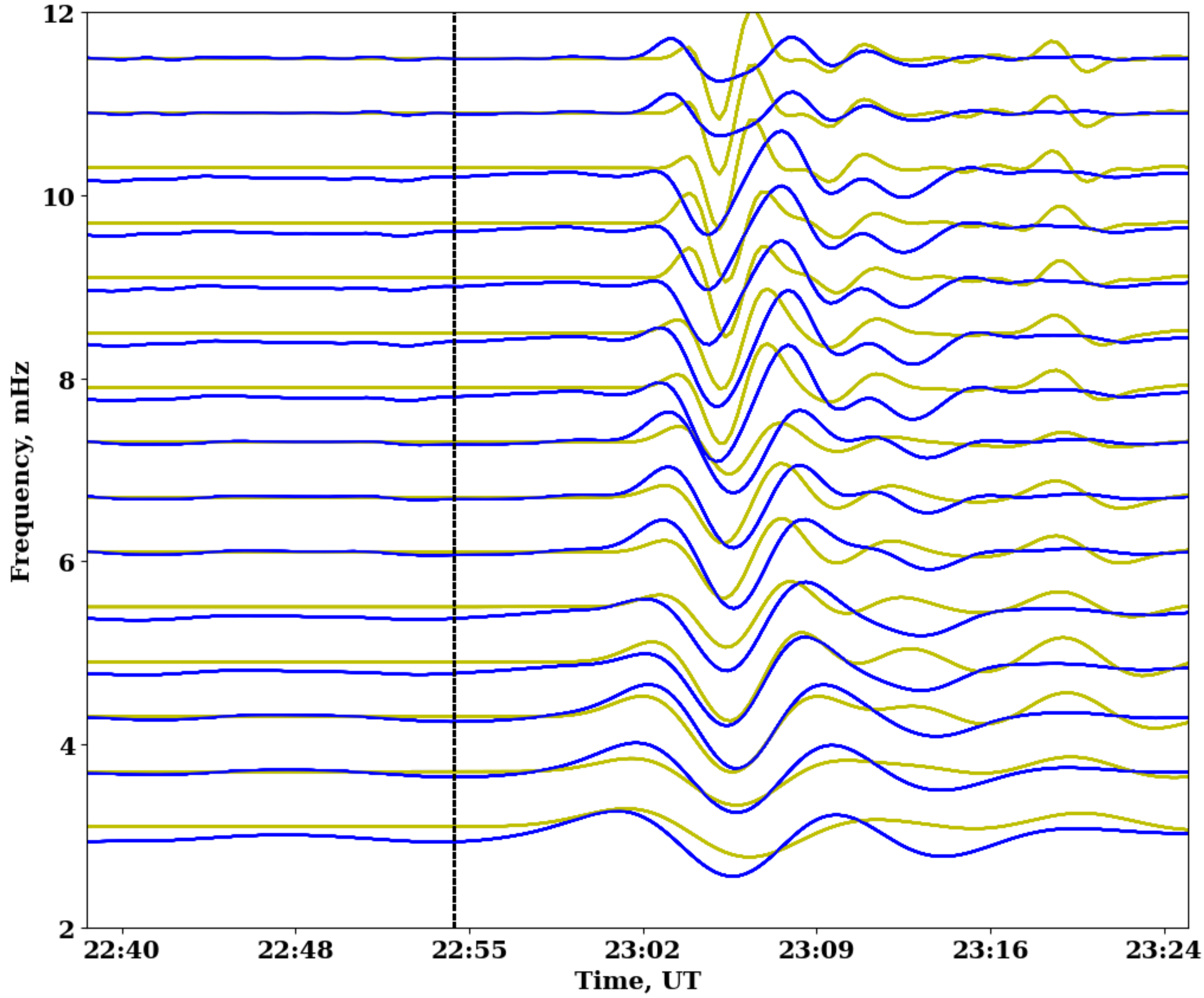


SOURCE: Author's production.

### 6.1.2 2014 Iquique EQ

In Figures 6.5-6.7, the results from the SAI-ANA code are shown for the Iquique EQ of 01 April 2014. Figure 6.5 displays results from the vertical propagation of AGWs and Ionospheric density disturbance above the epicenter. As observed for the Illapel EQ from the surface, numerous waves with wavefronts of different slopes are launched by the simulated forcings. It can be seen in Figure 6.5(B) that these wavefronts generate maximum disturbances around 200 km.

Figure 6.5 - Acoustic-gravity wave amplitude and ionospheric density disturbance, during the Mw8.3 Iquique EQ, 2014.

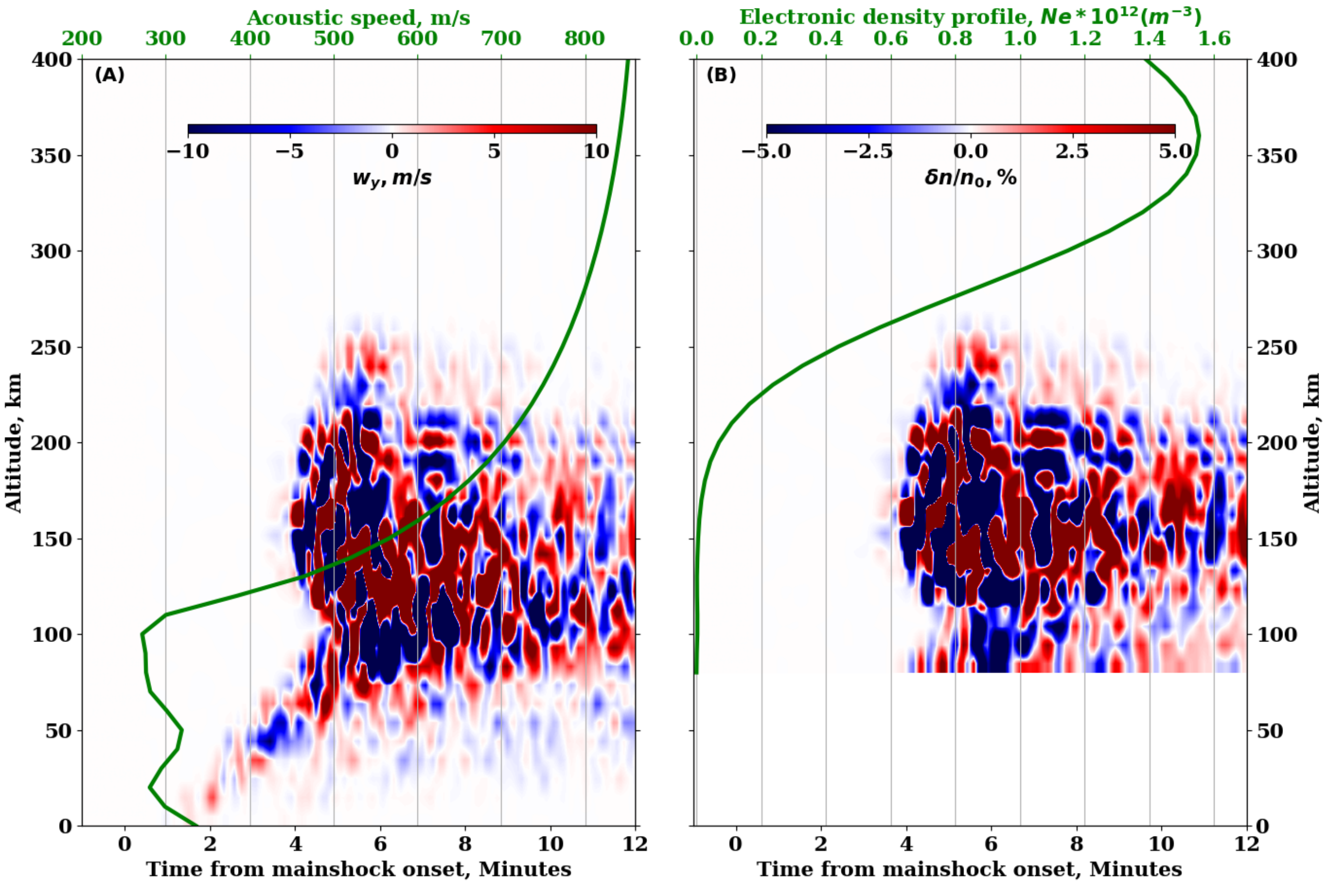


The same as in Figure 6.1.

SOURCE: Author's production.

Figure 6.6 reveals the temporal-spectral characteristics of uplift and TEC data generated with the SAI-ANA code. We obtain the detection of ionoquakes in the range of 380-600 seconds from the EQ onset for the acoustic frequency range of 3.2-12 mHz. Figure 6.7 reveals that observed and with SAI-ANA code waveforms of ionoquakes are fairly good in agreement.

Figure 6.6 - Spectrogram and detection time of ionoquakes with the SAI-ANA code, for the 2014 Iquique EQ.

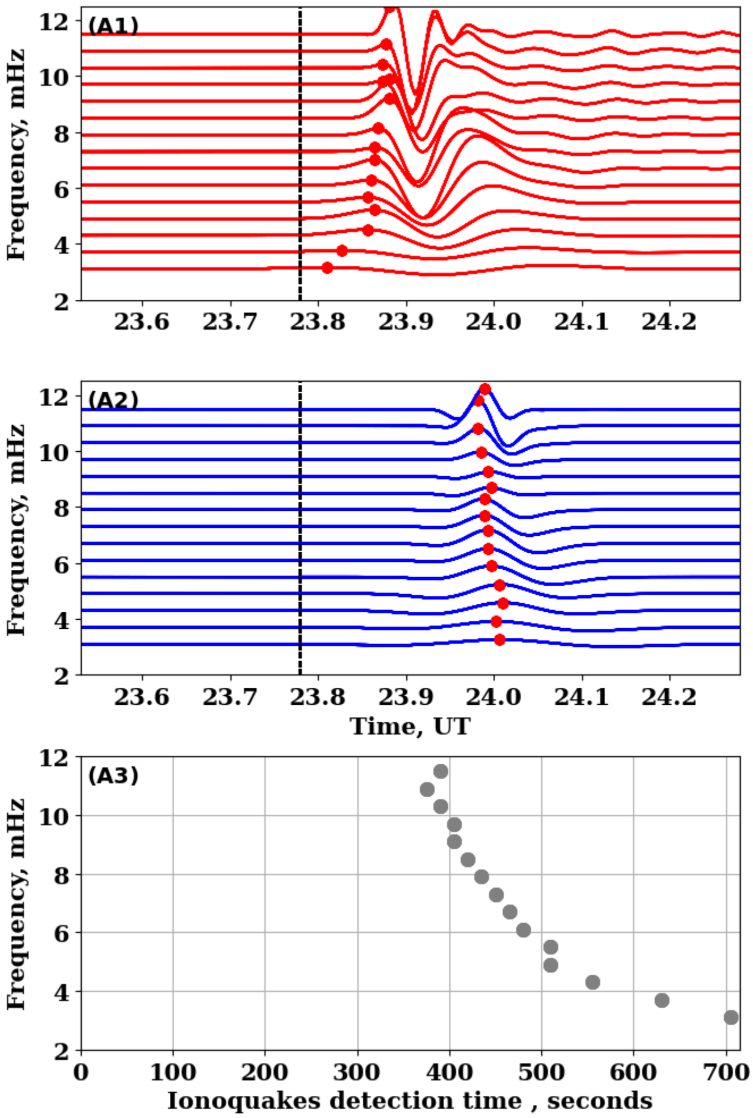


The same as in Figure 6.2

SOURCE: Author’s production.

Figure 6.7 - ΔTEC comparison between observation (blue) and simulation (yellow), for the Iquique EQ.

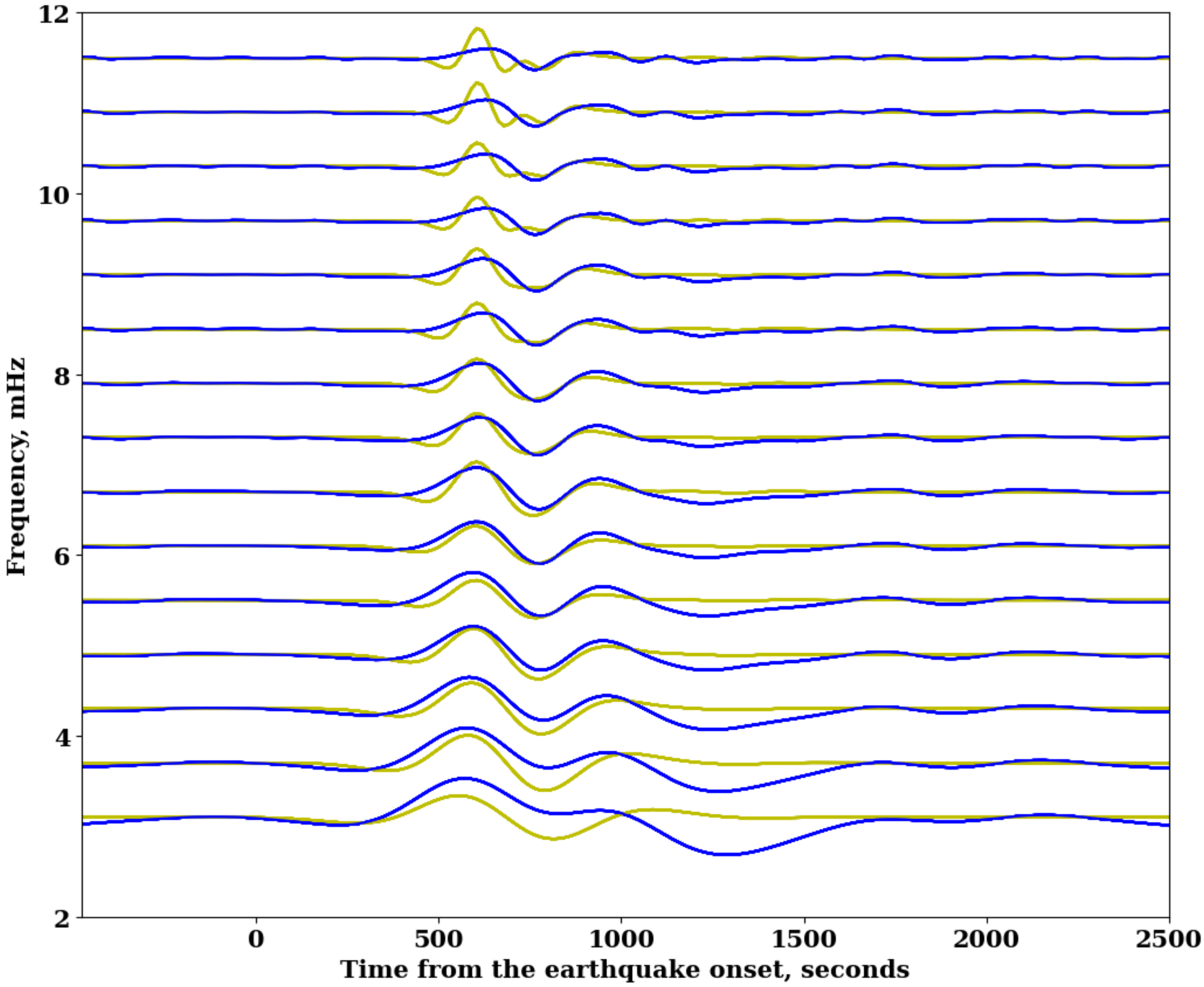


SOURCE: Author's production.

### 6.1.3 2011 Sanriku-Oki EQ

Figures 6.8-6.9 demonstrate the results from the SAI-ANA code for the 2011 Sanriku-Oki EQ. Figure 6.8 shows the vertical propagation of the AGWs. Unlike the two previous EQs, whose maximum amplitude of the velocity is concentrated around 300 seconds, then it dissipates quickly. The disturbance of the maximum ionospheric density is concentrated in approximately 320 seconds at an altitude of 180 km, so these values are consistent with the observational results of Chapter 5.

Figure 6.8 - Acoustic-gravity wave amplitude and ionospheric density disturbance, during the Mw7.3 Sanriku-Oki EQ, 2011.

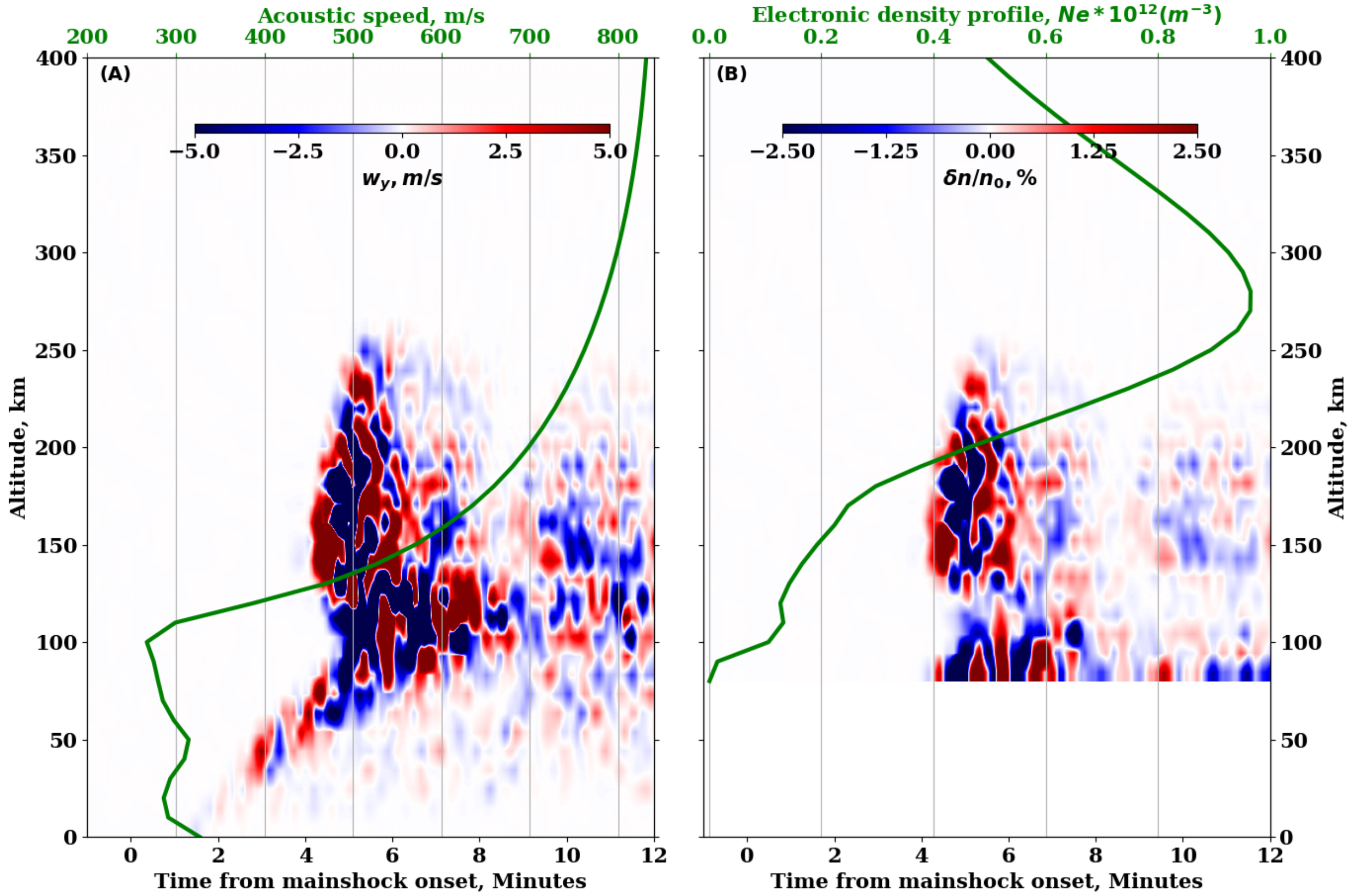


The same as in Figure 6.1

SOURCE: Author’s production.

Figure 6.9 shows temporal-spectral characteristics of uplift and TEC disturbances revealing the detection of ionoquakes in 280-320 seconds for the acoustic frequency range of 2.5 -12 mHz. Figure 6.10, as for the two EQs analyzed, shows a good correlation between the observational and simulated data.

Figure 6.9 - Spectrogram and detection time of ionoquakes with the SAI-ANA code, for the 2011 Sanriku-Oki EQ.

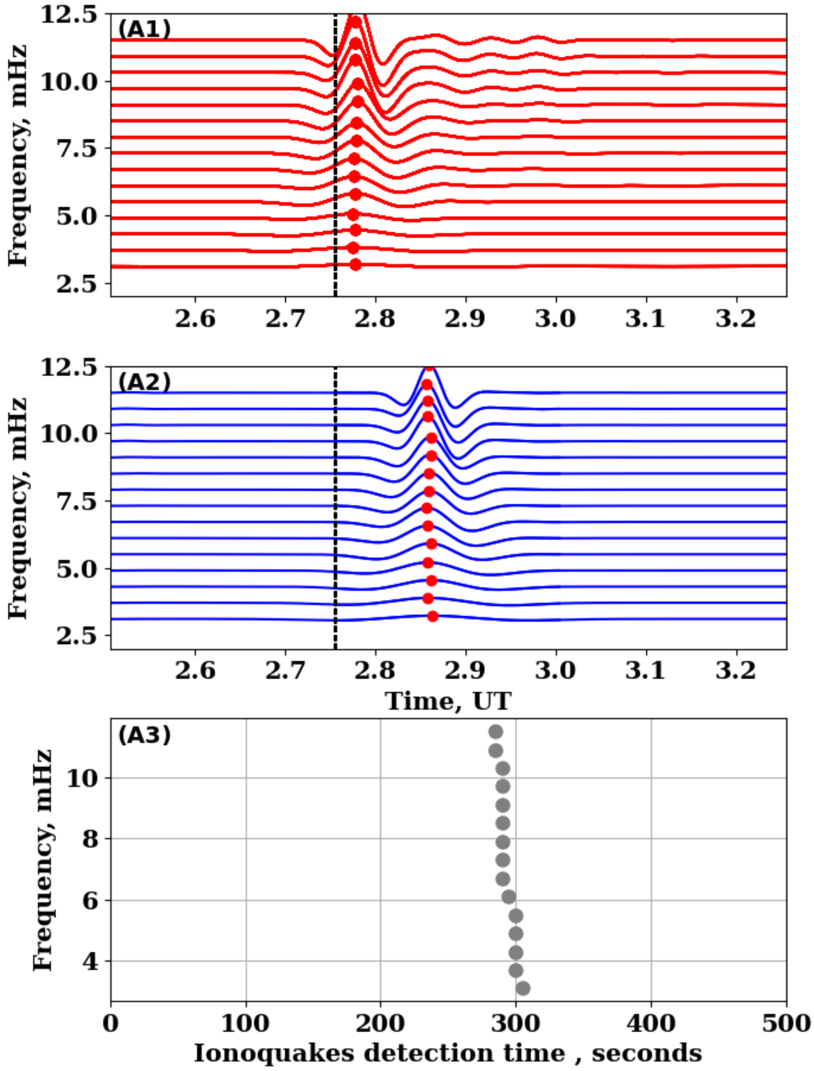


The same as in Figure 6.2

SOURCE: Author's production.

## 6.2 Discussion

Past simulation studies (e.g., Kherani et al. (2012), Kherani et al. (2016)) have found that the SAI coupling energized by the AGWs generates rapid ionoquakes in the upper thermosphere within 360 seconds from the EQ onset. The rapid ionoquakes of the present study are likely to be associated with this coupling mechanism. However, the simulation study of Kherani et al. (2016) was for the case of a tsunami. For an EQ, no simulation study is available to support the early arrival within 360 seconds from the mainshock onset of the present study. The simulation study of

Figure 6.10 - Spectral ΔTEC comparison between observation (blue) and simulation (yellow), for 2011 Sanriku-Oki EQ.

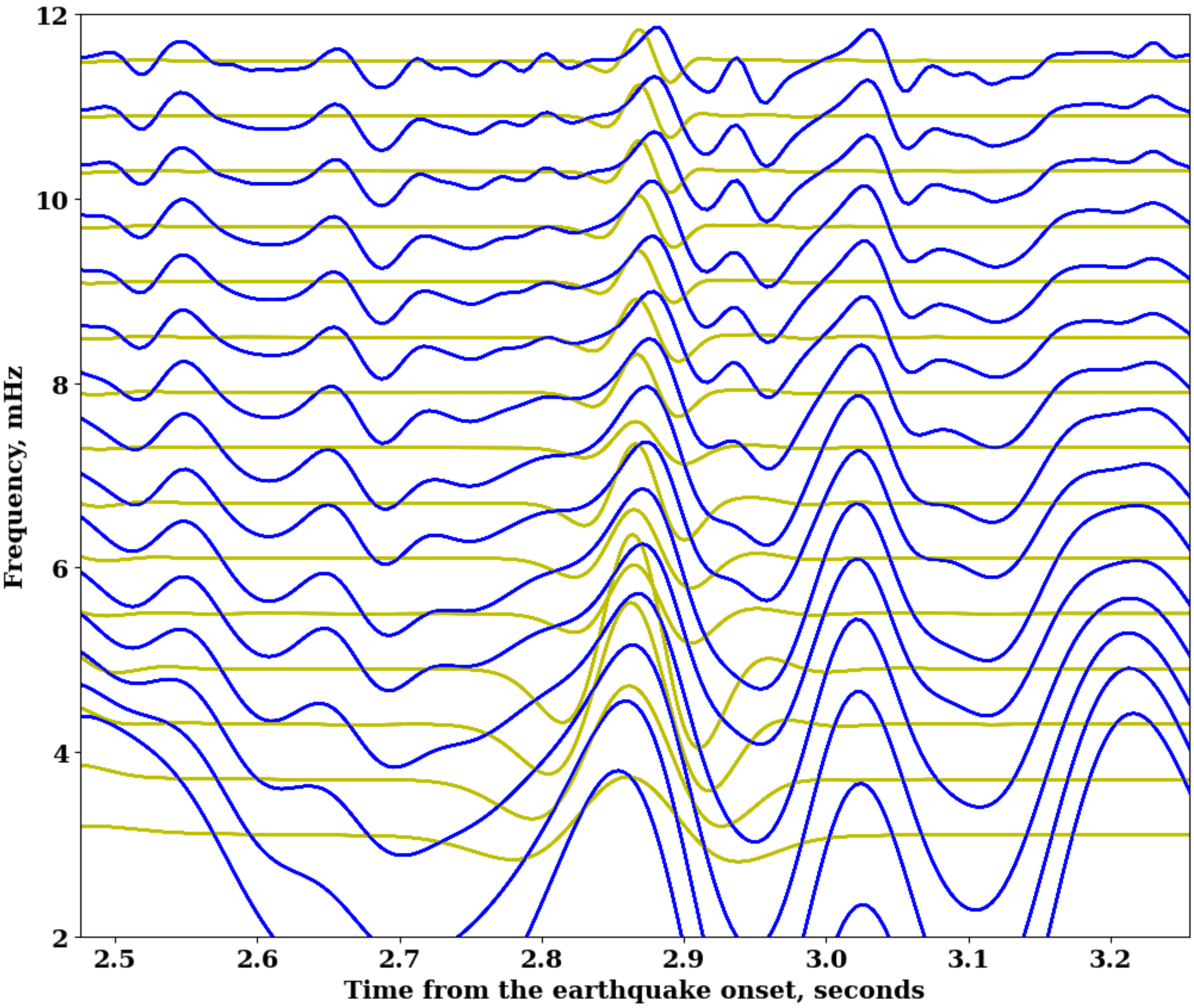


SOURCE: Author's production.

Chum et al. (2016) for the Illapel EQ demonstrates the onset time of air particle disturbances only 530 seconds after the EQ at 800 km epicentral distance. Consequently, in the vicinity of the epicenter the disturbance should be detected several hundred of seconds earlier.

We examine this possibility by using our new SAI-ANA code the coupled seismic uplift AGWs-Ionospheric disturbances numerical code of SAI coupling mechanism.

In the Figures of this chapter, we demonstrate the results of our SAI-ANA code, associated with the 2015 Illapel, the 2014 Iquique, and the 2011 Sanriku-oki EQs. We note in Figures 6.4, 6.7, and 6.10 that the observed and simulated waveforms of ionoquakes are fairly good in agreement.

Moreover, in Figures 5.3(A3), 5.6(A3) and 5.6(A3) observed and Figures 6.2(A3), 6.6(A3) and 6.9(A3) simulated ionoquake detection times are in the same time range of 240-700 seconds. Therefore, the physical mechanism responsible for the rapid ionoquakes is the Seismo-Atmosphere-Ionosphere coupling dynamics energized by the AGWs.

Figures 6.1(A), 6.5(A) and 6.8(A) demonstrates the vertical propagation of simulated acoustic-gravity waves above the epicenter. We note that from the surface, numerous waves with wavefronts of different phase speeds are launched. We remind that this is owing to the numerous scale heights and duct sizes present in the atmosphere, that allow numerous wavelengths at a given frequency to be sustained. We note that the waves with significant amplitudes of about 50 m/s arrive at 160 km altitude within 300 seconds from the mainshock onset.

These waves have wavelengths comparable to the size of the longest atmospheric duct of about 150 km and at the acoustic frequencies, they propagate with a phase speed of about 600 m/s or more. Therefore, in the rapid development of ionoquakes, the long wavelength AGWs participate, as also found by Kherani et al. (2012).

We note in Figure A.9 of Appendix A for the EQ Ilapel that although the phase speed is about 600 m/s or more, the amplitude of the wave is about 50 m/s, and so much slower than the average atmospheric sound speed. Therefore, such a fast propagating wave is not a shock acoustic wave as aforementioned, since the wave is characterized by a phase speed slower than the average atmospheric sound speed and an amplitude comparable to the thermospheric sound speed (ZETTERGREN et al., 2017).

### 6.3 Summary of rapid detection of ionoquakes with the SAI-ANA code

Based on SAI coupling mechanism and AGWs energetics, the present analysis demonstrates the rapid arrival of AGWs at the ionospheric heights and the development of ionoquakes as early as 4 minutes from the mainshock onset. Since the atmospheric acoustic speed is not uniform, the wave speed may range between minimum to maximum values, depending on local and non-local effects. The study finds the acoustic wave with a long wavelength of about 100 km, which propagates with the thermospheric acoustic speed and is responsible for the rapid ionoquakes. As the wavelength decreases, the contribution from the local acoustic speed increases, and as a result, acoustic waves with shorter wavelengths propagate with an average acoustic speed that is much smaller than the thermospheric acoustic speed. The SAI-ANA code of rapid ionoquakes reveals characteristics similar to their observations such as their time of development during 4-8 minutes from the EQ onset, their spectral peak in the 3.2-12 mHz frequency range, and their horizontal propagation larger than the thermospheric sound speed. In addition, the SAI-ANA code reveals that the altitude $H_{ION}$ of most intense rapid ionoquakes is located where both AWs and electron density are significant and not necessarily at the altitude of peak electron density.

## 7 QUANTITATIVE RELATIONSHIP BETWEEN EARTHQUAKE AND IONOQUAKE ENERGETICS

### 7.1 Moment magnitude (Mw)/ground uplift ($V_{SISM}$) of EQ vs amplitude ($\Delta$TEC) for 50 EQ events

EQs with Mw $\geq$ 6.6 and depth < 60 km can generate co-seismic ionospheric disturbances or ionoquakes which are disturbances in the electron density and electric field of the ionosphere. The present study establishes the relationship between the Mw/ground uplift ($V_{SISM}$) derived from the seismic data and amplitude ($\Delta$TEC) of the ionoquakes derived from TEC measurements. The study is associated with the EQs that occurred worldwide from 1994 to 2021 with Mw $\geq$ 6.6 and depth < 60 km. Considering all the EQs, the correlation obtained between the Mw and amplitude of the ionoquakes is in the range of 0.8-0.91. The relation between ground uplift and ionoquake amplitude is sensitive to the normal mode frequencies and reveals positive correlation with a tendency to transition from linear to exponential relation at large values of ground uplift. This method allows us to quickly determine the EQ parameters such as Mw and ground uplift from the amplitude ionoquake deduced from TEC measurements. This method is of priority interest to the detection of submarine EQs due to its direct link with the threat of tsunamis.

Previous studies have established that the amplitude of near-field ionoquakes is strongly dependent on the magnitude of co-seismic crustal vertical displacement. Thus, a stronger EQ is likely to have a greater impact on the ionosphere (ASTAFYEVA et al., 2013; ASTAFYEVA et al., 2014; CAHYADI; HEKI, 2015; SUNIL et al., 2021; BRAVO et al., 2022), and the water volume displaced (for submarine EQs) (MANTA et al., 2020). However, the amplitude of ionoquakes does not depend only on the magnitude of the EQ, but also on the focal depth, focal mechanism, surface deformation, propagation direction of the rupture, the background TEC, the magnetic field, and the geometry of the sounding (ASTAFYEVA et al., 2009; ASTAFYEVA et al., 2014; CAHYADI; HEKI, 2015; BAGIYA et al., 2019).

Astafyeva et al. (2013) investigated 11 reverse-fault EQs to correlate EQ magnitude to ionoquakes amplitudes. Later, Cahyadi and Heki (2015) also compiled TEC data from 21 EQs, considering the three types of seismic faults: reverse, normal, and slip. Cahyadi and Heki (2015) taking the measurement of the maximum amplitude of the ionoquakes as a reference, were able to confirm the relationship of this amplitude with the magnitude of the EQs. Also note that Astafyeva et al. (2014) reported that slip fault EQs generate ionospheric disturbances of similar amplitude to normal fault events, while Cahyadi and Heki (2015) found that slip fault events generate smaller disturbances.

We note that, to date, most studies that have sought to relate EQs properties to ionoquakes properties have used band-pass filters or polynomial fits on the TEC data. In addition, as the study is done separately, some authors consider background TEC and magnetic field, and some authors do not consider it, which could generate imprecision in the results.

This chapter reports 50 EQs of Mw $\geq 6.6$ with clear generation of ionoquakes that occurred around the globe, with a focus on examining the quantitative relationship between EQ energetics and ionoquake energetics. In the analysis, ionoquake amplitudes are derived without employing any spectral analysis. The advantage of such an approach is that it raises the possibility to estimate earthquake parameters in Near Real Time from the amplitude of the ionoquakes.

## 7.2 Data analysis

In this study, we analyzed 50 EQs that generated detectable ionoquakes using measurements of TEC derived from data of ground-based GNSS receivers networks including UNAVCO <http://www.unavco.org>, Japan <ftp://terras.gsi.go.jp/>, New Zealand <https://data.geonet.org.nz/>, National Seismological Center-Chile <http://gps.csn.uchile.cl/> and Observatory of Singapore <https://www.sonel.org/>. The magnitude of these EQs vary from $6.6 \leq \text{Mw} \leq 9.1$, according to the site <(https://earthquake.usgs.gov/)>. The EQ parameters are listed in Table 7.1, in the following order: name, date, DOY, magnitude, time, latitude, longitude, depth (according to USGS), and vertical ground velocity or uplift which is estimated from seismometer data using ObspyDMT software. Figure 7.1 shows the location of the epicenter of EQs with their respective Mw represented by color bar and proportional to the size of circles.

Figure 7.1 - The global map shows epicenters of 50 EQs with 6.6 ≤ Mw ≤ 9.1.

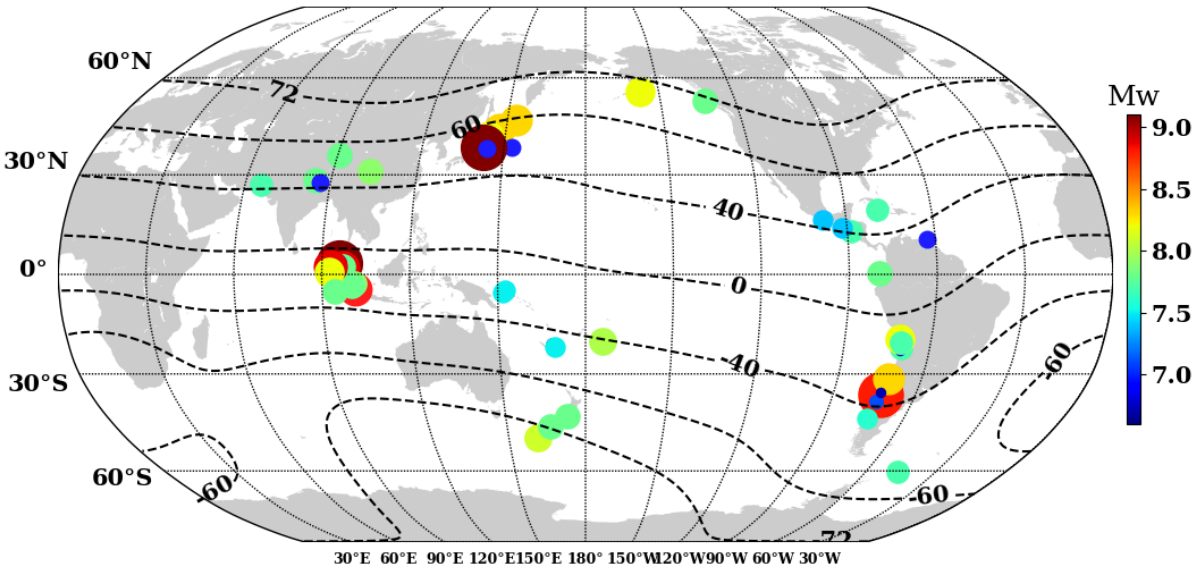


The colorbar represents the Mw of the EQs and the size of circles are proportional to the Mw. The black dotted lines represent geomagnetic inclination isolines obtained from the IGRF model for epoch 2015.

SOURCE: Author's production.

Table 7.1 - List of EQs and their epicentral and seismic parameters.

| Label | Date | Doy | Mw | UT | lat° | lon° | depth, km | $V_{SISM}$, m/s |
|---|---|---|---|---|---|---|---|---|
| Kuril | 1994-10-04 | 277 | 8.3 | 13:22:55 | 43.77 | 147.32 | 14 | 0.027 |
| ElSalvador | 2001-01-13 | 13 | 7.7 | 17:33:32 | 13.049 | -88.66 | 60 | 0.012 |
| Kunlun | 2001-11-14 | 318 | 7.8 | 09:26:10 | 35.946 | 90.541 | 10 | 0.021 |
| Tokachi | 2003-09-25 | 268 | 8.2 | 19:50:06 | 41.81 | 143.91 | 27 | 0.011 |
| Macquarie | 2004-12-23 | 358 | 8.1 | 14:59:04 | -49.31 | 161.34 | 10 | 0.0008 |
| Sumatra0 | 2004-12-26 | 361 | 9.1 | 00:58:53 | 3.32 | 95.85 | 30 | 0.011 |
| Nias | 2005-03-28 | 87 | 8.6 | 16:09:36 | 2.085 | 97.108 | 30 | 0.017 |
| Tonga | 2006-05-03 | 123 | 8 | 15:26:40 | -20.163 | -174.15 | 55 | 0.00497 |
| Kuril06 | 2006-11-15 | 319 | 8.3 | 11:14:13 | 46.592 | -153.226 | 10 | 0.0035 |
| Chuetsu | 2007-07-16 | 197 | 6.6 | 01:13:22 | 37.535 | 138.446 | 12 | 0.0066 |
| Bengkulu1 | 2007-09-12 | 255 | 8.4 | 11:10:26 | -4.438 | 101.37 | 34 | 0.018 |
| Bengkulu2 | 2007-09-12 | 255 | 7.9 | 23:49:03 | -2.625 | 100.84 | 35 | 0.013 |
| Tocopilla | 2007-11-14 | 318 | 7.7 | 15:40:50 | -22.25 | -69.89 | 40 | 0.022 |
| Antofagasta | 2007-11-15 | 319 | 6.8 | 15:05:58 | -22.925 | -70.23 | 26 | 0.018 |
| Wenchuan | 2008-05-12 | 133 | 7.9 | 06:28:01 | 31.002 | 103.232 | 19 | 0.018 |
| Iwate | 2008-06-13 | 165 | 6.9 | 23:43:45 | 39.03 | 140.88 | 7.8 | 0.0027 |
| NewZealand | 2009-07-15 | 196 | 7.8 | 09:22:29 | -45.762 | 166.562 | 12 | 0.024 |
| Maule | 2010-02-27 | 58 | 8.8 | 06:34:11 | -36.122 | -72.898 | 22.9 | 0.025 |
| Banyak | 2010-04-06 | 96 | 7.8 | 22:15:01 | 2.385 | 97.048 | 31 | 0.02 |
| Meulaboh | 2010-05-09 | 129 | 7.2 | 05:59:41 | 3.748 | 96.018 | 38 | 0.014 |
| Mentawai | 2010-10-25 | 298 | 7.8 | 14:42:22 | -3.487 | 100.082 | 20.1 | 0.0079 |
| Carahue | 2011-01-02 | 2 | 7.1 | 20:20:17 | -38.355 | -73.326 | 24 | 0.0013 |
| Sanriku-Oki | 2011-03-09 | 68 | 7.3 | 02:45:20 | 38.44 | 152.84 | 32 | 0.01 |
| Tohoku | 2011-03-11 | 70 | 9.1 | 05:46:24 | 38.297 | 142.37 | 29 | 0.016 |
| Santiago | 2012-03-20 | 80 | 7.4 | 18:02:47 | 16.493 | -98.231 | 20 | 0.011 |
| Sumatra1 | 2012-04-11 | 102 | 8.6 | 08:38:37 | 2.327 | 93.063 | 20 | 0.025 |
| Sumatra2 | 2012-04-11 | 102 | 8.2 | 10:43:09 | 0.802 | 92.462 | 25.1 | 0.019 |
| HaidaGwaii | 2012-10-28 | 302 | 7.8 | 03:04:08 | 52.788 | -132.1 | 14 | 0.02 |
| Chiapas | 2012-11-07 | 312 | 7.4 | 16:35:46 | 13.988 | -91.895 | 24 | 0.011 |
| Funato | 2012-12-07 | 342 | 7.3 | 08:18:23 | 37.89 | 143.949 | 31 | 0.0069 |
| Pakistan | 2013-09-24 | 267 | 7.7 | 11:29:47 | 26.951 | 65.501 | 15.5 | 0.0043 |
| Scotia | 2013-11-17 | 321 | 7.7 | 09:04:55 | -60.274 | -46.401 | 10 | 0.015 |
| Iquique0 | 2014-03-16 | 75 | 6.7 | 21:16:29 | -19.981 | -70.702 | 20 | 0.016 |
| Iquique1 | 2014-04-01 | 91 | 8.2 | 23:46:47 | -19.61 | -70.769 | 25 | 0.023 |
| Iquique2 | 2014-04-03 | 93 | 7.7 | 02:43:13 | -20.571 | -70.493 | 22.4 | 0.021 |
| Kokopo1 | 2015-03-29 | 88 | 7.5 | 23:48:31 | -4.729 | 152.562 | 41 | 0.024 |
| Gorkha | 2015-04-25 | 115 | 7.8 | 06:11:25 | 28.231 | 84.731 | 8.2 | 0.0055 |
| Kokopo2 | 2015-05-05 | 125 | 7.5 | 01:44:06 | -5.5462 | 151.875 | 55 | 0.031 |
| Kodari | 2015-05-12 | 132 | 7.3 | 07:05:19 | 27.809 | 86.066 | 15 | 0.034 |
| Illapel | 2015-09-16 | 259 | 8.3 | 22:54:32 | -31.573 | -71.674 | 22.4 | 0.043 |
| WestSumatra | 2016-03-02 | 62 | 7.8 | 12:49:48 | -4.952 | 94.33 | 24 | 0.0083 |
| Ecuador | 2016-04-16 | 107 | 7.8 | 23:58:36 | 0.382 | -79.922 | 20.6 | 0.0097 |
| Kaikoura | 2016-11-13 | 318 | 7.8 | 11:02:56 | -42.737 | 173.054 | 15.1 | 0.016 |
| Quellon | 2016-12-25 | 360 | 7.6 | 14:22:27 | -43.406 | -73.941 | 38 | 0.028 |
| Tadine0 | 2017-11-19 | 323 | 7 | 22:43:29 | -21.325 | 168.672 | 10 | 0.0068 |
| Carupano | 2018-08-21 | 233 | 7.3 | 21:31:47 | 10.773 | -62.902 | 146.8 | 0.026 |
| Tadine | 2018-12-05 | 339 | 7.5 | 04:18:08 | -21.95 | 169.427 | 10 | 0.029 |
| Constitucion | 2019-09-29 | 272 | 6.7 | 15:57:53 | -35.476 | -73.163 | 11 | 0.024 |
| Jamaica | 2020-01-28 | 28 | 7.7 | 19:10:24 | 19.419 | -78.756 | 14.9 | 0.01 |
| Perryville | 2021-07-29 | 210 | 8.2 | 06:15:49 | 55.364 | -157.88835 | 35 | 0.047 |

### 7.2.1 Estimation of uplift ($V_{SISM}$) from seismometer data

The obspyDMT library in Python is used to obtain the vertical ground velocity ($V_{SISM}$). This seismological data management toolbox called ObspyDMT is an open-source tool for managing seismic data sets (HOSSEINI; SIGLOCH, 2017). In ObspyDMT, the data was downloaded in the form of counts. Using a 0.02 s sampling, we downloaded the data considering the period from one hour prior to and one hour after the EQ. In the following stage of the process, obspyDMT performs corrections on the downloaded data. That includes the elimination of the frequency response of the seismometers, the effects of any amplifier, analog and digital filters, and digitalization.

## 7.3 Methodology to quantify the relationship between EQ and ionoquake energetics

### 7.3.1 Ionoquakes amplitude estimation

For each of the 50 EQ events, we selected the IPP trajectories that registered the most significant and distinguished variations in TEC after the mainshock onset. Table 7.2 describes definitions of ionoquake amplitude, based on the fundamental definition of TEC disturbance, ΔTEC1 which is described in Equations (7.1), along with another definition ΔTEC2, in Equation (7.2). Another definition ΔTEC3 is based on work by Sanchez et al. (2022) where wave decomposition spectral analysis is employed to obtain the ionoquake amplitudes at various frequencies between 1-10 mHz.

Table 7.2 - Definitions of Ionoquake amplitude.

| Name | Method |
|---|---|
| ΔsTEC1 | Astafyeva et al. (2014) |
| ΔvTEC1 | Astafyeva et al. (2014) |
| ΔsTEC2 | Cahyadi and Heki (2015) |
| ΔvTEC2 | Cahyadi and Heki (2015) |
| ΔvTEC3 | Sanchez et al. (2022) |

$$\Delta sTEC1 = sTEC_{peak} - sTEC_{min}, \quad \Delta vTEC1 = vTEC_{peak} - vTEC_{min} \tag{7.1}$$

$$\Delta\text{sTEC2} = \log10(\frac{\Delta\text{sTEC1}}{\text{TEC}_{\text{max}}} \times 100), \quad \Delta\text{vTEC2} = \log10(\frac{\Delta\text{vTEC1}}{\text{TEC}_{\text{max}}} \times 100) \quad (7.2)$$

Where $\Delta\text{sTEC}_{\text{min}}$ and $\Delta\text{vTEC}_{\text{min}}$ are the first minimum values before $\Delta\text{sTEC}_{\text{peak}}$ and $\Delta\text{vTEC}_{\text{peak}}$ respectively. Here $\text{TEC}_{\text{max}}$ is the maximum value of background TEC obtained from the IRI model for each EQ event. Since the observed TEC has biasing effects and does not represent the true background TEC, the IRI model is used to estimate the maximum.

#### 7.3.1.1 Choice of altitude ($\text{H}_{\text{ION}}$) of Sub-Ionospheric-Point (SIP)

Figure 7.2 (panels A) shows the time series associated with the Tohoku EQ of 2011-03-11, one of the biggest EQs investigated in this work. Figure 7.2 (panels B) shows the Chuetsu EQ of 6.6 on 2007-07-16, the smallest EQ to produce detectable ionoquakes without using a filter. Table 7.3 presents ionoquake amplitude ($\Delta\text{sTEC1}, \Delta\text{vTEC1}$) estimation for various $\text{H}_{\text{ION}}$ in between 160 to 360 km. It can be noted in panels A3 and B3 that the amplitude of the ionoquakes varies with $\text{H}_{\text{ION}}$ and the variation is more significant for strong EQs. For example, the $\Delta\text{vTEC1}$ variation for the Japan EQ was 0.32 vTECU, while it was 0.004 vTECU for the Chuetsu EQ in 2007. In other words, ionoquake amplitudes are sensitive to the choice of $\text{H}_{\text{ION}}$. Astafyeva et al. (2013) noted that the main contributor to TEC variations is the maximum ionization in the ionosphere. Also, higher background ionization density increases ionoquake amplitudes (BAGIYA et al., 2019). Therefore, in the estimation of ionoquake amplitude, the altitude of maximum ionospheric density is considered to be $\text{H}_{\text{ION}}$. The background density and corresponding altitude of maximum ionospheric density for each EQ are obtained from the empirical model IRI-2016, which can be downloaded at:<https://ccmc.gsfc.nasa.gov/modelweb/models/iri2016_vitmo.php>.

Figure 7.2 - Time series for the Tohoku EQ 2011/03/11 of Mw 9.1 in upper panels, and for the Chuetsu EQ 2007/07/16 Mw 6.6 in lower panels.

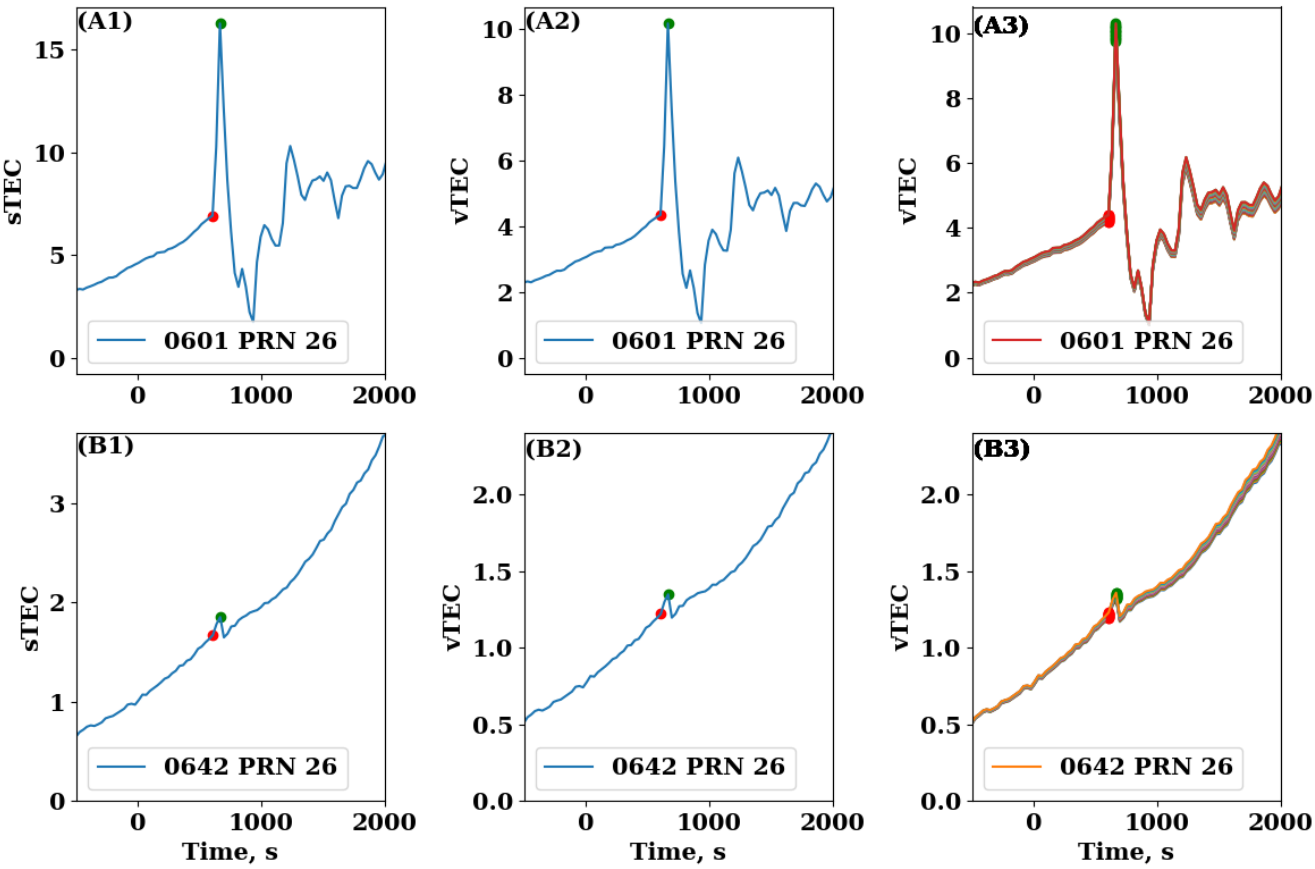


Panels (A1 and B1) represent sTEC, panels (A2, B2) represent vTEC, and panels (A3, B3) represent vTEC at different altitudes from $H_{ION} = 160$ up to 360 km. The green dot represents the maximum peak of Ionoquakes while the red dot the beginning of Ionoquakes.

SOURCE: Author's production.

### 7.3.2 Ground uplift estimation from the seismometers

We download data from seismometers located around 5 degrees from the epicenter to estimate ground uplift and corresponding maximum amplitude ($V_{SISM}$). After processing with ObspyDMT, we interpolate these data from the time series to attain an identical time resolution of 15 seconds for all EQs. As a result, all data will be in the same conditions for comparison later on. Based on these data, we calculate the maximum $V_{SISM}$ for each seismic station. Due to the fact that seismic stations are not always located near the epicenter, spatial interpolation is carried out based on

Table 7.3 - vTEC variation between 160 and 360 km in 40 km interval, for Tohoku Mw9.1 2011 and Chuetsu Mw6.6 2007 EQs.

| | | | Tohoku 2011 | | | |
|---|---|---|---|---|---|---|
| NameREC_PRN | Altitude | LON_SIP | LAT_SIP | DIS_EP_SIP | ΔsTEC1 | ΔvTEC1 |
| 0601G26 | 160 | -218.5 | 34.95 | 385.19 | 9.36 | 5.61 |
| 0601G26 | 200 | -218.06 | 35.2 | 350.36 | 9.36 | 5.67 |
| 0601G26 | 240 | -217.62 | 35.44 | 318.74 | 9.36 | 5.73 |
| 0601G26 | 280 | -217.2 | 35.67 | 290.86 | 9.36 | 5.79 |
| 0601G26 | 320 | -216.78 | 35.9 | 267.39 | 9.36 | 5.84 |
| 0601G26 | 360 | -216.37 | 36.12 | 249.05 | 9.36 | 5.9 |
| | | | Chuetsu 2007 | | | |
| NameREC_PRN | Altitude | LON_SIP | LAT_SIP | DIS_EP_SIP | ΔsTEC1 | ΔvTEC1 |
| 0642G26 | 160 | -223.33 | 36.18 | 208.54 | 0.18 | 0.125 |
| 0642G26 | 200 | -223.06 | 36.39 | 172.52 | 0.18 | 0.126 |
| 0642G26 | 240 | -222.8 | 36.6 | 137.33 | 0.18 | 0.127 |
| 0642G26 | 280 | -222.54 | 36.81 | 103.04 | 0.18 | 0.128 |
| 0642G26 | 320 | -222.28 | 37.01 | 69.86 | 0.18 | 0.128 |
| 0642G26 | 360 | -222.03 | 37.21 | 38.83 | 0.18 | 0.129 |

GNSS station 0601 and PRN 26 are used for the analysis of the Tohoku EQ, and GNSS station 0642 and PRN 26 for the analysis of the Chuetsu EQ. The table shows the following parameters: SIP Longitude = LON_SIP; SIP latitude= LAT_SIP; Distance from receiver to the epicenter = DIS_EP_REC; Distance from the epicenter to SIP = DIS_EP_SIP; sTEC1 and vTEC1.

the maximum values of $V_{\text{SISM}}$ found within a reasonable distance of the epicenter, that explanation is shown in the Figure 7.3.

Figure 7.3 - Ground uplift recorded by 100 seismometers, for the Tohoku EQ 2011/03/11 of Mw 9.1.

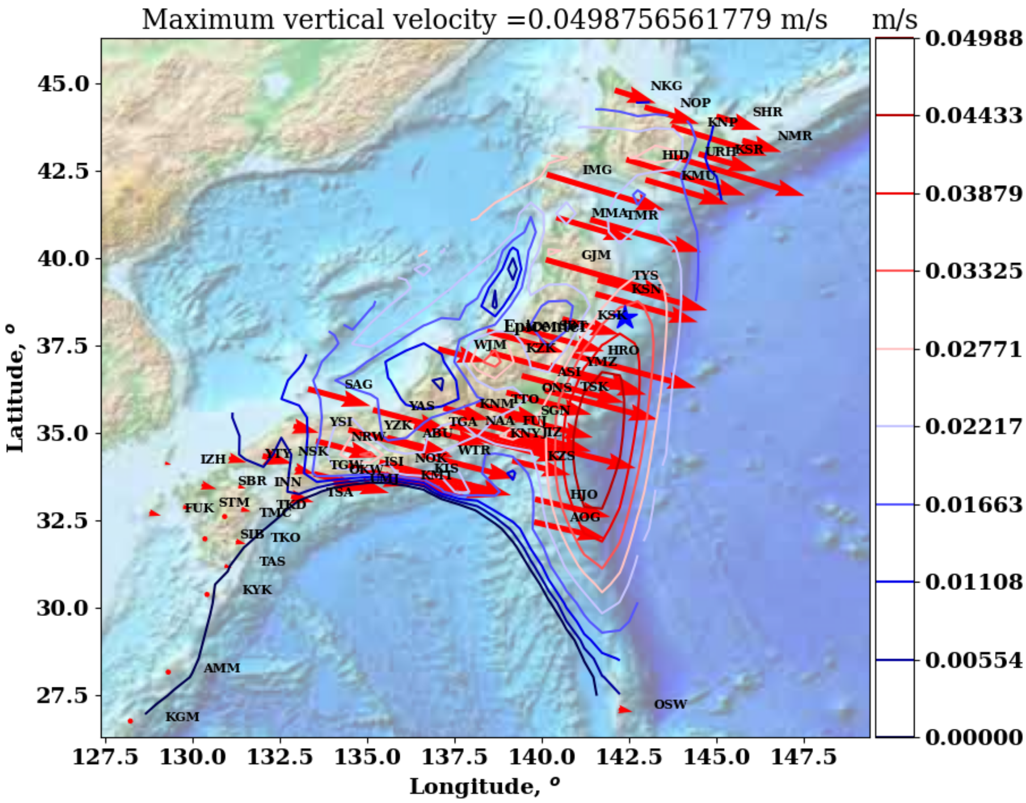


Seismic stations are located at the beginning of each arrow. The colored contours represent interpolated data from $V_{SISM}$. The blue star represents the epicenter of the EQ.

SOURCE: Author's production.

### 7.3.3 Results and discussion

The panels in Figure 7.4 show the location of the epicenter, the GNSS station, and chosen IPP trajectory that was nearest to the epicenter at mainshock onset time. These panels are arranged from smallest to greatest magnitude, i.e, from Chuetsu (smallest) to Tohoku EQs (largest). In most cases, the SIP was between the epicenter and the GNSS station. This scenario is described by Cahyadi and Heki (2015) as being the most favorable for ionoquakes to attain significant amplitude, but there are some exceptions, such as the Kokopo1 EQ and the Banyaks EQ. In contrast, Manta et al. (2020) report, for example, that the Banyaks EQ had very weak ionoquakes, despite favorable geometries.

Figure 7.4 - EQs epicenters, GNSS station coordinates, IPP trajectory, SIP, and Mw.

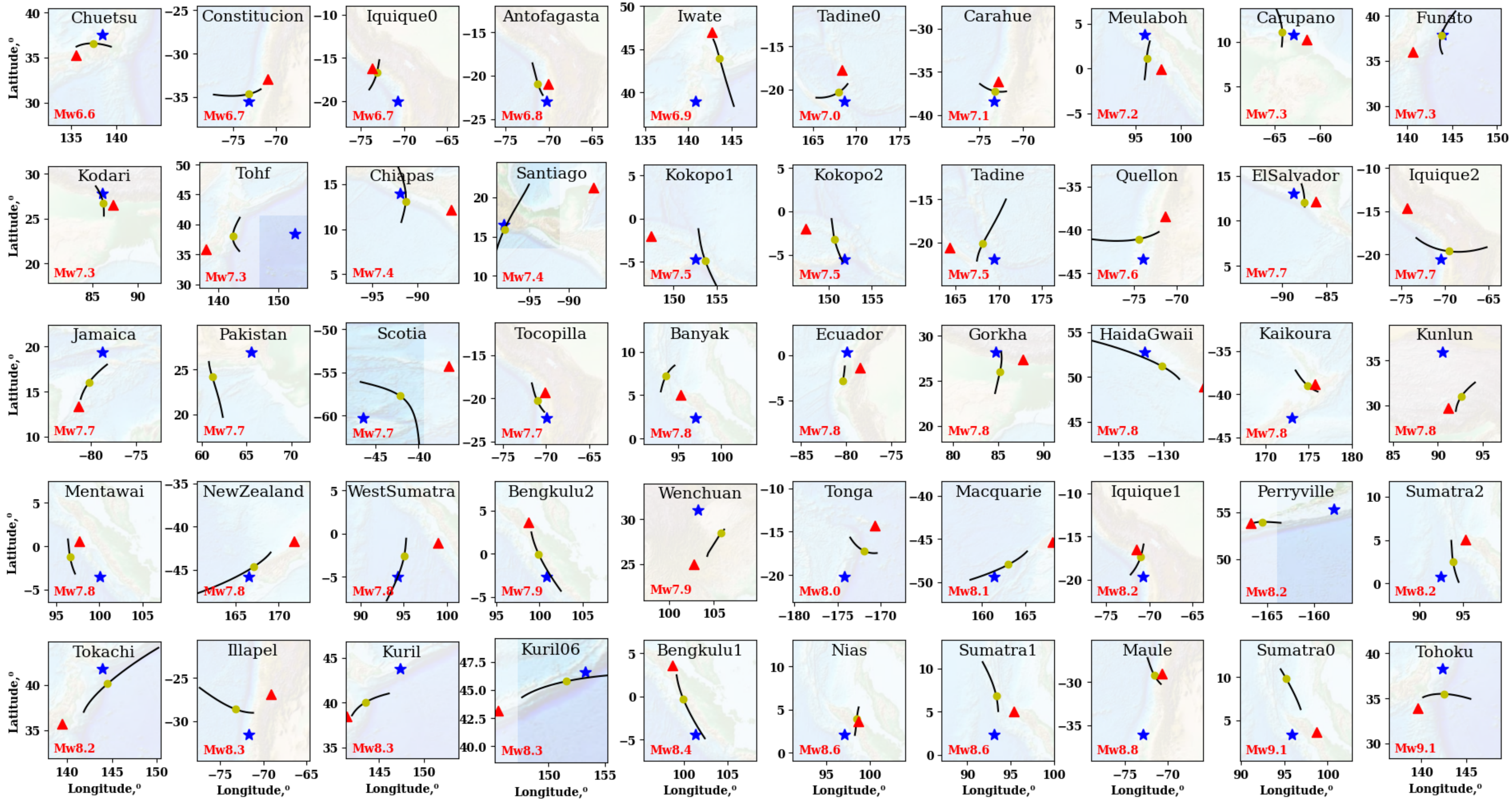


The SIP (yellow circle) in panels shows the location where the maximum Ionoquakes amplitude was detected for each EQ. Each panel shows the epicenter (blue star), receiver position (red triangle), IPP trajectory (black curve), and SIP (yellow circle).

SOURCE: Author’s production.

Figures 7.5 and 7.6 show the time series of sTEC and vTEC data, respectively. We observe that the unfiltered data distinctly reveal the minimum and maximum and therefore the ionoquake amplitudes in definitions (in Equations 7.1, 7.2) are estimated with reasonable accuracy. We note that the maximum peaks occur between 10 minutes and 16 minutes from the mainshock onset time.

Figure 7.5 - sTEC Time series along chosen IPP trajectories for the 50 EQs.

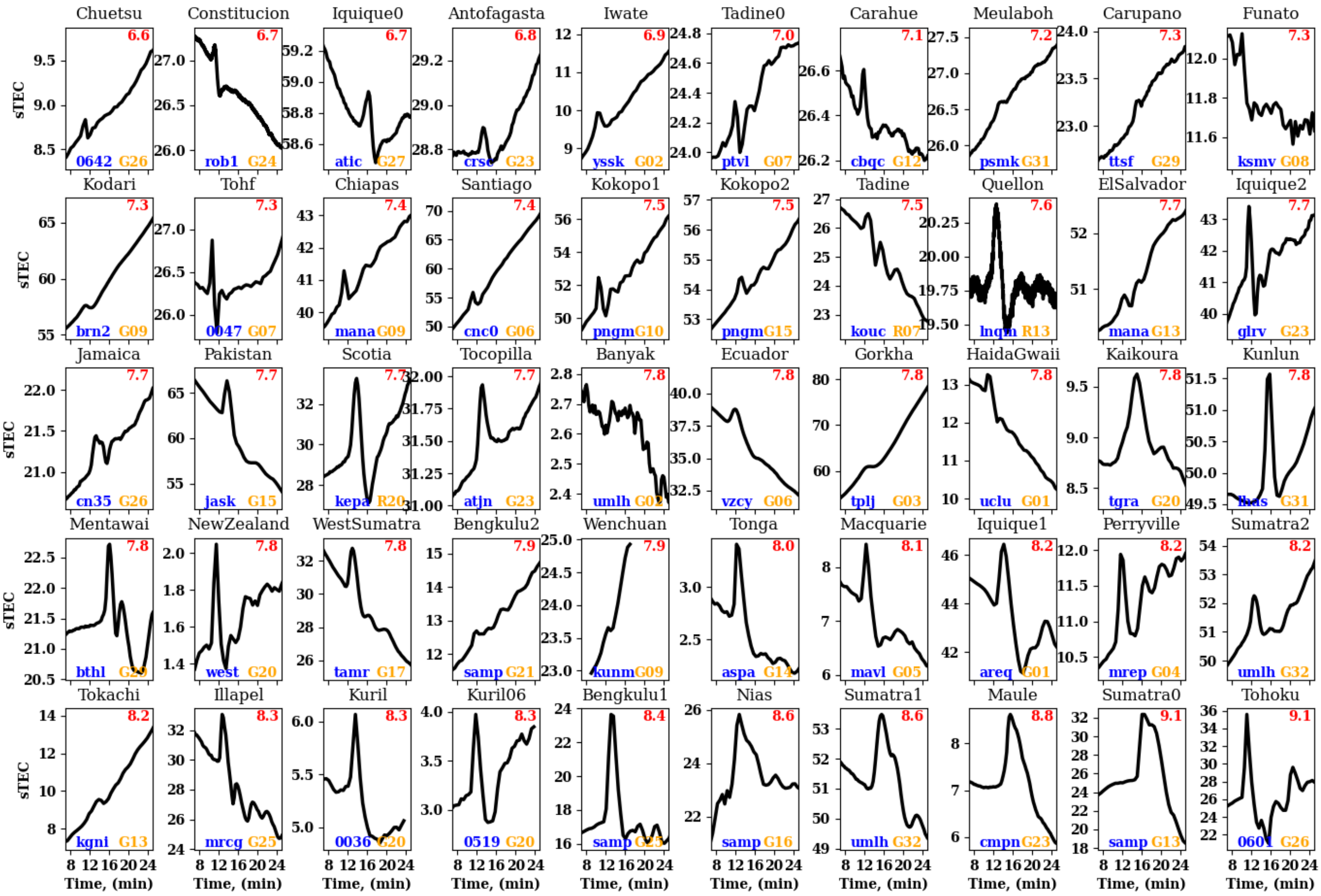


Each panel has in the title the name of the EQ, in the upper-right part in red, is the magnitude of the EQ, in the lower part in blue is the name of the GNSS receiver, the bottom right side in orange shows the satellite (G stands for GPS and R stands for GLONASS). The x-axis represents time in minutes, which are limited from 7 min to 25 min after the moment of the EQ for better visualization of the TEC data.

SOURCE: Author's production.

Figure 7.6 - vTEC Time series along chosen IPP trajectories for the 50 EQs.

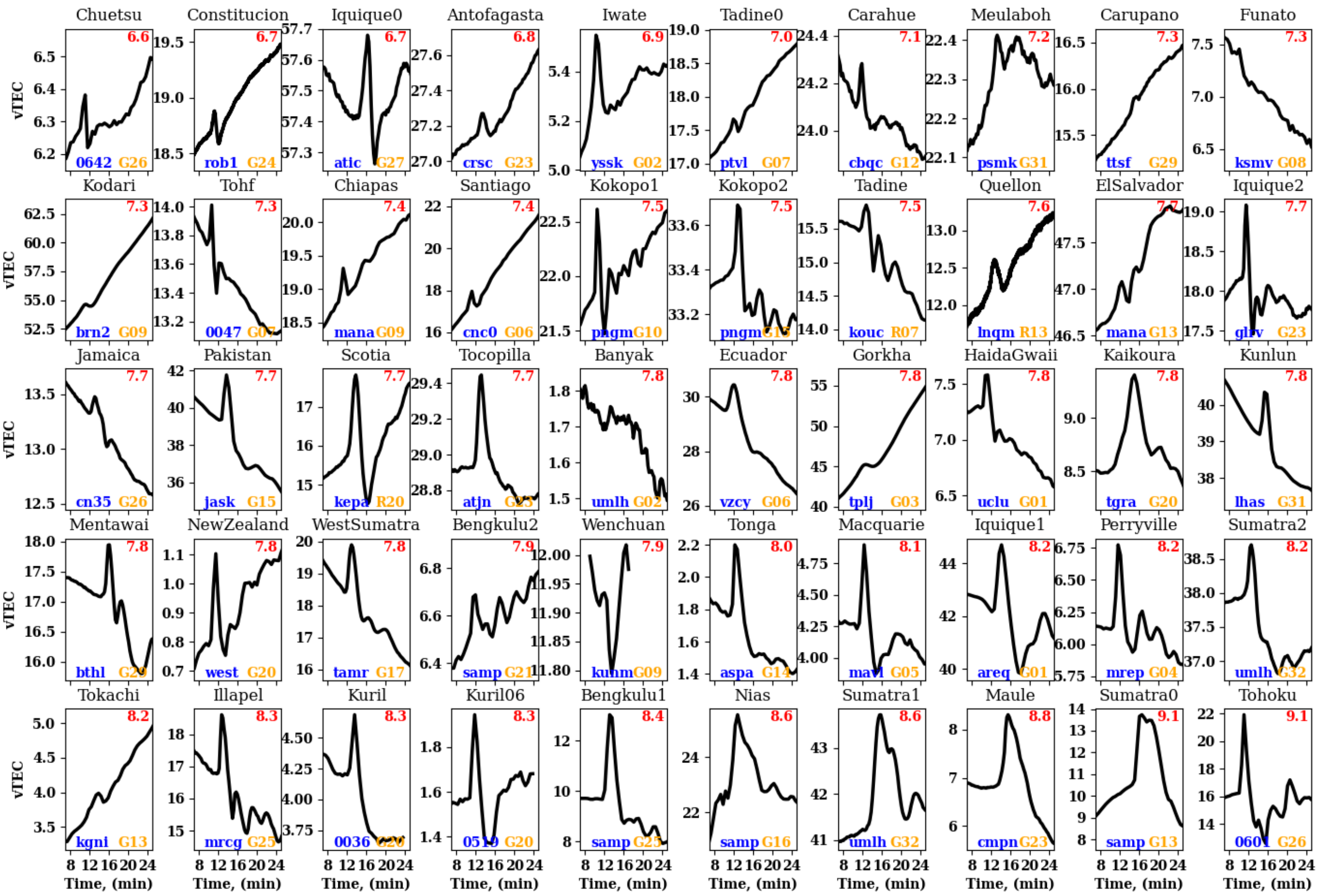

Description same as Figure 7.5

SOURCE: Author’s production.

The background TEC and geomagnetic parameters that are used in this study can be found in Table 7.4. Table 7.5 describes the SIP and Ionoquake parameters EQs. All these parameters correspond to the time of maximum amplitude of ionoquakes.

Table 7.4 - Background parameters at the time of mainshock onset.

| Label | $H_{ION}$ | $TEC_{H_{ION}}$ | $TEC_{max}$ | Decl | Incl |
|---|---|---|---|---|---|
| Kuril | 324 | 3.5 | 4.85 | -6.54 | 57.1 |
| ElSalvador | 321 | 37.94 | 50.21 | 2.17 | 41.42 |
| Kunlun | 283 | 38.05 | 49.52 | 0.64 | 53.76 |
| Tokachi | 293 | 5.44 | 7.21 | -7 | 55.68 |
| Macquarie | 325 | 4.44 | 6.03 | 25.03 | -75.01 |
| Sumatra0 | 290 | 14.68 | 18.49 | -1.18 | -11.84 |
| Nias | 308 | 15.92 | 21 | -1.06 | -14.64 |
| Tonga | 284 | 1.71 | 2.18 | 13.12 | -41.03 |
| Kuril06 | 306 | 1.99 | 2.66 | 14.66 | 62.56 |
| Chuetsu | 236 | 6.97 | 8.35 | -6.82 | 51.69 |
| Bengkulu1 | 297 | 12.33 | 16.02 | -0.59 | -28.35 |
| Bengkulu2 | 259 | 9.24 | 11.42 | -0.55 | -24.63 |
| Tocopilla | 345 | 24.28 | 31.02 | -2.55 | -18.38 |
| Antofagasta | 343 | 22.47 | 28.74 | -2.05 | -19.42 |
| Wenchuan | 276 | 18.72 | 22.96 | -1.64 | 47.04 |
| Iwate | 228 | 7.22 | 8.62 | -7.01 | 53.1 |
| NewZealand | 302 | 1.03 | 4.1 | 23.51 | -71.46 |
| Maule | 313 | 4.33 | 5.86 | 5.56 | -37.09 |
| Banyak | 261 | 1.92 | 2.37 | -1 | -13.35 |
| Meulaboh | 361 | 19.47 | 25.76 | -1.17 | -10.12 |
| Mentawai | 325 | 15.26 | 20.6 | -0.78 | -26.13 |
| Carahue | 277 | 21.06 | 26.19 | 7 | -39.35 |
| Sanriku-Oki | 274 | 20.62 | 25.79 | -3.93 | 51.07 |
| Tohoku | 250 | 17.09 | 21.02 | -6.54 | 52.09 |
| Santiago | 307 | 38.59 | 48.9 | 4.87 | 43.79 |
| Sumatra1 | 383 | 35.78 | 49.17 | -1.65 | -13.22 |
| Sumatra2 | 359 | 36.93 | 49.56 | -1.87 | -16.81 |
| HaidaGwaii | 278 | 7.58 | 9.88 | 18.08 | 71.19 |
| Chiapas | 269 | 31.63 | 39.36 | 2.37 | 41.63 |
| Funato | 267 | 9.01 | 11.47 | -6.14 | 51.45 |
| Pakistan | 290 | 42.23 | 52.83 | 1.14 | 41.65 |
| Scotia | 304 | 17.92 | 23.52 | -51.86 | -64.42 |
| Iquique0 | 349 | 44.61 | 58.48 | -3.69 | -15.4 |
| Iquique1 | 361 | 29.7 | 41.14 | -3.76 | -14.77 |
| Iquique2 | 331 | 29.51 | 39.39 | -3.68 | -16.43 |
| Kokopo1 | 321 | 38.59 | 49.12 | 6.33 | -23.75 |
| Gorkha | 323 | 42.01 | 52.99 | 0.25 | 43.53 |
| Kokopo2 | 306 | 42.18 | 52.54 | 6.31 | -25.4 |
| Kodari | 316 | 44.15 | 55.18 | 0.11 | 42.84 |
| Illapel | 288 | 18.81 | 24.39 | 1.64 | -32.39 |
| WestSumatra | 334 | 18.29 | 25.22 | -1.96 | -28.88 |
| Ecuador | 330 | 24.01 | 31.55 | -2.39 | 21.98 |
| Kaikoura | 326 | 6.01 | 8.35 | 22.8 | -67.94 |
| Quellon | 291 | 15.63 | 19.44 | 9.42 | -44.28 |
| Tadine0 | 296 | 19.17 | 23.93 | 12.32 | -46.92 |
| Carupano | 276 | 18.15 | 22.61 | -13.7 | 31.47 |
| Tadine | 285 | 17.77 | 22.37 | 12.63 | -47.6 |
| Constitucion | 263 | 21.5 | 25.86 | 4.29 | -37.1 |
| Jamaica | 258 | 16.88 | 20.62 | -6.51 | 47.62 |
| Perryville | 280 | 8.05 | 10.27 | 11.88 | 68.42 |

Height of maximum electron density (Hf2max or $H_{ION}$), absolute vertical TEC ($TEC_{H_{ION}}$) at Hf2max, the maximum value of absolute vertical TEC ($TEC_{max}$), geomagnetic field parameters (inclination (Incl) and declination (Decl) angles (deducted from the IGRF model).

Table 7.5 - SIP parameters and ionoquakes amplitudes.

| Label | Name_PRN | LON_SIP | LAT_SIP | DIS_EP_REC | DIS_EP_SIP | $T_d$ | ΔsTEC1 | ΔsTEC1_mean | ΔvTEC1 | ΔvTEC1_mean |
|---|---|---|---|---|---|---|---|---|---|---|
| Kuril | 0036G20.0 | 39.97 | 143.43 | 769.38 | 533.04 | 632 | 0.72 | 0.43 | 0.55 | 0.33 |
| ElSalvador | manaG13 | 12.03 | -87.37 | 280 | 180.53 | 656.02 | 0.35 | 0.28 | 0.32 | 0.27 |
| Kunlun | lhasG31 | 31.15 | -267.24 | 701.27 | 578.38 | 770 | 2.17 | 1.47 | 1.58 | 1.07 |
| Tokachi | kgniG13 | 40.23 | -215.36 | 778.87 | 194.15 | 744 | 0.61 | 0.46 | 0.22 | 0.2 |
| Macquarie | mavlG05 | -47.95 | -196.97 | 720.61 | 253.51 | 655.98 | 1.06 | 0.71 | 0.62 | 0.4 |
| Sumatra0 | sampG13 | 9.58 | 95.35 | 319.74 | 770.14 | 877 | 7.02 | 7.02 | 3.12 | 3.12 |
| Nias | lhwaG22 | -2.6 | 99.49 | 78.05 | 568.87 | 744 | 5.48 | 2.6 | 2.54 | 1.06 |
| Tonga | aspaG14 | -17.36 | -172 | 745.51 | 385.98 | 679.99 | 0.68 | 0.52 | 0.44 | 0.34 |
| Kuril06 | 0519G20.0 | 45.72 | 151.42 | 717.1 | 168.17 | 587 | 0.89 | 0.77 | 0.39 | 0.34 |
| Chuetsu | 0642G26 | 36.91 | -222.11 | 360.94 | 86.28 | 608 | 0.18 | 0.17 | 0.13 | 0.12 |
| Bengkulu1 | sampG25 | -0.22 | 99.89 | 937.31 | 477.32 | 694 | 6.35 | 1.14 | 3.48 | 0.76 |
| Bengkulu2 | sampG21 | 0.12 | 99.8 | 731.94 | 326.32 | 657 | 0.51 | 0.51 | 0.19 | 0.19 |
| Tocopilla | atjnG23 | -20.17 | -70.89 | 328.62 | 256.86 | 670 | 0.66 | 0.58 | 0.6 | 0.52 |
| Antofagasta | crscG23 | -20.97 | -71.11 | 223.8 | 239.84 | 737 | 0.12 | 0.11 | 0.11 | 0.11 |
| Wenchuan | kunmG09 | 28.83 | 106.13 | 673 | 367.35 | 662 | 0.38 | 0.38 | 0.19 | 0.19 |
| Iwate | ysskG02 | 43.22 | -216.15 | 901.94 | 522.54 | 585 | 0.38 | 0.27 | 0.21 | 0.16 |
| NewZealand | westG20 | -44.7 | -192.94 | 613.73 | 121.1 | 631 | 0.53 | 0.27 | 0.29 | 0.14 |
| Maule | cmpnG23 | -29.24 | -71.37 | 815.51 | 784.68 | 814 | 1.49 | 0.61 | 1.44 | 0.53 |
| Banyak | cariG02 | 13.55 | 91.16 | 1131.8 | 1393.98 | 839 | 0.16 | 0.14 | 0.12 | 0.1 |
| Meulaboh | psmkG31 | 0.99 | -263.5 | 473.31 | 321.83 | 754 | 0.17 | 0.16 | 0.13 | 0.12 |
| Mentawai | bthlG29 | -1.23 | 96.72 | 522.4 | 457.11 | 878 | 1.19 | 0.78 | 0.92 | 0.58 |
| Carahue | cbqcG12 | -37.31 | -73.23 | 249.81 | 117.32 | 658 | 0.19 | 0.11 | 0.17 | 0.08 |
| Sanriku-Oki | 0047G07 | 37.42 | -219 | 516.08 | 200.43 | 580 | 0.62 | 0.43 | 0.31 | 0.22 |
| Tohoku | 0601G26 | 35.79 | -216.99 | 549.75 | 284.08 | 606 | 9.36 | 8.6 | 5.82 | 5.36 |
| Santiago | cnc0G06 | 16.78 | -96.64 | 1322.54 | 177.13 | 613 | 2.92 | 2.55 | 0.85 | 0.74 |
| Sumatra1 | umlhG32 | 6.53 | -266.46 | 394.56 | 484.23 | 804 | 2.46 | 1.62 | 2.02 | 1.05 |
| Sumatra2 | lewkG32 | 0.78 | -265.63 | 439.92 | 211.59 | 455 | 1.59 | 1.04 | 1.02 | 0.6 |
| HaidaGwaii | ucluG01 | 51.3 | -130.45 | 629.15 | 197.22 | 622 | 0.42 | 0.15 | 0.25 | 0.09 |
| Chiapas | manaG09 | 13.1 | -90.94 | 644.82 | 147.66 | 614 | 1.06 | 0.85 | 0.49 | 0.4 |
| Funato | ksmvG08 | 38.05 | -215.87 | 363.13 | 18.6 | 517 | 0.16 | 0.16 | 0.1 | 0.1 |
| Pakistan | jaskG15 | 24.07 | -298.58 | 784.62 | 521.6 | 733 | 3.44 | 2.15 | 2.23 | 1.57 |
| Scotia | kepaR20 | -57.6 | -42.1 | 851.3 | 345.69 | 710 | 3.91 | 2.14 | 2.09 | 1.21 |
| Iquique0 | aticG27 | -16.52 | -73.17 | 523.48 | 456.81 | 871 | 0.22 | 0.11 | 0.22 | 0.11 |
| Iquique1 | areqG01 | -17.74 | -71.56 | 177.17 | 286.03 | 733 | 2.49 | 1.05 | 2.41 | 0.95 |
| Iquique2 | glrvG23 | -19.25 | -69.92 | 776.03 | 158.33 | 647 | 2.23 | 1.24 | 0.9 | 0.6 |
| Kokopo1 | pngmG10 | -4.65 | -206.72 | 649.47 | 83.17 | 599 | 1.87 | 1.87 | 0.79 | 0.79 |
| Gorkha | tpljG03 | 26.12 | -274.64 | 308.89 | 246.4 | 665 | 2.04 | 1.83 | 1.39 | 1.22 |
| Kokopo2 | pngmG15 | -3.28 | -209.35 | 634 | 288.62 | 714 | 0.72 | 0.72 | 0.43 | 0.43 |
| Kodari | brn2G09 | 26.69 | -273.75 | 186.53 | 129 | 596 | 0.68 | 0.38 | 0.66 | 0.37 |
| Illapel | mrcgG25 | -28.71 | -73.29 | 581.76 | 368.38 | 703 | 3.14 | 0.98 | 1.79 | 0.72 |
| WestSumatra | tamrG17 | -2.42 | -264.57 | 668.2 | 291.69 | 702 | 2.31 | 1.47 | 1.4 | 0.97 |
| Ecuador | vzcyG06 | -1.5 | -78.6 | 256.64 | 256.25 | 630 | 0.95 | 0.42 | 0.76 | 0.36 |
| Kaikoura | tgraG20 | -39.01 | -185.01 | 487.6 | 446.81 | 634 | 0.87 | 0.33 | 0.85 | 0.33 |
| Quellon | lnqmR13 | -41.34 | -76.56 | 591.55 | 256.59 | 675 | 0.53 | 0.32 | 0.33 | 0.24 |
| Tadine0 | ptvlG07 | -20.39 | -192.07 | 399.36 | 129.92 | 661 | 0.27 | 0.24 | 0.16 | 0.16 |
| Carupano | ttsfG29 | 11 | -64.38 | 166.46 | 167.98 | 853 | 0.22 | 0.22 | 0.15 | 0.15 |
| Tadine | koucR07 | -20.12 | -191.66 | 554.63 | 234.32 | 682 | 0.52 | 0.47 | 0.31 | 0.26 |
| Constitucion | rob1G24 | -34.92 | -73.49 | 340.92 | 68.5 | 627 | 0.16 | 0.13 | 0.12 | 0.09 |
| Jamaica | cn35G26 | 15.47 | -80.43 | 727.24 | 484.66 | 726 | 0.42 | 0.29 | 0.25 | 0.17 |
| Perryville | mrepG04 | 54.26 | -163.09 | 596.05 | 359.82 | 641 | 1.25 | 0.97 | 0.72 | 0.57 |

Name of PRN (Name_PRN), SIP Longitude (LON_SIP), SIP Latitude (LAT_SIP); Distance from receiver to the epicenter (DIS_EP_REC), Distance from the epicenter to SIP (DIS_EP_SIP). Ionoquake detection time ($T_d$); ΔsTEC1, Mean over several IPP trajectories around the trajectory of maximum ionoquake amplitude, ΔvTEC1, Mean over several IPP trajectories around the trajectory of maximum ionoquake amplitude.

Figure 7.7 presents a correlation analysis of Mw with ΔsTEC2 and ΔvTEC2. In Figure 7.7A and 7.7B we observe that the correlations are approximately 0.8 for both cases. To calculate a correlation we follow the method used by Cahyadi and Heki (2015), that is, we express the relationship between the Mw and the relative amplitude of ionoquakes as follows: $\log_{10}(\text{Ionoquakes amplitude}) = \text{a}(\text{Mw}-8.0)+\text{b}$, where we get slope $a = 0.72$ and intercept $b = 0.62$.

Figure 7.7 - Correlation analysis of moment magnitude (Mw) with ionoquakes amplitude ΔsTEC2 and ΔvTEC2.

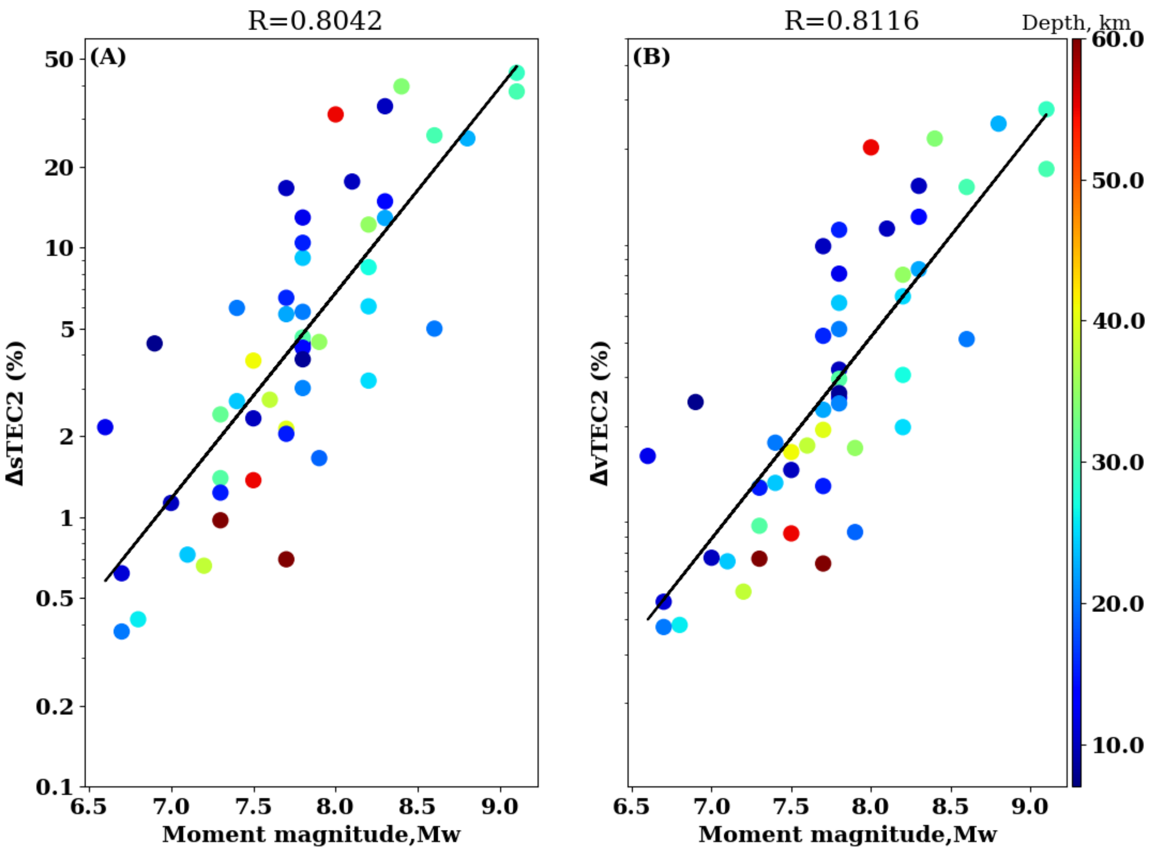


Panel (A-B) shows the correlation for ΔsTEC2 and ΔvTEC2, respectively. R represents the correlation coefficients. The color bar represents the depth of the EQs.

SOURCE: Author's production.

Ionoquakes energetics are also affected by the geomagnetic field parameters (inclination and declination) (ASTAFYEVA et al., 2013). To examine the geomagnetic field dependency, the data sets are ranked according to the geomagnetic inclination angle at the epicenters for EQ events occurring within ±40° and events occurring beyond ±40°(SUNIL et al., 2021). The correlation analysis for these two sets is presented in Figures 7.8 and 7.9. According to Figures 7.8 (A, B), the correlation coefficient is ∼0.91 for EQs with inclinations under ±40°, while Figures 7.9 (A, B) shows that the correlation is R∼0.7 for EQs with inclinations greater than ±40°. Therefore, besides the primary contribution from the moment magnitude, ionoquakes from the EQs with large inclinations have significant contributions from the geomagnetic field geometry.

Figure 7.8 - Correlation analysis for EQ events occurred within geomagnetic inclination angle ±40°.

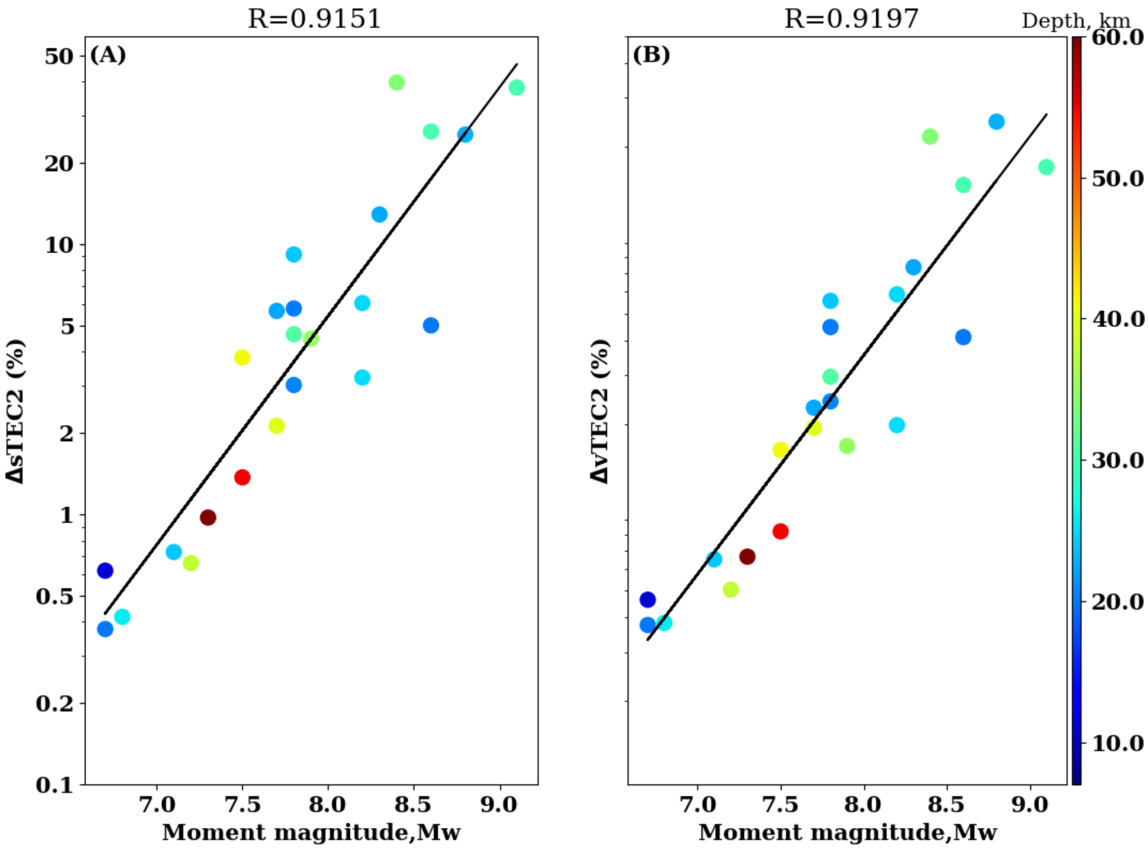


The same as in Figure 7.7.

SOURCE: Author's production.

Figure 7.9 - Correlation analysis for EQ events occurred beyond ±40°.

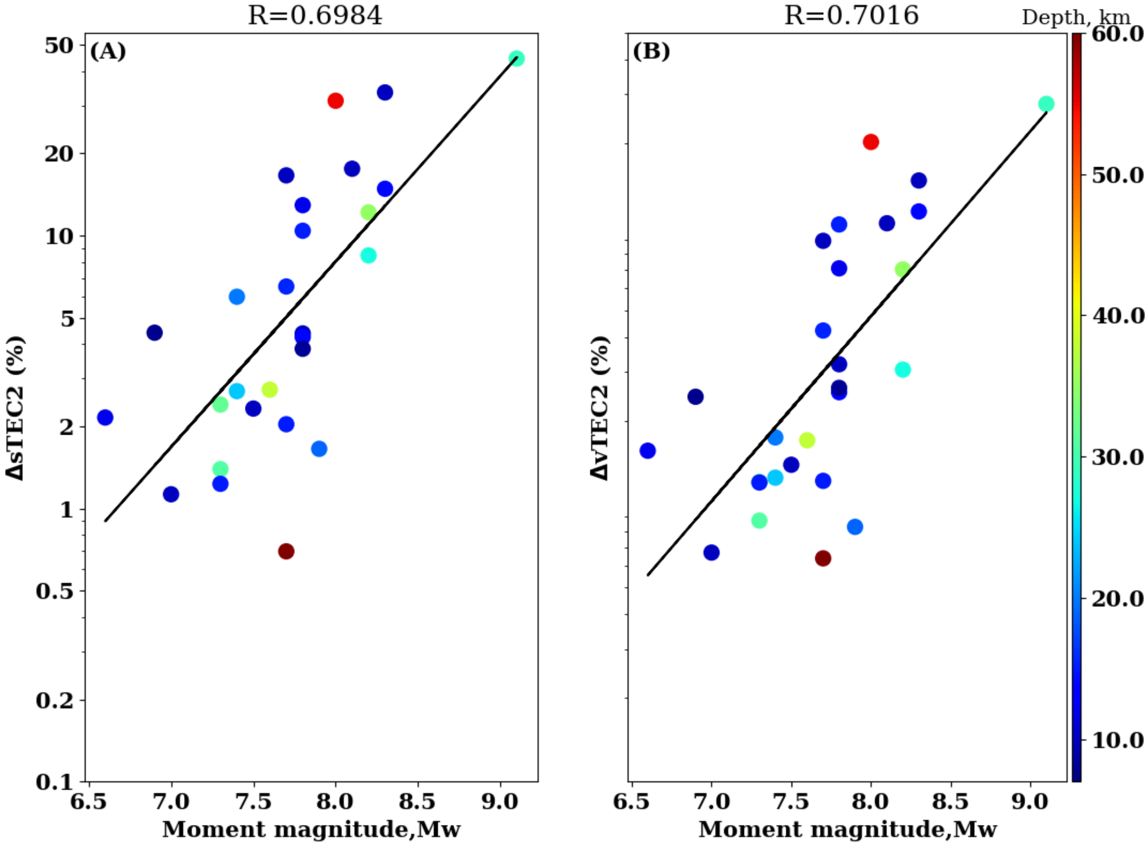


The same as in Figure 7.7.
SOURCE: Author's production.

Figure 7.10 presents the ionoquake amplitude (ΔsTEC1 and ΔvTEC1) variations with Mw. Figure 7.11 presents the variations for the mean of (ΔsTEC1 and ΔvTEC1) where the mean is taken over numerous IPP trajectories around the trajectory of maximum ionoquake amplitude. Both Figures reveal an exponential relationship confirming the logarithmic relation between Mw and ionoquake amplitude, as found by Cahyadi and Heki (2015) and as found with the definition ΔTEC2 in Figure 7.7. Such exponential dependency was not evident in previous studies by Astafyeva et al. (2013), Astafyeva et al. (2014), Sunil et al. (2021) that used the definition ΔTEC1. It is possible that more EQ events lead to a clear exponential dependency in the present study.

Figure 7.10 - Variation of ionoquake amplitude with Mw, using definition ΔTEC1 of Equation 7.1 for a particular IPP trajectory along which largest ionoquake amplitude was registered.

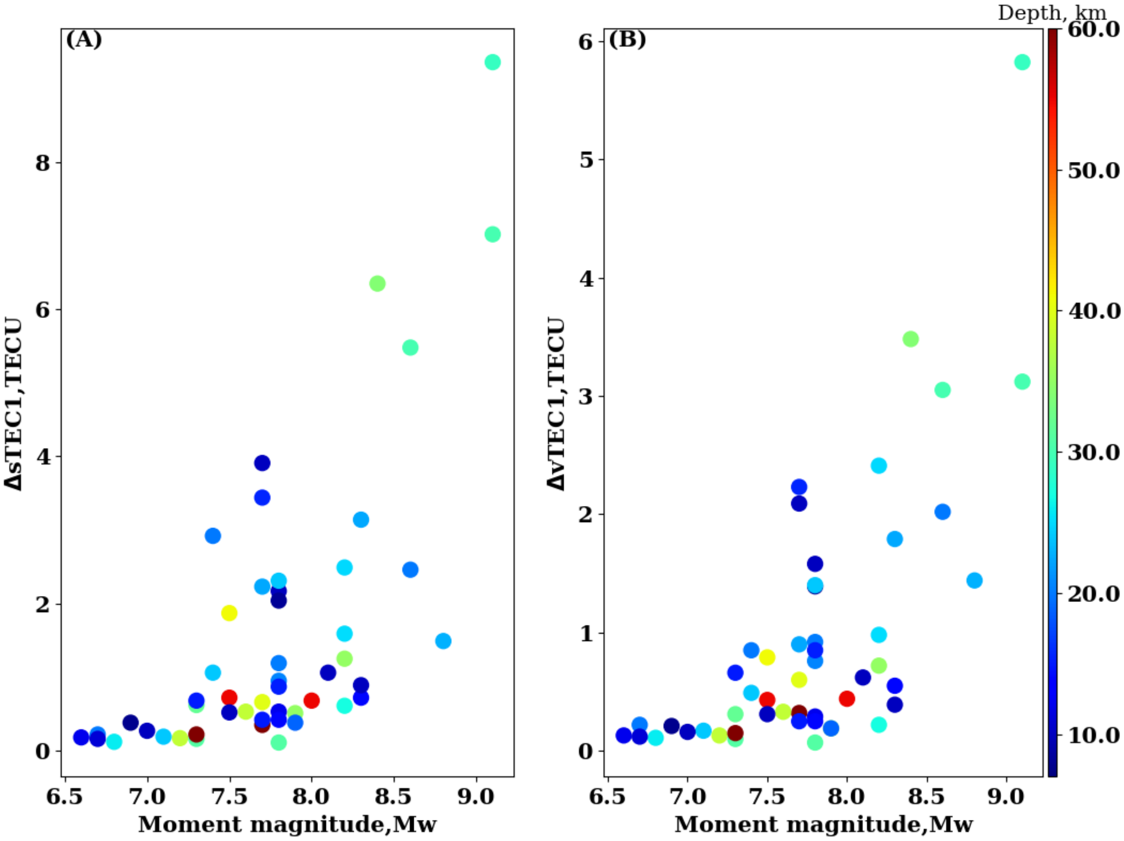


Panels (A-B) correspond to ΔsTEC1 and ΔvTEC1, respectively.

SOURCE: Author's production.

Figure 7.11 - Variation of ionoquake amplitude with Mw, using definition ΔTEC1 of Equation 7.1 and taking mean over several IPP trajectories.

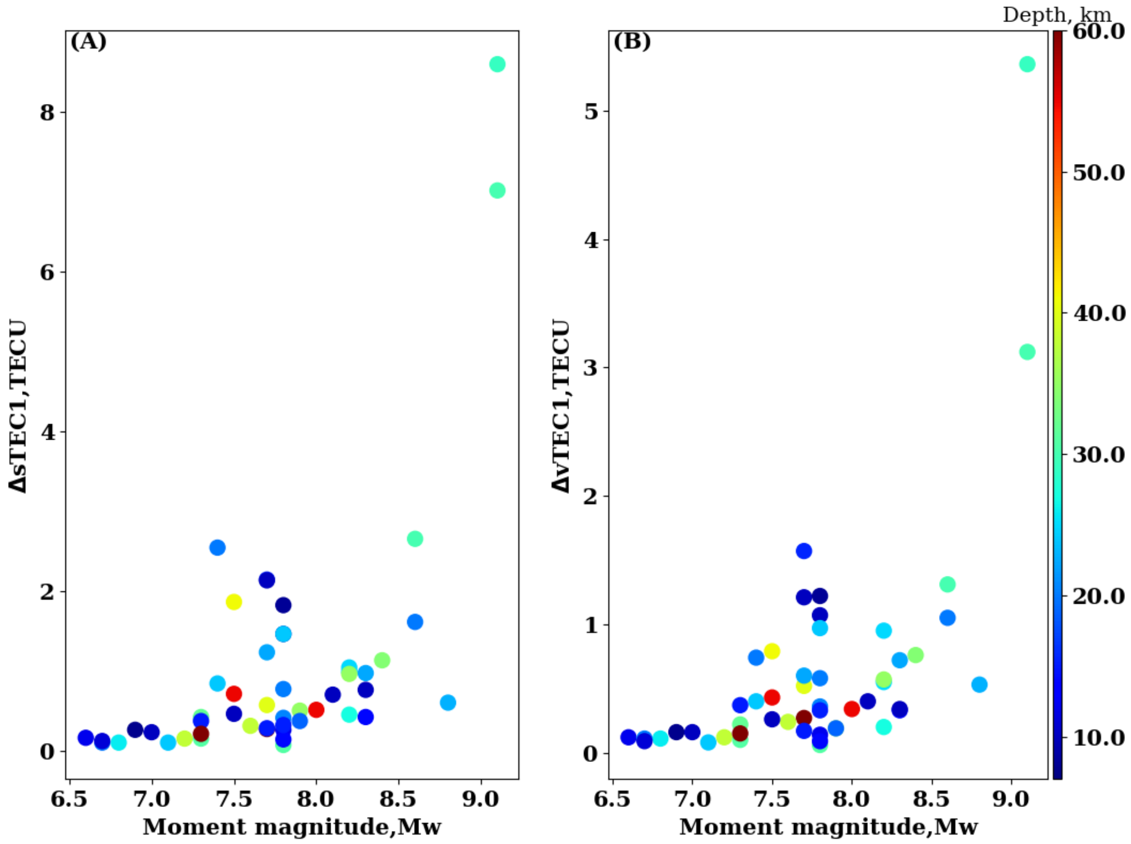


Panels (A-B) correspond to ΔsTEC1 and ΔvTEC1, respectively. The calculations in this Figure are similar to the calculations made by Astafyeva et al. (2014).

SOURCE: Author's production.

### 7.3.4 Relationship between the uplifts ($V_{SISM}$) and ionoquake amplitudes

Ground uplift from an EQ is another important parameter that reflects the resultant momentum and energy available at the ground for the SAI coupling mechanism and subsequent generation of ionoquakes. In the coupling mechanism and in the excitation of AGWs, the ground uplift is directly involved as a forcing (KHERANI et al., 2009) and therefore plays a determining role in deciding the amplitudes of ionoquakes. Figure 7.12 presents the variation of ΔsTEC1 with the ground uplift. It reveals no conclusive relationship for the definition ΔsTEC1.

Figure 7.12 - Comparison analysis of the ΔsTEC1 with uplift.

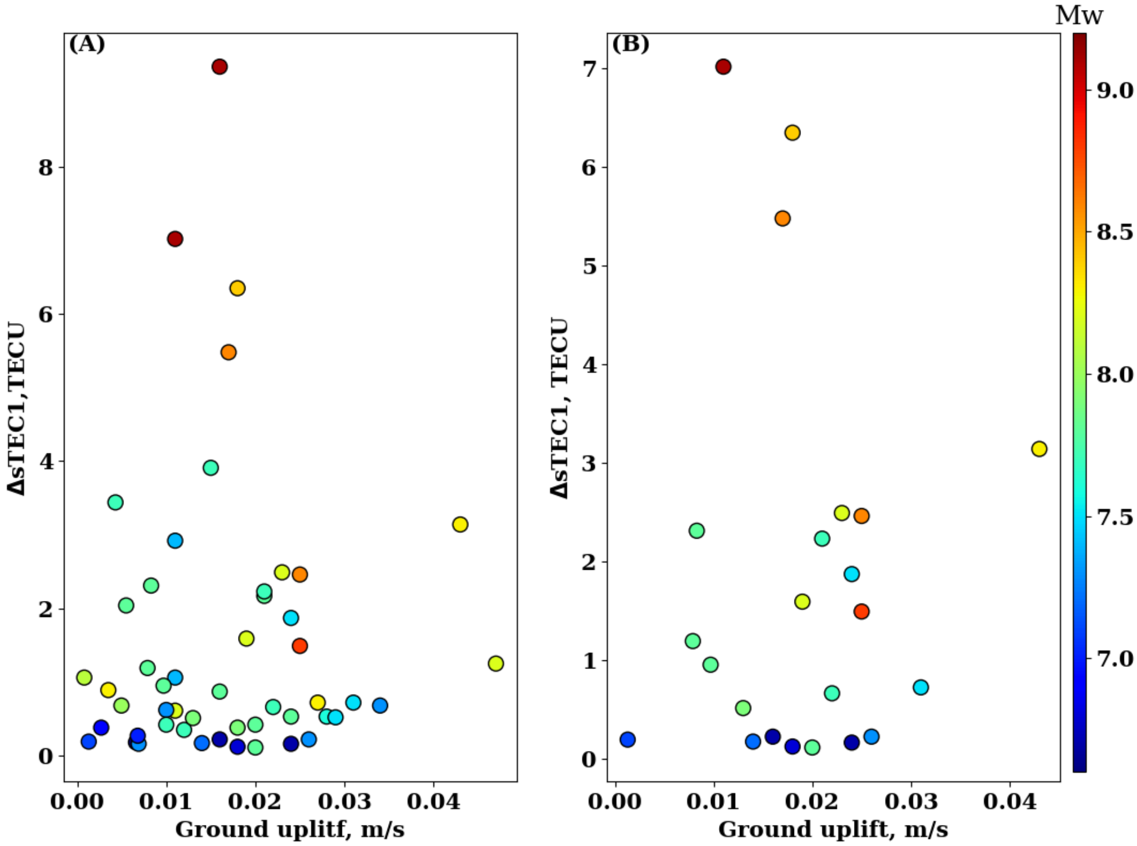


(A) For events that occurred within geomagnetic inclination angle of ±40°, (B) for events that occurred beyond ±40°.

SOURCE: Author's production.

Since ground uplift is dispersive in nature and reveals strong frequency dependency, it is likely that the relationship between the uplift and ionoquake amplitude also depends on the frequency. To examine the relationship in the frequency domain, we employ the wave decomposition method described in Chapter 3 and previously used by Sanchez et al. (2022) and estimate the ionoquake amplitude ΔvTEC3 listed in Table 7.2. Moreover, since the ground uplift estimation depends on instrument response, the study considers the EQ events in South America that have seismometers of similar characteristics. Therefore, the study in this section is based on spectrally relating $V_{\mathrm{SISM}}$ and vTEC time series for ionoquakes generated by EQs in South America. The following criteria were used to select the time series which recorded ionoquakes: we select time series that has a SIP less than 2 degrees with respect to the epicenter; we then select time series that have the maximum ionoquake amplitude within these two degrees. To calculate $V_{SISM}$, we select the seismic station closest to each EQ's epicenter. In all cases, the $V_{SISM}$ has a resolution of 15 seconds, the same as the TEC data. With identical spectral conditions for the seismometer and TEC data, the analysis aims to minimize the subjectivities arising from the wave decomposition analysis.

Figure 7.13A shows the relationship between Mw and ΔvTEC3 and Figure 7.13B shows the relationship between ground uplift and ΔvTEC3 at the atmospheric resonant frequency of 4.3 mHz for which strong ionoquake amplitude are reported from previous studies (e.g. Artru et al. (2004), Cahyadi and Heki (2015)). In Figure 7.13A, we can see that for EQs of the same magnitude as Constitucion and Iquique0 of Mw 6.8 or Tocopilla and Iquique2 of Mw 7.7, the amplitude of ionoquakes is different, so it is not entirely resolved to search for a relationship between the amplitude of ionoquakes and Mw. Additionally, the amplitude of Ionoquakes for the Maule Mw 8.8 EQ was lower than for the other EQs of Mw 8.4, 8.2, and 7.7. In contrast, the relationship between ground uplift and ionoquake amplitude distinctly reveals the expected exponential dependency.

Figure 7.13 - Relation analysis of Ionoquake amplitude ($\Delta$vTEC3) with seismic energetics ($M_w, V_{SISM}$) in the frequency domain at the acoustic resonant frequency of 4.3 mHz.

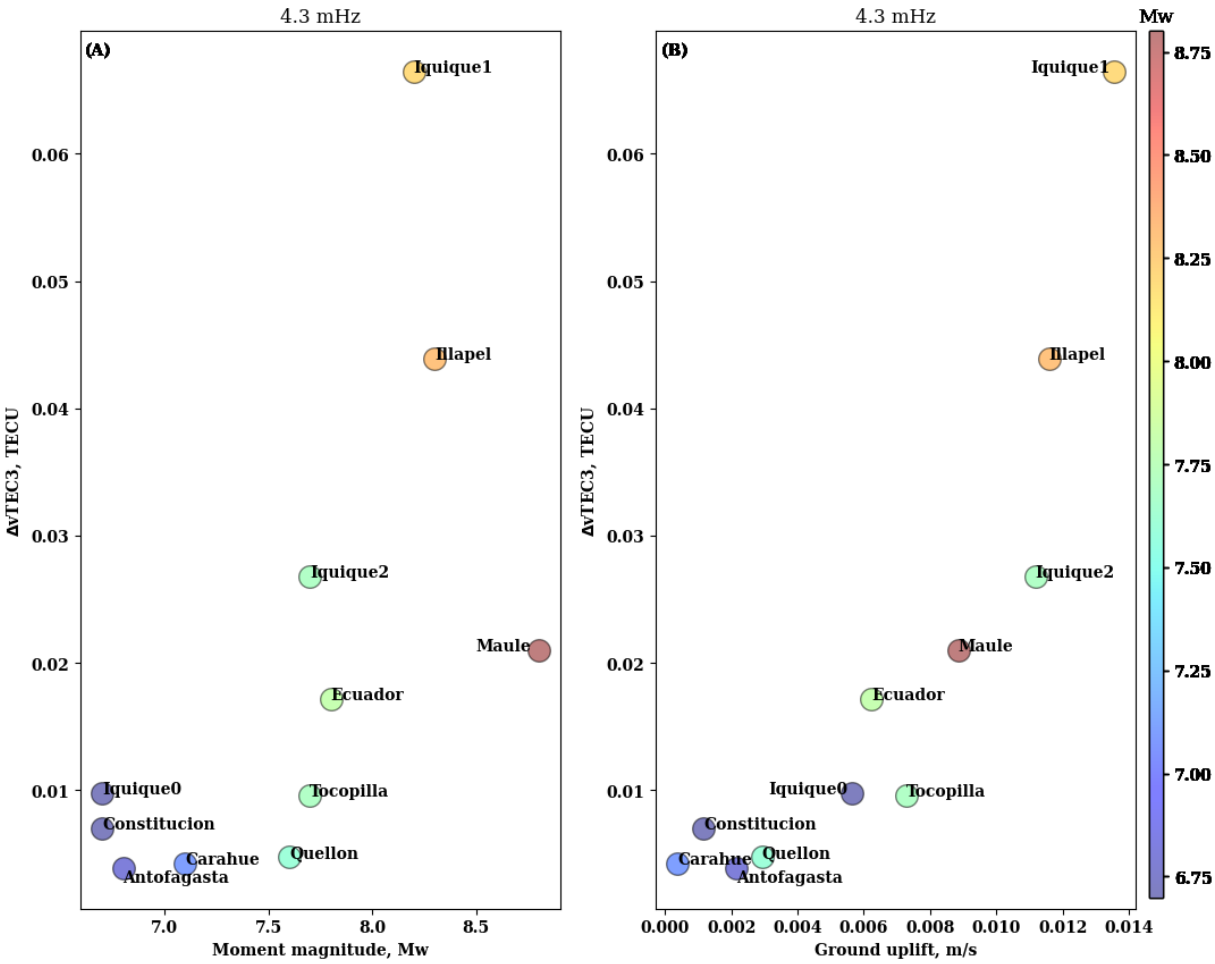


A) Relationship between Mw with ionoquake amplitude, and B) $V_{SISM}$ with ionoquake amplitude for frequency of 4.3 mHz. The colorbar represents the magnitude of the EQs, in which the red (blue) color indicates major (minor) events over South America.

SOURCE: Author's production.

Figure 7.14 presents the quantitative correlation analysis of the results presented in Figure 7.13. Note that the ionoquake amplitude axis is in logarithmic scale. Figure 7.14 reveals the linear correlation between ($M_w$, log10($\Delta$vTEC3)) in panel (A) and between ($V_{SISM}$, log10($\Delta$vTEC3)) in panel (B). Moreover, the correlation coefficient

($R$) is 0.723 and 0.9511 i.e., the ionoquake amplitude correlates strongly with the ground uplift, in comparison to the moment magnitude of the EQs. Interestingly, the R-value of 0.9511 is the largest among all the definitions of ionoquake amplitude, employed by the previous studies (e.g., (CAHYADI; HEKI, 2015; ASTAFYEVA et al., 2013)). Therefore, the present study finds an alternative definition ($\Delta$vTEC3) of ionoquake amplitude and an alternative EQ parameter ($V_{SISM}$) that results into the greater correlation coefficient of 0.9511.

Figure 7.14 - Quantitative correlation analysis of variations presented in Figure 7.13.

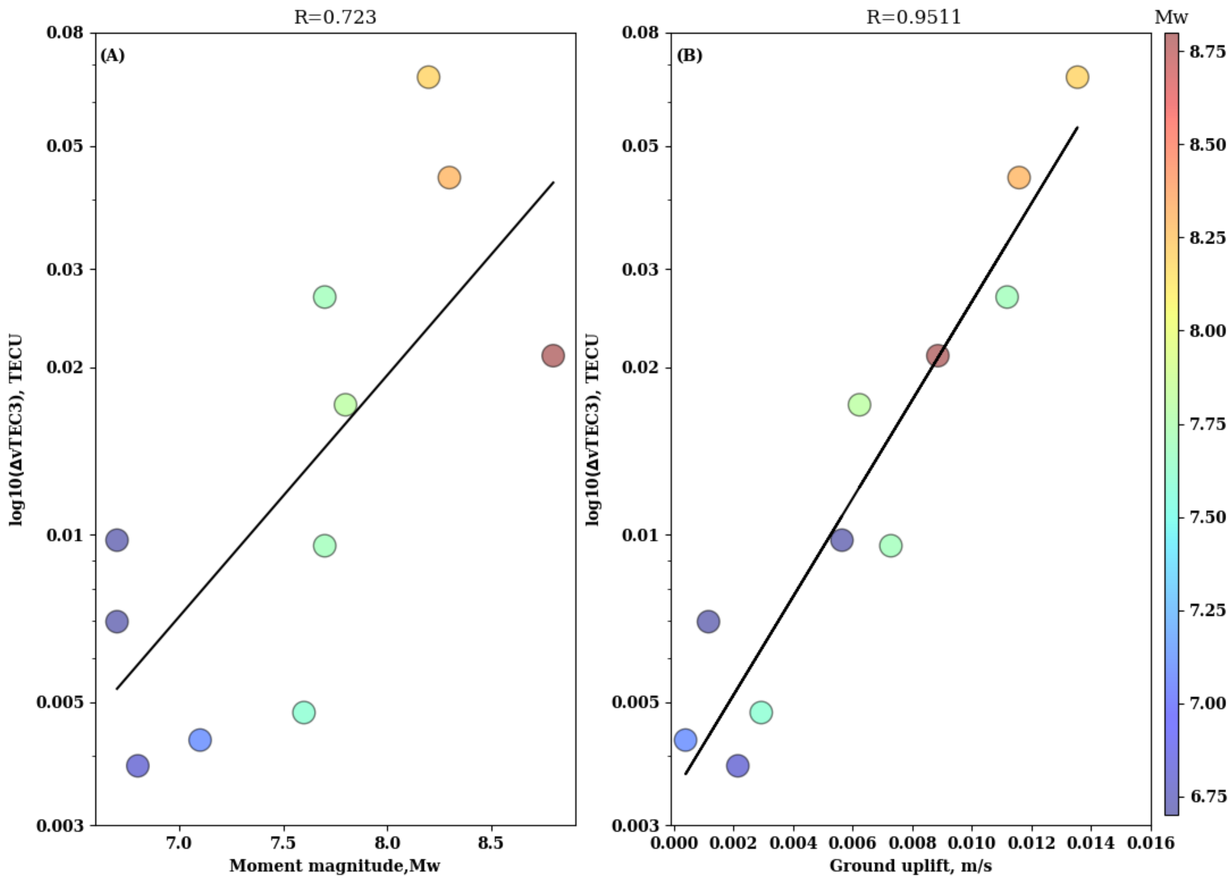


R represents the correlation coefficients. The colorbar represents the Mw of the earthquakes.

SOURCE: Author's production.

Figure 7.15 presents variations of ΔTEC with $V_{SISM}$ for various acoustic frequencies in the range of 3.3-5.8 mHz, confirming the exponential relationship in all cases.

Figure 7.15 - Relation analysis of Ionoquake amplitude (ΔvTEC3) with seismic energetics ($V_{SISM}$) at numerous acoustic frequencies.

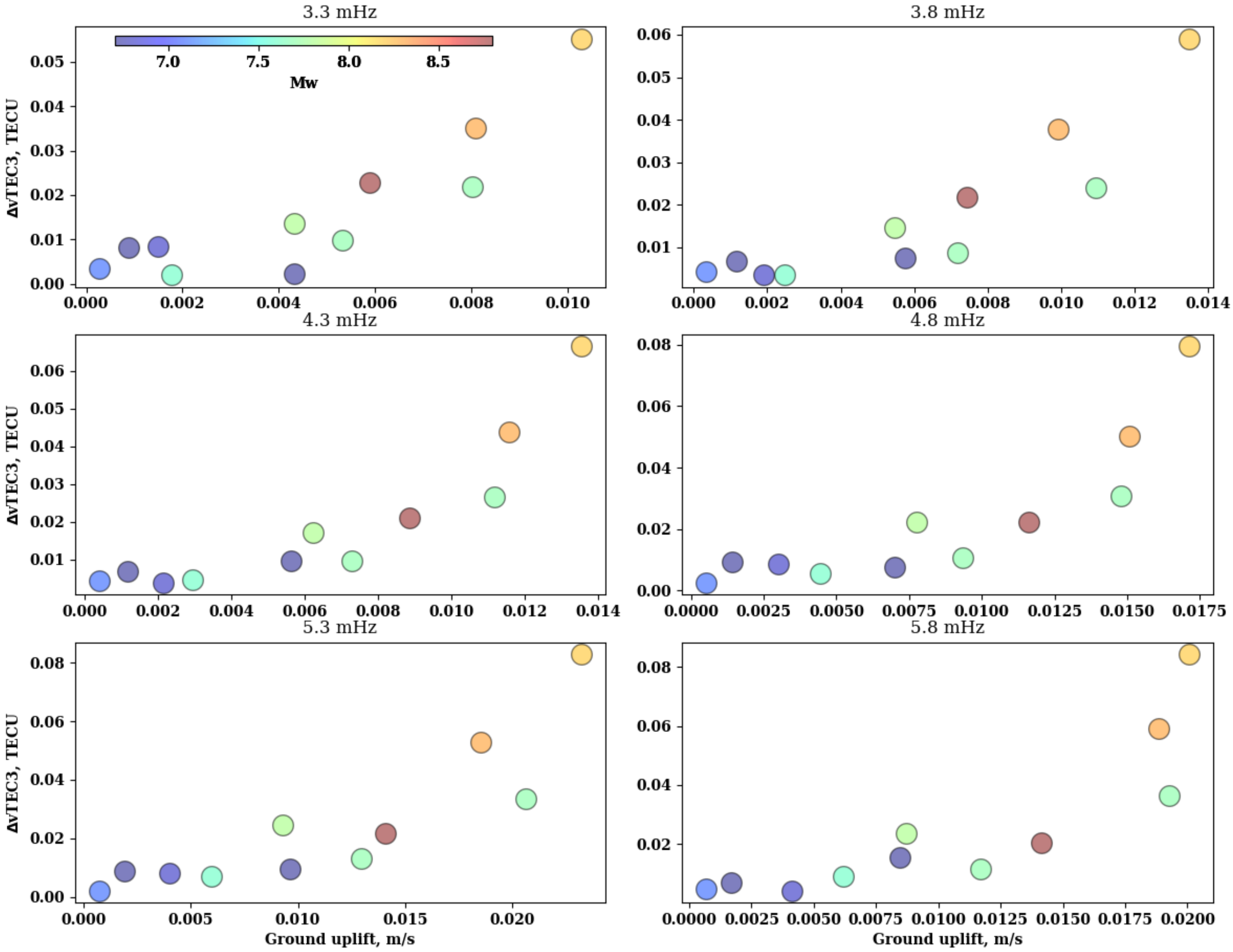


At the top of each panel is indicated the frequency for which was calculated the relationship of $V_{SISM}$ and ionoquake amplitude. The colorbar represents the magnitude of the EQs, in which the red (blue) color indicates major (minor) events.

SOURCE: Author's production.

In their study, Kherani et al. (2011) state that the ground velocity plays a crucial role in the excitation of AGWs, which leads to the ionospheric current generation and TEC disturbances. Sanchez et al. (2022) mention that the ground uplift, rather than the ground displacement, satisfies the threshold criteria for detectable ionoquake formation. The greater correlation coefficient between ground uplift ($V_{SISM}$)

and ionoquake amplitude (ΔTEC3) in Figure 7.14 is another evidence that the ground uplift, rather than the moment magnitude, primarily determines the ionoquake energetics.

## 7.4 Summary for the relationship between the amplitude of the ionoquakes with the characteristics of 50 EQs

The present study establishes the relationship of the amplitude of the ionoquakes with the characteristics of the EQs as Mw and vertical velocity. We have used measurements of seismic data and TEC-GNSS relative to 50 EQs that occurred worldwide from 1994 to 2021. Considering all the EQs, the correlation obtained between the amplitude of the ionoquakes and Mw was $\sim$0.8. For EQs that occurred in magnetic inclination less than $\pm 40°$, the correlation was $\sim$0.91. This work also presents a new method to quantify the relation between earthquake and ionoquake energetics. The method considers the ground uplift, rather than the moment magnitude, estimates the correlation in the frequency domain, and provides a greater correlation of about 0.95 at the acoustic frequency of 4.3 mHz. In the recent future, the method will be implemented to estimate the ground uplift, one of the most important EQ parameters, by estimating the ionoquake amplitude and using the correlation pattern of Figure 7.14. This work also intends to optimize the method to incorporate into the NRT monitoring of EQs. This method is of priority interest to the detection of submarine EQs due to its direct link with the threat of tsunamis.

# 8 CONCLUSIONS AND FUTURE WORKS

This thesis investigates energetics of co-seismic ionospheric disturbances or Ionoquakes, based on the Seismo–atmosphere–ionosphere (SAI) coupling mechanism energized by the acoustic-gravity waves. The focus is on the detection of ionoquakes using GNSS-TEC measurements and their validations from numerical simulation, and the SAI-ANA simulation code. The main findings of the thesis are following:

a) Considering 50 EQs of 6.6< Mw<9.1 that occurred worldwide from 1994 to 2021, a positive correlation greater than 0.8 is obtained between earthquake and ionoquakes parameters. For EQs that occurred at a magnetic dip less than $\pm 40°$, the correlation was greater than 0.91;

b) We find that the new methodology with GNSS-TEC data and simulation detects fast ionoquakes in 250-400 seconds from the beginning of the earthquake and the maximum seismic uplift. Further, it is possible to determine the ionoquakes generation altitude;

c) The SAI-ANA code produces rapid ionoquakes in a simulation time of 2 minutes. Furthermore, SAI-ANA code reproduces ionoquakes in a waveform similar to that of observation;

d) With GNSS-TEC and simulation, it is possible to detect the ionoquakes from moderate and weak earthquakes.

The rapid ionoquake detection and fast SAI-ANA simulation code are potential products, to be included the near-real-time (NRT) study in the ionospheric seismology. Together with the new findings of this thesis in the near future, continuous monitoring and rapid detection of ionoquakes in NRT will be progressively implemented.

Future work is to develop, an ionospheric seismology framework that will monitor earthquakes in NRT by determining earthquake energetics from the ionospheric measurements in NRT. Earthquakes and tsunamis are the most disastrous natural hazards and each year, they cause numerous loss of human life and significant economic losses. While any past attempt to forecast earthquakes is failed so far, existing early warning systems of the earthquake, based on the ionospheric seismology, is likely to be improved with the NRT monitoring of the ionoquakes.

In the thesis, the successful detection of ionoquakes from moderate/weak earthquakes present a promising scenario for the earthquake forecasting since number of weak earthquakes that occur before an strong earthquake, are likely to produce detectable ionoquakes energized by SAI coupling mechanism, from undetectable seismic signal of weak earthquakes at the ground. However, for the earthquake forecasting, challenges stem from the absence of any regular spatial/temporal pattern of weak earthquakes before a strong earthquake and such irregular characteristic may reflect upon the ionoquakes in spite that they are detectable. Moreover, though the findings are encouraging, it is not certain if the developed methodology in the thesis will be successful in detecting ionoquakes from other weak earthquakes around the globe. These challenges will be undertaken in future work of ionospheric seismology.

## REFERENCES


AFRAIMOVICH, E. L.; KOSOGOROV, E. A.; LESYUTA, O. S.; USHAKOV, I. I.; YAKOVETS, A. F. Geomagnetic control of the spectrum of traveling ionospheric disturbances based on data from a global GPS network. **Annales Geophysicae**, v. 19, n. 7, p. 723–731, 2001. 2, 10, 13, 17, 47

AFRAIMOVICH, E. L. et al. A review of GPS/GLONASS studies of the ionospheric response to natural and anthropogenic processes and phenomena. **Journal of Space Weather and Space Climate**, v. 3, p. A27, 2013. 1

ARTRU, J.; DUCIC, V.; KANAMORI, H.; LOGNONNÉ, P.; MURAKAMI, M. Ionospheric detection of gravity waves induced by tsunamis. **Geophysical Journal International**, v. 160, n. 3, p. 840–848, 2005. 11

ARTRU, J.; FARGES, T.; LOGNONNÉ, P. Acoustic waves generated from seismic surface waves: propagation properties determined from doppler sounding observations and normal-mode modelling. **Geophysical Journal International**, v. 158, n. 3, p. 1067–1077, 2004. 1, 8, 19, 22, 25, 29, 30, 103

ASTAFYEVA, E. Ionospheric detection of natural hazards. **Reviews of Geophysics**, v. 57, n. 4, p. 1265–1288, 2019b. 1, 2, 3, 5, 14, 15, 16, 17, 59, 65, 66, 68

ASTAFYEVA, E.; HEKI, K.; KIRYUSHKIN, V.; AFRAIMOVICH, E.; SHALIMOV, S. Two-mode long-distance propagation of coseismic ionosphere disturbances. **Journal of Geophysical Research: Space Physics**, v. 114, n. A10, 2009. 1, 5, 10, 11, 17, 18, 29, 83

ASTAFYEVA, E.; LOGNONNÉ, P.; ROLLAND, L. M. First ionosphere images for the seismic slip on the example of the Tohoku-oki earthquake. **Geophysical Research Letters**, v. 38, p. L22104, 2011. 3, 59

ASTAFYEVA, E.; ROLLAND, L. M.; SLADEN, A. Strike-slip earthquakes can also be detected in the ionosphere. **Earth and Planetary Science Letters**, v. 405, p. 180–193, 2014. 1, 2, 5, 13, 15, 17, 83, 87, 99, 101

ASTAFYEVA, E.; SHALIMOV, S.; OLSHANSKAYA, E.; LOGNONNE, P. Ionospheric response to earthquakes of different magnitudes: larger quakes perturb the ionosphere stronger and longer. **Geophysical Research Letters**, v. 40, n. 9, p. 1675–1681, 2013. 1, 2, 5, 11, 13, 14, 15, 16, 47, 59, 83, 88, 97, 99, 105

ASTAFYEVA, E.; SHULTS, K. Ionospheric gnss imagery of seismic source: possibilities, difficulties, and challenges. **Journal of Geophysical Research: Space Physics**, v. 124, n. 1, p. 534–543, 2019. 1, 3, 15, 69, 129

BAGIYA, M. S.; SUNIL, A.; ROLLAND, L.; NAYAK, S.; PONRAJ, M.; THOMAS, D.; RAMESH, D. S. Mapping the impact of non-tectonic forcing mechanisms on GNSS measured coseismic ionospheric perturbations. **Scientific Reports**, v. 9, n. 1, p. 1–15, 2019. 2, 15, 17, 83, 88

BAGIYA, M. S.; THOMAS, D.; ASTAFYEVA, E.; BLETERY, Q.; LOGNONNÉ, P.; RAMESH, D. S. The ionospheric view of the 2011 Tohoku-Oki earthquake seismic source: the first 60 seconds of the rupture. **Scientific Reports**, v. 10, n. 5232, 2020. 3

BEHNKE, R. Layer height bands in the nocturnal ionosphere over arecibo. **Journal of Geophysical Research**, v. 84, n. A3, p. 974–974, 1979. 10

BOLT, B. A. Seismic air waves from the great 1964 Alaskan earthquake. **Nature**, v. 202, n. 4937, p. 1095–1096, 1964. 5

BRAVO, M.; BENAVENTE, R.; FOPPIANO, A.; URRA, B.; OVALLE, E. Traveling ionospheric disturbances observed over South America after lithospheric events: 2010–2020. **Journal of Geophysical Research: Space Physics**, v. 127, n. 4, p. e2021JA030060, 2022. 1, 2, 13, 83

BUCHACHENKO, A. L.; ORAEVSKII, V. N.; POKHOTELOV, O. A.; SOROKIN, V. M.; STRAKHOV, V. N.; CHMYREV, V. Ionospheric precursors to earthquakes. **Physics-Uspekhi**, v. 39, n. 9, p. 959, 1996. 5

CAHYADI, M.; HEKI, K. Coseismic ionospheric disturbance of the large strike-slip earthquakes in North Sumatra in 2012: Mw dependence of the disturbance amplitudes. **Geophysical Journal International**, v. 200, n. 1, p. 116–129, 2015. 1, 2, 3, 5, 13, 14, 15, 17, 18, 19, 83, 84, 87, 91, 97, 99, 103, 105

CALAIS, E.; MINSTER, J. B. GPS detection of ionospheric perturbations following the January 17, 1994, Northridge earthquake. **Geophysical Research Letters**, v. 22, n. 9, p. 1045–1048, 1995. 1, 13

______. GPS, earthquakes, the ionosphere, and the Space Shuttle. **Physics of the Earth and Planetary Interiors**, v. 105, n. 3-4, p. 167–181, 1998. 1

CANDIDO, C.; BATISTA, I.; BECKER-GUEDES, F.; ABDU, M.; SOBRAL, J.; TAKAHASHI, H. Spread F occurrence over a southern anomaly crest location in Brazil during June solstice of solar minimum activity. **Journal of Geophysical Research: Space Physics**, v. 116, n. A6, 2011. 10

CHEN, C.; SAITO, A.; LIN, C.; LIU, J.; TSAI, H.; TSUGAWA, T.; OTSUKA, Y.; NISHIOKA, M.; MATSUMURA, M. Long-distance propagation of ionospheric disturbance generated by the 2011 off the Pacific coast of Tohoku Earthquake. **Earth, Planets and Space**, v. 63, n. 7, p. 881–884, 2011. 17

CHOOSAKUL, N.; SAITO, A.; IYEMORI, T.; HASHIZUME, M. Excitation of 4-min periodic ionospheric variations following the great Sumatra-Andaman earthquake in 2004. **Journal of Geophysical Research: Space Physics**, v. 114, n. A10, 2009. 19

CHUM, J.; CABRERA, M. A.; MOšNA, Z.; FAGRE, M.; BAšE, J.; FIšER, J. Nonlinear acoustic waves in the viscous thermosphere and ionosphere above earthquake. **Journal of Geophysical Research: Space Physics**, v. 121, n. 12, p. 12,126–12,137, 2016. 3, 62, 67, 80

COSTER, A.; WILLIAMS, J.; WEATHERWAX, A.; RIDEOUT, W.; HERNE, D. Accuracy of GPS total electron content: GPS receiver bias temperature dependence. **Radio Science**, v. 48, n. 2, p. 190–196, 2013. 13

DAVIES, K.; BAKER, D. M. Ionospheric effects observed around the time of the Alaskan earthquake of March 28, 1964. **Journal of Geophysical Research**, v. 70, n. 9, p. 2251–2253, 1965. 1, 5

DUCIC, V.; ARTRU, J.; LOGNONNé, P. Ionospheric remote sensing of the Denali earthquake rayleigh surface waves. **Geophysical Research Letters**, v. 30, n. 18, 2003. 1

EVANS, J.; HOLT, J.; WAND, R. A differential-Doppler study of traveling ionospheric disturbances from Millstone Hill. **Radio Science**, v. 18, n. 3, p. 435–451, 1983. 10

FIGUEIREDO, C.; WRASSE, C.; TAKAHASHI, H.; OTSUKA, Y.; SHIOKAWA, K.; BARROS, D. Large-scale traveling ionospheric disturbances observed by GPS dTEC maps over North and South America on Saint Patrick's Day storm in 2015. **Journal of Geophysical Research: Space Physics**, v. 122, n. 4, p. 4755–4763, 2017. 10

GALPERIN, Y. I. Alfven wave excited in the middle-latitude magnetosphere by a large-scale acoustic wave propagating in lower ionosphere. **Izvestiya ANSSSR Physics of the Earth**, n. 11, p. 88–98, 1985. 11

GALVAN, D. A.; KOMJATHY, A.; HICKEY, M. P.; STEPHENS, P.; SNIVELY, J.; SONG, Y. T.; BUTALA, M. D.; MANNUCCI, A. J. Ionospheric signatures of Tohoku-Oki tsunami of March 11, 2011: Model comparisons near the epicenter. **Radio Science**, v. 47, n. 04, p. 1–10, 2012. 18

HEKI, K. Ionospheric disturbances related to earthquakes. In: HUANG, C.; G., Z. Y. L.; J., P. L. (Ed.). **Ionosphere dynamics and applications**. [S.l.]: American Geophysical Union (AGU), 2021. chapter 21, p. 511–526. 1, 2, 13, 15

HEKI, K.; PING, J. Directivity and apparent velocity of the coseismic ionospheric disturbances observed with a dense GPS array. **Earth and Planetary Science Letters**, v. 236, n. 3-4, p. 845–855, 2005. 1, 2, 11, 13, 18, 47

HINES, C. O. Internal atmospheric gravity waves at ionospheric heights. **Canadian Journal of Physics**, v. 38, n. 11, p. 1441–1481, 1960. 6, 10

______. Observed ionospheric waves considered as gravity or Hydromagnetic waves. **Jounal of Atmospheric and Terrestrial Physics**, v. 36, p. 1205–1216, 1974. 10

HOFMANN-WELLENHOF, B.; LICHTENEGGER, H.; COLLINS, J. **Global positioning system**. [S.l.]: Springer, 2001. 11, 12

HOFMANN-WELLENHOF, B.; LICHTENEGGER, H.; WASLE, E. **GNSS - Global Navigation Satellite Systems**. Vienna: Springer-Verlag, 2008. 12

HOLTON, J. R. **An introduction to dynamic Meteorology.** New York: Academic Press, 1897. 135

HOSSEINI, K.; SIGLOCH, K. Obspydmt: a Python toolbox for retrieving and processing large seismological data sets. **Solid Earth**, v. 8, n. 5, p. 1047–1070, 2017. 52, 87

IYEMORI, T. et al. Geomagnetic pulsations caused by the Sumatra earthquake on december 26, 2004. **Geophysical Research Letters**, v. 32, n. 20, 2005. 1, 10, 19

______. Barometric and magnetic observations of vertical acoustic resonance and resultant generation of field-aligned current associated with earthquakes. **Earth, Planets and Space**, v. 65, n. 8, p. 901–909, 2013. 1, 10, 19

JONAH, O.; KHERANI, E.; PAULA, E. D. Observation of TEC perturbation associated with medium-scale traveling ionospheric disturbance and possible seeding mechanism of atmospheric gravity wave at a Brazilian sector. **Journal of Geophysical Research: Space Physics**, v. 121, n. 3, p. 2531–2546, 2016. 10

KEAREY, P.; BROOKS, M.; HILL, I. **An introduction to geophysical exploration**. 3.ed. London: Blackwell Science, 2002. 5

KELLEY, M. C. **The Earth's ionosphere: plasma physics and electrodynamics.** San Diego, California: Academic Press, 2009. 6, 9, 36, 135

KHERANI, E.; ROLLAND, L.; LOGNONNE, P.; SLADEN, A.; KLAUSNER, V.; PAULA, E. de. Traveling ionospheric disturbances propagating ahead of the Tohoku-Oki tsunami: a case study. **Geophysical Journal International**, v. 204, n. 2, p. 1148–1158, 2016. 7, 10, 18, 31, 35, 44, 67, 79, 131, 140

KHERANI, E. A.; ABDU, M.; PAULA, E. D.; FRITTS, D.; SOBRAL, J.; JUNIOR, F. de M. The impact of gravity waves rising from convection in the lower atmosphere on the generation and nonlinear evolution of equatorial bubble. **Annales Geophysicae**, v. 27, p. 1657–1668, 2009. 1, 13, 101

KHERANI, E. A.; ABDU, M. A.; FRITTS, D. C.; PAULA, E. R. de. The acoustic gravity wave induced disturbances in the equatorial ionosphere. In: ABDU M. A.; PANCHEVA, D. (Ed.). **Aeronomy of the Earth's Atmosphere and Ionosphere**. Dordrecht: Springer, 2011. p. 141–162. 7, 8, 10, 106

KHERANI, E. A.; LOGNONNE, P.; HÉBERT, H.; ROLLAND, L.; ASTAFYEVA, E.; OCCHIPINTI, G.; COÏSSON, P.; WALWER, D.; PAULA, E. D. Modelling of the total electronic content and magnetic field anomalies generated by the 2011 Tohoku-Oki tsunami and associated acoustic-gravity waves. **Geophysical Journal International**, v. 191, n. 3, p. 1049–1066, 2012. 1, 2, 3, 8, 9, 10, 11, 18, 62, 67, 79, 81

KHERANI, E. A.; SANCHEZ, S. A.; PAULA, E. R. de. Numerical modeling of coseismic tropospheric disturbances arising from the unstable acoustic gravity wave energetics. **Atmosphere**, v. 12, n. 6, p. 765, 2021. 11, 35

KLAUSNER, V.; ALMEIDA, T.; MENESES, F. D.; KHERANI, E.; PILLAT, V.; MUELLA, M. Chile2015: induced magnetic fields on the Z component by tsunami wave propagation. In: BRAITENBERG C.; RABINOVICH, A. B. (Ed.). **The Chile-2015 (Illapel) Earthquake and Tsunami**. [S.l.]: Springer, 2017. p. 193–208. 10

KLOBUCHAR, J. A. Ionospheric time-delay algorithm for single-frequency GPS users. **IEEE Transactions on Aerospace and Electronic Systems**, n. 3, p. 325–331, 1987. 13

KOSHEVAYA, S.; GRIMALSKY, V.; BURLAK, G.; ENRÍQUEZ, R. P.; KOTSARENKO, A. Magnetic perturbations excited by seismic waves. **Physica Scripta**, v. 64, n. 2, p. 172, 2001. 10, 11

KRISCHER, L.; MEGIES, T.; BARSCH, R.; BEYREUTHER, M.; LECOCQ, T.; CAUDRON, C.; WASSERMANN, J. ObsPy: a bridge for seismology into the scientific Python ecosystem. **Computational Science & Discovery**, v. 8, n. 1, p. 014003, 2015. 22

LIU, J.; CHEN, C. H.; SUN, Y. Y.; CHEN, C. H.; TSAI, H. F.; YEN, H. Y.; CHUM, J.; LASTOVICKA, J.; YANG, Q. S.; CHEN, W. S.; WEN, S. The vertical propagation of disturbances triggered by seismic waves of the 11 March 2011 M9.0 Tohoku earthquake over Taiwan. **Geophysical Research Letters**, v. 43, n. 4, p. 1759–1765, 2016. 3

LOGNONNÉ, P. Seismic waves from atmospheric sources and atmospheric/ionospheric signatures of seismic waves. In: PICHON, A. L.; BLANC, E.; HAUCHECORNE, A. (Ed.). **Infrasound monitoring for atmospheric studies**. [S.l.]: Springer, 2009. p. 281–304. 1, 5

LOGNONNÉ, P.; GARCIA, R.; CRESPON, F.; OCCHIPINTI, G.; KHERANI, A.; ARTRU-LAMBIN, J. Seismic waves in the ionosphere. **Europhysics News**, v. 37, n. 4, p. 11–15, 2006. 10, 11

LOWRIE, W. **Fundamentals of geophysics**. 2.ed. Cambridge: Cambridge University Press, 2007. 5

MANTA, F.; OCCHIPINTI, G.; FENG, L.; HILL, E. M. Rapid identification of tsunamigenic earthquakes using GNSS ionospheric sounding. **Scientific Reports**, v. 10, n. 1, p. 1–10, 2020. 2, 17, 18, 83, 91

MISRA, P.; ENGE, P. **Global Positioning System, signals, measurements, and performance**. 2. ed. [S.l.]: Ganga-Jamuna Press, 2006. 12

MONICO, J. F. G. **Posicionamiento pelo GNSS**. São Paulo: UNESP, 2008. 11, 12

MUNRO, G. H. Short-period changes in the f region of the ionosphere. **Nature**, v. 162, p. 886–887, 1948. 10

NAYAK, S.; BAGIYA, M. S.; MAURYA, S.; HAZARIKA, N. K.; KUMAR, A. S. S.; PRASAD, D. S. V. V. D.; RAMESH, D. S. Terrestrial resonant oscillations during the 11 April 2012 Sumatra doublet earthquake. **Journal of Geophysical Research: Space Physics**, v. 126, n. 12, p. e2021JA029169, 2021. 17

OCCHIPINTI, G. The seismology of the planet mongo: the 2015 ionospheric seismology review. In: MORRA, G.; YUEN, D. A.; KING, S.; LEE, S. M.; STEIN, S. (Ed.). **Subduction dynamics: from Mantle to mega disasters**. [S.l.]: AGU, 2015. 3

PICONE, J.; HEDIN, A.; DROB, D. P.; AIKIN, A. Nrlmsise-00 empirical model of the atmosphere: Statistical comparisons and scientific issues. **Journal of Geophysical Research: Space Physics**, v. 107, n. A12, p. SIA–15, 2002. 39, 46

PIMENTA, A.; KELLEY, M.; SAHAI, Y.; BITTENCOURT, J.; FAGUNDES, P. Thermospheric dark band structures observed in all-sky OI 630 nm emission images over the Brazilian low-latitude sector. **Journal of Geophysical Research: Space Physics**, v. 113, n. A1, 2008. 10

PROLSS, G. W. **Physics of the Earth's space environment**. Bonn, Germany: Springer Science, 2004. 8

ROLLAND, L. M.; LOGNONNÉ, P.; ASTAFYEVA, E.; KHERANI, E. A.; KOBAYASHI, N.; MANN, M.; MUNEKANE, H. The resonant response of the ionosphere imaged after the 2011 off the Pacific coast of Tohoku Earthquake. **Earth, Planets and Space**, v. 63, n. 7, p. 853–857, 2011. 19, 25, 28, 29

ROLLAND, L. M.; LOGNONNÉ, P.; MUNEKANE, H. Detection and modeling of Rayleigh wave induced patterns in the ionosphere. **Journal of Geophysical Research: Space Physics**, v. 116, n. A5, 2011. 1, 5, 10, 11, 18, 19

ROLLAND, L. M.; VERGNOLLE, M.; NOCQUET, J.-M.; SLADEN, A.; DESSA, J.-X.; TAVAKOLI, F.; NANKALI, H. R.; CAPPA, F. Discriminating the tectonic and non-tectonic contributions in the ionospheric signature of the 2011, Mw7. 1, dip-slip Van earthquake, Eastern Turkey. **Geophysical Research Letters**, v. 40, n. 11, p. 2518–2522, 2013. 2, 10, 12, 13, 17, 61

SANCHEZ, S. A.; KHERANI, E. A.; ASTAFYEVA, E.; PAULA, E. R. de. Ionospheric disturbances observed following the Ridgecrest Earthquake of 4 July 2019 in California, USA. **Remote Sensing**, v. 14, n. 1, p. 188, 2022. 1, 3, 5, 10, 19, 21, 22, 23, 24, 25, 30, 31, 32, 61, 87, 102, 106, 120, 121

______. Rapid detection of co-seismic ionospheric disturbances associated with the 2015 Illapel, the 2014 Iquique and the 2011 Sanriku-Oki earthquakes. **Journal of Geophysical Research**, 2023. 49, 51, 54, 55, 57, 59, 63, 64, 65, 66

SASTRY, V. R.; CHANDRA, G. R. Signal processing computation based seismic energy estimation of blast induced ground vibration waves. **2016 IEEE Distributed Computing, VLSI, Electrical Circuits and Robotics (DISCOVER)**, p. 216–220, 2016. 6

SHALIMOV, S.; GOKHBERG, M. Lithosphere–ionosphere coupling mechanism and its application to the earthquake in Iran on June 20, 1990. a review of ionospheric measurements and basic assumptions. **Physics of the Earth and Planetary Interiors**, v. 105, n. 3-4, p. 211–218, 1998. 5

SMS TSUNAMI WARNING. **Earthquakes: fault lines**. Capitol Avenue, Suite 413A, 2023. Available from: <<https://www.sms-tsunami-warning.com/pages/fault-lines>>. Access in: 25 May 2023. 14

SUBIRANA, J. S.; ZORNOZA, J. J.; HERNÁNDEZ-PAJARES, M. **GNSS data processing, Vol. I: Fundamentals and algorithms**. Noordwijk, the Netherlands: ESA, 2013. 12

SUNIL, A.; BAGIYA, M. S.; BLETERY, Q.; RAMESH, D. Association of ionospheric signatures to various tectonic parameters during moderate to large magnitude earthquakes: case study. **Journal of Geophysical Research: Space Physics**, v. 126, n. 3, p. e2020JA028709, 2021. 1, 2, 3, 13, 17, 83, 98, 99

SUNIL, A. S.; BAGIYA, M. S.; REDDY, C. D.; KUMAR, M.; RAMESH, D. S. Post-seismic ionospheric response to the 11 April 2012 East Indian Ocean doublet earthquake. **Earth, Planets and Space**, v. 67, n. 1, p. 1–12, 2015. 18

SUNIL, A. S.; SUNIL, P. S.; SHRIVASTAVA, M. N.; MAURYA, A. K.; THOMAS, D.; GONZALEZ, G. Seismic induced ground deformation and ionospheric perturbations of the 29 july 2021, mw 8.2 chignik earthquake, alaska. **Journal of Geophysical Research: Space Physics**, v. 127, n. 11, p. e2022JA030576, 2022. 1

THOMAS, D.; BAGIYA, M. S.; SUNIL, P. S.; ROLLAND, L.; SUNIL, A. S.; MIKESELL, T. D.; NAYAK, S.; MANGALAMPALLI, S.; RAMESH, D. S. Revelation of early detection of co-seismic ionospheric perturbations in GPS-TEC from realistic modelling approach: case study. **Scientific Reports**, v. 8, n. 1, p. 12105, 2018. 2, 3, 15, 18, 59, 65, 66, 129

TSUGAWA, T.; SAITO, A.; OTSUKA, Y.; NISHIOKA, M.; MARUYAMA, T.; KATO, H.; NAGATSUMA, T.; MURATA, K. T. Ionospheric disturbances detected by GPS total electron content observation after the 2011 off the Pacific coast of Tohoku earthquake. **Earth, Planets and Space**, v. 63, n. 7, p. 66, 2011. 18

UNITED STATES GEOLOGICAL SURVEY. **M 6.4-Ridgecrest Earthquake Sequence**. Reston, VA 20192, 2019. Available from: <<https://earthquake.usgs.gov/earthquakes/eventpage/ci38443183/shakemap/intensity>>. Access in: 30 May 2023. 122

UTADA, H.; SHIMIZU, H.; OGAWA, T.; MAEDA, T.; FURUMURA, T.; YAMAMOTO, T.; YAMAZAKI, N.; YOSHITAKE, Y.; NAGAMACHI, S. Geomagnetic field changes in response to the 2011 off the Pacific coast of Tohoku earthquake and tsunami. **Earth and Planetary Science Letters**, v. 311, p. 11–27, 2011. 1, 5, 10

YEN, H.-Y.; CHEN, C.-R.; LO, Y.-T.; SHIN, T.-C.; LI, Q. Seismo-geomagnetic pulsations triggered by Rayleigh waves of the 11 March 2011 m 9.0 Tohoku-oki earthquake. **Terrestrial, Atmospheric and Oceanic Science**, v. 26, p. 95–101, 2015. 3

ZETTERGREN, M. D.; SNIVELY, J. B.; KOMJATHY, A.; VERKHOGLYADOVA, O. P. Nonlinear ionospheric responses to large-amplitude infrasonic-acoustic waves generated by undersea earthquakes. **Journal of Geophysical Research: Space Physics**, v. 122, n. 2, p. 2272–2291, 2017. 81

## APPENDIX A - SUPPLEMENTARY FIGURES

Figure A.1 - TEC time series as registered from the BGIS station and ΔTEC decomposition, for Ridgecrest EQ.

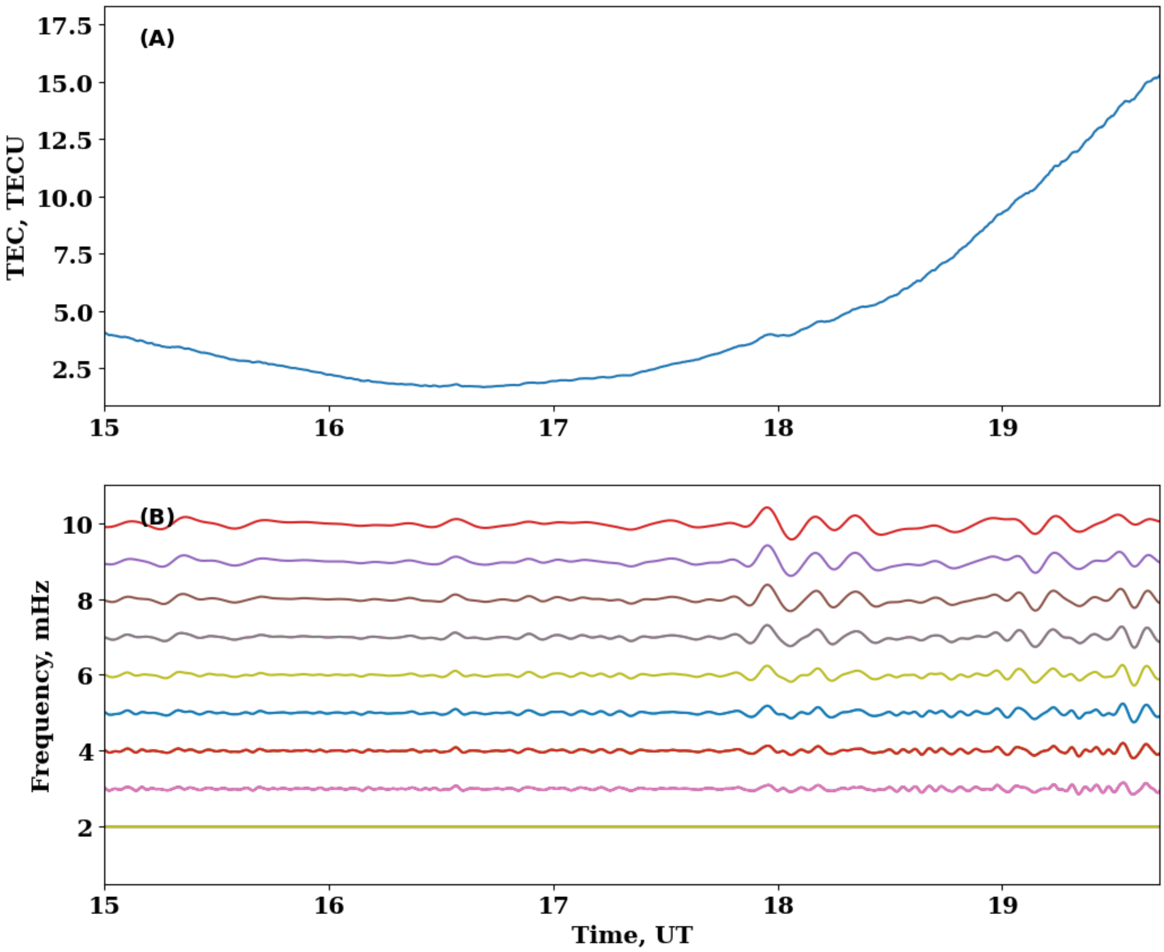


Panel (A) represents GNSS-TEC time series. Panel (B) is the decomposition of TEC of panel (A) at frequencies in the range of 1 - 10 mHz.

SOURCE: Author's production.

Figure A.2 - Satellite IPP trajectories (PRN=19) recorded by 600 GNSS receivers, for Ridgecrest- California EQs.

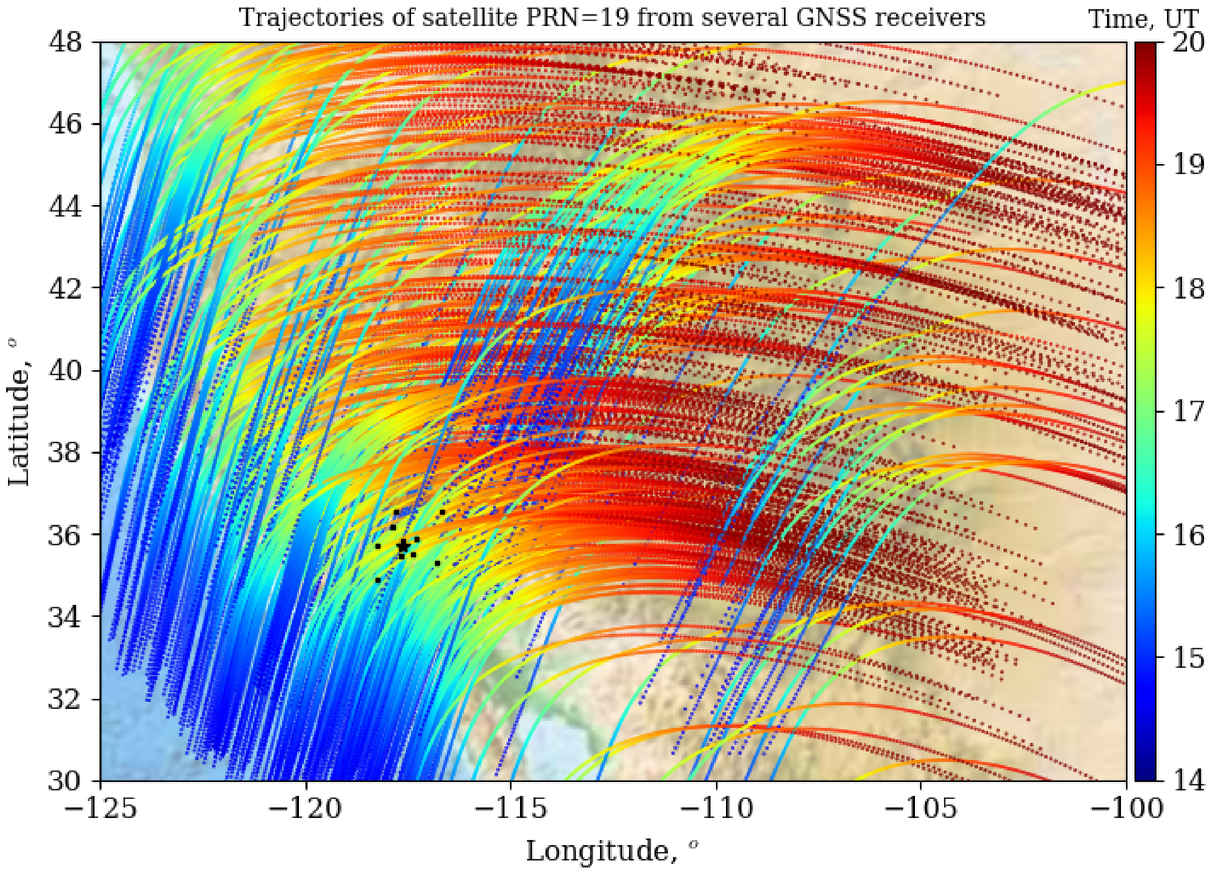


The color code represents an observation time between 14 and 20 UT. The star and squares represent earthquake epicenter and seismic stations, respectively.

SOURCE: Sanchez et al. (2022).

Figure A.3 - Hodogram of observed ΔTEC on the 4 July 2019 Ridgecrest Earthquakes.

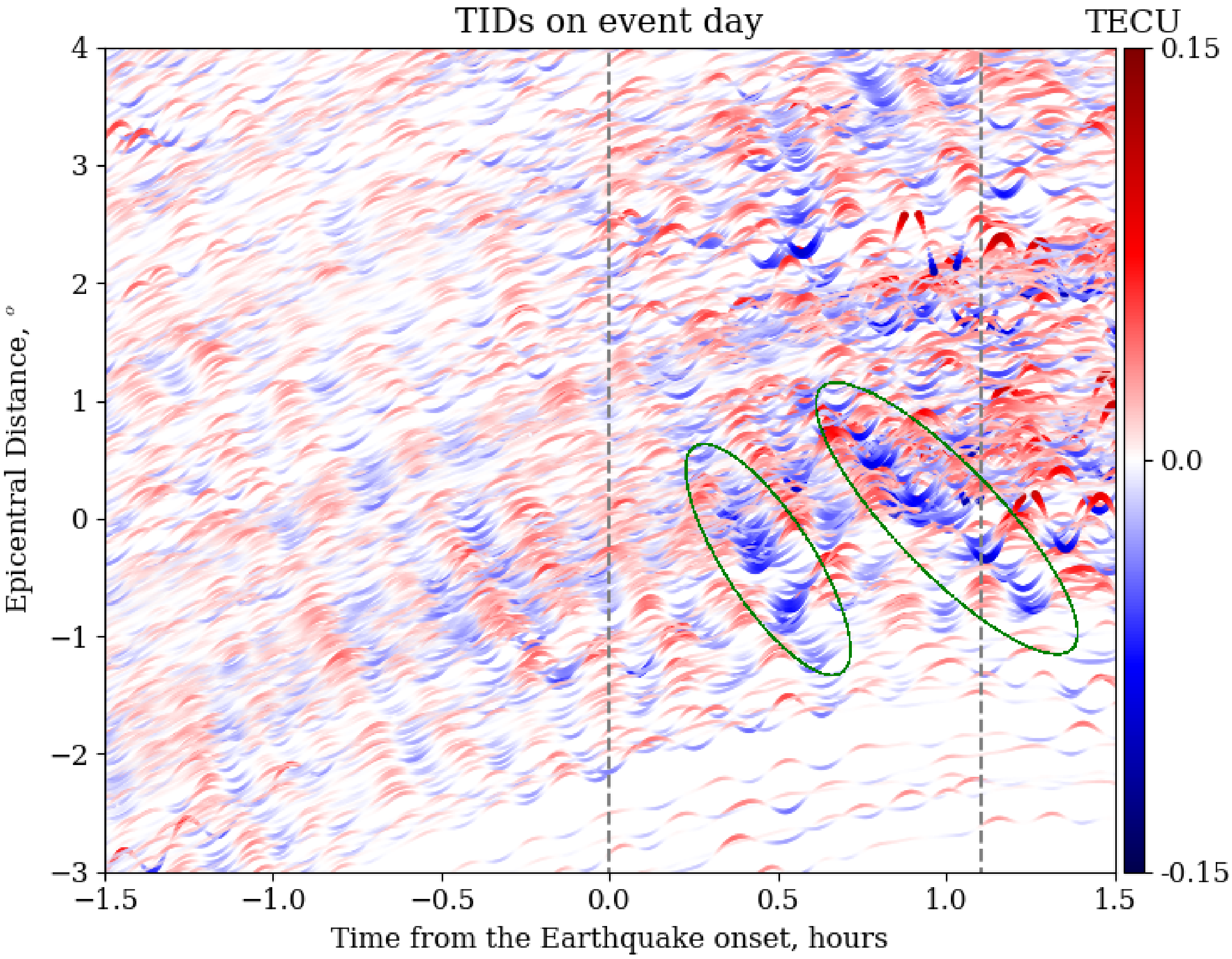


SOURCE: Sanchez et al. (2022).

Figure A.4 - Shakemap of the mainshock for Ridgecrest Earthquakes on the 4 July 2019.

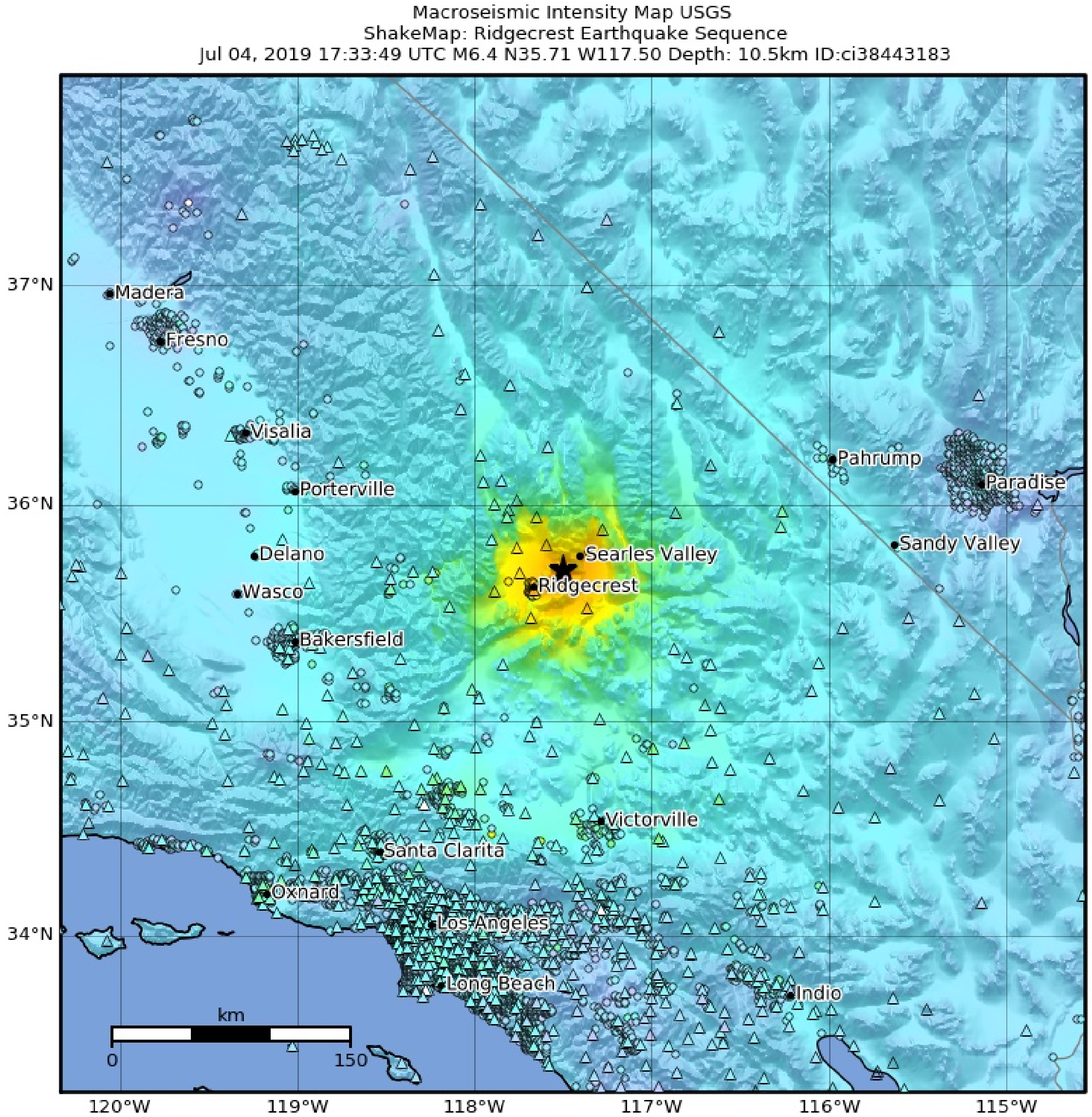


| SHAKING | Not felt | Weak | Light | Moderate | Strong | Very strong | Severe | Violent | Extreme |
|---|---|---|---|---|---|---|---|---|---|
| DAMAGE | None | None | None | Very light | Light | Moderate | Moderate/heavy | Heavy | Very heavy |
| PGA(%g) | <0.0464 | 0.297 | 2.76 | 6.2 | 11.5 | 21.5 | 40.1 | 74.7 | >139 |
| PGV(cm/s) | <0.0215 | 0.135 | 1.41 | 4.65 | 9.64 | 20 | 41.4 | 85.8 | >178 |
| INTENSITY | I | II-III | IV | V | VI | VII | VIII | IX | X+ |

Scale based on Worden et al. (2012) Version 1: Processed 2020-06-03T01:05:53Z

△ Seismic Instrument ○ Reported Intensity ★ Epicenter ▭ Rupture

The shakemap of the mainshock reveals that the seismic activity was confined in region between 117° –118° W and 35° –36° N.

SOURCE: United States Geological Survey (2019).

Figure A.5 - TEST1 cross-correlation analysis.

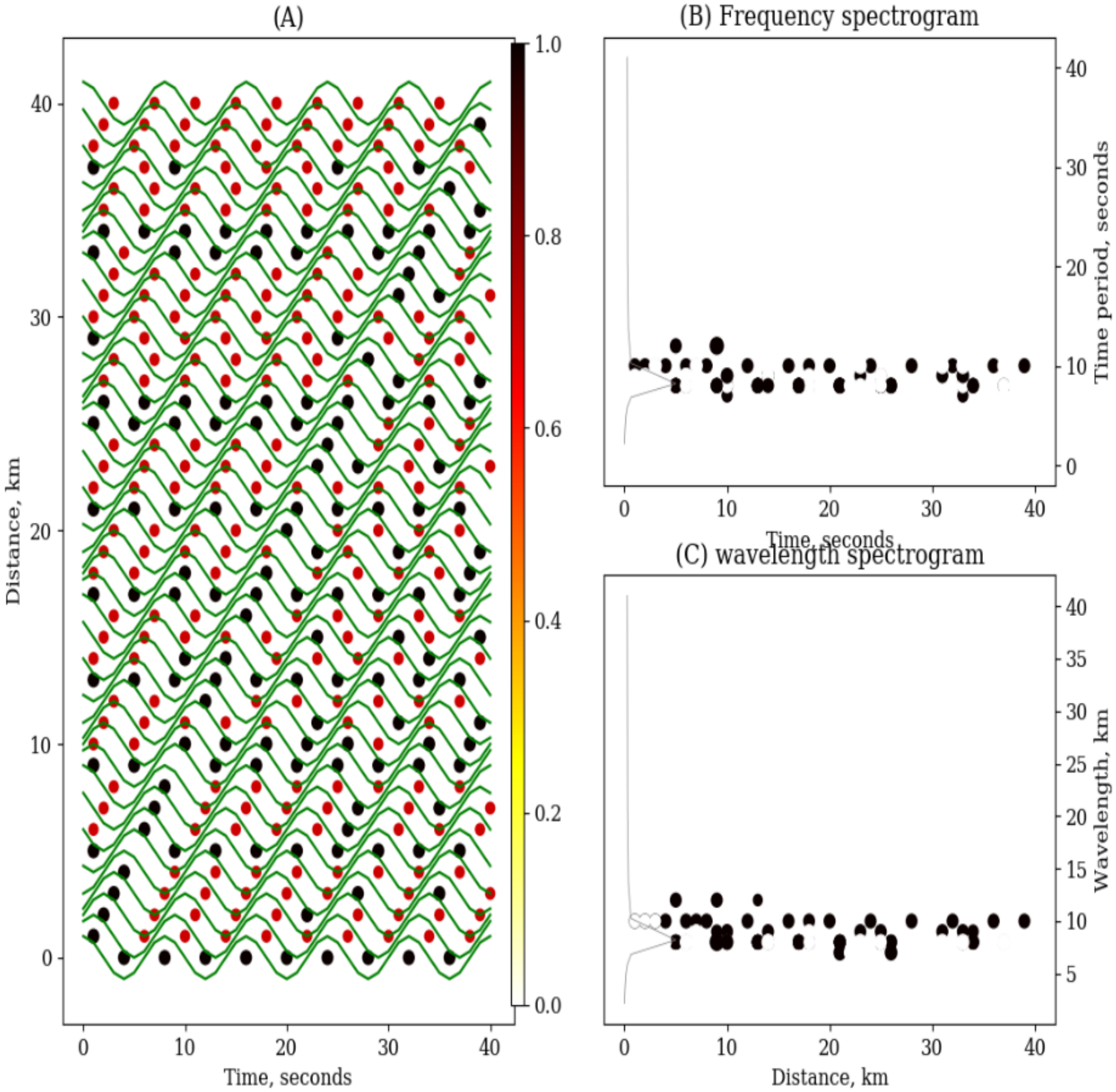


In (A), $\Delta$TEC and corresponding $C_{cf}(\mathrm{ymx}, \mathrm{tmx})$ are shown. In (B), Frequency spectrogram i.e., the distribution of $C_{cf}(\mathrm{ymx}, \mathrm{tmx})$ with time and $\tau$ is shown. In (C), Wavelength spectrogram i.e., the distribution of $C_{cf}(\mathrm{ymx}, \mathrm{tmx})$ with distance and $\lambda$ is shown. The gray curves in (B-C) represent the power spectral density of $\Delta$TEC obtained from the FFT analysis in time and space, respectively. In (B-C) respectively, $\Delta$TEC is averaged over distance and time are estimated.

SOURCE: Author's production.

Figure A.6 - TEST2 cross-correlation analysis.

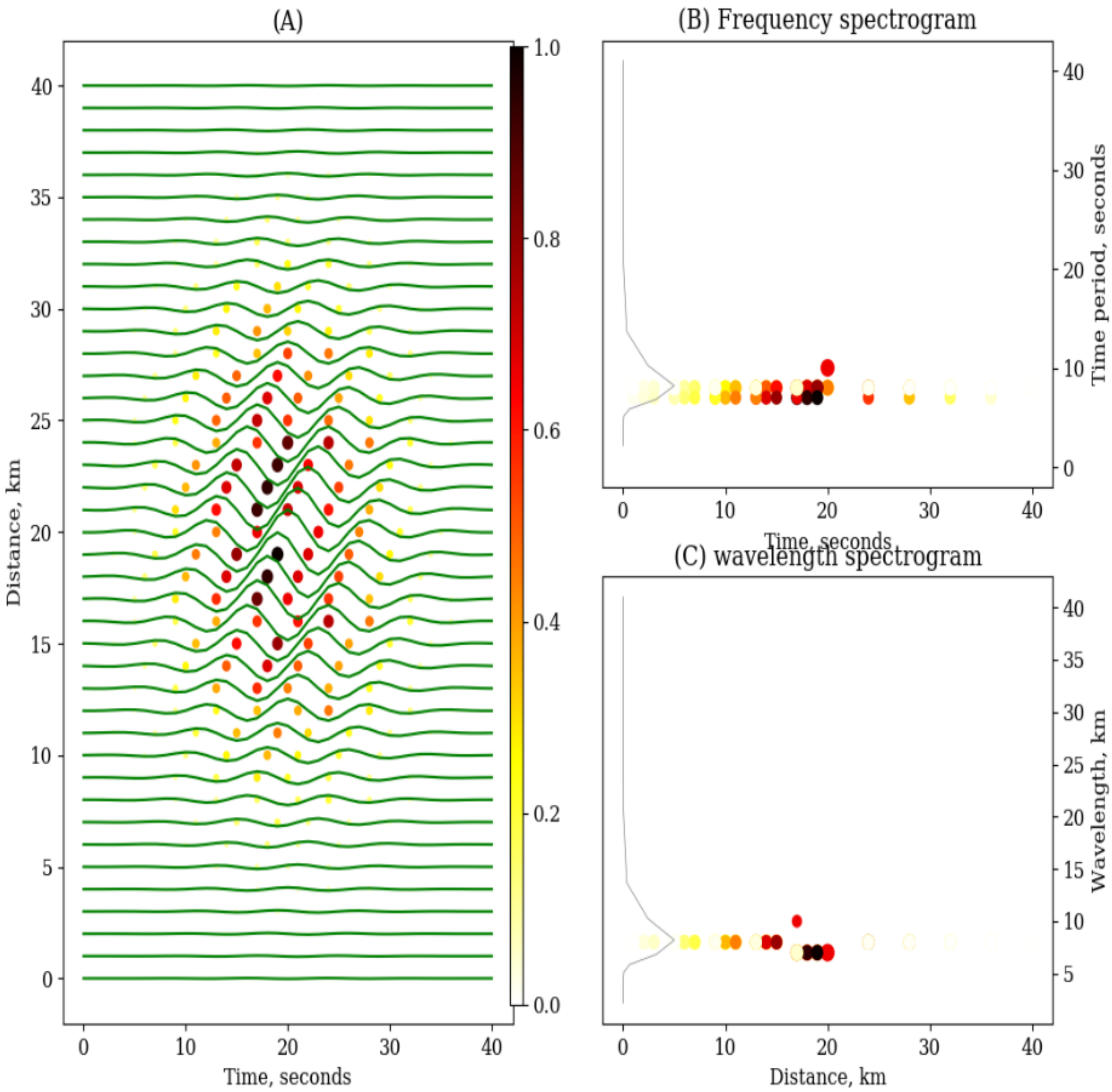


SOURCE: Author’s production.

Figure A.7 - TEST3 cross-correlation analysis.

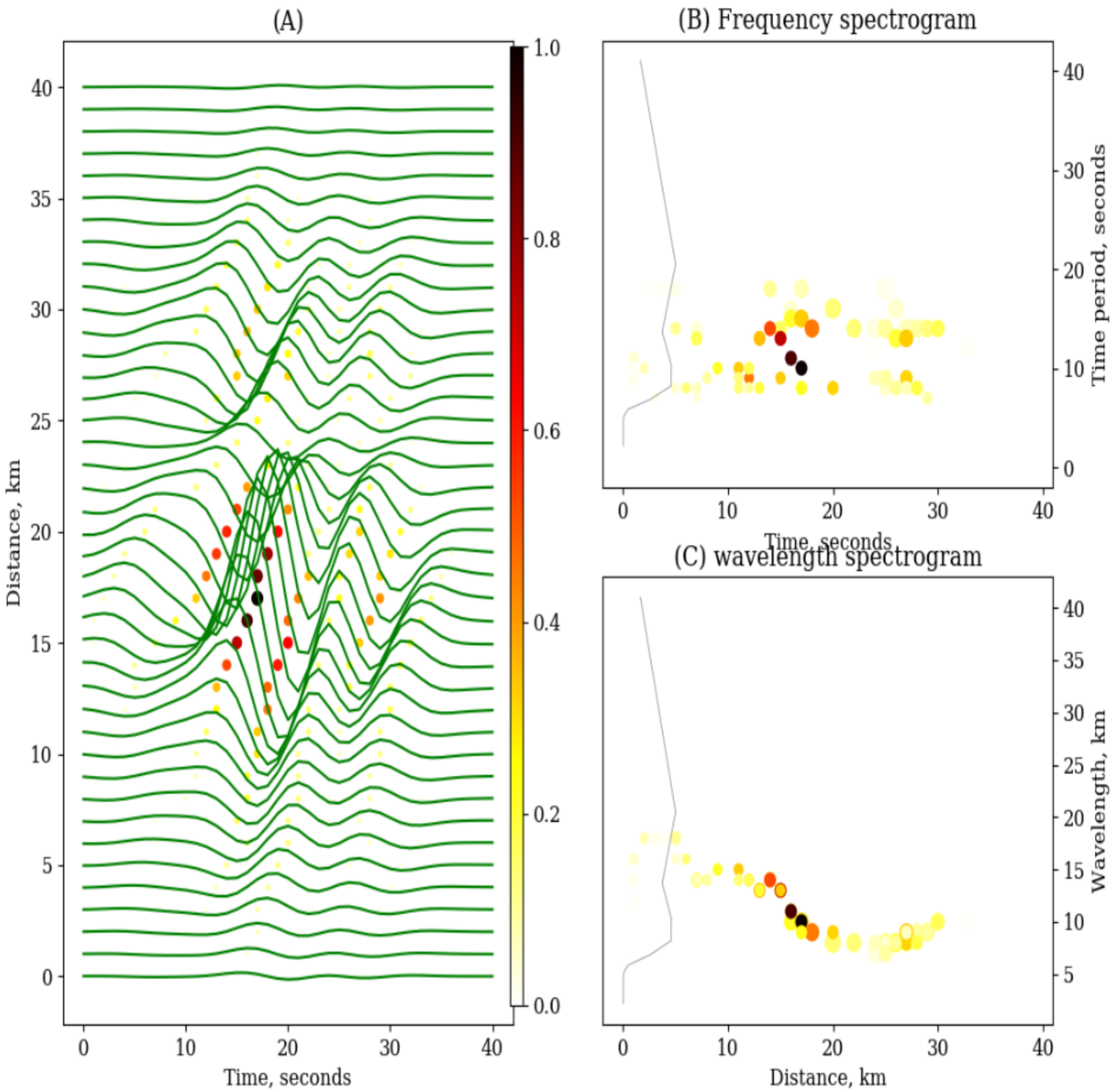


SOURCE: Author’s production.

Figure A.8 - The 2015 Illapel earthquake: Snapshots of the spatial distribution of ΔTEC at a frequency of 3.7 mHz.

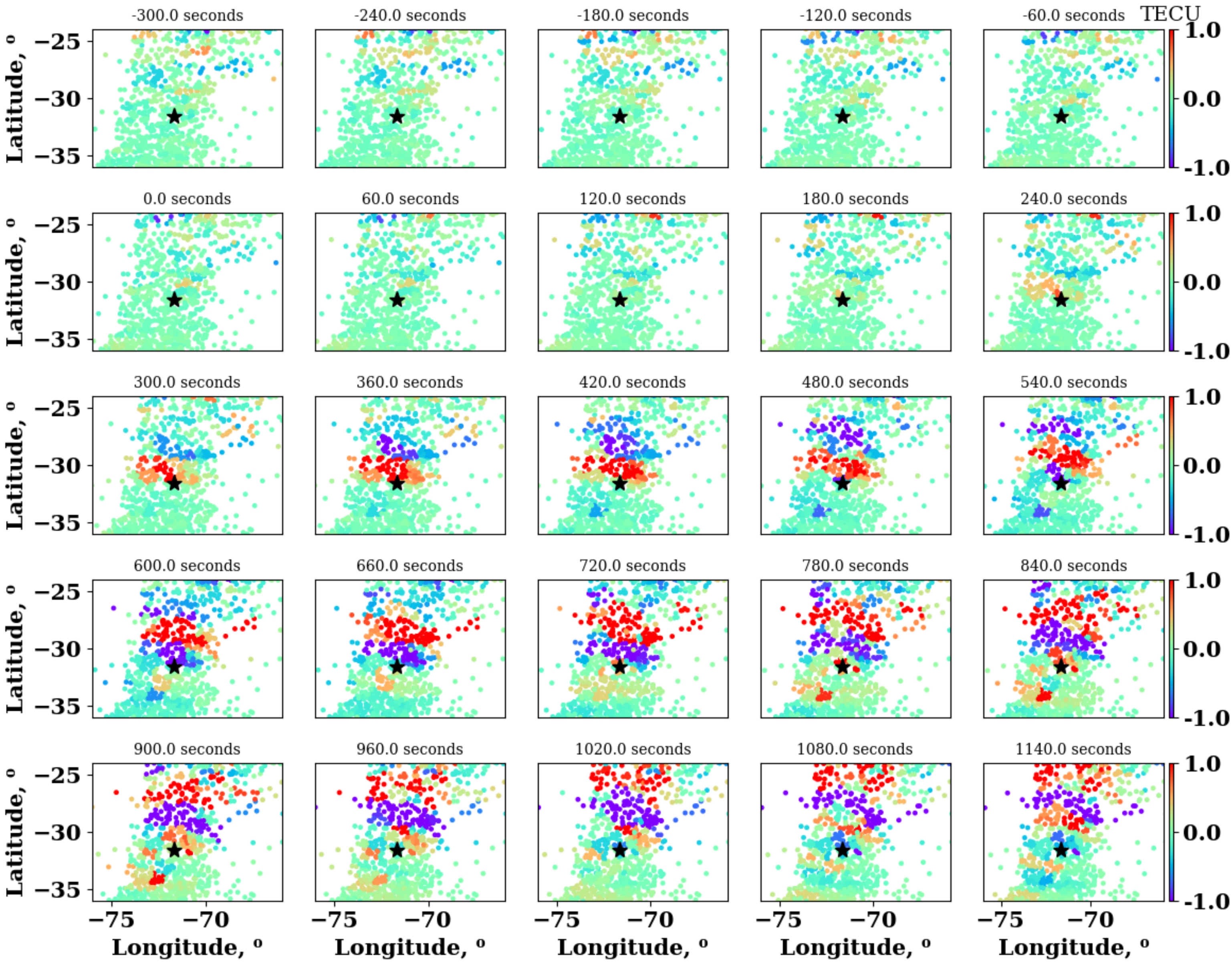


The top of each snapshot indicates $t_{detection}$ at a frequency of 3.7 mHz. $t_{detection} = 0$ corresponds to the time of peak seismic uplift at the frequency of 3.7 mHz.

SOURCE: Author's production.

Figure A.9 - The 2015 Illapel earthquake, $t_{detection}$-distance diagram for 4 different seismic stations (C004,VA01,VA03 and MT05).

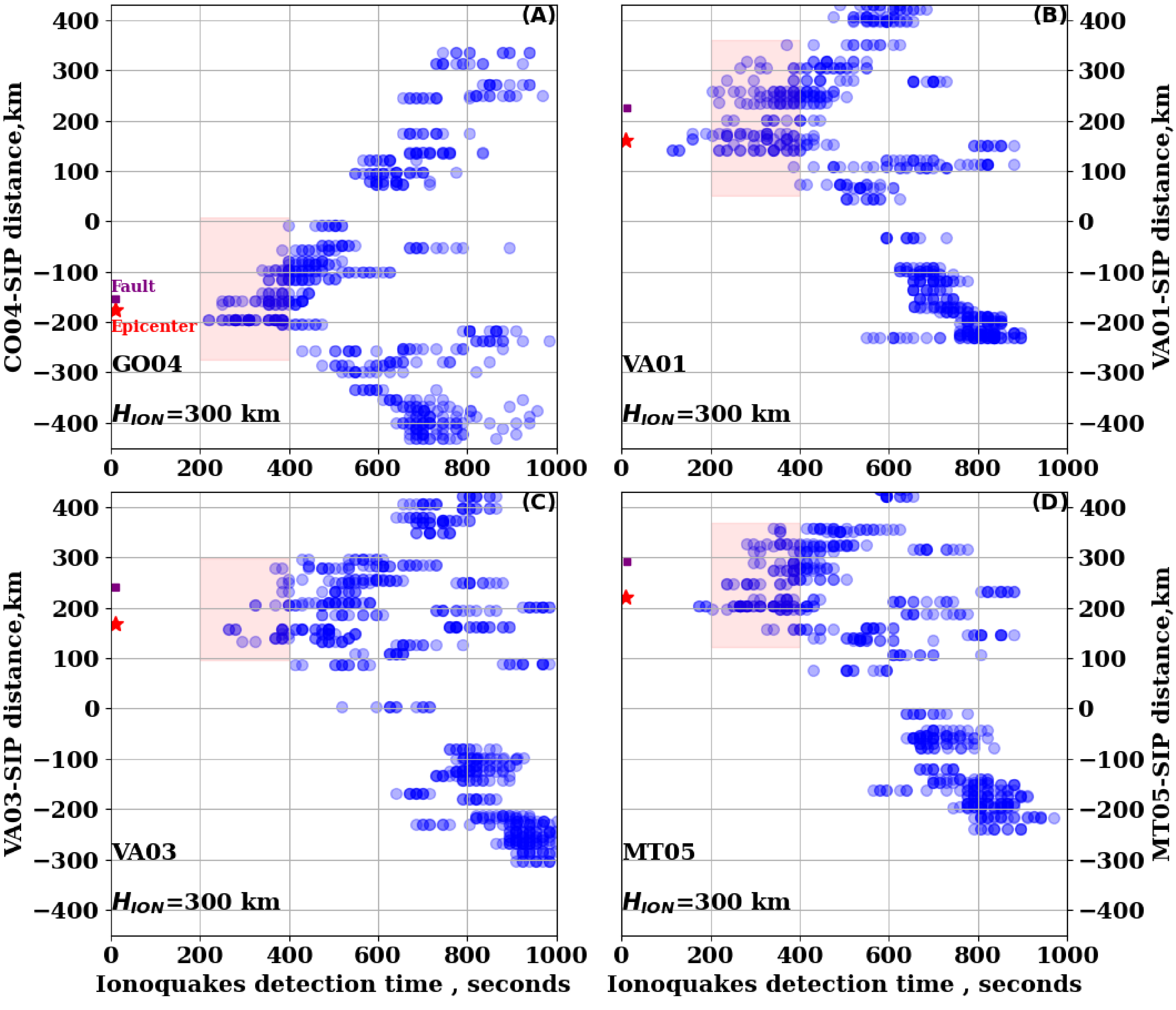


The frequency range is from 3.2 to 10 mHz. $t_{detection} = 0$ in the x-axis corresponds to the time of peak seismic uplift at each frequency in 3.2-10 mHz.

SOURCE: Author's production.

Figure A.10 - Limits of ionoquake propagation speed, The 2015 Illapel earthquake.

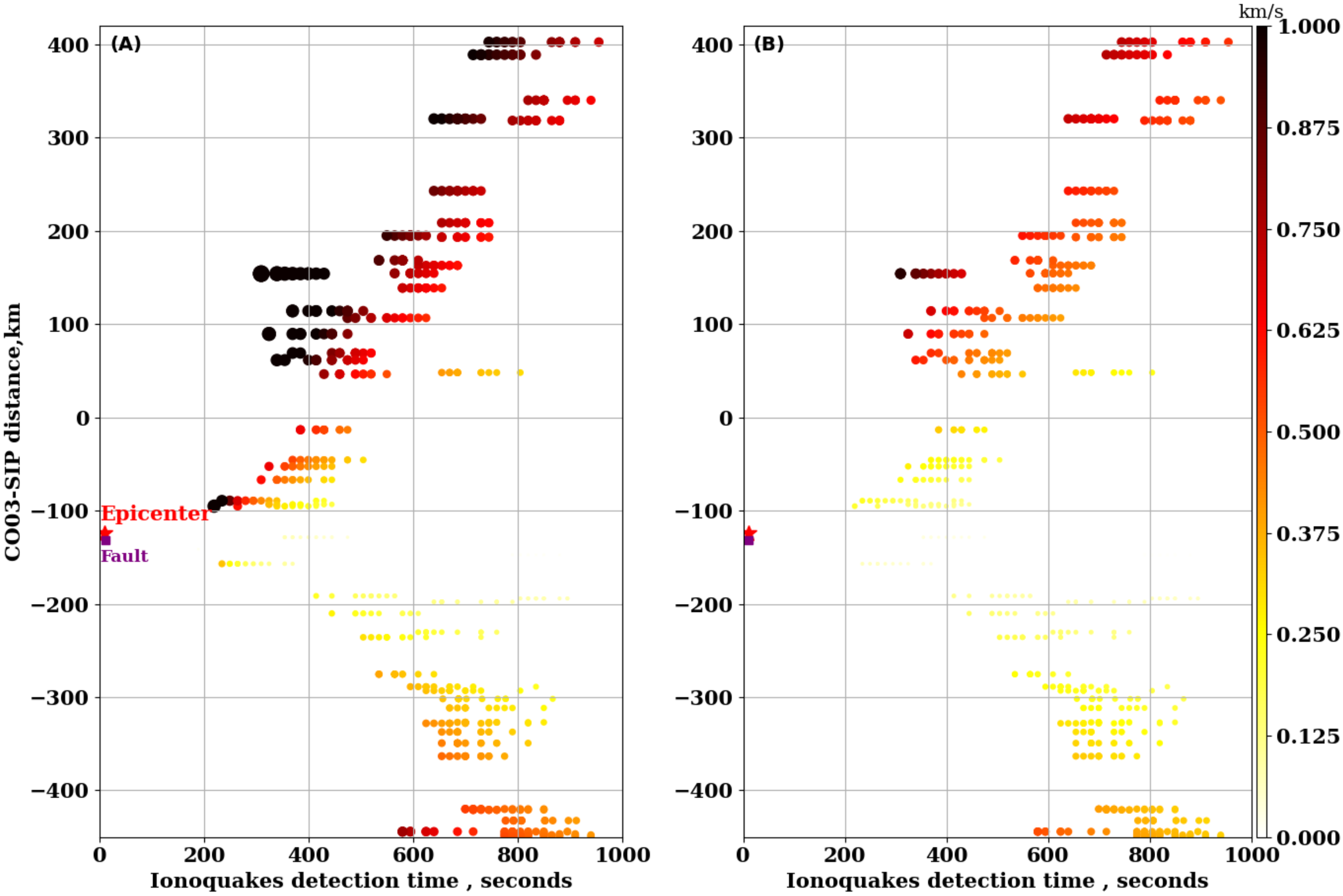


Panels (A-B) demonstrate respectively, upper and lower limits of ionoquake propagation speed, $(v1, v2)$ from definition (5.3) (shown in color) as a function of $\mathrm{t_{detection}}$-C003-SIP distance.

SOURCE: Author's production.

Figure A.11 - Application of TEST-1 for the 9 March 2011 Sanriku-oki earthquake with Mw7.3.

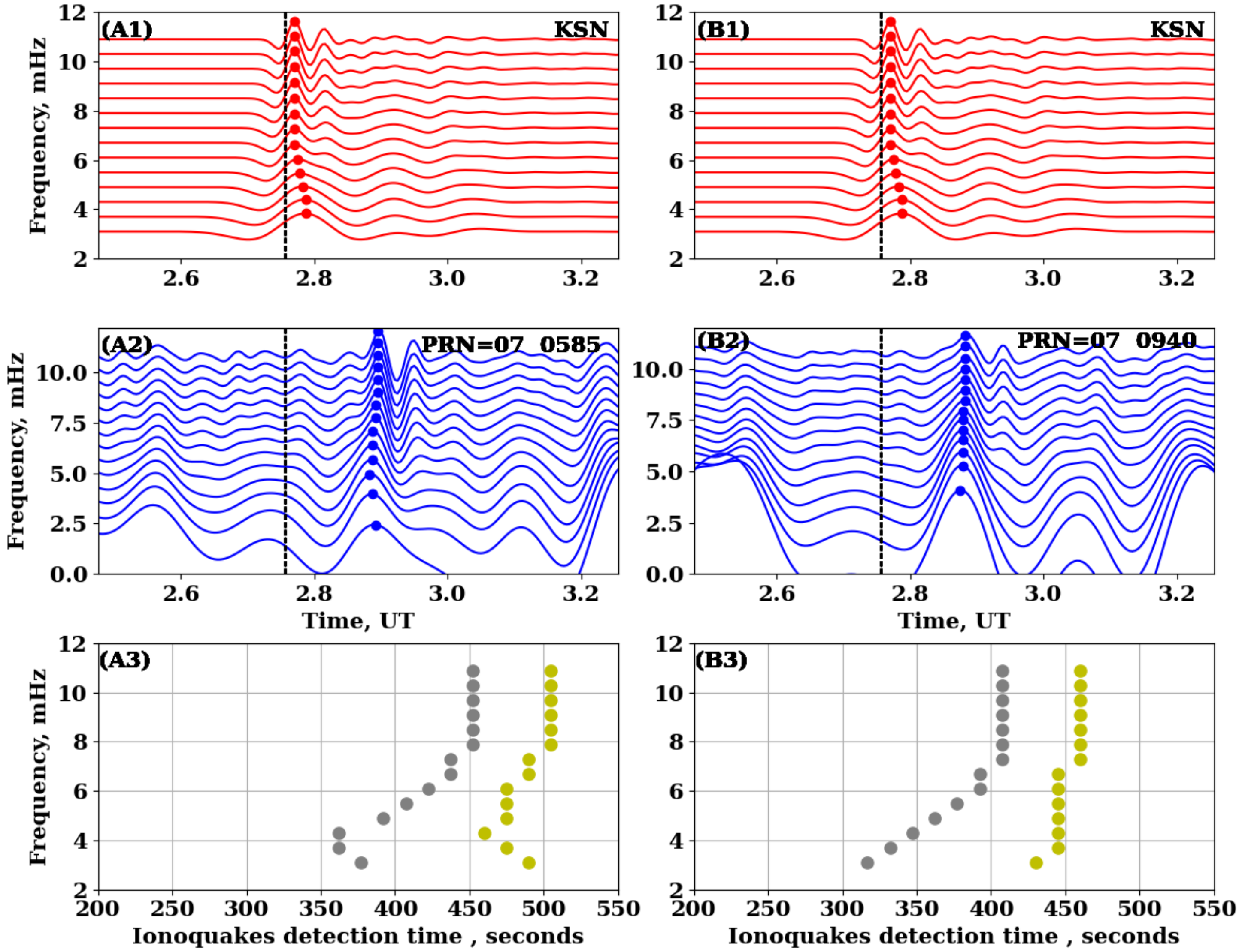


A) is generated for the GNSS station 0585 PRN 07 used by Astafyeva and Shults (2019). B) is generated for the GNSS station 0940 PRN 07 used by Thomas et al. (2018). The gray circles in panels A3-B3 represent the detection time of ionoquakes calculated using $t_{\text{detection}}$ in Equation (5.1), and the yellow circles are calculated using $t1_{\text{detection}} = t_{\text{TEC}} - 02:45:20$.

SOURCE: Author’s production.

Figure A.12 - $t1_{detection}$-distance diagram and $t_{detection}$, for the 9 March 2011 Sanriku-oki earthquake with Mw7.3.

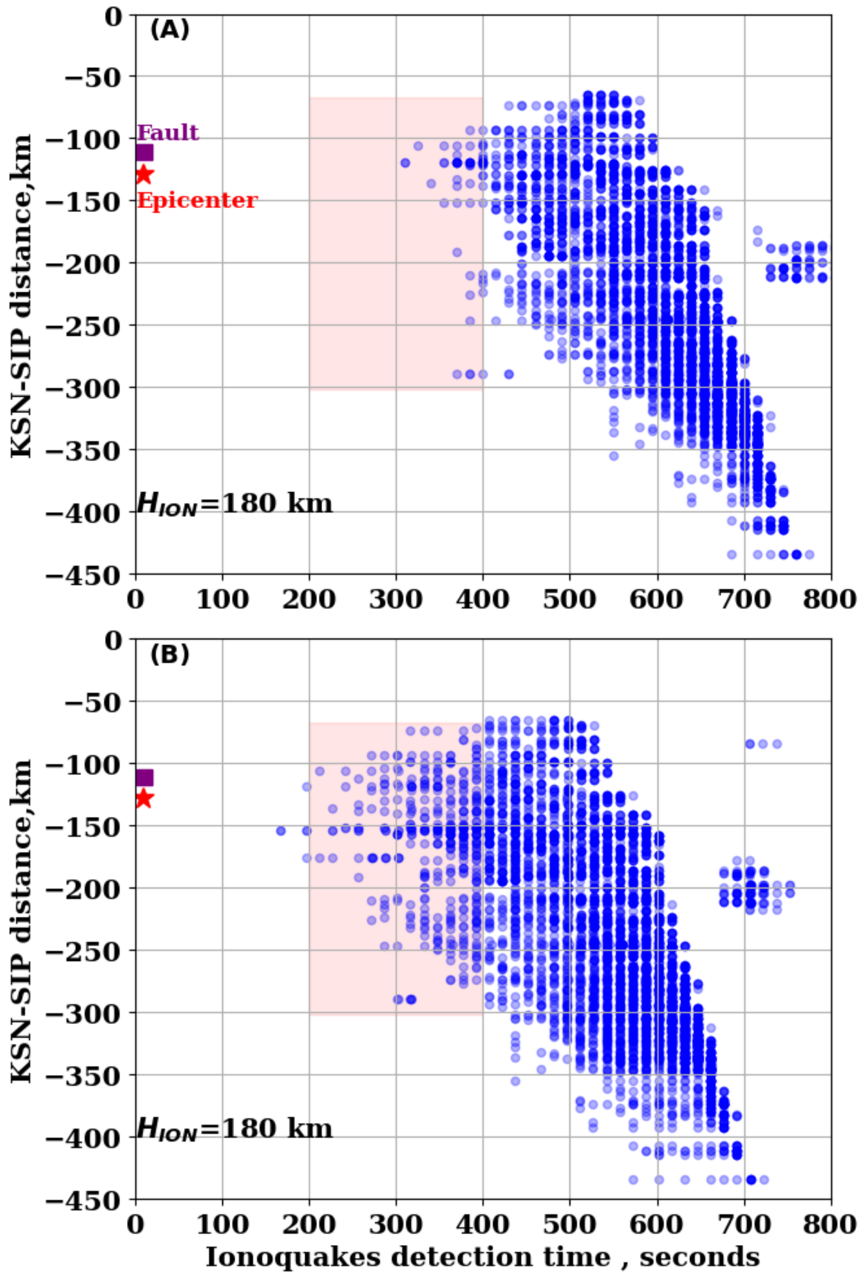


In (A), $t1_{detection}$-distance diagram and in (B) $t_{detection}$-distance diagram, for numerous SIPs and a frequency range of 3.2-10 mHz. In (A), 0 in the x-axis corresponds to the earthquake onset time. In (B), 0 in the x-axis corresponds to the time of peak seismic uplift at each frequency in 3.2-10 mHz.

SOURCE: Author’s production.

# APPENDIX B - ANALYTICAL SOLUTION OF NONLINEAR/DISSIPATIVE AGWS

## B.1 Analytical method of generation and propagation of AGWs

The wave Equation 2.5 of AGWs deduced by Kherani et al. (2016), can be written as follows, without considering the viscosity terms:

$$\frac{\partial^2 u}{\partial t^2} = c^2\nabla(\nabla.u) + (\gamma-1)\frac{\nabla p}{\rho}\nabla.u - \frac{\nabla p}{\rho}u.\nabla\log\rho + \frac{1}{\rho}\nabla(u.\nabla)p$$

In vertical ($z$)-horizontal ($h$) plane, waves equations are as follows:

$$\frac{\partial^2 u_z}{\partial t^2} = c^2\frac{\partial}{\partial z}(\nabla.u) + (\gamma-1)\nabla.u\frac{1}{\rho}\frac{\partial p}{\partial z} - u.\nabla\log\rho\frac{1}{\rho}\frac{\partial p}{\partial z} + \frac{1}{\rho}\frac{\partial}{\partial z}(u.\nabla)p$$

and

$$\frac{\partial^2 u_h}{\partial t^2} = c^2\frac{\partial}{\partial h}(\nabla.u) + (\gamma-1)\nabla.u\frac{1}{\rho}\frac{\partial p}{\partial h} - u.\nabla\log\rho\frac{1}{\rho}\frac{\partial p}{\partial h} + \frac{1}{\rho}\frac{\partial}{\partial h}(u.\nabla)p$$

Or

$$\frac{\partial^2 u_z}{\partial t^2} =$$

$$c^2\frac{\partial}{\partial z}\left(\frac{\partial u_z}{\partial z}+\frac{\partial u_h}{\partial h}\right)+(\gamma-1)\left(\frac{\partial u_z}{\partial z}+\frac{\partial u_h}{\partial h}\right)\frac{1}{\rho}\frac{\partial p}{\partial z}-\left(u_z\frac{\partial \rho}{\partial z}+u_h\frac{\partial \rho}{\partial h}\right)\frac{1}{\rho^2}\frac{\partial p}{\partial z}+\frac{1}{\rho}\frac{\partial}{\partial z}\left(u_z\frac{\partial p}{\partial z}+u_h\frac{\partial p}{\partial h}\right)$$

and

$$\frac{\partial^2 u_h}{\partial t^2} =$$

$$c^2\frac{\partial}{\partial h}\left(\frac{\partial u_z}{\partial z}+\frac{\partial u_h}{\partial h}\right)+(\gamma-1)\left(\frac{\partial u_z}{\partial z}+\frac{\partial u_h}{\partial h}\right)\frac{1}{\rho}\frac{\partial p}{\partial h}-\left(u_z\frac{\partial \rho}{\partial z}+u_h\frac{\partial \rho}{\partial h}\right)\frac{1}{\rho^2}\frac{\partial p}{\partial h}+\frac{1}{\rho}\frac{\partial}{\partial h}\left(u_z\frac{\partial p}{\partial z}+u_h\frac{\partial p}{\partial h}\right)$$

Considering ($\rho(z) \equiv$, $p \equiv p(z)$) which is a valid assumption for meso-scale primary AGWs:

$$\frac{\partial^2 u_z}{\partial t^2} = c^2\frac{\partial}{\partial z}\left(\frac{\partial u_z}{\partial z}+\frac{\partial u_h}{\partial h}\right)+(\gamma-1)\left(\frac{\partial u_z}{\partial z}+\frac{\partial u_h}{\partial h}\right)\frac{1}{\rho}\frac{\partial p}{\partial z}-\left(u_z\frac{\partial \rho}{\partial z}\right)\frac{1}{\rho^2}\frac{\partial p}{\partial z}+\frac{1}{\rho}\frac{\partial}{\partial z}\left(u_z\frac{\partial p}{\partial z}\right)$$

and

$$\frac{\partial^2 u_h}{\partial t^2} = c^2\frac{\partial}{\partial h}\left(\frac{\partial u_z}{\partial z}+\frac{\partial u_h}{\partial h}\right)+\frac{1}{\rho}\frac{\partial}{\partial h}\left(u_z\frac{\partial p}{\partial z}\right)$$

Or

$$\frac{\partial^2 u_z}{\partial t^2} = c^2\frac{\partial}{\partial z}\left(\frac{\partial u_z}{\partial z} + \frac{\partial u_h}{\partial h}\right) + (\gamma-1)\left(\frac{\partial u_z}{\partial z} + \frac{\partial u_h}{\partial h}\right)\frac{1}{\rho}\frac{\partial p}{\partial z} - \frac{1}{\rho}\left(\frac{1}{\rho}\frac{\partial \rho}{\partial z}\frac{\partial p}{\partial z} - \frac{\partial^2 p}{\partial z^2}\right)u_z + \frac{1}{\rho}\frac{\partial p}{\partial z}\frac{\partial u_z}{\partial z}$$

and

$$\frac{\partial^2 u_h}{\partial t^2} = c^2\frac{\partial}{\partial h}\left(\frac{\partial u_z}{\partial z} + \frac{\partial u_h}{\partial h}\right) + \frac{1}{\rho}\frac{\partial p}{\partial z}\frac{\partial u_z}{\partial h}$$

Or

$$\frac{\partial^2 u_z}{\partial t^2} = c^2\frac{\partial^2 u_z}{\partial z^2} + c^2\frac{\partial^2 u_h}{\partial z \partial h} + (\gamma-1)\zeta\frac{\partial u_z}{\partial z} + (\gamma-1)\zeta\frac{\partial u_h}{\partial h} + \frac{\partial \zeta}{\partial z}u_z + \zeta\frac{\partial u_z}{\partial z} \tag{B.1}$$

and

$$\frac{\partial^2 u_h}{\partial t^2} = c^2\frac{\partial^2 u_h}{\partial h^2} + c^2\frac{\partial^2 u_z}{\partial h \partial z} + \zeta\frac{\partial u_z}{\partial h} \tag{B.2}$$

Here

$$\zeta = \frac{1}{\rho}\frac{\partial p}{\partial z}, \qquad c^2 = \frac{\gamma p}{\rho} \tag{B.3}$$

### B.2 Non-linear wave solution + separation of variables

We consider solution of the following form:

$$u_z = u_z(z,t)e^{ik_z z + ik_h h}, \qquad u_h = u_h(z,t)e^{ik_z z + ik_h h} \tag{B.4}$$

Which will reduce derivatives into the following form:

$$\begin{aligned}
\frac{\partial}{\partial h} &\equiv ik_h \quad , \frac{\partial^2}{\partial h^2} \equiv -k_h^2 \\
\frac{\partial}{\partial z} &\equiv ik_z + \frac{\partial}{\partial z} \quad , \frac{\partial^2}{\partial z^2} \equiv -k_z^2 + \frac{\partial^2}{\partial z^2} + 2ik_z\frac{\partial}{\partial z} \\
\frac{\partial^2}{\partial z \partial h} &\equiv ik_h\frac{\partial}{\partial z} = ik_h\left(ik_z + \frac{\partial}{\partial z}\right) = -k_h k_z + ik_h\frac{\partial}{\partial z}
\end{aligned}$$

Therefore,

$$\frac{\partial^2 u_z}{\partial t^2} =$$

$$c^2\left(-k_z^2u_z+\frac{\partial^2 u_z}{\partial z^2}+2ik_z\frac{\partial u_z}{\partial z}\right)+c^2\left(-k_hk_zu_h+ik_h\frac{\partial u_h}{\partial z}\right)+\gamma\zeta\left(ik_zu_z+\frac{\partial u_z}{\partial z}\right)+(\gamma-1)\zeta ik_hu_h-\Omega_b^2u_z \tag{B.5}$$

and

$$\frac{\partial^2 u_h}{\partial t^2}=-c^2k_h^2u_h+c^2\left(-k_hk_zu_z+ik_h\frac{\partial u_z}{\partial z}\right)+\zeta ik_hu_z \tag{B.6}$$

Or

$$\frac{\partial^2 u_z}{\partial t^2}=$$

$$\frac{\mathrm{d}\zeta}{\mathrm{d}z}u_z-k_z^2c^2u_z+c^2\frac{\partial^2 u_z}{\partial z^2}+\gamma\zeta\frac{\partial u_z}{\partial z}-k_hk_zc^2u_h+i\left(2k_zc^2\frac{\partial u_z}{\partial z}+k_hc^2\frac{\partial u_h}{\partial z}+\gamma\zeta k_zu_z+(\gamma-1)\zeta k_hu_h\right) \tag{B.7}$$

and

$$\frac{\partial^2 u_h}{\partial t^2}=-k_h^2c^2u_h-k_hk_zc^2u_z+ik_h\left(c^2\frac{\partial u_z}{\partial z}+\zeta u_z\right) \tag{B.8}$$

Equations (B.7-B.8) are solved using method of separation of variable such that

$$u_z=u_{\mathrm{zs}}(z)u_{\mathrm{zt}}(t),\quad u_h=u_{\mathrm{hs}}(z)u_{\mathrm{ht}}(t) \tag{B.9}$$

## B.3 Governing non-local equations in space

Imaginary parts of (B.7-B.8) is written as follows:

$$c^2\frac{\partial u_z}{\partial z}+\zeta u_z=0\quad\Rightarrow\frac{\partial u_z}{\partial z}=-\frac{\zeta}{c^2}u_z\Rightarrow u_{\mathrm{zt}}\frac{\mathrm{d}u_{\mathrm{zs}}}{\mathrm{dz}}=-\frac{\zeta}{c^2}u_{\mathrm{zt}}u_{\mathrm{zs}}$$
$$\Rightarrow\frac{\mathrm{d}u_{\mathrm{zs}}}{\mathrm{dz}}=-k_0u_{\mathrm{zs}} \tag{B.10}$$

and

$$2k_zc^2\frac{\partial u_z}{\partial z}+k_hc^2\frac{\partial u_h}{\partial z}+\gamma\zeta k_zu_z+(\gamma-1)\zeta k_hu_h=0,\quad\frac{\partial u_h}{\partial z}+(\gamma-1)\frac{\zeta}{c^2}u_h+(\gamma-2)\frac{\zeta}{c^2}\frac{k_z}{k_h}u_z=0$$
$$\Rightarrow\frac{\mathrm{d}u_{\mathrm{hs}}}{\mathrm{dz}}+(\gamma-1)k_0u_{\mathrm{hs}}+(\gamma-2)k_0\frac{k_z}{k_h}\frac{u_{\mathrm{zt}}}{u_{\mathrm{ht}}}u_{\mathrm{zs}}=0 \tag{B.11}$$

$$\frac{\partial u_h}{\partial z}+(\gamma-1)k_0u_h+(\gamma-2)\frac{k_z}{k_h}k_0u_z=0$$

$$\frac{\partial^2 u_h}{\partial z^2} + (\gamma-1)^2 k_0^2 u_h + \gamma(\gamma-2)\frac{k_z}{k_h}k_0^2 u_z = 0$$

### B.3.1 Analytical non-local solutions

Solution of Equation (B.10) is written as follows:

$$u_{\mathrm{zs}} = u_{\mathrm{zs}}(z_o)e^{-\mu}, \quad \mu = \int k_0 \mathrm{dz}, \quad k_0 = \frac{\zeta}{c^2} \equiv \frac{d\mu}{dz} \tag{B.12}$$

Solution of Equation (B.11) is written as follows:

$$\Rightarrow u_{\mathrm{hs}} = u_{\mathrm{hs}}(z_o)e^{-(\gamma-1)\mu}\left[1 + \frac{\gamma-2}{u_{\mathrm{hs}}(z_o)}\frac{k_z u_{\mathrm{zt}}}{k_h u_{\mathrm{ht}}}\int k_0 u_{\mathrm{zs}} e^{(\gamma-1)\mu}\mathrm{dz}\right]$$

$$\Rightarrow u_{\mathrm{hs}} = u_{\mathrm{hs}}(z_o)e^{-(\gamma-1)\mu}\left[1 + (\gamma-2)\frac{u_{\mathrm{zs}}(z_o)}{u_{\mathrm{hs}}(z_o)}\frac{k_z u_{\mathrm{zt}}}{k_h u_{\mathrm{ht}}}\int \frac{d\mu}{\mathrm{dz}} e^{(\gamma-2)\mu}\mathrm{dz}\right]$$

$$\Rightarrow u_{\mathrm{hs}} = u_{\mathrm{hs}}(z_o)e^{-(\gamma-1)\mu}\left[1 + \frac{u_{\mathrm{zs}}(z_o)}{u_{\mathrm{hs}}(z_o)}\frac{k_z u_{\mathrm{zt}}}{k_h u_{\mathrm{ht}}} e^{(\gamma-2)\mu}\right]$$

$$\Rightarrow u_{\mathrm{hs}} = u_{\mathrm{hs}}(z_o)e^{-(\gamma-1)\mu} + \frac{k_z u_{\mathrm{zt}}}{k_h u_{\mathrm{ht}}} u_{\mathrm{zs}} \tag{B.13}$$

## B.4 Governing non-linear equations in time

Real parts of Equations (B.7-B.8) are written as follows:

$$\frac{\partial^2 u_z}{\partial t^2} = \frac{\mathrm{d}\zeta}{\mathrm{dz}}u_z - k_z^2 c^2 u_z + c^2\frac{\partial^2 u_z}{\partial z^2} + \gamma\zeta\frac{\partial u_z}{\partial z} - k_h k_z c^2 u_h$$

and

$$\frac{\partial^2 u_h}{\partial t^2} = -k_h^2 c^2 u_h - k_h k_z c^2 u_z$$

Or

$$\frac{d^2 u_{\mathrm{zt}}}{\mathrm{dt}^2} = \frac{\mathrm{d}\zeta}{\mathrm{dz}}u_{\mathrm{zt}} - k_z^2 c^2 u_{\mathrm{zt}} + c^2\frac{u_{\mathrm{zt}}}{u_{\mathrm{zs}}}\frac{d^2 u_{\mathrm{zs}}}{\mathrm{dz}^2} + \gamma\zeta\frac{u_{\mathrm{zt}}}{u_{\mathrm{zs}}}\frac{\mathrm{d}u_{\mathrm{zs}}}{\mathrm{dz}} - k_h k_z c^2\frac{u_{\mathrm{hs}}}{u_{\mathrm{zs}}}u_{\mathrm{ht}}$$

and

$$\frac{d^2 u_{\mathrm{ht}}}{\mathrm{dt}^2} = -k_h^2 c^2 u_{\mathrm{ht}} - k_h k_z c^2\frac{u_{\mathrm{zs}}}{u_{\mathrm{hs}}}u_{\mathrm{zt}}$$

From Equation (B.10) we have,

$$\frac{\mathrm{du_{zs}}}{\mathrm{dz}} = -k_0 u_{\mathrm{zs}}, \quad \frac{d^2 u_{\mathrm{zs}}}{\mathrm{dz}^2} = k_0^2 u_{\mathrm{zs}} - \frac{dk_0}{\mathrm{dz}} u_{\mathrm{zs}}$$

Therefore,

$$\frac{d^2 u_{\mathrm{zt}}}{\mathrm{dt}^2} = \frac{\mathrm{d}\zeta}{\mathrm{dz}} u_{\mathrm{zt}} - k_z^2 c^2 u_{\mathrm{zt}} + c^2 \left( k_0^2 - \frac{dk_0}{\mathrm{dz}} \right) u_{\mathrm{zt}} - \gamma \zeta k_0 u_{\mathrm{zt}} - k_h k_z c^2 \frac{u_{\mathrm{hs}}}{u_{\mathrm{zs}}} u_{\mathrm{ht}}$$

Or

$$\frac{d^2 u_{\mathrm{zt}}}{\mathrm{dt}^2} = \frac{\mathrm{d}\zeta}{\mathrm{dz}} u_{\mathrm{zt}} - k_z^2 c^2 u_{\mathrm{zt}} - c^2 \left( (\gamma - 1) k_0^2 + \frac{dk_0}{\mathrm{dz}} \right) u_{\mathrm{zt}} - k_h k_z c^2 \frac{u_{\mathrm{hs}}}{u_{\mathrm{zs}}} u_{\mathrm{ht}}$$

Or

$$\frac{d^2 u_{\mathrm{zt}}}{\mathrm{dt}^2} = -\Omega^2 u_{\mathrm{zt}} - k_h k_z c^2 \frac{u_{\mathrm{hs}}}{u_{\mathrm{zs}}} u_{\mathrm{ht}}, \quad \frac{d^2 u_{\mathrm{ht}}}{\mathrm{dt}^2} = -\Omega_h^2 u_{\mathrm{ht}} - k_h k_z c^2 \frac{u_{\mathrm{zs}}}{u_{\mathrm{hs}}} u_{\mathrm{zt}} \tag{B.14}$$

where

$$\Omega^2 = -\frac{\mathrm{d}\zeta}{\mathrm{dz}} + k_z^2 c^2 + \left[ (\gamma - 1) k_0^2 + \frac{dk_0}{\mathrm{dz}} \right] c^2 \equiv k_z^2 c^2 + \Omega_b^2, \quad \Omega_h^2 = k_h^2 c^2 \tag{B.15}$$

and

$$\Omega_b^2 = -\frac{\mathrm{d}\zeta}{\mathrm{dz}} + \left[ (\gamma - 1) k_0^2 + \frac{dk_0}{\mathrm{dz}} \right] c^2 \equiv \left[ (\gamma - 1) k_0^2 - \frac{k_o}{c^2} \frac{dc^2}{\mathrm{dz}} \right] c^2 \tag{B.16}$$

Here $\Omega_b$ is the non-isothermal Brunt-Vaisala frequency ( (HOLTON, 1897; KELLEY, 2009), Equation 6.7a).

### B.4.1 Analytical linear solution in time from method of characteristics

Equation (B.14) represent system of coupled oscillator with constant coefficient (in time) and can be resolved with method of characteristics with following solution:

$$u_{\mathrm{zt}} = \alpha e^{\eta t}, \quad u_{\mathrm{ht}} = \beta e^{\eta t} \tag{B.17}$$

This substitution reduces Equation (B.14) to following algebric equation:

$$\alpha(\eta^2 + \Omega_0^2 - i\omega_0^2) + k_h k_z c^2 \frac{u_{\mathrm{hs}}}{u_{\mathrm{zs}}} \beta = 0, \quad \beta(\eta^2 + \Omega_h^2) + k_h k_z c^2 \frac{u_{\mathrm{zs}}}{u_{\mathrm{hs}}} \alpha = 0$$

Therefore, considering $\alpha = u_{\text{zt}}(t_o)$, two equations can be solved for two unknowns $(\beta, \eta)$ as follows:

$$\beta = -\frac{(\eta^2 + \Omega_0^2)}{k_h k_z c^2} \frac{u_{\text{zs}}}{u_{\text{hs}}} u_{\text{zt}}(t_o), \quad (\eta^2 + \Omega_h^2)(\eta^2 + \Omega_0^2) = k_h^2 k_z^2 c^4$$

Or

$$\eta^4 + (\Omega_0^2 + \Omega_h^2)\eta^2 + \Omega_h^2\Omega_0^2 - k_h^2 k_z^2 c^4 = 0$$

Or

$$\eta^4 + \Omega_0^2\eta^2 + k_h^2 c^2 \Omega_b^2 = 0$$

Or

$$\omega^4 - \Omega_0^2\omega^2 + k_h^2 c^2 \Omega_b^2 = 0, \quad \eta = \pm i\omega$$

which is the dispersion relation of AGWs (Equation 6.3 of Kelley, 2009).

Let

$$\Omega^2 = \Omega_0^2 + \Omega_h^2$$

then

$$\omega^2 = \frac{\Omega^2 \pm [\Omega^4 - 4k_h^2 c^2 \Omega_b^2]^{1/2}}{2} \tag{B.18}$$

and therefore solutions of Equation (B.14) are following:

$$u_{\text{zt}} = u_{\text{zt}}(t_0)e^{\pm i\omega t}, \quad u_{\text{ht}} = -\frac{(\Omega_0^2 - \omega^2)}{k_h k_z c^2} \frac{u_{\text{zs}}}{u_{\text{hs}}} u_{\text{zt}}(t_o)e^{\pm i\omega t} \tag{B.19}$$

and thus using Equations ( B.9, B.12-B.13), general solution of AGWs is as follows:

$$u_z = u_{\text{zt}}(t_0)u_{\text{zs}}(z_o)e^{\pm i\omega t + ik_z z + ik_h h - \mu},$$

$$u_h = -\frac{(\Omega_0^2 - \omega^2)}{k_h k_z c^2} u_{\text{zt}}(t_o)u_{\text{zs}}(z_o)e^{\pm i\omega t + ik_z z + ik_h h - \mu} \equiv -\frac{(\Omega^2 - \omega^2 - \Omega_h^2)}{k_h k_z c^2} u_{\text{zt}} \tag{B.20}$$

where

$$\mu = \int k_0 \text{dz}, \quad k_0 = \frac{\zeta}{c^2}, \quad \zeta = \frac{1}{\rho}\frac{dp}{dz}, \quad c^2 = \frac{\gamma p}{\rho}$$

$$\omega^2 = \frac{\Omega^2 \pm [\Omega^4 - 4k_h^2 c^2 \Omega_b^2]^{1/2}}{2} \tag{B.21}$$

$$\Omega^2 = \Omega_b^2 + k_z^2 c^2 + k_y^2 c^2, \quad \Omega_b^2 = \left[(\gamma - 1)k_0^2 - \frac{k_o}{c^2}\frac{dc^2}{\mathrm{dz}}\right] c^2, \quad \Omega_h^2 = k_h^2 c^2$$

$$\Omega = k_z c \left(1 + \frac{\Omega_b^2}{k_z^2 c^2}\right)^{1/2} \equiv \alpha k_z c, \quad \alpha = \left(1 + \frac{c_g^2}{c^2}\right)^{1/2}, \quad c_g = \frac{\Omega_b}{k_z} \tag{B.22}$$

since $c_g \ll c$ in the atmosphere,

$$\Omega \approx k_z c$$

### B.4.2 Vertical group velocity and phase velocity of linear AGWs

From Equation (B.21), vertical group velocity of AGWs is obtained as follows:

$$\frac{d\omega}{dk_z} = \frac{1}{4\omega}\left[2k_z c^2 \pm \frac{1}{2}\frac{2\Omega^2 2k_z c^2}{[\Omega^4 - 4k_h^2 c^2 \Omega_b^2]^{1/2}}\right] = \frac{k_z c^2}{2\omega}\left[1 + \frac{\Omega^2}{2\omega^2 - \Omega^2}\right] \equiv \frac{\omega}{k_z}\frac{k_z^2 c^2}{2\omega^2 - \Omega^2} \tag{B.23}$$

$$\frac{\omega}{k_z} = \pm\frac{\Omega}{k_z}\left[\frac{1}{2} \pm \frac{1}{2}\left(1 - 4\frac{\Omega_b^2}{\Omega^2}\frac{\Omega_h^2}{\Omega^2}\right)^{1/2}\right]^{1/2}$$

### B.4.3 Linear arrival time

$$\tau_{\text{phase}}(z) = \int_{z_o}^{z}\left(\frac{\omega}{k_z}\right)^{-1}\mathrm{dz} \quad \text{e} \quad \tau_{\text{group}}(z) = \int_{z_o}^{z}\left(\frac{d\omega}{dk_z}\right)^{-1}\mathrm{dz}$$

## B.5 Non-linear analytical solution

Equation (B.14) represent system of coupled oscillator with time-varying coefficient and can be resolved with following for of non-linear solution:

$$u_{\text{zt}} = \alpha e^{(\eta t)^n}, \quad u_{\text{ht}} = \beta e^{(\eta t)^n} \tag{B.24}$$

Here $n \geqslant 1$ is the non-linear parameter and for linear case ($n = 1$), above solution reduces to solution the Equation (B.17)

$$(\eta t)^n = \tau, \quad n\eta(\eta t)^{n-1}\mathrm{dt} = d\tau \quad \Rightarrow n\eta\tau^{1-1/n} = \frac{d\tau}{dt}$$

$$\frac{d}{dt} \equiv \frac{d\tau}{dt}\frac{d}{d\tau} = n\eta\tau^{1-1/n}\frac{d}{d\tau}$$

$$\frac{d^2}{dt^2} = n^2\eta^2\tau^{1-1/n}\frac{d}{d\tau}\left(\tau^{1-1/n}\frac{d}{d\tau}\right) = n^2\eta^2\tau^{2-2/n}\left[\frac{d^2}{d\tau^2} + \left(1 - \frac{1}{n}\right)\frac{1}{\tau}\frac{d}{d\tau}\right]$$

Thus (B.24) becomes

$$\alpha n^2\eta^2\tau^{2-2/n}\left[\frac{d^2}{d\tau^2} + \left(1 - \frac{1}{n}\right)\frac{1}{\tau}\frac{d}{d\tau}\right]e^\tau + \alpha\Omega^2 e^\tau + \beta k_h k_z c^2\frac{u_{\mathrm{hs}}}{u_{\mathrm{zs}}}e^\tau = 0$$

Or

$$\alpha n^2\eta^2\tau^{2-2/n}\left[1 + \frac{n-1}{n\tau}\right] + \alpha\Omega^2 + \beta k_h k_z c^2\frac{u_{\mathrm{hs}}}{u_{\mathrm{zs}}} = 0$$

Or

$$\alpha n^2\eta^2(\eta t)^{2n-2}\left[1 + \frac{n-1}{n\tau}\right] + \alpha\Omega^2 + \beta k_h k_z c^2\frac{u_{\mathrm{hs}}}{u_{\mathrm{zs}}} = 0$$

Or

$$\alpha(\sigma^2 + \Omega^2) + k_h k_z c^2\frac{u_{\mathrm{hs}}}{u_{\mathrm{zs}}}\beta = 0, \quad \beta(\sigma^2 + \Omega_h^2) + k_h k_z c^2\frac{u_{\mathrm{zs}}}{u_{\mathrm{hs}}}\alpha = 0$$

where

$$\sigma^2 = n^2\tau^2 t^{-2}\left[1 + \frac{n-1}{n\tau}\right] \equiv n^2 t^{-2}\tau^2 + n(n-1)t^{-2}\tau$$

$$\sigma^4 + \Omega^2\sigma^2 + k_h^2 c^2\Omega_b^2 = 0$$

Or

$$2\sigma^2 = -\Omega^2 \pm (\Omega^4 - 4\Omega_h^2\Omega_b^2)^{1/2}$$

Or

$$n^2\tau^2 + n(n-1)\tau = \frac{t^2}{2}[-\Omega^2 \pm (\Omega^4 - 4\Omega_h^2\Omega_b^2)^{1/2}] \equiv -t^2\omega^2$$

Here $\omega^2$ is given by (B.21).

Or

$$n^2\tau^2 + n(n-1)\tau + \omega^2 t^2 = 0$$

Or

$$\tau = \frac{-n(n-1) \pm [n^2(n-1)^2 - 4n^2\omega^2 t^2]^{1/2}}{2n^2}$$

Or

$$\tau = \omega t \frac{1}{n}\left[-\frac{(n-1)}{2\omega t} \pm \left(-1+\frac{(n-1)^2}{4\omega^2 t^2}\right)^{1/2}\right] \equiv \omega t \frac{1}{n}\left[-\frac{(n-1)}{2\omega t} \pm i\left(1-\frac{(n-1)^2}{4\omega^2 t^2}\right)^{1/2}\right] \tag{B.25}$$

It is evident that for $n = 1$, $\tau = i\omega t$ and solution reduces to linear solution given by Equation (B.19).

Therefore, from Equation (B.24), analytical solution of non-linear AGWs is written as follows:

$$u_{\rm zt} = u_{\rm zt}(t_0) u_{\rm nl} \exp(\pm i\omega_{\rm nl} t), \quad u_{\rm ht} = -\frac{(\Omega_B^2 - \omega^2)}{k_h k_z c^2}\frac{u_{\rm zs}}{u_{\rm hs}} u_{\rm zt}(t_o) u_{\rm nl} \exp(\pm i\omega_{\rm nl} t) \tag{B.26}$$

Here

$$u_{\rm nl}(t) = \exp\left(-\frac{n-1}{2n}\right), \quad \omega_{\rm nl} = \frac{1}{n}\left(1-\frac{(n-1)^2}{8\omega^2 t^2}\right)\omega \equiv \frac{\alpha_{\rm nl}}{n}\omega \tag{B.27}$$

and thus using Equations (B.9, B.12 - B.13), general solution of non-linear/non-local AGWs is written as follows:

$$u_z = u_{\rm zt}(t_0) u_{\rm zs}(z_o) u_{\rm nl} \exp(\pm i\omega_{\rm nl} t - \mu), \quad u_h = -\frac{(\Omega^2 - \omega^2)}{k_h k_z c^2} u_{\rm zt} \tag{B.28}$$

here

$$\mu = \int k_0 \mathrm{dz}, \quad k_0 = \frac{\zeta}{c^2}, \quad \zeta = \frac{1}{\rho}\frac{dp}{dz}, \quad c^2 = \frac{\gamma p}{\rho}$$

$$\omega^2 = \frac{\Omega^2 \pm [\Omega^4 - 4\Omega_h^2 \Omega_b^2]^{1/2}}{2}$$

$$\Omega^2 = \Omega_b^2 + k_z^2 c^2, \quad \Omega_b^2 = \left[(\gamma-1)k_0^2 - \frac{k_o}{c^2}\frac{dc^2}{\mathrm{dz}}\right]c^2, \quad \Omega_h^2 = k_h^2 c^2$$

$$\Omega = k_z c\left(1+\frac{\Omega_b^2}{k_z^2 c^2}\right)^{1/2} \equiv \alpha k_z c, \quad \alpha = \left(1+\frac{c_g^2}{c^2}\right)^{1/2}, \quad c_g = \frac{\Omega_b}{k_z}$$

### B.5.1 Non-linear limit

In the above analysis, non-linearity is determined by parameter $n \geqslant 1$. As n increases, non-linearity increases but waves maintain the oscillations i.e. till $\omega_{nl}$ remains real and this condition will set the upper limit of $n$ such that

$$\frac{n-1}{z\omega t} < 1 \Rightarrow 1 \leq n < +2\omega t$$

For $n > 1 + 2\omega t$, wave cease to exist and becomes solitons since $\omega_{nl}$ becomes imaginary. Since $\omega t \sim< k_o ct \sim k_O/\Omega_b$ for wave to propagate a scale height to experience buoyancy,

$$0 \leq \omega t \leq \frac{k_o ct}{\Omega_b} = \frac{1}{(\gamma-1)^{1/2}} \equiv \left(\frac{3}{2}\right)^{1/2} \approx 1 \Rightarrow 1 \leq n \leq 3$$

### B.5.2 Group and phase velocities of Non-linear AGWs

$$\frac{\omega_{\rm nl}}{k_z} = \frac{\alpha_{\rm nl}}{n}\frac{\omega}{k_z}, \quad \frac{d\omega_{\rm nl}}{dk_z} = \frac{\alpha_{\rm nl}}{n}\frac{d\omega}{dk_z}$$

### B.5.3 Non-linear arrival time

$$\tau^{\rm nl}_{\rm phase}(z) = \int_{z_o}^{z}\left(\frac{\omega_{\rm nl}}{k_z}\right)^{-1} {\rm dz} \quad {\rm e} \quad \tau^{\rm nl}_{\rm group}(z) = \int_{z_o}^{z}\left(\frac{d\omega_{\rm nl}}{dk_z}\right)^{-1} {\rm dz}$$

## B.6 Viscous dissipation effects

Governing wave equations of dissipative AGWs are as follows (KHERANI et al., 2016):

$$\frac{\partial^2 u}{\partial t^2} - \frac{\partial}{\partial t}(\nu\nabla^2 u) = c^2\nabla(\nabla.u) + (\gamma-1)\frac{\nabla p}{\rho}\nabla.u - \frac{\nabla p}{\rho}u.\nabla\log\rho + \frac{1}{\rho}\nabla(u.\nabla)p$$

where

$$\nu = \frac{\mu}{\rho}$$

$(\nu, u)$ are dynamic and kinematic viscocities.

In vertical ($z$)-horizontal ($h$) plane, waves equations are as follows:

$$\frac{\partial^2 u_z}{\partial t^2} - \frac{\partial}{\partial t}(\nu \nabla^2 u_z) =$$

$$c^2 \frac{\partial}{\partial z}\left(\frac{\partial u_z}{\partial z} + \frac{\partial u_h}{\partial h}\right) + (\gamma - 1)\left(\frac{\partial u_z}{\partial z} + \frac{\partial u_h}{\partial h}\right)\frac{1}{\rho}\frac{\partial p}{\partial z} - \left(u_z \frac{\partial \rho}{\partial z} + u_h \frac{\partial \rho}{\partial h}\right)\frac{1}{\rho^2}\frac{\partial p}{\partial z} + \frac{1}{\rho}\frac{\partial}{\partial z}\left(u_z \frac{\partial p}{\partial z} + u_h \frac{\partial p}{\partial h}\right)$$

and

$$\frac{\partial^2 u_h}{\partial t^2} - \frac{\partial}{\partial t}(\nu \nabla^2 u_h) =$$

$$c^2 \frac{\partial}{\partial h}\left(\frac{\partial u_z}{\partial z} + \frac{\partial u_h}{\partial h}\right) + (\gamma - 1)\left(\frac{\partial u_z}{\partial z} + \frac{\partial u_h}{\partial h}\right)\frac{1}{\rho}\frac{\partial p}{\partial h} - \left(u_z \frac{\partial \rho}{\partial z} + u_h \frac{\partial \rho}{\partial h}\right)\frac{1}{\rho^2}\frac{\partial p}{\partial h} + \frac{1}{\rho}\frac{\partial}{\partial h}\left(u_z \frac{\partial p}{\partial z} + u_h \frac{\partial p}{\partial h}\right)$$

Or

$$\frac{\partial^2 u_z}{\partial t^2} - \frac{\partial}{\partial t}\left[\nu\left(-k_z^2 + \frac{\partial^2}{\partial z^2} + 2ik_z \frac{\partial}{\partial z}\right)\right] u_z =$$

$$c^2\left(-k_z^2 u_z + \frac{\partial^2 u_z}{\partial z^2} + 2ik_z \frac{\partial u_z}{\partial z}\right) + c^2\left(-k_h k_z u_h + ik_h \frac{\partial u_h}{\partial z}\right) + \gamma\zeta\left(ik_z u_z + \frac{\partial u_z}{\partial z}\right) + (\gamma - 1)\zeta ik_h u_h - \Omega_b^2 u_z \tag{B.29}$$

$$\frac{\partial^2 u_h}{\partial t^2} - \frac{\partial}{\partial t}\left[\nu\left(-k_z^2 + \frac{\partial^2}{\partial z^2} + 2ik_z \frac{\partial}{\partial z}\right)\right] u_h = -c^2 k_h^2 u_h + c^2\left(-k_h k_z u_z + ik_h \frac{\partial u_z}{\partial z}\right) + \zeta ik_h u_z \tag{B.30}$$

Here viscous terms are written as follows:

$$\frac{\partial}{\partial t}\left[\nu\left(-k_z^2 u_z + \frac{\partial u_z^2}{\partial z^2} + 2ik_z \frac{\partial u_z}{\partial z}\right)\right] = \frac{\partial}{\partial t}\left[\nu\left(-k_z^2 u_z - 2ik_z k_0 u_z + k_0^2 u_z - \frac{dk_0}{\mathrm{dz}} u_z\right)\right]$$

Or

$$\frac{\partial}{\partial t}\left[\nu\left(-k_z^2 u_z + \frac{\partial u_z^2}{\partial z^2} + 2ik_z \frac{\partial u_z}{\partial z}\right)\right] = \nu\left(-k_z^2 - 2ik_z k_0 + k_0^2 - \frac{dk_0}{\mathrm{dz}}\right)\frac{\partial u_z}{\partial t} \equiv \nu_z^{\mathrm{col}} \frac{\partial u_z}{\partial t}$$

and

$$\frac{\partial}{\partial t}\left[\nu\left(-k_z^2 u_h + \frac{\partial^2 u_h}{\partial z^2} + 2ik_z \frac{\partial u_h}{\partial z}\right)\right] =$$

$$\nu(-k^2+(\gamma-1)^2k_o^2-2ik_z(\gamma-1)k_o)\frac{\partial u_h}{\partial t}+\nu\left(\gamma(\gamma-2)\frac{k_z}{k_h}k_o^2-2ik_z(\gamma-2\frac{k_z}{k_h})\right)\frac{\partial u_z}{\partial t}\equiv\nu_h^{\mathrm{col}}\frac{\partial u_h}{\partial t}$$

$$\frac{\partial}{\partial t}\left[\nu\left(-k_z^2u_h+\frac{\partial^2u_h}{\partial z^2}+2ik_z\frac{\partial u_h}{\partial z}\right)\right]=$$

$$\frac{\partial}{\partial t}\left[\nu\left(-k^2u_h+(\gamma-1)^2k_0^2u_h+\gamma(\gamma-2)\frac{k_z}{k_h}k_0^2u_z-2ik_z(\gamma-1)k_0u_h-2ik_z(\gamma-2)\frac{k_z}{k_h}k_0u_z\right)\right]$$

Or

$$\frac{\partial}{\partial t}\left[\nu\left(-k_z^2u_h+\frac{\partial^2u_h}{\partial z^2}+2ik_z\frac{\partial u_h}{\partial z}\right)\right]=$$

$$\nu\left(-k^2+(\gamma-1)^2k_0^2+-2ik_z(\gamma-1)k_0\right)\frac{\partial u_h}{\partial t}+\nu\left(\gamma(\gamma-2)\frac{k_z}{k_h}k_0^2-2ik_z(\gamma-2)\frac{k_z}{k_h}k_0\right)\frac{\partial u_z}{\partial t}$$

and therefore Equation (B.14) for coupled oscillators becomes coupled damped oscillator of the following form:

$$\frac{d^2u_{\mathrm{zt}}}{\mathrm{dt}^2}-\nu_h^{\mathrm{col}}\frac{\mathrm{du_{zt}}}{\mathrm{dt}}=-\Omega^2u_{\mathrm{zt}}-k_hk_zc^2\frac{u_{\mathrm{hs}}}{u_{\mathrm{zs}}}u_{\mathrm{ht}},\quad\frac{d^2u_{\mathrm{ht}}}{\mathrm{dt}^2}-\nu_h^{\mathrm{col}}\frac{\mathrm{du_{ht}}}{\mathrm{dt}}=-\Omega_h^2u_{\mathrm{ht}}-k_hk_zc^2\frac{u_{\mathrm{zs}}}{u_{\mathrm{hs}}}u_{\mathrm{zt}}\tag{B.31}$$

where

$$\nu_z^{\mathrm{col}}=\nu\left(-k_z^2-2ik_zk_0+k_0^2-\frac{dk_0}{\mathrm{dz}}\right)\quad\mathrm{e}\quad\nu_h^{\mathrm{col}}=\nu\left(\gamma(\gamma-2)\frac{k_z}{k_h}k_o^2-2ik_z(\gamma-2\frac{k_z}{k_h})\right)$$

Non-linear solution of the form Equation (B.24) leads to the following algebric equations:

$$\alpha n^2\eta^2\tau^{2-2/n}\left[1+\frac{n-1}{n\tau}\right]-\nu_z^{\mathrm{col}}\alpha n\eta\tau^{1-1/n}+\alpha\Omega^2+\beta k_hk_zc^2\frac{u_{\mathrm{hs}}}{u_{\mathrm{zs}}}=0$$
$$\alpha n^2\eta^2(\eta t)^{2n-2}\left[1+\frac{n-1}{n\tau}\right]-\nu_z^{\mathrm{col}}\alpha n\eta(\eta t)^{n-1}+\alpha\Omega^2+\beta k_hk_zc^2\frac{u_{\mathrm{hs}}}{u_{\mathrm{zs}}}=0$$

$$\alpha(\sigma^2 + \Omega^2) + k_h k_z c^2 \frac{u_{\rm hs}}{u_{\rm zs}} \beta = 0, \quad \beta(\sigma^2 + \Omega_h^2) + k_h k_z c^2 \frac{u_{\rm zs}}{u_{\rm hs}} \alpha = 0$$

where

$$\sigma^2 = n^2\tau^2 t^{-2}\left[1 + \frac{n-1}{n\tau}\right] \equiv n^2 t^{-2}\tau^2 + n(n-1)t^{-2}\tau, \quad \Omega_\nu^2 = \Omega_z^2 - n\nu_z^{\rm col} t^{-1}\tau, \quad \Omega_{h\nu}^2 = \Omega_h^2 - n\nu_h^{\rm col} t^{-1}\tau$$

$$\sigma^4 + \Omega_\nu^2 \sigma^2 + \Omega_{h\nu}^2 \Omega_b^2 = 0$$

$$2\sigma^2 = -\Omega^2 \pm (\Omega^4 - 4\Omega_{h\nu}^2\Omega_b^2)^{1/2} \approx n\nu_z^{\rm col} t^{-1}\tau - \omega^2$$

where collision effects inside the quotient is neglected for simplicity

$$n^2\tau^2 + n(n-1)\tau - n\nu_z^{\rm col} t\tau = -t^2\omega^2$$

$$n^2\tau^2 + [n(n-1) - n\nu_z^{\rm col} t]\tau = -t^2\omega^2$$

$$\tau = \frac{-n(n-1) + n\nu_z^{\rm col} t\tau \pm [n^2[(n-1) - \nu_z^{\rm col} t]^2 - 4n^2\omega^2 t^2]^{1/2}}{2n^2}$$

Neglecting viscous terms inside the quotient,

$$\tau \approx \frac{1}{2n}\nu_z^{col} t + \tau_o$$

where $\tau_0$ is given by (B.25). Therefore, from (B.24), analytical solution of dissipative non-linear AGWs is written as follows:

$$u_{\rm zt} = u_{\rm zt}(t_0) u_{\rm nl} \exp(\pm i\omega_{\rm nl} + \frac{1}{2n}\nu_z^{col})t, \quad u_{\rm ht} = -\frac{(\Omega_B^2 - \omega^2)}{k_h k_z c^2}\frac{u_{\rm zs}}{u_{\rm hs}} u_{\rm zt}(t_o) u_{\rm nl} \exp(\pm i\omega_{\rm nl} + \frac{1}{2n}\nu_z^{col})t \tag{B.32}$$

Here

$$u_{\mathrm{nl}}(t) = \exp\left(-\frac{n-1}{2n}\right), \quad \omega_{\mathrm{nl}} = \frac{1}{n}\left(1 - \frac{(n-1)^2}{4\omega^2 t^2}\right)\omega \equiv \frac{\alpha_{\mathrm{nl}}}{n}\omega, \quad \nu_z^{\mathrm{col}} = \nu\left(-k_z^2 - 2ik_z k_0 + k_0^2 - \frac{dk_0}{\mathrm{dz}}\right) \tag{B.33}$$

and from Equation (B.28), general solution of non-linear/non-local AGWs is written as fol- lows:

$$u_{\mathrm{z}} = u_{\mathrm{zt}}(t_0)u_{\mathrm{zt}}(z_0)u_{\mathrm{nl}} \exp\left(\pm i\omega_{\mathrm{nl}} t + \frac{1}{2n}\nu_z^{col} t + ik_z z - \mu\right), u_h = -\frac{(\Omega^2 - \omega^2)}{k_h K_z c^2} u_{\mathrm{zt}}, \tag{B.34}$$

With the analytical solutions of the nonlinear differential equations of AGWs, in 2 dimensions analytical formulas are chosen for amplitudes ($u_z$, $u_h$), phase and group velocities, and the corresponding arrival time at a given time we may be able to estimate AGWs parameters quickly without performing simulation.

# APPENDIX C - CODES

## C.1 Wave decomposition and Cross-correlation code

The Signal-alam code is able to provide a time-frequency-energy description of practically any type of time series.

```
""Instituto Nacional de Pesquisas Espaciais - INPE""
from scipy.ndimage import *
import numpy as np
from pylab import *
from scipy import fftpack
from scipy.signal import *

#%%
def shift(data,n):
    e = empty_like(data)
    if n >= 0:
        e[:n] = data[n]
        e[n:] = data[:-n]
    else:
        e[n:] = data[n]
        e[:n] = data[-n:]
    return e

#%%
def find_peaks(data):
    ns=len(data)
    gr_d=gradient(data);
    a=shift(gr_d,1)*shift(gr_d,-1)
    peak_values=a[a<0]
    peak_number=len(peak_values)
    peak_pos=argwhere(a<0)[::2]
    return peak_pos


#%%
def cross_correlate(t_all,y_all,data_all):
#t_all is in hours
#y_all is in degrees
#i_smooth=1 does filtering and smoothning of data

    ny=len(t_all[:,0]);s=[];y=[];t=[]
    for i in range (ny):
        t_i=t_all[i];data_i=data_all[i];y_i=y_all[i]
```

```
#         i_1=abs(t_i-14.55).argmin();i_2=abs(t_i-19.55).argmin()
#         t_i=t_i[i_1:i_2];data_i=data_i[i_1:i_2];
#         y_i=y_i[i_1:i_2];
        s.append(data_i)
        y.append(y_i)
        t.append(t_i)

    s=array(s);t=array(t);y=array(y)

    nt=len(t[0,:]);
    print (nt,ny)
    nt2=int(nt/2);ny2=int(ny/2)

    tmx=[];ymn=[];cmx=[];ymn0=[];smx=[]
    for i in range (ny):
        for j in range (ny):
            if j!=i:
                s_mx=max(abs(s[i]).max(),abs(s[j]).max())
                cin=convolve(s[i],s[j],mode='same')#[nt-nt2:nt+nt2]
                imx=argmax(cin);imn=argmin(cin);
                tmx.append(t[j][imx])
                ymn.append(y[j][imx]-y[i][imx]);
                ymn0.append((y[j][imx]+y[i][imx])/2.);
                cmx.append(cin[imx])
                smx.append(s[i][imx])

    tmx=array(tmx);ymn=array(ymn);ymn0=array(ymn0);cmx=array(cmx)
    smx=array(smx)
    return (t,y,s,tmx,ymn,ymn0,cmx,smx)

#%%
def cross_correlate_atual(t,y,data):

    """all inputs are two dimensions numpy array with first and
    second  dimensions as for space and time resepctively. All
    entries are two-dimensional with 1 and 2 representing space and
    time respectively. Time and Space is in seconds and kilometers
    """
    t2=t;y2=y
    if len(shape(t))==1 and len(shape(y))==1:
        [t2,y2]=meshgrid(t,y)
    nt=len(t2[0,:]);ny=len(y2[:,0])

    tmx=[];ymx=[];cmx=[];vmx=[];wl_mx=[];tau=[];vel=[]
    cin_p=zeros((nt))
```

```
    tmx2=zeros((ny,nt));ymx2=zeros((ny,nt));cmx2=zeros((ny,nt));
    wl2=zeros((ny,nt));tau2=zeros((ny,nt));vel2=zeros((ny,nt));
    for i in range (1,ny-1):
        cin=0*data[i,:]
        for j in range (1,ny-1):
            if j!=i:
                for it in range (nt):
                    cin=cin+data[i,:]*data[j,it]
        if cin.any() != 0:
#             cin=cin/cin.max()
            wl=0.5*(y2[i,:]-y2[i-1,:])*(cin+cin_p)/(cin-cin_p)
            imx=find_peaks(cin)[:,0]
            tmx.append(t2[i,imx])
            tmx2[i,imx]=t2[i,imx];ymx2[i,imx]=y2[i,imx];cmx2[i,imx
]=abs(cin[imx])
            wl2[i,imx]=wl[imx];tau2[i,imx]=gradient(t2[i,imx])/2.;
            vel2[i,imx]=2*wl[imx]/gradient(t2[i,imx])
        cin_p=cin

    wl_max=y2.max()-y2.min()
    tau_min=(gradient(t2)[1]).min()/2
    vmx=wl_max/tau_min
    cmx2=cmx2/cmx2.max()
#    wl2[abs(wl2)>wl_max]=0
#    tau2[abs(tau2)<tau_min]=0
#    vel2[abs(vel2)>vmx]=0

    return (tmx2,ymx2,cmx2,wl2,tau2,vel2)

#%%
def cross_correlate_einsum(t,y,data):

    """all inputs are two dimensions numpy array with first and
    second dimensions as for space and time resepctively. All
    entries are two-dimensional with 1 and 2 representing space and
    time respectively. Time and Space is in seconds and kilometers
    """
    t2=t;y2=y
    if len(shape(t))==1 and len(shape(y))==1:
        [t2,y2]=meshgrid(t,y)
    nt=len(t2[0,:]);ny=len(y2[:,0])

    tmx=[];ymx=[];cmx=[];vmx=[];wl_mx=[];tau=[];vel=[]
    cin_p=zeros((nt))
    tmx2=zeros((ny,nt));ymx2=zeros((ny,nt));cmx2=zeros((ny,nt));
```

```
    wl2=zeros((ny,nt));tau2=zeros((ny,nt));vel2=zeros((ny,nt));
    cin=einsum('ij,kl->ij', data, data)
    wl=cin*gradient(y2)[0]/gradient(cin)[0]
    for i in range (ny):
#        if cin.any() != 0:
#            cin=cin/cin.max()
        imx=find_peaks(cin[i,:])[:,0]
        if len(imx)>1:
            tmx.append(t2[i,imx])
            tmx2[i,imx]=t2[i,imx];ymx2[i,imx]=y2[i,imx];cmx2[i,imx]=abs(cin[i,imx])
            wl2[i,imx]=wl[i,imx];tau2[i,imx]=gradient(t2[i,imx]);
            vel2[i,imx]=wl2[i,imx]/tau2[i,imx]#wl[i,imx]/gradient(t2[i,imx])

    wl_max=(y2.max()-y2.min())/2.
    tau_min=(gradient(t2)[1]).min()/2.
    vmx=wl_max/tau_min
#    cmx2=cmx2/cmx2.max()
#    wl2[abs(wl2)>wl_max]=0
#    tau2[abs(tau2)<tau_min]=0
#    vel2[abs(vel2)<vmx]=0
    return (tmx2,ymx2,cmx2,wl2,tau2,vel2)

#%%
def convolve_al(data,f):
    nd=len(data);nf=len(f);
    data_n=zeros((nd))
    if nd==nf:
        for i in range (nd):
            for j in range (i,nf):
                data_n[i]=data_n[i]+data[j]*f[i-j]
    else:
        for i in range (nd-nf):
            for j in range (nf):
                data_n[i]=data_n[i]+data[i+j]*f[j]


    #%%
    nf2=int(nf/2)
    data_n=shift(data_n,nf2)

    if nf % 2 !=0:
        nf2=nf2+1

```

```
    x=[0,nf2];y=[data[0],data_n[nf2]]
    xvals=arange(0,nf2)
    data_n[0:nf2]=interp(xvals,x,y)
##
    x=[-nf2-1,-1];y=[data_n[-nf2-1],data[-1]]
    xvals=linspace(x[0],x[-1],nf2)
    data_n[-nf2:]=interp(xvals,x,y)

#        print (nf2,x,y,xvals,data_n[-nf2],data_n[-nf2:])
    return data_n

#%%
def wave_fft(t,data):
    nt=len(t);dt=(t[1]-t[0]);dt_s=(t[-1]-t[0])
    fn=1./dt;fs=1./(1.*dt_s)
    data_sine=cos(2*pi*(t-t[0])*60./10.)
    pwr=abs(fftpack.fft(data))
    freqs=fftpack.fftfreq(len(data))*fn
    pd=1./freqs;n_fft=int(len(pd)/2.)
    pwr=pwr[:n_fft];pd=pd[:n_fft]
    pwr=abs(data).max()*pwr/pwr.max()
    return (pd,pwr)

#%%
def wave_fft_alam(t,data,n_mode):
    nt=len(t);dt=(t[1]-t[0]);dt_s=(t[-1]-t[0])
    fn=1./dt;fs=1./(1.*dt_s)
    modes=logspace(log10(2./fn),log10(nt/(2.*fn)),num=n_mode);

#    n_mode=len(modes);
    pd=[];pwr=[]
    for i in range (n_mode):
        pd_o=modes[i]
        win=cos(2.*pi*t/pd_o)
        pwr_cos=convolve(data,win)#,mode='same')
        win=sin(2.*pi*t/pd_o)
        pwr_sin=convolve(data,win)#,mode='same')
        pwr_abs=(sqrt(pwr_cos**2.+pwr_sin**2.)).mean()
        pwr.append(pwr_abs)
        pd.append(pd_o)
    pwr=array(pwr);pd=array(pd);
    pwr=abs(data).max()*pwr/abs(pwr).max()
    pwr[pwr<abs(data).max()/100.]=0
    return (pd,pwr,modes)
```

```
#%%
def wavelet(iw,t,data,n_mode): # t is in minutes
    def wave_ones():
        win=ones((int(modes[i]),))/int(modes[i]);
#         pwr=(data-real(np.convolve(data,win,mode='same')))
        pwr=(data-convolve_al(data,win))
        return pwr
    def wave_morlet():
        wo=5.;so=1
        win=morlet(modes[i],w=wo,s=so,complete=True);#pd[i]=pd[i
    ]/(2.*so*wo)
        pwr=real(np.convolve(data,win,mode='same'))
        return pwr
    def wave_hat():
        win=ricker(nt,modes[i])
        pwr=real(np.convolve(data,win,mode='same'))
        return pwr

    data_0=data
    f=wave_fft_alam(t,data,n_mode);pd_fft=f[0];pwr_fft=f[1];
    modes_fft=f[2]
    data_fft=[]
    data_fft.append([f[0],f[1]])

    nt=len(t);dt=(t[1]-t[0]);dt_s=(t[-1]-t[0])
    fn=1./dt;fs=1./(1.*dt_s)
    modes=modes_fft/dt

    pd_all=[];pwr_all=[];emd_all=[];

    for i in range (n_mode):
        if iw==0:pwr=wave_ones();data=data-pwr
        if iw==1:pwr=wave_morlet()
        if iw==2:pwr=wave_hat()

        if iw==0:
            peaks=find_peaks(pwr);
            imx=peaks[-1];imn=peaks[0];
            pd=pd_fft[i]#(t[imx]-t[imn])/(len(peaks)/2.)
            if imx==imn:
                pd=pd_prev
                #print ('NO MORE HARMONICS AFTER PERIOD, MINUTES=',
    i, pd)
                break
            if pd >=nt*dt/2.:
```

```
                #print ('NO MORE HARMONICS AFTER PERIOD, MINUTES=', i, pd)
                break
        if iw !=0:
            pd=2.*dt*modes[i];

        i_fft=abs(pd_fft-pd).argmin();
        emd=(modes_fft.mean()/pd)*pwr*pwr_fft[i_fft]/abs(pwr_fft).mean()
        pd_prev=pd
        pd_all.append(pd)
        pwr_all.append(pwr)
        emd_all.append(emd)
    #print ('Modes=',i, 'period, Minutes=',array(pd_all).min(),array(pd_all).max())
    return(array(pd_all),array(pwr_all),array(emd_all),array(data_fft))

#%%
def data_filt(t,data,tl,tu):
    dt=t[1]-t[0]
    nm1=int(tl/dt);nm2=int(tu/dt)
    if nm1==0:
        data_filt=data-np.convolve(data,ones((nm2,))/nm2,mode='same')
    else:
        data_filt=np.convolve(data,ones((nm1,))/nm1,mode='same')\
                -np.convolve(data,ones((nm2,))/nm2,mode='same')
    data_filt[:nm2]=data_filt[nm2]
    data_filt[-nm2:]=data_filt[-nm2]
    return data_filt

#%%

#dt=0.01
#t=arange(0,2.,dt);nt=len(t)
#data=0*t
#for i in range (11):
#    pd=(i+1)*2.5*dt;omega=2.*pi/pd
#    data=data+cos(omega*t)/(0+1)
#
#f=wavelet(0,t,data,32)
#pd=f[0];pwr=f[1];emd=f[2];data_fft=f[3]
#fr=1./pd;#Hz
#
```

```
##%
#fig = figure(1,figsize=(12,12))
#subplot(211)
#plot(t,data)
#i=find_peaks(data)
##plot(t[i],data[i],'ro')
#
#subplot(212)
#plot(t,data,'r',lw=4)
#plot(t,pwr[:,:].sum(0),'b',lw=2)
#plot(t,emd[:,:].mean(0),'b--')
#
##%
#figure(2,figsize=(12,12))
#subplot(212)
#for i in range (len(pd)):
#    plot(t,fr[i]+1.*emd[i,:])
#
#figure(3,figsize=(12,12))
#f=wave_fft_alam(t*60.,data,32)
#pd=f[0];pwr=f[1]
#semilogx(1.e+03/(pd*60.),pwr,'r')
#f=wave_fft(t*60,data)
#pd=f[0];pwr=f[1]
#semilogx(1.e+03/(pd*60.),pwr,'b')
#
#figure(5,figsize=(12,12))
#plot(t,data,'r-o')
#n_smooth=2
#win=ones((n_smooth,))/n_smooth#cos(2.*pi*t/(10.*dt))#ones((5,))/5
#f=convolve(data,win,mode='same')
#plot(t,f,'b-')
#f=convolve_al(data,win)
#plot(t,f,'b--')


f=load('bgis_04.npy')#TEC BGIS station PRN 19, for the 4 July 2019 Ridgecrest EQ.

tec=f[3];t=f[0,:]
fig = figure(3,figsize=(12,12),facecolor='w',edgecolor='k')
subplot(2,1,1)
plot(t,tec)
title('$\mathbf{(A)}$',x=0.05,y=0.88,fontsize=14)
ylabel('TEC, TECU')
```

```
xlim(15,19.7)
f=wavelet(2,t,tec,32)
pd=f[0];pwr=f[1];emd=f[2];
fr=1.e+03/(pd*3600.)
fr_cut=arange(3.7-5*0.6,12,0.6)

subplot(2,1,2)
title('$\mathbf{(B)}$',x=0.05,y=0.88,fontsize=14)
for i in range (len(fr_cut)):
    f1_cut=fr_cut[i]
    i_freq1=abs(fr-f1_cut).argmin();
    emd_f=emd[i_freq1]
    plot(t,0.6*emd_f+i_freq1)
    xlim(15,19.7)
    ylim(0.5,11)
    ylabel('Frequency, mHz')
    xlabel('Time, UT')
```

Listing C.1 - Signal-alam

## C.2 Fast SAI-ANA simulation code

SAI-analytical code implemented in Python during PhD. The equations used are found in Chapter 4 and are explained in more detail in Appendix B.

```
"""The SAI-ANA code is an extension of the analytical model
developed by Kherani et al (2011 https://doi.org/10.3390/atmos12060765) from the AGW wave equation of Kherani et al. (2016). The deduction of the equations and the SAI-ANA code results can be found in the doctoral thesis titled (Observational and simulation study of rapid and small amplitude ionoquake during weak to strong earthquakes). This method is subjective code can reproduce observations up to 70%-80% qualitatively."""
"""sigma_t is Gaussian packet thickness of time t_o is time when forcing reaches largest amplitude and must be greater than 2*sigma_t t_f is the final simulation time and must be more than 2*t_o"""

'''(wx,wy) are amplitudes of the AGWs in the (x,y) directions i.e. Longitudinal and transverse  (rho_o,tn_o,pn_o) are density, temperature and atmospheric pressure  (wx_m,wy_m)=(wx(t-dt,x,y),wy(t-dt,x,y)) (wx_o,wy_o)=(wx(t,x,y),wy(t,x,y) (rho_o,tn_o,pn_o)=(rho(t-dt,x,y),tn(t-dt,x,y),pn(t-dt,x,y))'''

```

```python
'''Simulation plane (X-Y) represents the plane where (+X,+Y)
    represent west OR north and vertical upwards (altitude)
    respectively.'''

from pylab import *
from numpy import *
from iri2016 import IRI
import spaceweather as sw
from nrlmsise_2000 import *
from scipy import *
from scipy.ndimage import *
from scipy.special import erf
from scipy.integrate import trapz
from signal_alam import *
from mpl_toolkits.axes_grid1 import make_axes_locatable
matplotlib.rc("mathtext",fontset="cm")
matplotlib.rc("font",family="serif",size=12)

def d1_3(n2,n3,data):
    return repeat(repeat(data[newaxis,:],n3,axis=0)[newaxis,:,:],n2
    ,axis=0)

def d1_2(n,data):
    return repeat(data[newaxis,:],n,axis=0)

def d1_23(n,data):
    return repeat(data[:,:,newaxis],n,axis=2)

def mask_b():
    mask=1+zeros((nx,ny))
    rad_m=nx/4
    for j in range (0,nx):
        if j<rad_m or j>=int(nx/2)+rad_m:
            mask[j,:]=exp(-(0.5*j/rad_m)**2.)
    return mask
def div_f(f0,f1):
    return gradient(f0)[0]/dx_m+gradient(f1)[1]/dy_m

#%%
def sum_gr(ndim,ndata,data):
    data_n=0*data

    if ndim==0:
        for j in range (ndata):
            if j==0:
```

```
                data_n[j,:]=(data[j+1,:]+data[j,:])/2.
            elif j==ndata-1:
                data_n[j,:]=(data[j-1,:]+data[j,:])/2.
            else:
                data_n[j,:]=data[j+1,:]+data[j-1,:]

    if ndim==1:
        for j in range (ndata):
            if j==0:
                data_n[:,j]=(data[:,j+1]+data[:,j])/2.
            elif j==ndata-1:
                data_n[:,j]=(data[:,j-1]+data[:,j])/2.
            else:
                data_n[:,j]=data[:,j+1]+data[:,j-1]
    return data_n
#%%
def data_antes(dim,ndim,data):
    data_n=0*data
    if dim==1:
        data_n=0*data
        data_n[1:-1]=data[0:-2]
        data_n[0]=data_n[1];data_n[-1]=data_n[-2];
    else:
        if ndim==1:
            data_n[:,1:-1]=data[:,0:-2]
            data_n[:,0]=data_n[:,1];data_n[:,-1]=data_n[:,-2];
    return data_n
#%%
def data_proximo(dim,ndim,data):
    data_n=0*data
    if dim==1:
        data_n=0*data
        data_n[1:-1]=data[2:]
        data_n[0]=data_n[1];data_n[-1]=data_n[-2];
    else:
        if ndim==1:
            data_n[:,1:-1]=data[:,2:]
            data_n[:,0]=data_n[:,1];data_n[:,-1]=data_n[:,-2];
    return data_n

#%%
def ambiente_atmos(x2,y2):
    global rho_amb,tn_amb,r_g,nu_nn,lambda_c
    global pn, sn
    df_d = sw.sw_daily()
```

```
    pos=where((df_d['year']==year)& (df_d['month']==month)&(df_d['day']==day))[0]
    ap=df_d['Apavg'][pos][0]
    f107=df_d['f107_obs'][pos][0]  #units of 1.e+22 W/m2/Hz.
    f107A=df_d['f107_81ctr_obs'][pos][0]#Centered 81-day arithmetic average of F10.7 (observed).

    d0 = datetime.date(year,1,1)
    d1 = datetime.date(year, month, day)
    delta = d1 - d0
    doy=delta.days
    ut=hour+minute/60+second/3600;lt=ut+lon_ep/15.

    f=nrl_msis(doy,ut*3600.,lt,f107A,f107,ap,lat_ep,lon_ep,dy,y[0],ny)
    tn_msis=f[1];#tn_msis=0*tn_msis+tn_msis.mean()
    den_ox=f[2]*1.e+06;den_n=f[3]*1.e+06;den_o2=f[4]*1.e+06;den_n2=f[5]*1.e+06;
    n_msis=den_ox+den_n+den_o2+den_n2;
    rho_msis=f[6]*1.e+03
    mean_mass=rho_msis/n_msis

    b_c=1.38e-23;
    rg_msis=b_c/mean_mass;
    pn_msis=rg_msis*rho_msis*tn_msis;
    sn_msis=sqrt(1.33*pn_msis/rho_msis)

    nu_msis=pi*(7*5.6e-11)**2.*sn_msis*n_msis
    visc_mu_1=3.563e-07*tn_msis**(0.71);
    visc_mu_2=1.3*pn_msis/nu_msis;
    lambda_msis=sn_msis**2./nu_msis     #thermal conductivity
    rho_amb=d1_2(nx,rho_msis)           #Mass density (kg/m3)
    tn_amb=d1_2(nx,tn_msis)             #Atmospheric temperature (K)
    sn=d1_2(nx,sn_msis)                 #speed of sound
    r_g=d1_2(nx,rg_msis)                #constante Boltzman/massa
    nu_nn=d1_2(nx,nu_msis)              #constant Boltzmann/mass
    lambda_c=d1_2(nx,lambda_msis)       #thermal conductivity
    return
def amb_iono(x2,y2):
    global no_y,n_o,nu_in,nu_0,gyro_i,b_o

    yi=y2[0,8:]
    altlim=[yi[0],yi[-1]]

```

```
    timeIRI='%s-%02d-%02d/%02d:%02d:%02d' % (year,month,day,hour,
   minute,second)
    altkm=[yi[0],yi[-1],10]

    fn=IRI(timeIRI, altkm, lat_ep, lon_ep)
    ne_iri=fn['ne'][:].data/10**12.
    ti = fn['Ti'][:].data
    te = fn['Te'][:].data
    n_o=d1_2(nx,ne_iri)
    # subplot(111)
    # semilogx(n_o[0,:], yi[:],'gray',lw=2,label='$n_o, m^{-3}$')
    # ylabel('Altitude, km')
    # title('(B)')# Ionospheric Number Density')
    # legend(fontsize=12,loc='best')
    sc_h=30.
    nu_in=1.e+03*exp(-(yi-80.)/sc_h)#The profile (in altitude) of
   the collision frequency (nu in)
    b_o=30.e-06               #the magnetic field, in Tesla
    q_c=1.6e-19;m_i=1.67e-27;z_i=16.
    gyro_i=q_c*b_o/(z_i*m_i)#the frequency of rotation of the ions
    gyro_e=-gyro_i*1837.

    return ()
#%%
def rho_tn(rho_o,tn_o,pn_o):
    div_w=0*div_f(wx_ana,wy_ana)
    div_flux=div_f(rho_o*wx_ana,rho_o*wy_ana)
    div_flux_x=wx_ana*gradient(rho_o)[0]/gradient(x2_m)[0]
    div_flux_y=wy_ana*gradient(rho_o)[1]/gradient(y2_m)[1]
    div_flux=div_flux_x+div_flux_y
    rho=rho_o-0.1*dt*div_flux

    div_flux=div_f(tn_o*wx_ana,tn_o*wy_ana)
    div_flux_x=wx_ana*gradient(tn_o)[0]/gradient(x2_m)[0]
    div_flux_y=wy_ana*gradient(tn_o)[1]/gradient(y2_m)[1]
    div_flux=div_flux_x+div_flux_y

    gma=1.33#rho_ho/rho
    tn=tn_o-0.1*dt*(div_flux+(gma-1.)*tn_o*div_w)

    div_flux=div_f(pn_o*wx_ana,pn_o*wy_ana)
    div_flux_x=wx_ana*gradient(pn_o)[0]/gradient(x2_m)[0]
    div_flux_y=wy_ana*gradient(pn_o)[1]/gradient(y2_m)[1]
    div_flux=div_flux_x+div_flux_y

```

```python
    pn=pn_o-0.1*dt*(div_flux+(gma-1.)*pn_o*div_w)/1.
    rho_t=rho_to
    rho_h=rho_ho
    return (rho,tn,pn)

#%%ANALTICAl
def AGW_ana():
    i_xo=abs(x-x.mean()).argmin()
    gma=1.33#0.33+rho_ho/rho_o#1.4#0.01+rho_ho/(rho_ho+rho_to)
    pn=pn_o#r_g*rho_o*tn_o;
    c_s=sn#sqrt(gma*pn/rho_o);#c_s=0*c_s+c_s.mean()
    gr_pn=gradient(pn)[1];dy_m2=2.*dy_m
    zeta=(1./rho_o)*gr_pn/dy_m2
    k0=zeta/c_s**2.
    k0_antes=data_antes(2,1,k0)
    k0_proximo=data_proximo(2,1,k0)

    mu=0.5*(k0_proximo+k0_antes)*dy_m2/2.
    mu=cumsum(mu,1);mu=7.*mu/abs(mu).max()

    omega_c2=(gma**2.*k0*c_s)**2./4.
    omega_b2=((gma-1)*k0**2-1.*(k0/c_s**2.)*gradient(c_s**2.)[1]/dy_m2)*c_s**2.
    i_pos=argwhere(omega_b2[i_xo,:]>=0);i_neg=argwhere(omega_b2[i_xo,:]<0)
    ob2_real=0*omega_b2;ob2_im=0*omega_b2
    ob2_real[:,i_pos]=omega_b2[:,i_pos]
    ob2_im[:,i_neg]=omega_b2[:,i_neg]
    omega_h2=wk_x**2.*c_s**2.
    omega_2=omega_b2+(wk_y**2.+0*k0**2./4.)*c_s**2.+omega_h2
    omega_mais=sqrt(omega_2+sqrt(omega_2**2.-4.*omega_h2*omega_b2))/sqrt(2)
    omega_menos=sqrt(abs(omega_2-sqrt(omega_2**2.-4.*omega_h2*omega_b2)))/sqrt(2)
    visc_mu=1.3*pn_amb/nu_nn;visc_ki=visc_mu/rho_amb
    nu_col=visc_ki*(-wk_x**2-wk_y**2.+k0**2.-gradient(k0)[1]/dy_m2)
    wx_mais=(omega_mais**2.+omega_h2-omega_2)/(wk_x*wk_y*c_s**2.)
    wx_menos=(omega_menos**2.+omega_h2-omega_2)/(wk_x*wk_y*c_s**2.)

    gamma_ad=(gma-1)*k0**2.
    gamma_e=(k0/c_s**2.)*gradient(c_s**2.)[1]/dy_m2
    return (mu,omega_mais,omega_menos,nu_col,wx_mais,wx_menos,omega_b2,\
             omega_c2,ob2_im,gamma_ad,gamma_e,c_s)
#%%ANALTICAl
```

```
def AGW_ana_x():
    gma=1.33#0.33+rho_ho/rho_o#1.4#0.01+rho_ho/(rho_ho+rho_to)
    pn=pn_o#r_g*rho_o*tn_o;
    c_s=sn#sqrt(gma*pn/rho_o);
    gr_pn=gradient(pn)[0];dx_m2=2.*dx_m
    zeta=(1./rho_o)*gr_pn/dx_m2
    k0=zeta/c_s**2.
    omega_c2=(gma**2.*k0*c_s)**2./4.
    omega_b2=((gma-1)*k0**2-0.*(k0/c_s**2.)*gradient(c_s**2.)[0]/dx_m2)*c_s**2.
    omega_h2=wk_y**2.*c_s**2.
    omega_2=omega_b2+(wk_x**2.+k0**2.)*c_s**2.+omega_h2
    omega_mais=sqrt(omega_2+sqrt(omega_2**2.-4.*omega_h2*omega_b2))/sqrt(2)
    omega_menos=sqrt(omega_2-sqrt(omega_2**2.-4.*omega_h2*omega_b2))/sqrt(2)
    return (omega_mais,omega_menos)

#============================================================
def vel(b_o,nu,gyro,wx,wy):
    global mu_p
    # |vx| | mu_p mu_h | |Ex|
    # |  |=|           | |  |
    # |vy| |-mu_h mu_p | |Ey|
    kappa=gyro/nu
    mu_p=kappa/(b_o*(1.+kappa**2.))           #PEDERSON MOBILITY
    mu_h=kappa**2./(b_o*(1.+kappa**2.))       #HALL MOBILITY
    lat=radians(-31.573)
    mag_m=8.e+15          #Tm^3
    r_ea=6.371e+06
    by=-2.*mag_m*sin(abs(lat))/r_ea**3.;
    bz=mag_m*cos(lat)/r_ea**3.;
    bx=0
    wz=0
    ey=wz*bx-wx*bz
    ex=wy*bz-wz*by
    ez=wx*by-wy*bx
#    ex=wy*b_o*cos(lat);ey=-wx*b_o*cos(lat)
    vx=mu_p*ex+mu_h*ey
    vy=mu_p*ey-mu_h*ex
    return (vx,vy)


data_sism= load('V_SISM.npy')#seismic data
t_s=3600*data_sism[0,310000:-30000:200]
```

```
vel_s=data_sism[1,310000:-30000:200]#m/s
i_max=argmax(abs(vel_s))
vel_s[0:i_max][abs(vel_s[0:i_max])<1.e-05]=0
t_s=t_s-t_s[0]
f=wavelet(2,t_s,vel_s,32)
pd=f[0];pwr=f[1];emd=f[2];amp_sism=f[3][:,1][0]
fr_sism=1.e+00/(pd)

def fonte(v_phase,v_phase_x):
    global sigma_t,t0,sigma_x,v_s
    nx=len(v_phase[:,0]);ny=len(v_phase[0,:])
    vel_ana=0
    for iw in range (len(pd)):
        idx_peaks=find_peaks(abs(emd[iw,:]))[:,0]
        n_peaks=len(idx_peaks)
        t0=t_s[idx_peaks[:]]
        amp=emd[iw,idx_peaks[:]]
        n_peaks=len(t0)
        sigma_t=pd[iw]/2.
        [tn0,yt]=meshgrid(t0,y2[0,:])#d1_2(ny,t0)
        [ampn,yt]=meshgrid(amp,y2[0,:])#d1_2(ny,amp)
        if abs(v_phase).min() !=0:
            t_phase_y=y2_m/v_phase
        else:
            t_phase_y=0+0*y2_m

        if abs(v_phase_x).min() !=0:
            t_phase_x=0*x2_m/v_phase_x+0*abs(x2)/3
        else:
            t_phase_x=0
        t_phase=t_phase_y+t_phase_x
        t_phase=t_phase.mean(0)
        tn_phase=transpose(d1_2(n_peaks,t_phase))
        f_sism=skew(t-tn_phase,tn0,sigma_t,0)
        vel_ana=vel_ana+(f_sism*ampn).sum(1)
    wy0_t=vel_s.max()*vel_ana/emd.max()

    sigma_x=(4)*dx_m*1.e-03;x_o=x2.mean();v_s=0*3.e-00;x_o=0
    f_lon=skew(x2,x_o+v_s*t,sigma_x,0)

    wy0=wy0_t*(f_lon-0*f_lon[-1,0])
    idx=abs(t_s-t).argmin()
    if t<t_s[i_max] and vel_s[idx]==0:
        wy0=0*wy0
    return wy0
```

```


#%%========================MAIN==============================

global wx_m,wy_m,wx_o,wy_o
global rho_o,tn_o,pn_o,rho_amb,tn_amb,pn_amb
global fac_amp,mask
global wk_x,wk_y
global lat_ep,lon_ep,year,month,day,hour,minute,second

#%%
lat_ep=-31.573;lon_ep=-71.674
year,month,day=2015,9,16
hour,minute,second=22,54,32
#%%
dy=10;dx=1.*dy;dt=dy/2.;  #The spatial resolutions in kilometers
y=arange(0,400+dy,dy);ny=len(y)    #The altitude range
x=arange(-100,100+dx,dx);nx=len(x) # Longitude range
[y2,x2]=meshgrid(y,x)
y2_m=y2*1.e+03;x2_m=x2*1.e+03
dy_m=dy*1.e+03;dx_m=dx*1.e+03#The spatial resolutions in meters
it=0;nt=0.1*360;t=0;t_f=dt*180
vnx=dx_m/dt;vny=dy_m/dt               #Numeric speed
#%%
wx_m=zeros((nx,ny));wy_m=zeros((nx,ny));
wx_o=0*wx_m;wy_o=0*wy_m;
time=[]
dtn3=[];wx3=[];wy3=[];wy3_ray=[];n3=[];vw3=[];data_arrival=[]
wave_all=[];data_amb=[];eta=[];pr3=[];rho3=[];tn3=[];
o_br=[];omega_all=[];gr_ci3=[]

#%%==============================================================

f=ambiente_atmos(x2,y2)
f=amb_iono(x2,y2)
f=fonte(1.*y2,y2)
g_e=(1./tn_amb)*gradient(tn_amb)[1]/gradient(y2)[1];
ln_tn=log(tn_amb[0,0])+1.33*cumsum(dy*g_e,1)
tn_new=exp(ln_tn)
data_amb.append((rho_amb[0,:],sn[0,:]))

#%%===================INTIALIZATION============================

pn_amb=r_g*rho_amb*tn_amb
rho_o=rho_amb;tn_o=tn_amb;pn_o=pn_amb
```

```
rho_to=0*rho_o;rho_ho=rho_amb

#%%ANALYTICAL SOLUTION

a_frente=1.+zeros((nx,ny))
a_tras=1.+zeros((nx,ny))
a_frente[x<0]=0
a_tras[x>=0]=0
lambda_y0=arange(2.*dy_m,ny*dy_m/3.,2*dy_m)#
lambda_x0=arange(2.*dx_m,nx*dx_m/3.,2*dx_m)
while t <=t_f/1.:
    wy_ray=zeros((nx,ny))
    wy_ana=zeros((nx,ny));wx_ana=zeros((nx,ny));
    for ik in range (len(lambda_y0)):
        lambda_x=10.*dx_m;
        lambda_y=lambda_y0[ik]
        lambda_x0=arange(lambda_y,nx*dx_m/2.,2*dx_m)
        for ikx in range (len(lambda_x0)):
            lambda_x=lambda_x0[ikx]#max(sigma_x,2*ikx*dx_m)
            wk_x=2.*pi/lambda_x;wk_y=2.*pi/lambda_y

            f=AGW_ana()
            mu=f[0];omega_mais=f[1];omega_menos=f[2];nu_col=f[3];
            wx_mais=f[4];wx_menos=f[5]
            omega_br=sqrt(f[6]);omega_ac=sqrt(f[7]);
            omega_ci=sqrt(abs(f[8]))
            gamma_ad=f[9];gamma_e=f[10]
            c_s=f[11]

            f=AGW_ana_x()
            omega_awx=f[0];omega_gwx=f[1]

            if ik==0 and ikx==ik and omega_ci.any()!=0:
                print ('CONVECTIVELY UNSTABLE GWs')
            w_amp=1
            if omega_mais.max()/(2.*pi) > 1./(2.*dt) or omega_awx.
    max()/(2.*pi) > 1./(2.*dt):
                w_amp=0
            wy_alt=exp(-mu)
            n=1.
            wy_damp=exp(1*2.*nu_col*dt/(2.*n))*exp(-lambda_c*t*wk_y
    **2.)
            wy_growth=exp(0*omega_ci*t/(2.*pi))
            #%%ACOUSTIC WAVES
```

```
            omega_aw=(1./n)*sqrt(1.-(n-1)**2./(4.*omega_mais.max()*
   t_f)**2.)*omega_mais
            #GRAVITY WAVES
            omega_gw=(1./n)*sqrt(1.-(n-1)**2./(4.*omega_menos.max()
   *t_f)**2.)*omega_menos
            omega_gw=omega_menos
            if omega_aw.any() < omega_ac.any():
                continue
            for i_wv in range (2):
                if i_wv==0:
                    omega=omega_aw
                    wx_amp=wx_mais/100.
                    omega_x=omega_awx
                if i_wv==1:
                    omega=omega_gw
                    wx_amp=wx_menos/100.
                    omega_x=omega_gwx

                x2_mv=x2_m+v_s*t*1.e+03
                v_phase=omega/wk_y;
                v_phase_x=omega_x/wk_x
                wy0=fonte(v_phase,v_phase_x);
                ondas_frente=cos(-omega*t+wk_y*y2_m+0*wk_x*x2_m)
                ondas_tras=cos(omega*t+wk_y*y2_m+0*wk_x*x2_m)
                wy_frente=wy0*ondas_frente*wy_alt*wy_damp*wy_growth
                wy_tras=wy0*ondas_tras*wy_alt*wy_damp*wy_growth
                wy_ondas=w_amp*(wy_frente+wy_tras)/2.

                v_phase_x=omega_x/wk_x
                if abs(v_phase_x).min() !=0:
                    t_phase=x2_m/v_phase_x
                else:
                    t_phase=0
                sigma_tx=2.*pi/omega_x;sigma_x2=2.*pi/wk_x

                ondas_frente=cos(-omega_x*t+wk_x*x2_mv)
                ondas_tras=cos(omega_x*t+wk_x*x2_mv)
                wy0_x=(wy_ondas.max(0)+wy_ondas)/2.
                wy_frente=wy0_x*ondas_frente
                wy_tras=wy0_x*ondas_tras
                wx_ondas=(a_frente*wy_frente+a_tras*wy_tras)*skew(
   x2_mv,0,sigma_x2,0)

                f_smooth=1.-0.9*skew(4.*x2_mv,0,sigma_x2,0)
                wy_ana=wy_ana+(wy_ondas+wx_ondas)*f_smooth
```

```
                wy_ana[:,0]=wy0[:,0]
                wx_ana=wx_ana+wx_amp*gradient(wy_ana)[0]

            #%%RAY TRACING
            omega_ray=wk_y*sn#omega_menos
            v_phase=omega_ray/wk_y
            wy0=fonte(v_phase,v_phase_x);
            ondas_tras=cos(omega_ray*t+wk_y*y2_m+wk_x*x2_m)
            wy_tras=wy0*ondas_tras*wy_alt*wy_damp

            wy_x=wy_tras.max(0)*cos(wk_x*x2_m)*pdf(wk_x*x2_m/(2.*pi))
            wy_ray=wy_ray+wy_tras+wy_x
            wy_ray[:,0]=wy0[:,0]

            if it==0:
                wave_all.append([omega_aw[0,:],omega_gw[0,:],omega_ray[0,:],\
                                 wk_x,wk_y,omega_br,omega_ac,c_s[0,:]])

#    print (omega_menos.max(),omega_mais.max())
    #%%
    f=rho_tn(rho_o,tn_o,pn_o)
    rho=f[0];tn=f[1];pn=f[2]
#    pn=r_g*rho*tn
    gma=rho_amb/rho
    print (gma.max())

#%%SIMULACAO NAO-LINEAR
    f=vel(b_o,nu_in,gyro_i,wx_ana[:,8:],wy_ana[:,8:])
    vx=f[0];vy=f[1]
    n=den_iono(n_o,vx,vy,vnx,vny)

#%%==========================TIME UPDATE===================#
    dtn=rho_amb/rho
    drho=100*(rho-rho_o)/rho_amb
    dn=abs(n-n_o)/n_o
    rho_o=rho;tn_o=tn;pn_o=pn
    n_o=n

    time.append(t/60.)
    rho3.append(rho);tn3.append(tn)
    pr3.append(pn);
    wx3.append(wx_ana)
```

```
    wy3.append(wy_ana)
    wy3_ray.append(wy_ray)
    gr_ci3.append(omega_ci)
    i_xo=abs(x-x.mean()).argmin()
    omega_all.append([omega_ac[i_xo,:],omega_br[i_xo,:],omega_ci[
   i_xo,:],\
                          gamma_ad[i_xo,:],gamma_e[i_xo,:]])
    n3.append(n)

#%%============================================================#

    print ('=============================================')
    print ("TIME=", t,'TIME_STEP=',dt)
    print ('FORCING AMPLITUDE=',round(wy0[:,0].max(),5))
    print ('AGWs Amplitudes=',round(wx_ana.max(),5),round(wy_ana.
   max(),5))
    print ('Amplification ratio=',abs(wy_alt).max())
    print ('TIDs Amplitudes %=',round(100*dn.max(),2))

    t=t+dt
    it=it+1

#%%
i_xo=abs(x-x.mean()).argmin()
t=array(time);
n3=array(n3);dn3=(len(t)/2.)*gradient(n3)[0];

wy3=array(wy3)
wx3=array(wx3)

#%% ARRIVAL TIME ESTIMATION
t_arrival=t[(abs(wy3[:,i_xo,:])>abs(wy3[:,i_xo,0]).max()).argmax(
   axis=0)]
y_arrival=y
t_arrival_0=t_arrival[abs(y_arrival-5).argmin()+1]#.min()
t_hr=t#-t_arrival_0#+t_s[0]/3660#-5

#%%
fig=figure(figsize=(12,12),facecolor='w',edgecolor='k')
ax=subplot(111)
ext=[0,t[-1],x2[0,0],x2[-1,0]]
data=wy3[:,:,0]
vm=1.e-02#data.max()/10.
plot(t,1.e+03*data[:,i_xo])
```

```
im=imshow(data.T,origin='lower',extent=ext,cmap=cm.seismic,vmin=-vm
    ,vmax=vm)
im.set_interpolation('bilinear')
axis('tight');
title('Forcante ou uplift de epicentro')
xlabel('Time, minutos');ylabel('Longitude/Latitude, km')
divider = make_axes_locatable(ax);
cax = divider.append_axes("right", size="2%", pad=0.05)
cbar=colorbar(im,cax=cax);gca().set_title('m/s')


#%% Acoustic-gravity wave amplitude
fig=figure(figsize=(14,12),facecolor='w',edgecolor='k')
ax = fig.add_subplot(121)
ax2 = ax.twiny()
ax2.plot(sn[0],y,'g',lw=3)
ax2.set_xlim(200,840)
ax2.tick_params('x',colors='g')
ax2.set_xlabel('Acoustic speed, m/s',color='g')
ylabel('Altitude,km')
grid('on')

data=5*wy3[:,:,:].mean(1)
vm=10
ext=[t_hr[0],t_hr[-1],y2[0,0],y2[0,-1]]
im=ax.imshow(data.T,origin='lower',extent=ext,cmap=cm.seismic,vmin
    =-vm,vmax=vm)
im.set_interpolation('bilinear')
ax.axis('tight');#axis((0.5,t[-1],-10,400))
ax.set_ylabel('Altitude, km')

ax.set_xlabel('Time from mainshock onset, Minutes')
title('$\mathbf{(A)}$',x=0.05,y=0.96,fontsize=14)
ax.set_xlim(-1,12)
ax.set_ylim(0,400)
ax.yaxis.set_ticks_position('both')
cbar=colorbar(im, cax =fig.add_axes([0.15, 0.85, 0.3, 0.01]),\
            orientation='horizontal')
gca().set_xlabel('$w_y, m/s$')
cbar.set_ticks(linspace(-vm,vm,5))
#%%Ionospheric density disturbance

data=20*dn3[:,:,:].mean(1).T
vm=5
ax = fig.add_subplot(122)
```

```
ax2 = ax.twiny()
ax2. plot(n3[0,i_xo,:],y[8:],'g',lw=3)
ax2.set_xlim(-0.01,1)
ax2.tick_params('x',colors='g')
ax2.set_xlabel('Electronic density profile, $Ne*10^{12}(m^{-3})$',
    color='g')
grid('on')

ext=[t_hr[0],t_hr[-1],y2[0,8],y2[0,-1]]
im=ax.imshow(100*data/(n3[:,i_xo,:].T),origin='lower',extent=ext,
          cmap=cm.seismic,vmin=-vm,vmax=vm)
im.set_interpolation('bilinear')
ax.axis('tight');
ax.set_xlabel('Time from mainshock onset, Minutes')
title('$\mathbf{(B)}$',x=0.05,y=0.96,fontsize=14)
ax.set_xlim(-1,12)
ax.set_ylim(y2[0,0],y2[0,-1])
ax.yaxis.set_label_position("right")
ax.set_ylabel('Altitude, km')
ax.yaxis.tick_right()
ax.yaxis.set_ticks_position('both')
cbar=colorbar(im, cax =fig.add_axes([0.575, 0.85, 0.3, 0.01]),\
             orientation='horizontal')
gca().set_xlabel('$\delta n/n_0, \%$')
cbar.set_ticks(linspace(-vm,vm,5))

show()
```

Listing C.2 - SAI-ANA code

## PUBLICAÇÕES TÉCNICO-CIENTÍFICAS EDITADAS PELO INPE

### Teses e Dissertações (TDI)

Teses e Dissertações apresentadas nos Cursos de Pós-Graduação do INPE.

### Notas Técnico-Científicas (NTC)

Incluem resultados preliminares de pesquisa, descrição de equipamentos, descrição e ou documentação de programas de computador, descrição de sistemas e experimentos, apresentação de testes, dados, atlas, e documentação de projetos de engenharia.

### Propostas e Relatórios de Projetos (PRP)

São propostas de projetos técnico-científicos e relatórios de acompanhamento de projetos, atividades e convênios.

### Publicações Seriadas

São os seriados técnico-científicos: boletins, periódicos, anuários e anais de eventos (simpósios e congressos). Constam destas publicações o Internacional Standard Serial Number (ISSN), que é um código único e definitivo para identificação de títulos de seriados.

### Pré-publicações (PRE)

Todos os artigos publicados em periódicos, anais e como capítulos de livros.

### Manuais Técnicos (MAN)

São publicações de caráter técnico que incluem normas, procedimentos, instruções e orientações.

### Relatórios de Pesquisa (RPQ)

Reportam resultados ou progressos de pesquisas tanto de natureza técnica quanto científica, cujo nível seja compatível com o de uma publicação em periódico nacional ou internacional.

### Publicações Didáticas (PUD)

Incluem apostilas, notas de aula e manuais didáticos.

### Programas de Computador (PDC)

São a seqüência de instruções ou códigos, expressos em uma linguagem de programação compilada ou interpretada, a ser executada por um computador para alcançar um determinado objetivo. Aceitam-se tanto programas fonte quanto os executáveis.